Computational tools for nonlinear analysis of steel and composite steelconcrete structures considering connection bahaviour : Application to buildings and bridges

Anas Alhasawi

Thèse

UNIVERSITE
BRETAGNE
LOIRE

THESE INSA Rennes
sous le sceau de l'Université Bretagne Loire
pour obtenir le titre de
DOCTEUR DE L'INSA RENNES
Spécialité : Génie Civil (Mécanique des Structures)

présentée par
Anas ALHASAWI
ECOLE DOCTORALE : *SDLM*
LABORATOIRE : *LGCGM*

Computational tools for nonlinear analysis of steel and composite steelconcrete structures considering connection behaviour: Application to buildings and bridges.

Thèse soutenue le 17.01.2017
devant le jury composé de :

Zhi-Qiang FENG
Professeur, Université d'Evry (France) / Président du jury
Jean-Pierre JASPART
Professeur, Université de Liège (Belgique) / Rapporteur
Hamid BOUCHAIR
Professeur, Université Blaise Pascal (France) / Rapporteur
Ali LIMAM
Professeur, INSA de Lyon (France) / Examinateur
Maël COUCHAUX
Maître de Conférences, INSA de Rennes (France) / Examinateur
Samy GUEZOULI
Maître de Conférences, INSA de Rennes (France) / Co-Encadrant
Mohammed HJIAJ
Professeur, INSA de Rennes (France) / Directeur de thèse

to my parents…

to my wife, my beloved daughter, my sisters and brothers

to my native country Syria

Acknowledgements

***

I would never have been able to finish my dissertation without excellent guidance, expert advice, endless patience, of my supervisor, Prof. Mohammed Hjiaj. I am also grateful to him for the time he has given me during this work. I have been extremely lucky to have a supervisor who cared so much about my work.

I would like to express my sincere gratitude to my co-supervisor, Dr. Samy Guezouli, for his encouragement, his endless support and for all the efforts he devoted supervising this research.

I would like to thank the thesis jury members for their precious time which they have spent for my thesis. I am grateful to Prof. Zhi-Qiang Feng for having accepted to be president of the thesis jury. I thank him for the scientific advice he has given. I would like to thank Prof. Jean-Pierre Jaspart and Prof. Hamid Bouchair for agreeing to be referee of my thesis manuscript and for their suggestions to improve it. I am also thankful to Prof. Ali Limam and Dr. Maël Couchaux to accept to participate to the thesis jury.

I would like to thank my colleagues and all the members of the laboratory of LGCGM for their friendly atmosphere that I always found during my PhD thesis.

I am grateful to my friends in particular Ghyath Ghafraje and Aladdin Alshahwan for their endless help. I appreciate their sincerity and their honesty. I

will not forget the continued support and hard work they have done for me.

I especially thank to my country Syria for the financial support provided for this thesis and for giving me the opportunity to continue my PhD study in France.

I gratefully acknowledge the financial support provided by the European Commission (Research Fund for Coal and Steel) through the project ROBUST-IMPACT under grant agreement RFSR-CT-2012-00029.

Finally, I owe a debt of gratitude to my parents, my wife, my sisters and brothers, in particular my big brother Ayman for his indeterminable aid and for his valuable advice. They were always supporting me and encouraging me with their best wishes.

Abstract

***

The goal of this thesis is to develop computational tools for the nonlinear analysis of steel and composite steel-concrete structures under cyclic loading taking into account the actual behaviour of joint, material and geometry non-linearities and contact conditions at the steel-to-concrete interface. In particular, our efforts focuses on typical bolted end-plate connection between steel or composite beam and steel column. The objective is to develop a new «joint finite element" able to reproduce accurately the cyclic behavior of the beam-to-column connection. Next this model is combined with a non-linear steel/composite beam element considering slip and possible uplift at the interface. The thesis consists of three major parts.

The first part deals with the behavior of a steel beam-to-column bolted end-plate connection under arbitrarily cyclic loading. The proposed model is based on an improved component method that closely follows the deformation of each component taking into account non-linearities induced by possible gap between the column flange and the end-plate. This model has been developed for a single row connection. In the case of multiple row bolted connection group effects may develop. Possible group effect between two bolt-rows has been implemented considering the model proposed by Cerfontaine based on the definition of the multi-surface yield criterion and the associated flow rule that govern deformation of equivalent springs. Only the case of perfect plasticity is considered. It is shown that the influence of the group effect is not negligible on the nonlinear response of the joint.

In the second part, we have developed a flexible co-rotational two-noded beam with generalized elasto-plastic hinges at the beam ends. It is assumed that plastic deformations concentrate at these hinges. These hinges have the ability to elongate/shorten along the beam axis and to rotate. A family of asymmetric and convex yield surfaces of super-elliptic shape is considered for the plastic behavior of the hinges. By varying the roundness factor, an infinite number of yield surface are obtained. It is shown that the nonlinear response of bolted connections subjected to both bending and tension are conveniently modeled with such a yield surface. It was observed that cyclic loading produces pinching effect, cyclic softening and ductile behavior. Advantages and limitations of the approach are discussed.

Finally, the third part is dedicated to the problem of contact at the interface of steel-concrete composite beams. A "new" finite element for composite steel-concrete beam is proposed. The beam element has 6 degrees of freedom per node. The concrete beam is allowed to separate from the steel beam. An efficient contact algorithm is proposed. The Flying node concept is introduced and used to determine the extent of the contact area within a single element and modify the mesh of the beam structure. The contact problem is solve using the Augmented Lagrangian Method. The influence of contact on the loading capacity of the beam and also its influence on some design variables are highlighted.

Key words: Steel structure, composite beam steel-concrete, bolted end-plate connections, component-based method, nonlinear analysis, cyclic loading, contact, generalized plastic hinge, co-rotational.

Résumé

***

Cette thèse a pour objectifs de développer une modélisation aussi fine que possible des structures aciers et mixtes acier-béton sous sollicitations cycliques avec prise en compte d'une part du comportement des assemblages et d'autre part des non-linéarités géométriques et du contact à l'interface acier-béton. Notre attention porte en particulier sur l'assemblage de type poutre acier/mixte sur poteau métallique par platine d'extrémité boulonnée. L'objectif étant de proposer un modèle « élément fini » d'assemblage qui reproduit aussi fidèlement que possible le comportement cyclique de ce dernier pour ensuite l'assembler à un élément fini de poutre non-linéaire acier ou mixte avec prise en compte, pour ce dernier, du soulèvement à l'interface. Le travail se compose de 3 parties distinctes.

Un premier modèle qui se base sur la méthode des composantes a été développé ayant pour objectif de suivre la déformation de chaque composante au cours des cycles et de prendre en compte les non-linéarités induites par la séparation entre la platine d'extrémité et la semelle du poteau auquel elle est boulonnée. Ce modèle type composantes, a été développé pour une rangée de boulons. Dans le cas le plus fréquent, de deux rangées de boulons, une résistance de groupe (en plus des résistances individuelles de chacune des rangées) est susceptible de se développer. Pour rendre compte de ce phénomène, nous avons implanté le modèle proposé par Cerfontaine qui repose sur la définition d'une surface de charge et une règle d'écoulement associée pour déterminer les allongements des ressorts équivalents. Seul le cas de plasticité parfaite est considéré. Il est mis en évidence que l'influence de l'effet de groupe s'avère non négligeable sur le comportement post-élastique

de l'assemblage et donc de la structure.

Dans une seconde phase, nous proposons un modèle de poutre métallique classique en grands déplacements (approche co-rotationnelle) avec rotules généralisées aux extrémités. Nous faisons l'hypothèse que les déformations plastiques sont concentrées aux rotules dont le comportement plastique est contrôlé par une surface de charge asymétrique (anisotrope) qui peut prendre différentes formes selon la valeur donnée à un facteur q dit « facteur de forme ». Chacune de ces rotules plastiques comprend un ressort longitudinal pour l'effort normal N et un ressort spiral pour le moment fléchissant M. L'interaction (M-N) entre ces deux efforts dans le domaine plastique est régie par le critère de plasticité. Le modèle de rotule plastique généralisé proposé permet de rendre compte de l'adoucissement cyclique, de la ductilité et du « pinching effect ». Nous montrons aux travers de plusieurs exemples la pertinence mais également les limites d'une telle approche. Dans une troisième partie, nous proposons un nouvel élément fini de poutre mixte (à 6 ddl par nœud) en petits déplacements avec prise en compte de la non-linéarité matérielle de la poutre ainsi que du contact entre l'acier et le béton. Une stratégie efficace de type nœud mobile (Flying Node) est proposée pour déterminer l'étendue de la surface de contact au sein d'un élément fini et d'adapter le maillage de l'élément poutre/poteau. Pour la résolution du problème de contact, la technique du Lagrangien Augmenté a été retenue. On montre que dans certaines situations, le soulèvement modifie la redistribution des efforts.

Mots-clés : Structure métallique, poutre mixte acier-béton, assemblage boulonné par platine d'extrémité, méthode des composantes, analyse non-linéaire, chargement cyclique, contact, rotule plastique généralisée, co-rotation

Contents

***

List of Figures

***

List of Tables

***

Chapter 1

Introduction

***

The development of sophisticated models for the elastic global analysis of steel and composite structures (steel and concrete) has witnessed significant development over the past two decades. In particular, joint modeling as well as partial interaction affect strongly the structure behaviour (strength and ductility) and accurate models are welcome.

This work aims to provide solutions through simple models to some of phenomena that were actually observed either in experimental tests or in advanced three dimensional numerical simulations. A good model has to reproduce as faithfully as possible the behavior of steel and composite structures and their connections to ensure correct transfer of the efforts under monotonic or cyclic loading. However these models should have a reasonable level of complexity to be used by engineers. The thesis consists of three parts each of which correspond to a journal paper.

Mechanical model for the bolted end-plate connections...

The first part deals with the modelling of bolted end-plate connection. The performance of this type of assembly has already been proven by various studies and confirmed by numerous experimental tests. This connection provides a semi-

rigid joint appreciated in the case of cyclic loading due to its dissipative character, its economic aspect and lastly, the simplicity of its execution.

This study was conducted as part of a European research project entitled ROBUSIMPACT with the collaboration of: Universität Stuttgart, Université de Liège, Università degli Studi di Trento, Rheinisch Westfälische Technische Hochschule Aachen, ArcelorMittal Belval & Differdange S.A, MS3 Materials & Systems for Safety & Security and Institut National des Sciences Appliquées de Rennes. This European project extended over a period of 36 months from 01/07/2012. The objective was to make experimental tests and numerical models to investigate the behavior of structural frames subjected to lost-column due to an impact. The robustness of the structure is the key word of the study. We were in charge of Work Package 8 untitled: development of a new joint element.

In order to propose a model of connection easy to implement and useful for the study of full-scale structures, one focuses this work on the development of a mechanical model based on the components method that is nowadays well-known and adopted by the Eurocodes (EC3 and EC4). The mechanical model to be developed must be formulated as a zero-length finite element to ease its incorporation into a finite element code. By doing so the assembly procedure with others structural elements such as beam element can be easily accomplished. In order to reproduce as closely as possible the experimentally and numerically observed phenomena, the proposed model should include the two following important phenomena:

- The separation between the end-plate and the column flange (called ”gap”). This phenomenon result in a complex behaviour under cyclic loading and has never been taken into account.

- The group behavior (of two or more rows of bolts) which is added to the individual behavior of each row. This is also to be included to reproduce the overall behavior of the connection under monotonic and cyclic loading.

The study includes the following steps:

• description of mechanical model.

- modeling the separation between the column flange and the end-plate and analysis of its effect on the cyclic behavior response of the connection.

- inserting the group effect of two bolt-rows using the plasticity formalism and performing a consistent integration.

- connecting the mechanical model to a beam to study numerically the (M-N) interaction within the joint.

Finally, one obtains a new Finite Element able to provide an accurate response of bolted joint connection for structural frames under monotonic and cyclic loading.

Simplified model for connections...

The aim of this part is to propose a simple model for the joint behaviour using the concept of generalized hinge and new yield surface for the M-N interaction. The generalized plastic hinges are modeled with combined axial and rotational springs and used to reproduce the plastification of the member including the full interaction between axial force and bending moment. A family of symmetric/asymetric and convex yield surface of super-elliptic shape is considered for the plastic behaviour of the hinges. The yield function that best fit experimental data of any type of cross-sections and materials have to be adopted for the plastic hinges. This yield surface could be selected among those obtained by varying the roundness factor 'q'. Between both hinges, the beam is assumed to remain elastic. Geometrical and material non-linearities have been considered. The use of a condensation process of internal d.o.f facilitates the incorporation of this formulation in a classic co-rotational approach. Numerical examples demonstrate the accuracy of the model in predicting the large displacement inelastic response of framed structures. Effect of the roundness factor on the ultimate load strongly depends on the structure typology. It was observed that cyclic loading produces pinching effect, cyclic softening and ductile behavior. Those effects are more pronounced with anisotropic yield criteria.

Behaviour at the steel-concrete interface...

In order to extend the proposed model of steel beam-to-column connection to a composite beam-to-steel column connection, the objective of this third part aims to propose an efficient model of steel-concrete composite beam.

The force transfer mechanisms through the steel-concrete interface insures the performance of the composite structure. Besides taking into account the slip connection at the interface (which is nowadays already assimilated), it should also include the behavior of the studs in tension in case of uplift on one hand and the contact without penetration between both materials (by the use of appropriate algorithm) in case of compression, on the other hand.

In this third part, one proposes an improvement for classical contact models usually used to model the behavior at the interface between two materials. The contact algorithm is solved in small displacements by the use of the Augmented Lagrangian Method (ALM). In addition, in order to extend the unilateral "node to node" contact to a continuous contact, a concept so-called "Flying Node Concept" (FNC) is proposed. This concept is based on the principle of an adaptive mesh updated during the non-linear iterative process.

The Finite element of composite beam with 12 degrees of freedom will be easily used to be connected a steel column to the proposed connection model developed previously.

Several approaches can be found in the literature to solve the unilateral contact problem such as: the Lagrange Multiplier Method (LMM), the Penalty Method (PM), Nitsche Method (NM) and Augmented Lagrangian Method (ALM). Although most computer codes use the PM, we prefer the ALM because it does not need to increment the penalty factor to very high values to achieve convergence; the computation time is by this fact, very reduced (especially for bridge continuous beams at real scale).

Even if the contact problem is solved with the assumption of no penetration, the algorithm should be also able to locate the zones on the beam where the uplift occurs. In these zones, the contact algorithm is not active. It should be

noted that these zones can vary along the beam during the loading history. In the zones where the contact occurs, the problem consists of minimizing the potential energy and respecting the condition of no-penetration. Numerically, if the ALM is used, one must add an equation to solve the system for each concerned node in the mesh. This equation includes the Lagrange multiplier, the penalty factor and the actual penetration. When the penalty factor increases, the Lagrange multiplier corresponding to the reaction induced by a fictive spring increases, and thereby the penetration between the two materials is reduced. When penetration is deemed eligible, the contact is considered to be corrected at this node. It is clear that each node has its one penalty factor obtained automatically.

Like the uplift, the penetration may involve a number of variable nodes during the loading history of the beam. If the actual size of the system to solve is N and the number of nodes whose the contact should be solved, at a given stage of loading is N_c, the dimension of the system becomes $(N + N_c)$. The first improvement of the proposed algorithm is to locate automatically all additional equations following those relating to the standard problem (corresponding to N) and not at the real location of the nodes involved in the system to solve. This arrangement facilitates the computational algorithm by avoiding a complex reorganization of variable size system. When, for a given load level, N_c becomes equal to zero, the system recovers its real dimension N and the load can be incremented.

The second improvement of the proposed algorithm concerns the solution for the continuous contact during the iteration process. Indeed, during the load history, it can occur for particular geometric configurations and loading cases, that the contact concerns "a line" of length $\tilde{x}$ instead of only "a node".

It is easy to show that this length may be determined using interpolation functions of the finite element of composite beam. If the calculated length of continuous contact is found not equal to zero, the length of the finite element is automatically corrected and therefore the location of the stud that remains bound to the mesh moves also.

For current version of the used program, if all continuous contacts are corrected at an actual load increment, the mesh changes in accordance with the

studs distribution along the beam. For next load increment, the contact procedure continues with the "node-to-node" algorithm and the new mesh.

This adaptive mesh leads to the final distribution of the connection and ensures that the contact can continue at the nodes of the mesh and processed by the algorithm "node-to-node".

The new algorithm have been carried out on a continuous beam of composite bridge with 2 spans (reduced scale). The result shows a good agrement, in terms of force-displacement curve, with the experimental ones. The following observations can be drawn from these numerical applications:

i. the concerned zones are those located under the concentrated loads,

ii. the penetration between both materials has been corrected,

iii. the uplift zones have been found (light uplift near the internal support),

iv. the rotations of the cross-sections under loads have been consequently corrected,

v. the slip of the studs changes also due to the contact algorithm.

Chapter 2

Bolted end-plate connection

***

Component-based model versus stress-resultant plasticity modeling of bolted end-plate connection: Numerical implementation.

This part deals with the behavior of a steel beam-to-column bolted end-plate connection under arbitrarily cyclic loading. The proposed model consists of an improved component-based approach that closely follows the joint deformation taking into account possible gap between the column flange and the end-plate. The behavior of joints with several bolt rows is described using surface plasticity in tension and a normal rule to evaluate the plastic deformation within the connection. The chapter reminds the component-based analysis and shows how to implement the proposed modifications towards the elastic-plastic formulation of the joint behavior. A first example of simulation that consists of a steel beam connected to a steel column is performed in order to to show the influence of the gap effect. A second example concerns the simulation of the joint behavior with or without the group effect. Finally, a new joint finite element was implemented and calibrated against the experimental results. These applications highlight the improvements proposed to the component-based model. This new variant remains an easy-to-implement in structural analysis codes.

2.1 Introduction

Safe and economic design of steel and composite structures requires a deep understanding of the joint response. Semi-rigid connections can provide several advantages including : economy and fabrication costs, robustness of the frames, ... Two different approaches have been adopted to model the behavior of semi-rigid connections, one can distinguish between:

- *Theoretical models:* these models propose empirical or semi-empirical Moment-Rotation curves generally fitted of experimental test data. Parameters of these models are often related to material/geometrical characteristics of the joint. They are formulated in a way to ease their implementation in a standard displacement-based analysis of frame. A nonlinear finite element analysis of frames considering the actual joint behavior provides a more accurate representation of the structure deformation and the corresponding internal forces. Significant improvements have been made to this approach since the 1980s with: Richard et al. [1] proposed to include experimental curves directly in a finite element procedure; several authors proposed multi-linear curves still dependent on a mathematical curve fitting such as: Moncarz and Gerstle [2] in 1981, Poggi and Zandonini [3] in 1985, Nethercot [4] in 1989, ... The FEM has been used to investigate the joint behavior; 2D and 3D models have been developed by different authors such as: Patel and Chen [5] in 1985 for bolted connections, Bursi and Jaspart [6] in 1997, Yang et al. [7] in 2000, Maggi et al. [8] in 2002 and more recently, Concepcion Diaz et al. [9] in 2011, Bo Yang and Kang Hai Tan [10] in 2012. All these results were used to obtain mathematical equations for the Moment-Rotation curves.

- *Mechanical models:* these models well-known as the component-based models appear as a viable alternative between semi-empirical models and complicated 3D ones. The basic idea is to distinguish within a joint a set of individual components. Each component is characterized by its own mechanical

behavior (stiffness, strength, deformability, ...). Main developments have been proposed by Jaspart [11] in 1996, Jaspart et al. [12] in 1999, Cerfontaine [13] in 2004, Del Savio et al. [14] in 2009, Bayo et al. [15] in 2006, Minas et al. [16] in 2009 and Chang et al. [17] in 2015. Component-based mechanical models use tension/compression springs connected to rigid links. Each spring reproduces the behavior of a component inside the joint resisting either in tension or in compression. The models proposed by different authors concern various types of connections (welded, double seats, bolted, ..).

Most of the above described models have been developed to describe the joint behavior under monotonic loading. Generally, these studies focused mainly on the evaluation of the resisting bending moment, the rotational stiffness and the rotational capacity (ductility) of the joint. However, some of these theoretical models were adapted to reproduce the mechanical response of connection under cyclic loading: Moncarz and Gerstle [2] in 1981 and Mazzolani [18] in 1988. In this section, The mechanical response of joints under cyclic loading has been investigated using a component-based model. Gang Shi et al. [19] undertook several experimental tests on different typologies of bolted end-plate connection. This investigation has been focused on the comparison between flush and extended end-plate configurations: considering different end-plate thicknesses, bolt diameters, number of bolts and including or not stiffeners. Some specimens have been tested under monotonic and cyclic loading. Under cyclic loading, one can observe that in case of a flush end-plate joint, the gap between the column flange and the end-plate is more significant than in case of an extended end-plate connection (specimen JD1). Pu Yang et al. [20] proposed a model for bolted extended en-plate connection to describe the joint behavior under cyclic loadings. The model includes linear springs connected to a rotational spring for beam plastic hinge on one side and a rotational spring for the column panel in shear on the other side. The simulations were compared to six full-scale experiments. One can observe that the experimental results (specimen ES-1-1/2-24a) show evidence of an end-plate separation at the bottom of the beam flange. It appears that this

separation (gap) has a significant influence on the bending moment. More recently, Da Silva et al. [21] in 2016 proposed a cyclic component-based model. The proposed model concerns steel joints subjected to a bending moment. Under cyclic loading, the proposed model included the possibility of load reversal for any rotation magnitude. The objective is to reproduce the hysteretic behavior with degradation of performance. Possible separation (gap) is not discussed. To conclude for the bolted end-plate connection, it appears that the literature does not give efficient mechanical models able to accurately reproduce the joint behavior under cyclic loading. The newly proposed model concerning this research includes two aspects that significantly influence the joint behavior:

- The separation (gap) between the column flange and the end-plate and its effect on the global behavior of the joint. This phenomenon should take into account the collapse models of the T-stub as defined in Eurocode 3 [23].

- The group effect of some bolt-rows and how to include it within the plasticity algorithm. We remind that Eurocode 3 [23] takes into account the group effect through the limit resistance of the bolt-rows only.

From a computational view point, the constitutive equations for each component are discretized using an implicit scheme and the consistent stiffness matrix for the joint is derived using a standard assemblage procedure.

2.2 Component-based analysis

The main idea of this approach is to reflect each source of deformation within the joint by a nonlinear spring and combine them within an arrangement to best reproduce the mechanical response of the connection. This method requires the following steps:

- Identification of active component,

- Evaluation of the force deformation response of each component,

Table 2.1: List and effect of different components

Symbols	**Components**
CWT	Column Web in Tension
CFB	Column Flange in Bending
EPB	End-Plate in Bending
BWT	Beam Web in Tension
BT	Bolt in Tension
CWC	Column Web in transverse Compression
BFWC	Beam Flange and Web in Compression

- Assembly of the active components for the evaluation of the whole joint response.

Fig. 2.1 shows the connection and its corresponding mechanical model. The components which contribute to the deformation of the bolted beam-to-column connection are defined in Table 2.1.

Notice: the component BWT does not appear in Fig. (2.1) because this component is considered only for the bolt-rows located between the beam flanges. Indeed, in Fig. (2.1), the joint configuration is double extended end-plate without bolt-rows between the beam flanges, so no component “BWT” in this configuration.

2.2.1 Joint Type characterisation

Each set of individual springs in series is replaced by an equivalent spring denoted ”Type”, in order to distinguish with individual components denoted ”component” (see Fig. 2.1). Each equivalent spring is identified with a label depending on its location. The corresponding activation mode (tension or compression) is highlighted. Each Type can be defined as follows:

- $T2$ and $T4$ are the compression equivalent springs located at the beam flanges.

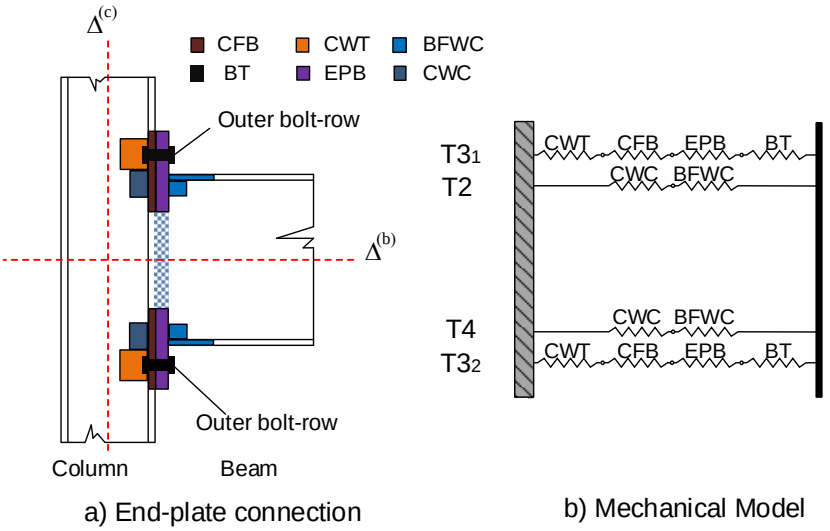

Figure 2.1: Components effects and corresponding springs - equivalent springs "$Types, r$"

They both contain the same components. $T2$ is located at the top beam flange level and $T4$ at the bottom one.

- $T3_i$ concerns bolt-rows $i = 1, ..., m$ that work only in tension. During the cyclic loading only the bolt-rows being in tension are activated, the others are temporarily disabled.

The force-displacement relationship of each Type within the joint may be characterized by a bi-linear, tri-linear or non-linear curve. In this study, we consider a bi-linear elastic perfectly plastic model obtained by assembling all relevant components. Each component (individual spring) behave elastically except the end-plate and the column flange in bending which have an elastic-perfectly plastic behaviour. For each component "α" the initial stiffness k^{α} and the plastic resistance F^{α}_{Rd} are calculated according to Eurocode 3 [23]. Considering the index "T" related to "Type" and "r" to its number, the plastic strength for each Type $F_{Tr,Rd}$ is the minimum between individual plastic resistances of the concerned components: $F_{Tr,\ Rd} = \underset{\alpha=1,...,n_c}{Min}\ (F^{\alpha}_{Rd})$, where n_c is the number of components in the

corresponding Type. The stiffness of the Type k_{Tr} can be calculated as follows:

- The stiffness of $T2$ (or $T4$) is obtained by condensing out the internal degree of freedom (Fig. 2.2).

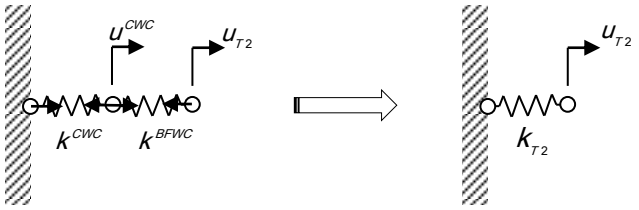

Figure 2.2: Equivalent component - T2 (or T4)

$$k_{T2/T4} = \frac{1}{\sum\limits_{\alpha}^{n_c} \frac{1}{k^{\alpha}}} = \frac{1}{\frac{1}{k^{CWC}} + \frac{1}{k^{BFWC}}} = \frac{k^{BFWC} k^{CWC}}{k^{BFWC} + k^{CWC}} \tag{2.1}$$

- The stiffness of $T3_i$ is obtained by condensing out internal degrees of freedom (Fig. 2.3). The index "i" is added for each Type 3 including bolt-rows and corresponding number in the joint ($i = 1$ for the top bolt-row, $i = m$ for the last bottom bolt-row).

$$k_{T3_i} = \frac{1}{\sum\limits_{\alpha}^{n_c} \frac{1}{k^{\alpha}}} = \frac{1}{\frac{1}{k^{CWT}} + \frac{1}{k^{CFB}} + \frac{1}{k^{EPB}} + \frac{1}{k^{BT}}} \tag{2.2}$$

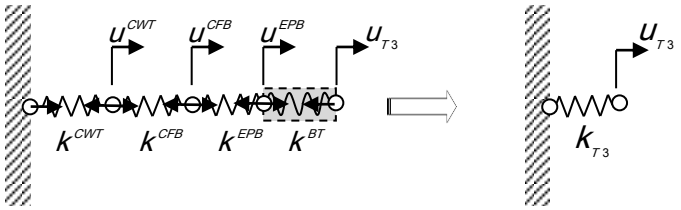

Figure 2.3: Equivalent component - $T3_i$

2.3 Mechanical model formulation

The proposed mechanical model consists of two rigid links, the left one represents the column web centerline and the right one represents the end-beam line. These lines are connected by series of springs that are replaced by spring Types: T_r. The

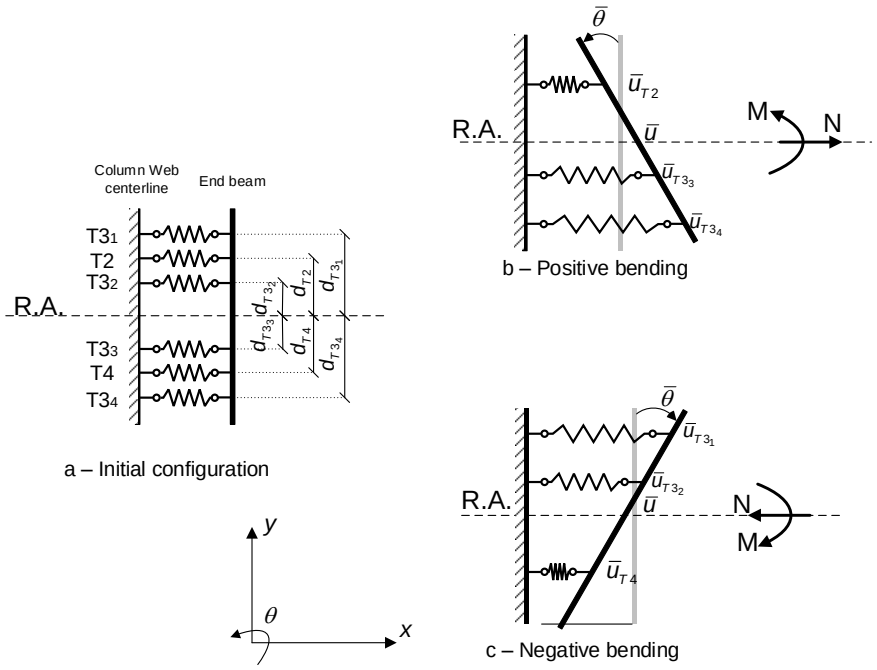

Figure 2.4: Proposed mechanical model

details of the proposed mechanical model are given in Fig. 2.4 and an example of a deformed state in both cases negative and positive bending (Fig. 2.4b and Fig. 2.4c). The index i of the bolt-row begins from the top. In case of negative bending, only $T3_1$, $T3_2$ and $T4$ are activated and the others are temporarily disabled. At each "r" level, the lengthening (shortening) $\bar{u}_{Tr}$ are highlighted and at the reference axis ($R.A.$) the global variables of the joint are represented by the couple $(\bar{u}, \theta)$: axial displacement and relative rotation. These variables are related to the applied loads (N, M): axial force and bending moment, respectively. In the case of positive bending, Fig. (2.4b), $T3_3$, $T3_4$ and $T2$ will be activated and

the others will be disabled. The global force vector is defined as follows:

$$\mathbf{F} = \left\{ \begin{array}{cc} N & M \end{array} \right\}^T \tag{2.3}$$

and corresponding global displacement vector is:

$$\boldsymbol{U} = \left\{ \begin{array}{cc} \bar{u} & \bar{\theta} \end{array} \right\}^T \tag{2.4}$$

The displacement of each Tr can be geometrically calculated assuming small local rotations, as follows:

$$\bar{u}_{T3_i} = \bar{u} - d_{T3_i}\,\bar{\theta} \quad \Leftrightarrow \quad \bar{u}_{T3_i} = \left\{ \begin{array}{cc} 1 & -d_{T3_i} \end{array} \right\} \boldsymbol{U} \tag{2.5}$$

$$\bar{u}_{T2} = \bar{u} - d_{T2}\,\bar{\theta} \quad \Leftrightarrow \quad \bar{u}_{T2} = \left\{ \begin{array}{cc} 1 & -d_{T2} \end{array} \right\} \boldsymbol{U} \tag{2.6}$$

In the above equations, d_{Tr} are the vertical coordinates of the corresponding Type r, positive value for the Type above the reference axis and negative value for those under the reference axis.

The stiffness matrix of the mechanical model is obtained by the use of the principle of virtual work. The equilibrium equation between the variation of the internal virtual work, δW^{int}, and external one , δW^{ext} is defined by:

$$\delta W^{\text{int}} = \delta W^{ext} \tag{2.7}$$

where:

$$\delta W^{\text{int}} = \sum_r \delta \bar{\boldsymbol{u}}_{Tr}^T \boldsymbol{k}_{Tr}\, \bar{\boldsymbol{u}}_{Tr} + \sum_i^n \delta \bar{\boldsymbol{u}}_{T3_i}^T \boldsymbol{k}_{T3_i}\, \bar{\boldsymbol{u}}_{T3_i} \tag{2.8}$$

The first term of Eq. (2.8) corresponds to the virtual work of activated top or bottom beam flange rows ($r = 2$ or 4), whilst the second term represents the virtual work of all activated bolt-rows.

External virtual work is given by:

$$\delta W^{ext} = \delta \mathbf{U}^T \mathbf{F} \tag{2.9}$$

replacing Eg.(2.5) into Eq. (2.8) and substituting it with Eq. (2.9) into Eq. (2.7), it leads to:

$$\left[\begin{array}{cc} C_{11} & C_{12} \\ C_{12} & C_{22} \end{array} \right] \left\{ \begin{array}{c} \bar{u} \\ \bar{\theta} \end{array} \right\} = \left\{ \begin{array}{c} N \\ M \end{array} \right\} \tag{2.10}$$

where:

$$C_{11} = \sum_r k_{Tr} + \sum_i^m k_{T3_i}$$
$$C_{12} = -\sum_r k_{Tr} d_{Tr} - \sum_i^m k_{T3_i} d_{T3_i}$$
$$C_{22} = \sum_r k_{Tr} d_{Tr}^2 + \sum_i^m k_{T3_i} d_{T3_i}^2$$

The model uses a displacement control procedure to solve the non-linear system of equations, Eq. (2.10), (mechanical non-linearity).

2.4 Cyclic behaviour of bolted end-plate connection

A general model of a beam-to-column joint should include a component related to the column shear deformation, Fig. 2.5. The total rotation of the end-beam cross-section is therefore the sum of the column centerline rotation γ and the end-beam cross-section rotation relatively to column centerline θ. During cycling loading, each activated bolt-row is loaded in tension and it elongates according to its own stiffness. In the elastic domain, the gap vanishes once the equivalent spring is unloaded. By increasing the load, if the end-plate or the column flange component is in plastic range, a permanent gap appears. An accurate component-based model should be able to follow the evolution of this gap and the deformation during the loading history.

The gap rotation is provided by relative deformation of the end-pate in bending, the column flange in bending and the bolt in tension. This individual components that related to the gap rotation are characterized in the component method based on the T-stub model. An example of 3D finite element simulation show clearly

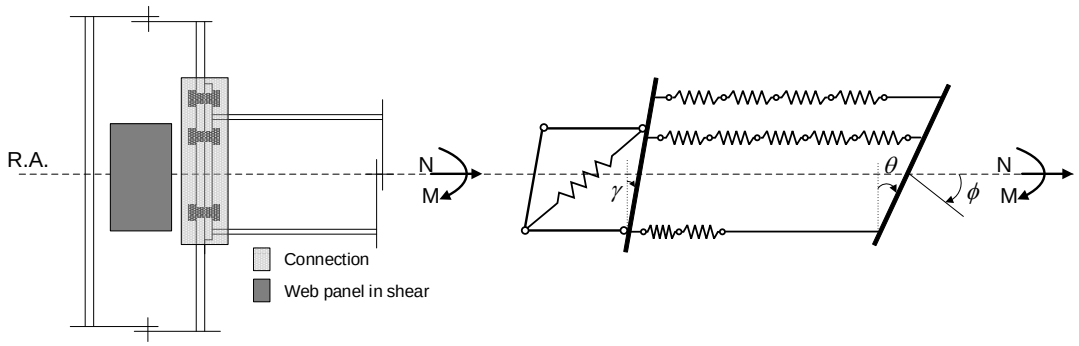

Figure 2.5: General mechanical model for the joint

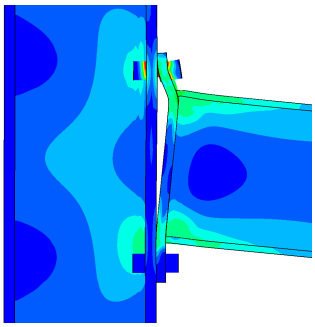

Figure 2.6: The gap - 3D finite element model

that a gap might occur between the column flange and the end-plate due to plastic deformations (Fig. 2.6).

2.4.1 Joint mechanical response during cyclic loading

In the aim to simplify the analysis of the joint behaviour under cyclic loading, the case of two bolt-rows is considered. This analysis could be easily extended to the case of more then two bolt-rows.
It is worth to mention that the specimen is loaded firstly by a negative rotation Fig. 2.7 followed by a positive rotation Fig. 2.8. The following stages can be distinguish:

- Stage 1 - loading in negative bending: top bolt-row $T3_1$ is in tension. Assuming that the gap at this top level g_t occurs due to plastic deformations of one or both components (EPB and/or CFB see Table 2.1) of $T3_1$.

- Stage 2 - unloading from negative bending: previous plastic deformation remain permanent in corresponding component(s). In order to close the gap g_t, a slip must occur in the behaviour curve $(F_{T3_1} - \bar{u}_{T3_1})$, Fig. 2.7(c). This slip allows the bottom bolt-row $T3_2$ to be activated.

- Stage 3 - loading in positive bending: bottom bolt-row $T3_2$ is in tension and the top one $T3_1$ is disabled. Assuming that the gap at this bottom level g_b occurs due to plastic deformations of one or both components (EPB and/or CFB see Table 2.1).

- Stage 4 - unloading from positive bending (and finish one cycle): in order to close the gap g_b, a slip must occur in the behaviour curve $(F_{T3_2} - \bar{u}_{T3_2})$, Fig. 2.8(f).

Starting the next cycle loading both gaps (g_t and g_b) must be closed before to allow the activation of concerned Type. This remark is represented as slips in the behaviour model. Following loading-unloading cycles use the same procedure taking care to close previously the gaps.

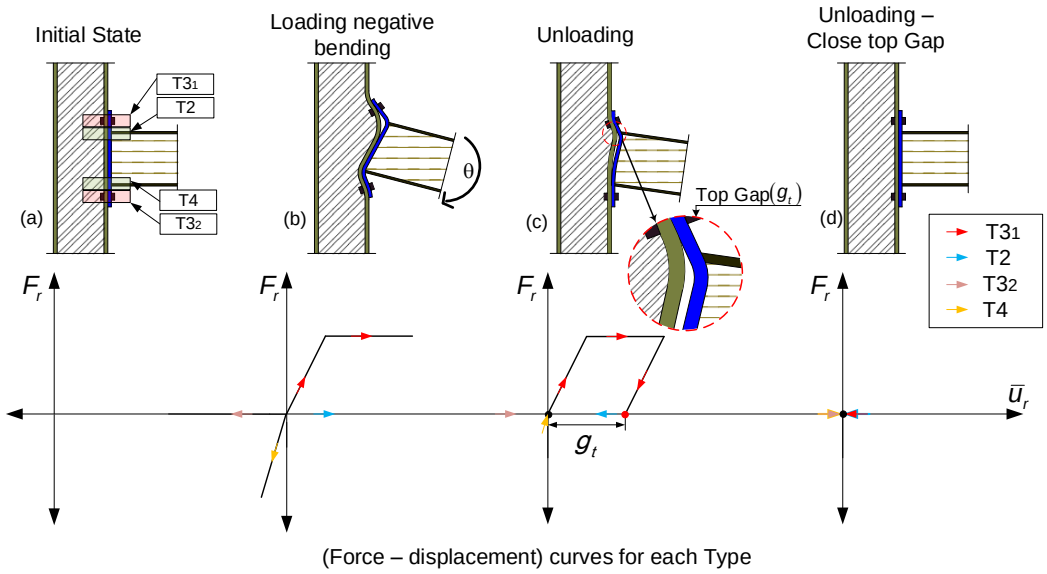

Figure 2.7: First Loading-Unloading stage (half cycle)

2.5 Group of bolt-rows effect

Cerfontaine [13] proposed to consider the group of bolt-rows effect by the use of a multi-linear failure criterion based on the lower bound theorem of limit analysis applied to the joint. In this section, it is proposed to show how to take into account this effect through plasticity modeling.

Assuming normality and associate rules, the plastic flow direction is given by the gradient to the yield surface. Plastic elongation and normal force are evaluated for each bolt-row within a group and the model provides automatically plastic redistribution of this forces within the group of bolt-rows during the loading. It is worth to mention that, the theory that developed for the case of 2 bolt-rows per group is presented in section 2.5.1 and that one for more than two bolt-rows per group is demonstrated in section 2.5.2.

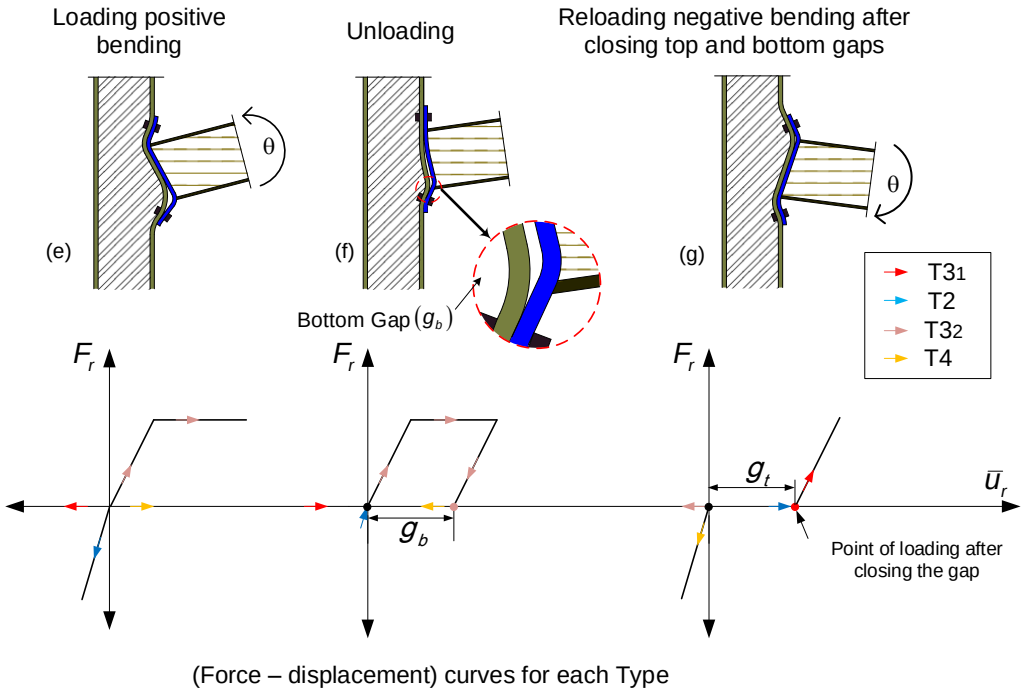

Figure 2.8: Second Loading-Unloading stage (complete cycle) - Beginning of second cycle

2.5.1 Group of two bolt-rows

The proposed formulation is detailed for the case of the group of two bolt-rows ($T3_1$ and $T3_2$)(Fig. 2.9) and will be generalized for groups with more than two bolt-rows.

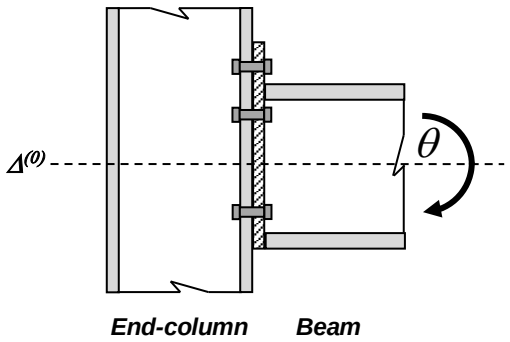

Figure 2.9: Extended end-plate connection

2.5.1.1 Yield surface definition

The yield criteria depend on three lines (see Fig. 2.10). Horizontal and vertical yield lines (Φ_1 and Φ_2) correspond individual strength of each bolt-rows and third line (Φ_3) corresponds to the group strength. Eurocode 3 part 1.8 provides the method to calculate specific strengths. We denote $F_{T3_1,Rd}$ and $F_{T3_2,Rd}$: individual strength of the bolt-rows $T3_1$ and $T3_2$ respectively, and $F_{12,Rd}$ is the strength of the group of these bolt-rows.

The group effect of two bolt-rows creates five zones that can be distinguished as shown in Fig. 2.10:

- The lines (Φ_1, Φ_2 and Φ_3) that allow to respect the yield criteria are defined by the following equations:

$$\begin{aligned} &\Phi_1\left(F_{T3_1}, F_{T3_1,\,Rd}\right) = F_{T3_1} - F_{T3_1,Rd} \\ &\Phi_2\left(F_{T3_2}, F_{T3_2,\,Rd}\right) = F_{T3_2} - F_{T3_2,Rd} \\ &\Phi_3\left(F_{T3_1},\, F_{T3_2},\, F_{12,\,Rd}\right) = F_{T3_1} + F_{T3_2} - F_{12,Rd} \end{aligned} \quad . \tag{2.11}$$

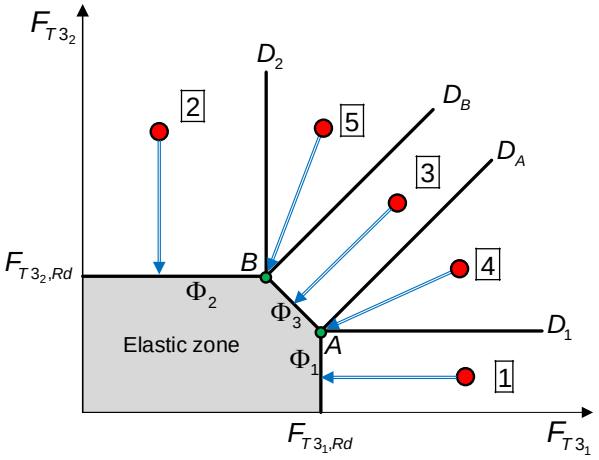

Figure 2.10: Yield surface for 2 bolt-rows per group

- and the lines that allow to respect normal projections:
  - The lines D_A and D_B separate respectively the zones (3 and 4) and the zones (3 and 5).
  - The lines D_1 and D_2 separate respectively the zones (1 and 4) and the zones (2 and 5). As-soon-as the trial force is known, appropriate projection is automatically detected. For this aim, firstly the coordinates of the points A and B are obtained using:

$$F_{1A} = F_{T3_1,Rd} \qquad F_{1B} = F_{12,Rd} - F_{T3_2,Rd}$$
$$F_{2A} = F_{12,Rd} - F_{T3_1,Rd} \qquad F_{2B} = F_{T3_2,Rd}$$

Therefore, the lines (D_A, D_B, D_1 and D_2) are defined as follows:

$$D_A\left(F_{T3_1},\, F_{T3_2}\right) = F_{T3_1} - F_{T3_2} - \left(2F_{T3_1,\,Rd} - F_{12,\,Rd}\right) \tag{2.12}$$
$$D_B\left(F_{T3_1},\, F_{T3_2}\right) = F_{T3_1} - F_{T3_2} + \left(2F_{T3_2,\,Rd} - F_{12,\,Rd}\right) \tag{2.13}$$
$$D_1\left(F_{T3_2}\right) = F_{T3_2} - \left(F_{12,\,Rd} - F_{T3_1,Rd}\right) \tag{2.14}$$
$$D_2\left(F_{T3_1}\right) = F_{T3_1} - \left(F_{12,\,Rd} - F_{T3_2,\,Rd}\right) \tag{2.15}$$

Finally, the different zones are defined as follows:

- Elastic zone: the following inequations respect the behaviour of the bolt-rows remain to in the elastic range.

$$\begin{cases} \Phi_1\left(F_{T3_1}, F_{T3_1,\,Rd}\right) \leq 0 \\ \Phi_2\left(F_{T3_2}, F_{T3_2,\,Rd}\right) \leq 0 \\ \Phi_3\left(F_{T3_1},\ F_{T3_2},\ F_{12,\,Rd}\right) \leq 0 \end{cases} \Rightarrow \begin{cases} \Delta\bar{u}_{T3_1,\,p} = 0 \\ \Delta\bar{u}_{T3_2,\,p} = 0 \end{cases} \tag{2.16}$$

  Herein $\Delta\bar{u}_{T3_1,\,p}$ and $\Delta\bar{u}_{T3_2,\,p}$ represent respectively the plastic deformation for the first and second bolt-rows.

- Zone 1: it is limited by the lines Φ_1 and D_1. The corresponding criterion must respect the following inequations:

$$\begin{cases} \Phi_1\left(F_{T3_1}, F_{T3_1,\,Rd}\right) \geq 0 \\ D_1\left(F_{T3_2}\right) \leq 0 \end{cases} \Rightarrow \begin{cases} \Delta\bar{u}_{T3_1,\,p} = \Delta\lambda_1 \frac{\partial\Phi_1}{\partial F_{T3_1}} \\ \Delta\bar{u}_{T3_2,\,p} = 0 \end{cases} \tag{2.17}$$

- Zone 2: it is limited by the lines Φ_2 and D_2. The corresponding criterion must respect the following inequations:

$$\begin{cases} \Phi_2\left(F_{T3_2}, F_{T3_2,\,Rd}\right) \geq 0 \\ D_2\left(F_{T3_1}\right) \leq 0 \end{cases} \Rightarrow \begin{cases} \Delta\bar{u}_{T3_1,\,p} = 0 \\ \Delta\bar{u}_{T3_2,\,p} = \Delta\lambda_2 \frac{\partial\Phi_2}{\partial F_{T3_2}} \end{cases} \tag{2.18}$$

- Zone 3: it is limited by the lines Φ_3, D_A and D_B. The corresponding criterion must respect the following inequations:

$$\begin{cases} \Phi_3\left(F_{T3_1}, F_{T3_2}, F_{12,Rd}\right) \geq 0 \\ D_A\left(F_{T3_1}, F_{T3_2}, F_{T3_1,\,Rd}, F_{12,\,Rd}\right) \leq 0 \\ D_B\left(F_{T3_1}, F_{T3_2}, F_{T3_2,\,Rd}, F_{12,\,Rd}\right) \geq 0 \end{cases} \Rightarrow \begin{cases} \Delta\bar{u}_{T3_1,\,p} = \Delta\lambda_3 \frac{\partial\Phi_3}{\partial F_{T3_1}} \\ \Delta\bar{u}_{T3_2,\,p} = \Delta\lambda_3 \frac{\partial\Phi_3}{\partial F_{T3_2}} \end{cases} \tag{2.19}$$

- Zone 4: the projection reaches directly the point A, this zone is limited by the lines Φ_1, Φ_3, D_A and D_1. The corresponding criterion must respect the

following inequations:

$$\begin{cases} \Phi_1\left(F_{T3_1}, F_{T3_1,\,Rd}\right) > 0 \\ \Phi_3\left(F_{T3_1}, F_{T3_2}, F_{12,\,Rd}\right) > 0 \\ D_A\left(F_{T3_1}, F_{T3_2}, F_{T3_1,\,Rd}, F_{12,\,Rd}\right) > 0 \\ D_1\left(F_{T3_2}\right) > 0 \end{cases} \Rightarrow \begin{cases} \Delta\bar{u}_{T3_1,\,p} = \Delta\lambda_1 \frac{\partial \Phi_1}{\partial F_{T3_1}} + \Delta\lambda_3 \frac{\partial \Phi_3}{\partial F_{T3_1}} \\ \Delta\bar{u}_{T3_2,\,p} = \Delta\lambda_3 \frac{\partial \Phi_3}{\partial F_{T3_2}} \end{cases} \tag{2.20}$$

- Zone 5: the projection reaches directly the point B, this zone is limited by the lines Φ_2, Φ_3, D_B and D_2. The corresponding criterion must respect the following inequations:

$$\begin{cases} \Phi_2\left(F_{T3_2}, F_{T3_2,\,Rd}\right) > 0 \\ \Phi_3\left(F_{T3_1}, F_{T3_2}, F_{12,\,Rd}\right) > 0 \\ D_B\left(F_{T3_1}, F_{T3_2}, F_{T3_2,\,Rd}, F_{12,\,Rd}\right) < 0 \\ D_2\left(F_{T3_1}\right) > 0 \end{cases} \Rightarrow \begin{cases} \Delta\bar{u}_{T3_1,\,p} = \Delta\lambda_3 \frac{\partial \Phi_3}{\partial F_{T3_1}} \\ \Delta\bar{u}_{T3_2,\,p} = \Delta\lambda_2 \frac{\partial \Phi_2}{\partial F_{T3_2}} + \Delta\lambda_3 \frac{\partial \Phi_3}{\partial F_{T3_2}} \end{cases} \tag{2.21}$$

2.5.1.2 Incremental algorithm of projection

In accordance with the previous definition of different zones, incremental plasticity algorithm [25] can be established for zone 1 to zone 5:

- Zone 1: in this case, $T3_1$ is in the plastic range:

$$\Phi_1^{n+1} = F_{T3_1}^{n+1} - F_{T3_1,Rd} > 0 \tag{2.22}$$

whilst $T3_2$ as-well-as the group of ($T3_1$ and $T3_2$) are in the elastic range:

$$\begin{aligned} \Phi_2^{n+1} &= F_{T3_2}^{n+1} - F_{T3_2,Rd} \leq 0 \;\Rightarrow\; k_{T3_2}^{n+1} = k_{e2} \\ \Phi_3^{n+1} &= F_{T3_1}^{n+1} + F_{T3_2}^{n+1} - F_{12,\,Rd} \leq 0 \end{aligned} \tag{2.23}$$

Herein k_{e2} is the elastic stiffness of $T3_2$, Eq. (2.2).
The current force in the $T3_1$ at (n+1) increment is given as:

$$\begin{aligned} F_{T3_1}^{n+1} &= k_{e1}\left(\bar{u}_{T3_1}^{n+1} - \bar{u}_{T3_1,\,p}^{n+1}\right) \\ &= F_{T3_1,\,trial}^{n+1} - k_{e1}\Delta\lambda_1 \end{aligned} \tag{2.24}$$

where k_{e1} is the elastic stiffness of $T3_1$, Eq. (2.2).
The yield function becomes:

$$\Phi_1^{n+1} = \left(F_{T3_1,\,trial}^{n+1} - k_{e1}\Delta\lambda_1\right) - F_{T3_1,\,Rd} = 0 \tag{2.25}$$

- The increment of plastic multiplier:

$$\Delta\lambda_1 = \frac{\Phi_{1,\,trial}^{n+1}}{k_{e1}} \tag{2.26}$$

- The tangent stiffness

Derivation of Eq. (2.24) gives:

$$k_{T3_1}^{n+1} = \frac{\partial F_{T3_1}^{n+1}}{\partial \bar{u}_{T3_1}^{n+1}} = \frac{\partial F_{T3_1,\,trial}^{n+1}}{\partial \bar{u}_{T3_1}^{n+1}} - \frac{\partial \Delta\lambda_1}{\partial \bar{u}_{T3_1}^{n+1}} k_{e1} \tag{2.27}$$

Substituting Eq. (2.26) into Eq. (2.27) leads to:

$$k_{T3_1}^{n+1} = 0 \tag{2.28}$$

- Zone 2: in this case, $T3_1$ and the group of ($T3_1$ and $T3_2$) are in the elastic domain:

$$\begin{aligned} \Phi_1^{n+1} &= F_{T3_1}^{n+1} - F_{T3_1,Rd} \leq 0 \Rightarrow k_{T3_1}^{n+1} = k_{e1} \\ \Phi_3^{n+1} &= F_{T3_1}^{n+1} + F_{T3_2}^{n+1} - F_{12,Rd} \leq 0 \end{aligned} \tag{2.29}$$

whilst $T3_2$ is in the plastic range:

$$\Phi_2^{n+1} = F_{T3_2}^{n+1} - F_{T3_2,Rd} > 0 \tag{2.30}$$

The same procedure as for the first bolt-row is followed for the second bolt-row, therefore we can define

- The increment of plastic multiplier:

$$\Delta\lambda_2 = \frac{\Phi_{2,\,trial}^{n+1}}{k_{e2}} \tag{2.31}$$

- The tangent stiffness

$$k_{T3_2}^{n+1} = 0 \tag{2.32}$$

- Zone 3: the group criterion is activated:

$$\Phi_3^{n+1} = F_{T3_1}^{n+1} + F_{T3_2}^{n+1} - F_{12,\,Rd} > 0 \tag{2.33}$$

Trial force of the group ($T3_1$ and $T3_2$)

$$F_{12,\,trial}^{n+1} = F_{T3_1,\,trial}^{n+1} + F_{T3_2,\,trial}^{n+1} \tag{2.34}$$

and corrected force is:

$$\begin{aligned} F_{12}^{n+1} &= F_{T3_1}^{n+1} + F_{T3_2}^{n+1} \\ &= k_{e1}\left(\bar{u}_{T3_1}^{n+1} - \bar{u}_{T3_1,p}^{n+1}\right) + k_{e2}\left(\bar{u}_{T3_2}^{n+1} - \bar{u}_{T3_2,p}^{n+1}\right) \\ &\Rightarrow F_{12}^{n+1} = F_{12,\,trial}^{n+1} - \Delta\lambda_3\left(k_{e1} + k_{e2}\right) \end{aligned} \tag{2.35}$$

where: $F_{12,\,trial}^{n+1} = F_{T3_1,\,trial}^{n+1} + F_{T3_2,\,trial}^{n+1}$
The yield function can be written as follows:

$$\Phi_3^{n+1} = F_{12,\,Trial}^{n+1} - \Delta\lambda_3\left(k_{e1} + k_{e2}\right) - F_{12,\,Rd} = 0$$

- The increment of plastic multiplier:

$$\Delta\lambda_3 = \frac{\Phi_{3,\,Trial}^{n+1}}{k_{e1} + k_{e2}} \tag{2.36}$$

where: $\Phi_{3,\,trial}^{n+1} = F_{T3_1,\,trial}^{n+1} + F_{T3_2,\,trial}^{n+1} - F_{12,\,Rd}$

- The tangent stiffness:

  i. Tangent stiffness for $T3_1$ is given by:

$$k_{T3_1}^{n+1} = \frac{\partial F_{T3_1}^{n+1}}{\partial \bar{u}_{T3_1}^{n+1}} = \frac{\partial F_{T3_1,\,trial}^{n+1}}{\partial \bar{u}_{T3_1}^{n+1}} - k_{e1}\frac{\partial\left(\Delta\lambda_3\right)}{\partial \bar{u}_{T3_1}^{n+1}} = \frac{k_{e1}k_{e2}}{k_{e1} + k_{e2}} \tag{2.37}$$

  ii. Tangent stiffness for $T3_2$ is given by:

$$k_{T3_2}^{n+1} = \frac{\partial F_{T3_2}^{n+1}}{\partial \bar{u}_{T3_2}^{n+1}} = \frac{\partial F_{T3_2,\,trial}^{n+1}}{\partial \bar{u}_{T3_2}^{n+1}} - k_{e2}\frac{\partial\left(\Delta\lambda_3\right)}{\partial \bar{u}_{T3_2}^{n+1}} = \frac{k_{e1}k_{e2}}{k_{e1} + k_{e2}} \tag{2.38}$$

- Zone 4: in this case we have:

$$\begin{aligned}\Phi_1^{n+1} &= F_{T3_1}^{n+1} - F_{T3_1,\,Rd} > 0\\ \Phi_3^{n+1} &= F_{T3_1}^{n+1} + F_{T3_2}^{n+1} - F_{12,\,Rd} > 0\end{aligned} \tag{2.39}$$

The yield function is written as:

$$\begin{aligned}\Phi_1^{n+1} &= F_{T3_1,\,trial}^{n+1} - k_{e1}\Delta\lambda_1 - k_{e1}\Delta\lambda_3 - F_{T3_1,\,Rd} = 0\\ &\Rightarrow k_{e1}\Delta\lambda_1 + k_{e1}\Delta\lambda_3 = \Phi_{1,\,trial}^{n+1}\end{aligned} \tag{2.40}$$

On the other side, the yield surface function Φ_3 can be defined as follows:

$$\begin{aligned}\Phi_3^{n+1} &= F_{T3_1,\,trial}^{n+1} - k_{e1}\Delta\lambda_1 - k_{e1}\Delta\lambda_3 + F_{T3_2,\,trial}^{n+1} - k_{e2}\Delta\lambda_3 - F_{12,\,Rd}\\ &\Rightarrow k_{e1}\Delta\lambda_1 + \Delta\lambda_3\left(k_{e1} + k_{e2}\right) = \Phi_{3,\,trial}^{n+1}\end{aligned} \tag{2.41}$$

Combining the last equations of Eqs. (2.40) and (2.41), we obtain:

$$\begin{bmatrix} k_{e1} & k_{e1} \\ k_{e1} & k_{e1}+k_{e2} \end{bmatrix} \begin{Bmatrix} \Delta\lambda_1 \\ \Delta\lambda_3 \end{Bmatrix} = \begin{Bmatrix} \Phi_{1,\,trial}^{n+1} \\ \Phi_{3,\,trial}^{n+1} \end{Bmatrix} \tag{2.42}$$

Solving Eq. (2.42) leads to:

- Plastic multipliers:

  i.

$$\Delta\lambda_1 = \frac{\Phi_{1,\,trial}^{n+1}\left(k_{e1}+k_{e2}\right) - \Phi_{3,\,trial}^{n+1}k_{e1}}{k_{e1}k_{e2}} \tag{2.43}$$

  ii.

$$\Delta\lambda_3 = \frac{\Phi_{3,\,trial}^{n+1} - \Phi_{1,\,trial}^{n+1}}{k_{e2}} \tag{2.44}$$

- Tangent stiffness:

  i. Tangent stiffness for $T3_1$ is defined by:

$$k_{T3_1}^{n+1} = \frac{\partial F_{T3_1}^{n+1}}{\partial \bar{u}_{T3_1}^{n+1}} = \frac{\partial F_{T3_1,\,trial}^{n+1}}{\partial \bar{u}_{T3_1}^{n+1}} - k_{e1}\frac{\partial\left(\Delta\lambda_3\right)}{\partial \bar{u}_{T3_1}^{n+1}} - k_{e1}\frac{\partial\left(\Delta\lambda_1\right)}{\partial \bar{u}_{T3_1}^{n+1}} \tag{2.45}$$

where

$$k_{e1}\frac{\partial\left(\Delta\lambda_1\right)}{\partial\bar{u}_{T3_1}^{n+1}}=k_{e1}$$
$$k_{e1}\frac{\partial\left(\Delta\lambda_3\right)}{\partial\bar{u}_{T3_1}^{n+1}}=0 \tag{2.46}$$

Replace Eq. (2.46) into Eq. (2.45) gives

$$k_{T3_1}^{n+1}=0 \tag{2.47}$$

ii. Tangent stiffness for $T3_2$ is defined by:

$$k_{T3_2}^{n+1}=\frac{\partial F_{12}^{n+1}}{\partial\bar{u}_{T3_2}^{n+1}}=\frac{\partial F_{T3_2,\,trial}^{n+1}}{\partial\bar{u}_{T3_2}^{n+1}}-k_{e2}\frac{\partial\left(\Delta\lambda_3\right)}{\partial\bar{u}_{T3_2}^{n+1}} \tag{2.48}$$

where

$$k_{e2}\frac{\partial\left(\Delta\lambda_3\right)}{\partial\bar{u}_{T3_2}^{n+1}}=k_{e2} \tag{2.49}$$

Combining Eq. (2.48) and Eq. (2.49) gives

$$k_{T3_2}^{n+1}=0 \tag{2.50}$$

- Zone 5:

  in this case we have two activated yield surfaces: one concerns $T3_2$ and the other corresponds to the group of ($T3_1$ and $T3_2$).

$$\Phi_2^{n+1}=F_{T3_2}^{n+1}-F_{T3_2,\,Rd}>0$$
$$\Phi_3^{n+1}=F_{T3_1}^{n+1}+F_{T3_2}^{n+1}-F_{12,\,Rd}>0$$

  i. The increment of plastic multiplier can be defined by:

$$\begin{bmatrix} k_{e2} & k_{e2} \\ k_{e2} & k_{e1}+k_{e2} \end{bmatrix}\begin{Bmatrix} \Delta\lambda_2 \\ \Delta\lambda_3 \end{Bmatrix}=\begin{Bmatrix} \Phi_{2,\,trial}^{n+1} \\ \Phi_{3,\,trial}^{n+1} \end{Bmatrix} \tag{2.51}$$

  ii. The tangent stiffnesses of the ($T3_1$ and $T3_2$) are:

$$k_{T3_1}^{n+1}=0 \tag{2.52}$$
$$k_{T3_2}^{n+1}=0 \tag{2.53}$$

2.5.2 General formulation for the group effect criterion

- The general formulation for the bolt-rows interaction criterion can be written as follows:

$$F_{T3_q} + F_{T3_s} \leq Min \left[F_{qs,Rd}, \left(F_{ks,Rd} - \sum_{i=k}^{q-1} F_{T3_i} \right)_{k=1,..,(q-1)} \right] \tag{2.54}$$

  where $q = 2,...m-1$; and $s= q+1,....., m$, in which m is the total number of the bolt-rows in the joint. F_{qs} and F_{ks} are the group resistances including the bolt-rows from (q to s) or (k to s), respectively.

- Example of a group of three bolt-rows: in the aim to take into account the effect of three bolt-rows (Fig. 2.11), successive group effects of two bolt-rows are proposed. The steps of the group effect occurrence in the case of positive bending can be described. The method remains available in case of negative bending.

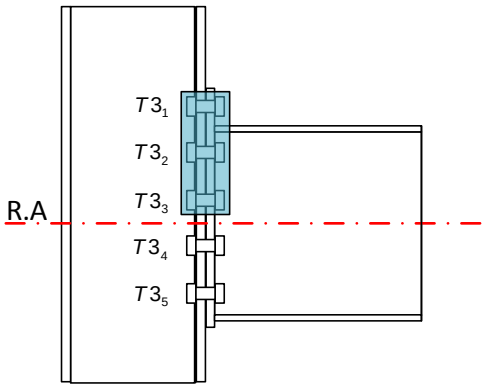

Figure 2.11: End-plate connection with several bolt-rows

It can be distinguished:

- Group effect 1 ($T3_1,\ T3_2$).
- Group effect 2 ($T3_2,\ T3_3$).

According to EC3, individual and group resistances can be easily obtained and denoted as follows:

- Individual: ($F_{T3_1,Rd}$, $F_{T3_2,Rd}$).
- Group 1: ($F_{12,Rd}$).
- Group 2: ($F_{23,Rd}$).

In case of negative bending:

- Group effect 1 is controlled by following criterion:

$$F_{T3_1} + F_{T3_2} \leq F_{12,Rd} \tag{2.55}$$

- Group effect 2 is controlled by the combination of both following criteria:

$$F_{T3_2} + F_{T3_3} \leq F_{23,Rd} \quad \text{and} \quad F_{T3_1} + F_{T3_2} + F_{T3_3} \leq F_{13,Rd} \tag{2.56}$$

The first equation of Eqs. (2.56) corresponds to the group effect of the two bolt-rows $T3_2$ and $T3_3$ and the second equation corresponds the group effect of the three bolt-rows $T3_1$, $T3_2$ and $T3_3$. The combination of these equations leads to the following criterion:

$$F_{T3_2} + F_{T3_3} \leq Min\left[F_{23,Rd}, (F_{13,Rd} - F_{T3_1})\right]. \tag{2.57}$$

2.6 Beam element with semi-rigid connection

Generally, mathematical expression is required to incorporate the joint behaviour, that obtained from its corresponding model, into structural analysis packages. But in this section tow zero-length component-based mechanical model, that have been developed in section 2.3, are incorporated at the ends of standard beam element to simulate connection behaviour.

2.6.1 Beam kinematics

This model consists of three subelements: a flexible beam element and two semi-rigid connections that are modelled by component-based mechanical model, see Fig. 2.12. The co-rotational framework is applied to the proposed member in

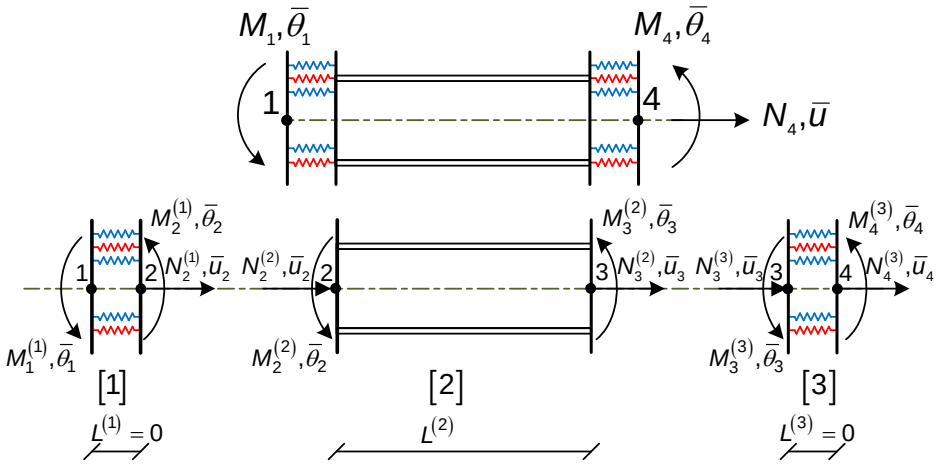

Figure 2.12: Finite joint element

which a rotational and extensional springs are used to represent the semi-rigid connections at the beam ends. The origin of the co-rotational frame is taken at node 1 which corresponds to the centroid of the cross-section. The x-axis of the local coordinate system is defined by the line connecting node 1 to node 4. The y-axis is orthogonal to the x-axis so that the result is right-handedly orthogonal coordinate system. The motion of the element from the original undeformed to the actual deformed configuration can thus be separated into two parts. The first one, which corresponds to rigid motion of the local frame, is the translation of node 1 and the rotation α of the x-axis (see Fig. 2.13). The second one refers to the deformations in the co-rotational element frame which are made of an elastic beam element and two semi-rigid connections.

The notations used in this section are defined in Figs. 2.12 and 2.13. The

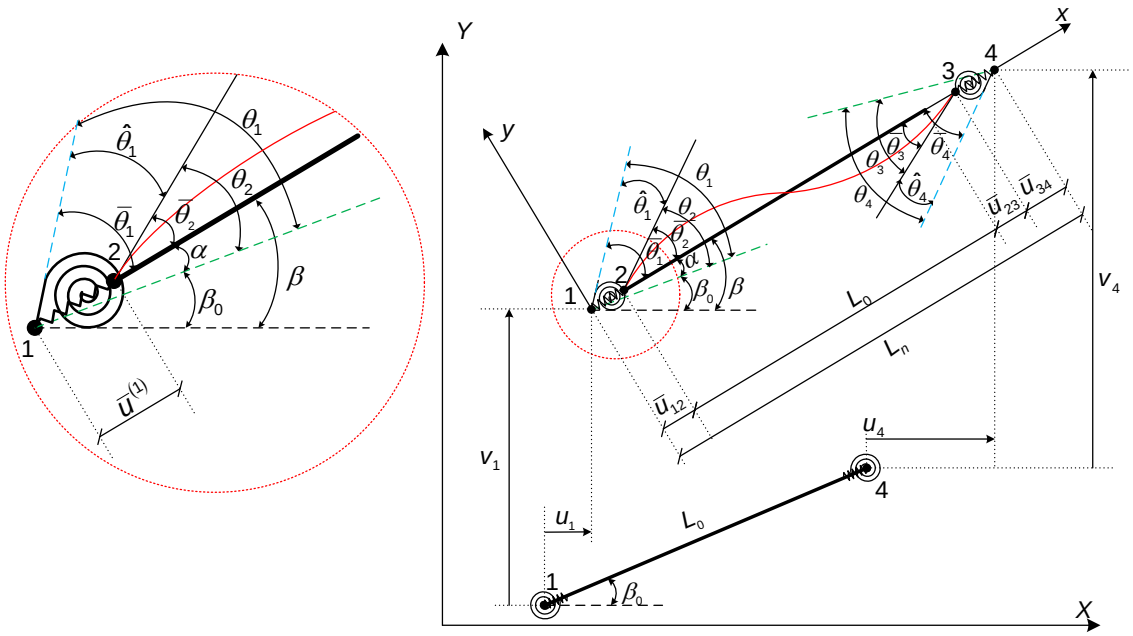

Figure 2.13: Initial and final configuration for the finite joint element

subscript and the superscript denote the node number and the subelement number, respectively. The coordinates of the nodes 1 and 4 in the global coordinate system (X, Y) are (X_1, Y_1) and (X_4, Y_4), respectively. In the deformed configuration (see Fig. 2.13), the global nodal rotations of the superelement nodes (node 1 and node 4) are θ_1 and θ_4 and the local ones are $\bar{\theta}_1$ and $\bar{\theta}_4$, respectively. In addition to this, the global rotations of the elastic beam element nodes (node 2 and 3) are described by θ_2 and θ_3 and the local ones by $\bar{\theta}_2$ and $\bar{\theta}_3$, respectively.

$$\begin{aligned} \theta_2 &= \theta_1 - \hat{\theta}_1 \\ \theta_3 &= \theta_4 - \hat{\theta}_4 \end{aligned} \tag{2.58}$$

where $\hat{\theta}_1$ and $\hat{\theta}_4$ are the relative rotations between the connected element at node 1 and node 4 respectively. The total elongation, $\bar{u}$, is composed of the elongations of the first connection $\bar{u}_{(12)}$, the elastic beam element $\bar{u}_{(23)}$ and the second connection $\bar{u}_{(34)}$

$$\bar{u} = \bar{u}_{(12)} + \bar{u}_{(23)} + \bar{u}_{(34)} \tag{2.59}$$

with

$$\begin{aligned} \bar{u}_{(12)} &= \bar{u}_2 - \bar{u}_1 \\ \bar{u}_{(23)} &= \bar{u}_3 - \bar{u}_2 \\ \bar{u}_{(34)} &= \bar{u}_4 - \bar{u}_3 \end{aligned} \tag{2.60}$$

The vectors of global and local displacements are respectively defined by: The vectors of global and local displacements are respectively defined by:

$$\boldsymbol{d}_g = \begin{bmatrix} u_1 & v_1 & \theta_1 & u_4 & v_4 & \theta_4 \end{bmatrix}^{\mathrm{T}} \tag{2.61}$$

$$\boldsymbol{d}_l = \begin{bmatrix} \bar{\mathrm{u}} & \bar{\theta_1} & \bar{\theta_4} \end{bmatrix}^{\mathrm{T}} \tag{2.62}$$

Referring to the definition of the co-rotating frame, the components of the local displacement vector $\mathbf{d}_l$ can be calculated from the geometric shape (see Fig. 2.13) as

$$\bar{u} = L_n - L_0 \tag{2.63a}$$

$$\bar{\theta_1} = \theta_1 - \alpha \tag{2.63b}$$

$$\bar{\theta_4} = \theta_4 - \alpha \tag{2.63c}$$

where the initial and final length of the element defined as L_0 and L_n, respectively, are obtained by.

$$L_0 = \sqrt{(X_4 - X_1)^2 + (Y_4 - Y_1)^2} \tag{2.64a}$$

$$L_n = \sqrt{(X_4 - X_1 + u_4 - u_1)^2 + (Y_4 - Y_1 + v_4 - v_1)^2} \tag{2.64b}$$

in which $(X_1 + u_1, Y_1 + v_1)$ and $(X_4 + u_4, Y_4 + v_4)$ are the global coordinates in the deformed configuration for node 1 and node 4, respectively. The rigid rotation of the x-axis α, that was mentioned in Eqs. (2.63b) and (2.63c), is obtained by using the geometrical relations as

$$\sin\alpha = c_0 s - s_0 c \tag{2.65a}$$

$$\cos\alpha = c_0 c + s_0 s \tag{2.65b}$$

with

$$c = \cos\beta = \frac{1}{L_n}(X_4 - X_1 + u_4 - u_1) \tag{2.66a}$$

$$c_0 = \cos\beta = \frac{1}{L_0}(X_4 - X_1) \tag{2.66b}$$

$$s = \sin\beta = \frac{1}{L_n}(Y_4 - Y_1 + v_4 - v_1) \tag{2.66c}$$

$$s_0 = \sin\beta = \frac{1}{L_0}(Y_4 - Y_1) \tag{2.66d}$$

The local - global displacement relationship can be derived through differentiation of Eqs. (2.63), therefore one can write:

$$\delta\bar{u} = \delta L_n \tag{2.67a}$$

$$\delta\bar{\theta_1} = \delta\theta_1 - \delta\alpha = \delta\theta_1 - \delta\beta \tag{2.67b}$$

$$\delta\bar{\theta_4} = \delta\theta_4 - \delta\alpha = \delta\theta_4 - \delta\beta \tag{2.67c}$$

By using (2.64b)and (2.66c), one obtains

$$\delta\bar{u} = c(\delta u_2 - \delta u_1) + s(\delta v_4 - \delta v_1) = \begin{bmatrix} -c & -s & 0 & c & s & 0 \end{bmatrix} \delta\mathbf{d}_g \tag{2.68}$$

$$\delta\beta = \frac{1}{cL_n} \begin{bmatrix} s & -c & 0 & -s & c & 0 \end{bmatrix} \delta\mathbf{d}_g \tag{2.69}$$

Finally, the global displacement vector is related to the local deformation vector by

$$\delta\mathbf{d}_l = \mathbf{B}\delta\mathbf{d}_g \tag{2.70}$$

where the transformation matrix, $\mathbf{B}$ is given by

$$\mathbf{B} = \begin{bmatrix} -c & -s & 0 & c & s & 0 \\ -\frac{s}{L_n} & \frac{c}{L_n} & 1 & \frac{s}{L_n} & -\frac{c}{L_n} & 0 \\ -\frac{s}{L_n} & \frac{c}{L_n} & 0 & \frac{s}{L_n} & -\frac{c}{L_n} & 1 \end{bmatrix} \tag{2.71}$$

2.6.2 Element formulation

The co-rotational method is convenient for establishing the relationship between the local and global variables. The relation between the global force vector $\boldsymbol{f}_g$ and the local one $\boldsymbol{f}_l$ is obtained by equating the virtual work in the local and global system as

$$\delta \boldsymbol{d}_g^{\mathrm{T}} \boldsymbol{f}_g = \delta \boldsymbol{d}_l^{\mathrm{T}} \boldsymbol{f}_l = \delta \boldsymbol{d}_g^{\mathrm{T}} \boldsymbol{B}^{\mathrm{T}} \boldsymbol{f}_l \tag{2.72}$$

Eq. (2.72) must apply for any arbitrary $\delta \boldsymbol{d}_g$. Hence, the global force vector $\boldsymbol{f}_g$ is given by

$$\boldsymbol{f}_g = \boldsymbol{B}^{\mathrm{T}} \boldsymbol{f}_l \tag{2.73}$$

By taking the differentiation of Eq. (2.73) with respect to global displacement vector, the global stiffness matrix is obtained as

$$\boldsymbol{k}_g = \boldsymbol{B}^{\mathrm{T}} \boldsymbol{k}_l \boldsymbol{B} + \frac{\boldsymbol{z}\boldsymbol{z}^{\mathrm{T}}}{L_n} N_4 + \frac{1}{L_n^2} \left(\boldsymbol{r}\boldsymbol{z}^{\mathrm{T}} + \boldsymbol{z}\boldsymbol{r}^{\mathrm{T}} \right) (M_1 + M_4) \tag{2.74}$$

where

$$\boldsymbol{r} = \begin{bmatrix} -c & -s & 0 & c & s & 0 \end{bmatrix}^{\mathrm{T}} \tag{2.75}$$

$$\boldsymbol{z} = \begin{bmatrix} s & -c & 0 & -s & c & 0 \end{bmatrix}^{\mathrm{T}} \tag{2.76}$$

2.6.3 Local element formulation

This section will be devoted to the elaboration of the local stiffness matrix. Illustrated by Fig. 2.12, the new joint finite element is composed of three subelements: an elastic flexible beam element and two semi-rigid connections. The introduction of the joints at the ends of the element has increased extra degrees of freedom exceeding the original ones in the standard co-rotational formulation. The condensing equations are then introduced to cancel out those extra degrees of freedom. To establish the assembled tangent stiffness of the joint finite element with the co-rotational format, the displacement of node 1 is restrained ($\bar{u}_1 = 0$). The elongation/shortening or relative axial displacement jump of each subelement are denoted by $\bar{u}_{(ij)} = \bar{u}_j - \bar{u}_i$ (Eqs. 2.60). The subelement 1, i.e.

semi-rigid connection modeled by a component method, has an axial elongation $\bar{u}_{(12)}$ and a relative rotation $\hat{\theta}_1 = \bar{\theta}_1 - \bar{\theta}_2$. The incremental relation between the stress-resultants and their conjugates can be formally written as

$$\left\{ \begin{array}{c} \Delta N_2^{(1)} \\ \Delta M_2^{(1)} \end{array} \right\} = \begin{bmatrix} C_{11}^{(1)} & C_{12}^{(1)} \\ C_{21}^{(1)} & C_{22}^{(1)} \end{bmatrix}_{n+1} \left\{ \begin{array}{c} \Delta \bar{u}_2 \\ \Delta \bar{\theta}_2 - \Delta \bar{\theta}_1 \end{array} \right\} \tag{2.77}$$

where the tangent operator matrix $\mathbb{C}$ defined in Eq. (2.10) is obtained from an isolated component-based mechanical model that is given in Section 2.3.

$$\mathbb{C}_{n+1}^{(1)} = \begin{bmatrix} C_{11}^{(1)} & C_{12}^{(1)} \\ C_{21}^{(1)} & C_{22}^{(1)} \end{bmatrix}_{n+1} \tag{2.78}$$

The incremental equilibrium of the first element imposes that

$$\Delta M_1^{(1)} + \Delta M_2^{(1)} = 0 \tag{2.79}$$

Combining Eqs. (2.77) and (2.79) gives

$$\left\{ \begin{array}{c} \Delta M_1^{(1)} \\ \Delta N_2^{(1)} \\ \Delta M_2^{(1)} \end{array} \right\} = \begin{bmatrix} C_{22}^{(1)} & -C_{12}^{(1)} & -C_{22}^{(1)} \\ -C_{12}^{(1)} & C_{11}^{(1)} & C_{12}^{(1)} \\ -C_{22}^{(1)} & C_{12}^{(1)} & C_{22}^{(1)} \end{bmatrix}_{n+1} \left\{ \begin{array}{c} \Delta \bar{\theta}_1 \\ \Delta \bar{u}_2 \\ \Delta \bar{\theta}_2 \end{array} \right\} \tag{2.80}$$

Using the same manipulation, the relation between the stress-resultants and their conjugates in the second connection, that is the subelement 3, is obtained

$$\begin{aligned} \Delta M_3^{(3)} + \Delta M_4^{(3)} &= 0 \\ \Delta N_3^{(3)} + \Delta N_4^{(3)} &= 0 \end{aligned} \tag{2.81}$$

Hence,the relation between the stress-resultants and their conjugates in the second semi-rigid connection is given as

$$\left\{ \begin{array}{c} \Delta N_3^{(3)} \\ \Delta M_3^{(3)} \\ \Delta N_4^{(3)} \\ \Delta M_4^{(3)} \end{array} \right\} = \begin{bmatrix} C_{11}^{(3)} & C_{12}^{(3)} & -C_{11}^{(3)} & -C_{12}^{(3)} \\ C_{12}^{(3)} & C_{22}^{(3)} & -C_{12}^{(3)} & -C_{22}^{(3)} \\ -C_{11}^{(3)} & -C_{12}^{(3)} & C_{11}^{(3)} & C_{12}^{(3)} \\ -C_{12}^{(3)} & -C_{22}^{(3)} & C_{12}^{(3)} & C_{22}^{(3)} \end{bmatrix}_{n+1} \left\{ \begin{array}{c} \Delta \bar{u}_3 \\ \Delta \bar{\theta}_3 \\ \Delta \bar{u}_4 \\ \Delta \bar{\theta}_4 \end{array} \right\} \tag{2.82}$$

On the other hand, the beam element (subelement 2) is assumed to deform elastically. Having an elastic elongation $\bar{u}_{(12)}$ and elastic rotations θ_2 and θ_3 on each

side of its ends, the incremental stress-resultants are related to their conjugates, for this subelement, by

$$\begin{Bmatrix} \Delta N_2^{(2)} \\ \Delta M_2^{(2)} \\ \Delta N_3^{(2)} \\ \Delta M_3^{(2)} \end{Bmatrix} = \begin{bmatrix} k_{11}^{(2)} & 0 & -k_{11}^{(2)} & 0 \\ 0 & k_{22}^{(2)} & 0 & k_{24}^{(2)} \\ -k_{11}^{(2)} & 0 & k_{11}^{(2)} & 0 \\ 0 & k_{42}^{(2)} & 0 & k_{44}^{(2)} \end{bmatrix}_{n+1} \begin{Bmatrix} \Delta \bar{u}_2 \\ \Delta \bar{\theta}_2 \\ \Delta \bar{u}_3 \\ \Delta \bar{\theta}_3 \end{Bmatrix} \tag{2.83}$$

in which, $k_{11}^{(2)} = \dfrac{EA}{L}$, $k_{22}^{(2)} = k_{44}^{(2)} = \dfrac{4EI}{L}$ and $k_{24}^{(2)} = k_{42}^{(2)} = \dfrac{2EI}{L}$. E, I, A and L denote the Young modulus, the second moment of area, the cross-section area and the beam length, respectively. The tangent stiffness matrix of the superelement and the corresponding force vector are assembled using the nodal force equilibrium equations, redand force/deformation and compatibility equations member stiffness equations) The tangent stiffness matrix for the joint finite element is assembled using the standard direct stiffness method based which involve nodal equilibrium. The sum of internal forces exerted by all members that meet at a joint balances the external force applied to that joint. Further, as shown in Fig. 2.12, the flexural beam element has two ends: node 2 and 3. The nodal equilibrium equations for these nodes, used to eliminate the extra degrees of freedom, are given as follows

$$\begin{aligned} \Delta N_2^{(1)} + \Delta N_2^{(2)} &= 0 \\ \Delta M_2^{(1)} + \Delta M_2^{(2)} &= 0 \\ \Delta N_3^{(2)} + \Delta N_3^{(3)} &= 0 \\ \Delta M_3^{(2)} + \Delta M_3^{(2)} &= 0 \end{aligned} \tag{2.84}$$

The above equilibrium equations are supplemented with equilibrium equations pertaining to the end nodes (node 1 and node 4):

$$\begin{aligned} \Delta M_1 &= \Delta M_1^{(1)} \\ \Delta N_4 &= \Delta N_4^{(3)} \\ \Delta M_4 &= \Delta M_4^{(3)} \end{aligned} \tag{2.85}$$

Equilibrium equations Eq.2.84 and Eq.2.85 are combined together with the member stiffness equations Eq.2.80, Eq.2.82 and Eq.2.83 to give:

$$\Delta \boldsymbol{f} = [\boldsymbol{k}]_{n+1}\, \Delta \boldsymbol{d} \tag{2.86}$$

with

$$\boldsymbol{f}^{\mathrm{T}} = \begin{bmatrix} M_1 & 0 & 0 & 0 & 0 & N_4 & M_4 \end{bmatrix} \quad , \quad \boldsymbol{d}^{\mathrm{T}} = \begin{bmatrix} \bar{\theta}_1 & \bar{u}_2 & \bar{\theta}_2 & \bar{u}_3 & \bar{\theta}_3 & \bar{u}_4 & \bar{\theta}_4 \end{bmatrix} \tag{2.87}$$

and

$$[\boldsymbol{k}]_{n+1} = \begin{bmatrix} C_{22}^{(1)} & -C_{12}^{(1)} & -C_{22}^{(1)} & 0 & 0 & 0 & 0 \\ -C_{12}^{(1)} & C_{11}^{(1)} + k_{11}^{(2)} & C_{12}^{(1)} & -k_{11}^{(2)} & 0 & 0 & 0 \\ -C_{22}^{(1)} & C_{12}^{(1)} & C_{22}^{(1)} + k_{22}^{(2)} & 0 & k_{24}^{(2)} & 0 & 0 \\ 0 & -k_{11}^{(2)} & 0 & k_{11}^{(2)} + C_{11}^{(3)} & C_{12}^{(3)} & -C_{11}^{(3)} & -C_{12}^{(3)} \\ 0 & 0 & k_{42}^{(2)} & C_{21}^{(3)} & k_{44}^{(2)} + C_{22}^{(3)} & -C_{12}^{(3)} & -C_{22}^{(3)} \\ 0 & 0 & 0 & -C_{11}^{(3)} & -C_{12}^{(3)} & C_{11}^{(3)} & C_{12}^{(3)} \\ 0 & 0 & 0 & -C_{12}^{(3)} & -C_{22}^{(3)} & C_{12}^{(3)} & C_{22}^{(3)} \end{bmatrix} \tag{2.88}$$

To carry out the condensation process, the assembled stiffness equations of the superelement (Eq.2.86) are rearranged and partitioned as follows:

$$\begin{Bmatrix} \Delta \boldsymbol{f}_l \\ \boldsymbol{0} \end{Bmatrix} = \begin{bmatrix} [\boldsymbol{k}_{ll}]_{n+1} & [\boldsymbol{k}_{li}]_{n+1} \\ [\boldsymbol{k}_{il}]_{n+1} & [\boldsymbol{k}_{ii}]_{n+1} \end{bmatrix} \begin{Bmatrix} \Delta \boldsymbol{d}_l \\ \Delta \boldsymbol{d}_i \end{Bmatrix} \tag{2.89}$$

where the subvector $\Delta \boldsymbol{d}_i$ collects the interior degrees of freedom and the subvector $\Delta \boldsymbol{d}_l$ comprises the co-rotational kinematic variables pertaining to the superelement (elongation and local rotations at the end nodes):

$$\boldsymbol{d}_l = \begin{Bmatrix} \bar{u}_4 \\ \bar{\theta}_1 \\ \bar{\theta}_4 \end{Bmatrix} \quad , \quad \boldsymbol{d}_i = \begin{Bmatrix} \bar{u}_2 \\ \bar{\theta}_2 \\ \bar{u}_3 \\ \bar{\theta}_3 \end{Bmatrix} \tag{2.90}$$

In the above equation, the subvector $\boldsymbol{f}_l$ collect the independent stress-resultants pertaining to the superelement which corresponds to the so-called local force

vector in the co-rotational formulation:

$$\boldsymbol{f}_l = \left\{ \begin{array}{c} N_4 \\ M_1 \\ M_4 \end{array} \right\} \tag{2.91}$$

The sub-matrices in Eq.(2.89) have the following expressions:

$$\boldsymbol{k}_{ll} = \left[\begin{array}{ccc} C_{11}^{(3)} & 0 & C_{12}^{(3)} \\ 0 & C_{22}^{(1)} & 0 \\ C_{12}^{(3)} & 0 & C_{22}^{(1)} \end{array} \right]_{n+1} \tag{2.92}$$

$$\boldsymbol{k}_{li} = \left[\begin{array}{cccc} 0 & 0 & -C_{11}^{(3)} & -C_{12}^{(3)} \\ -C_{12}^{(1)} & -C_{22}^{(1)} & 0 & 0 \\ 0 & 0 & -C_{12}^{(3)} & -C_{22}^{(3)} \end{array} \right]_{n+1} \tag{2.93}$$

$$\boldsymbol{k}_{il} = \left[\begin{array}{ccc} 0 & -C_{12}^{(1)} & 0 \\ 0 & -C_{22}^{(1)} & 0 \\ -C_{11}^{(3)} & 0 & -C_{12}^{(3)} \\ -C_{12}^{(3)} & 0 & -C_{22}^{(3)} \end{array} \right]_{n+1} \tag{2.94}$$

$$\boldsymbol{k}_{ii} = \left[\begin{array}{cccc} C_{11}^{(1)} + k_{11}^{(2)} & C_{12}^{(1)} & -k_{11}^{(2)} & 0 \\ C_{12}^{(1)} & C_{22}^{(1)} + k_{22}^{(2)} & 0 & k_{24}^{(2)} \\ -k_{11}^{(2)} & 0 & k_{11}^{(2)} + C_{11}^{(3)} & C_{12}^{(3)} \\ 0 & k_{42}^{(3)} & C_{12}^{(3)} & C_{22}^{(3)} + k_{33}^{(3)} \end{array} \right]_{n+1} \tag{2.95}$$

Solving for the interior degrees of freedom:

$$\Delta \boldsymbol{d}_i = - \left[\boldsymbol{k}_{ii} \right]_{n+1}^{-1} \left[\boldsymbol{k}_{il} \right]_{n+1} \Delta \boldsymbol{d}_l \tag{2.96}$$

and replacing the outcome into the first matrix equation yield the condensed stiffness equations

$$\Delta \boldsymbol{f}_l = \left[\boldsymbol{k}_l \right]_{n+1} \Delta \boldsymbol{d}_l \tag{2.97}$$

with

$$[\boldsymbol{k}_l]_{n+1} = [\boldsymbol{k}_{ll}]_{n+1} - [\boldsymbol{k}_{li}]_{n+1} \, [\boldsymbol{k}_{ii}]^{-1}_{n+1} \, [\boldsymbol{k}_{il}]_{n+1} \tag{2.98}$$

$[\boldsymbol{k}_l]_{n+1}$ is the local tangent stiffness matrix. To ease the computations, the above stiffness equations are slightly modified by replacing the axial displacements with sub-element elongations using

$$\begin{aligned} \Delta\bar{u}_2 &= \Delta\bar{u}_{(12)} \\ \Delta\bar{u}_3 &= \Delta\bar{u}_{(12)} + \Delta\bar{u}_{(23)} \\ \Delta\bar{u}_4 &= \Delta\bar{u}_{(12)} + \Delta\bar{u}_{(23)} + \Delta\bar{u}_{(34)} = \Delta\bar{u} \end{aligned} \tag{2.99}$$

where $\Delta\bar{u}$ is the elongation of the superelement. Full expressions of the new assembled stiffness matrix along with the corresponding sub-matrices are given in the appendix.

2.7 Numerical applications

Three numerical applications based on the above mentioned algorithm are presented in this section. The purpose of the first one is to show the gap effect on the hysteric behaviour of the joint whilst the second example illustrates the influence of the bolt-group in the joint response. The third one address the influence of the axial force in the connection on the bending moment capacity in one hand. And the interaction diagrams between axial force and bending moment in the other hand.

2.7.1 Example for the gap effect

The simple example of two bolt-rows (Fig. 2.14) is used to investigate the influence of the gap effect on the joint behavior. Two cycles of rotations are applied to this joint according to the diagram given in Fig. 2.15. Corresponding mechanical model is given in Fig. 2.16. The steel grade that adopted is S355 and the Young's Modulus is 210 GPa. This example has been solved using proposed mechanical model analysis and 3D finite element modelling.

2.7.1.1 Proposed mechanical model analysis

In this section the proposed mechanical model will be used to capture the cyclic response of the connection. It is worth to point out that the strength of equivalent Type spring is obtained as the minimum of the strengths of included components (highlighted values in Table 2.2).

For each component within the joint, material hardening has been considered

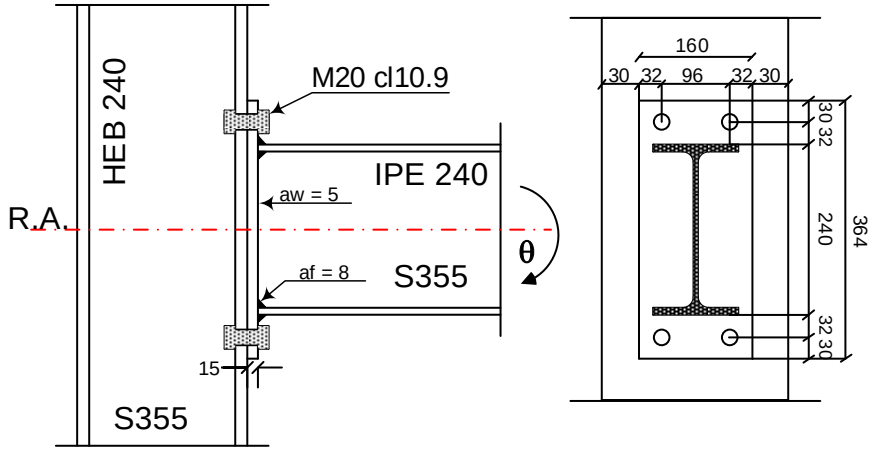

Figure 2.14: Example for the gap effect

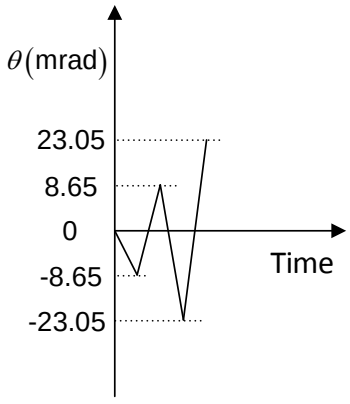

Figure 2.15: Cyclic loading history

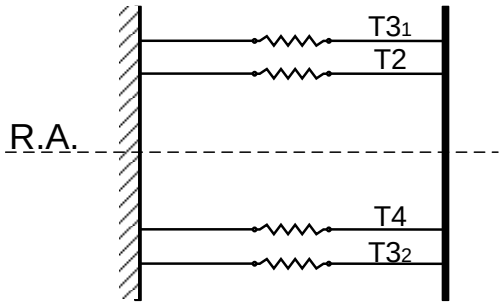

Figure 2.16: Mechanical model

Table 2.2: Initial stiffness and resistance force (kN/mm and kN)

Component	$T3_1$ and $T3_2$		T2 and T4	
	F_{Rd}	k_{ini}	F_{Rd}	k_{ini}
CFB	352	8498	-	-
CWT	508	1475	-	-
EPB	**258**	4221	-	-
CWC	-	-	642	2150
BFWC	-	-	**565**	∞
BT	441	1630	-	-

very light ($k_{eq,r}/1000$) but not equal to zero. In accordance with the cyclic loading history (Fig. 2.15), the (Moment - Rotation) curve obtained as the response of the joint behavior is given in Fig. 2.17. It appears clearly that the gaps obtained at both top and bottom levels of the joint generate slipping at both sides of the zero-rotation axis of the curve (horizontal dashed arrows). Alternatively between top and bottom bolt-rows, the gap obtained by the tension of the top bolt-row for example, must be first recovered before beginning the tension at the bottom bolt-row. The proposed algorithm follows these sequences very rigorously in order to insure an accurate solution of the proposed model (the index t corresponds to the $T3_1$ in tension and the index b to the $T3_2$ in tension).

- First loading cycle ($-8.65\ mrad \leq \theta \leq 8.65\ mrad$):

$(O - A_t - B_t)$	Loading in negative bending (1 - 2)
$(B_t - C_t)$	Unloading (3)
$(C_t - O)$	Slipping (4)
$(O - A_b - B_b)$	Loading in positive bending
$(B_b - C_b)$	Unloading
$(C_b - O)$	Slipping

- Second loading cycle ($-23.05\ mrad \leq \theta \leq 23.05\ mrad$):

$(C_t - B_t - D_t)$	Reloading in negative bending (5 - 6)
$(D_t - E_t)$	Unloading (7)
$(E_t - C_t - O - C_b)$	Slipping
$(C_b - B_b - D_b)$	Reloading in positive bending
$(D_b - E_b)$	Unloading

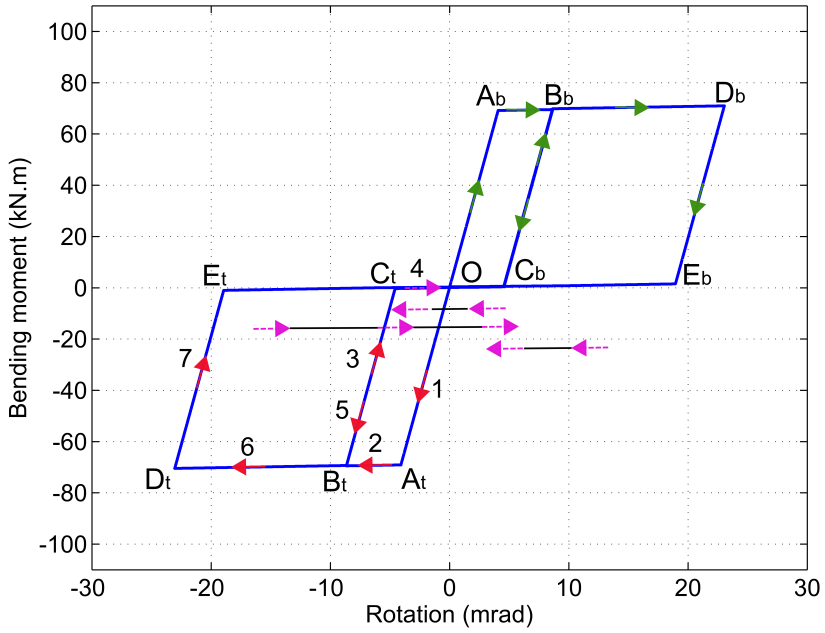

Figure 2.17: Moment vs. Rotation curve

After each load cycle, the plastic deformation of the components within each equivalent spring are cumulated. At the end of the unloading stage, permanent deformation defining the so-called gap needs to be closed to allow the activation of the others rows. In accordance with Fig. 2.17, following values of couples (Moment - Rotation) of the joints are obtained when the top bolt-row is active (same results when the bottom bolt-row is active because of symmetry):

- First loading cycle ($-8.65\ mrad \leq \theta \leq 8.65\ mrad$):

$(O - A_t - B_t)$	(0,0), (-69.09,-4.08), (-69.45,8.65)
$(B_t - C_t)$	(-69.45,-8.65), (0,-4.49)
$(C_t - O)$	(0,-4.49), (0,0)

- Second loading cycle ($-23.05\ mrad \leq \theta \leq -23.05\ mrad$):

$(O - C_t)$	(0,0), (0,-4.49)
$(C_t - B_t - D_t)$	(0,-4.49), (-69.45,-8.65), (-70.46,-23.05)
$(D_t - E_t)$	(-70.46,-23.05), (0,-18.94)
$(E_t - O)$	(0,-18.94) , (0,0)

It worth to precise that the couple of springs ($T3_1$ – $T4$) are active in same time and ($T3_2$ – $T2$) also, and both couples are active alternatively (Fig. 2.18); therefore:

- Negative displacement obtained in the spring $T4$ (bottom beam-flange row) is due to a compression force whilst the tension is active in the spring $T3_1$ (top bolt-row).

- Negative displacement obtained in the spring $T3_2$ (bottom bolt-row) is due to a slipping (the spring does not support any compression force) whilst the positive displacement obtained in the spring T_2 (top beam-flange row) is also a slipping (this row does not support any tension).

It is clear that the behavior of each equivalent spring "Type" (Fig. 2.18) follows both sleeps occurred during these two loading cycles. The slipping values obtained from these curves are:

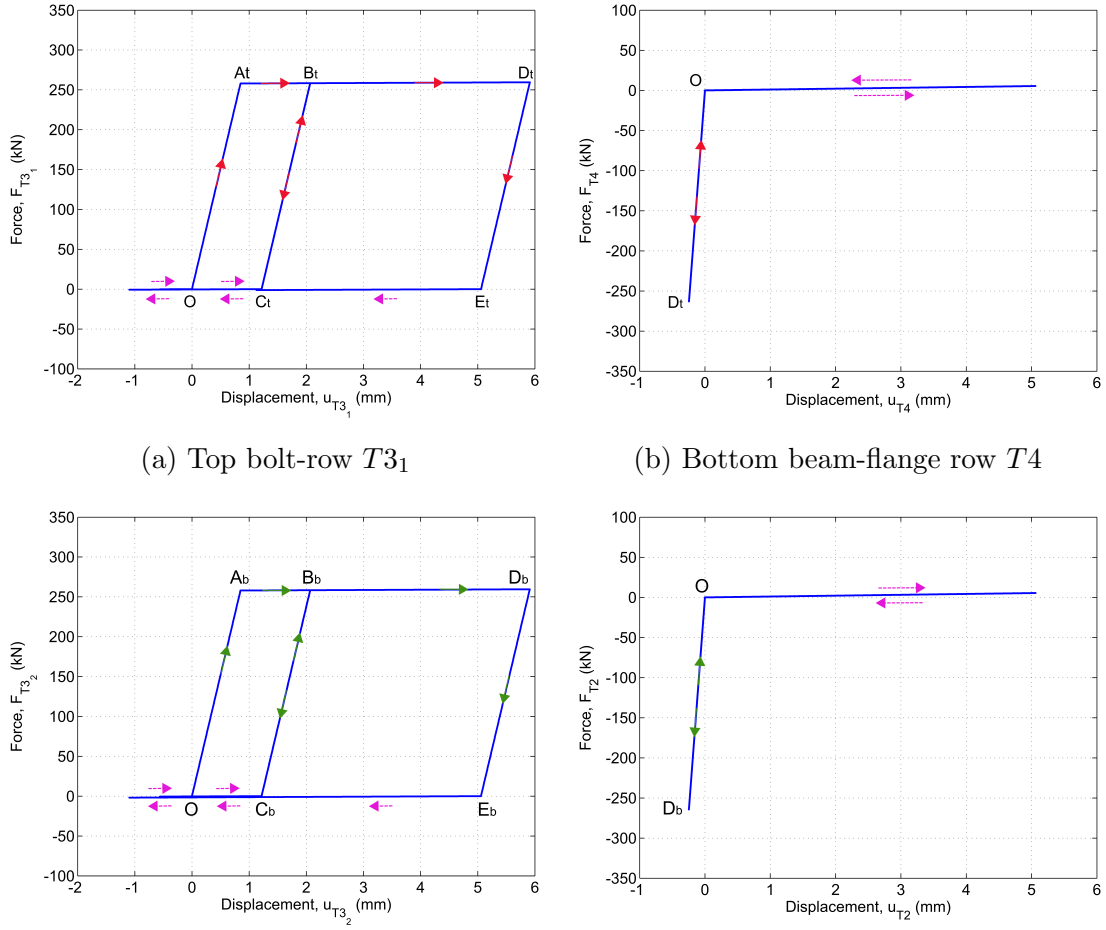

(a) Top bolt-row $T3_1$

(b) Bottom beam-flange row $T4$

(c) Bottom bolt-row $T3_2$

(d) Top beam-flange row $T2$

Figure 2.18: Force-displacement curves for each row of the joint

- $(C_t$ - $O) = 1.208\ mm$
- $(E_t$ - $O) = 5.056\ mm$

2.7.1.2 3D finite element modelling

In order to validate our proposed mechanical model, a 3D model of the previous end-plate connection, Fig. 2.14, is investigated with the finite element codes ABAQUS. The three-dimensional solid element type C3D8R have been used.

The contact element between the end-plate and the column flange surfaces as well as between the end-plate, the column flange and the bolts surface are used with friction coefficient of 0.3. All the nodes of the top and bottom section of the column are restrained in all directions. In order to achieve reliable results,a fine mesh was employed in the contact zone as shown in the general view of the mesh pattern for the connection, Fig. 2.19.

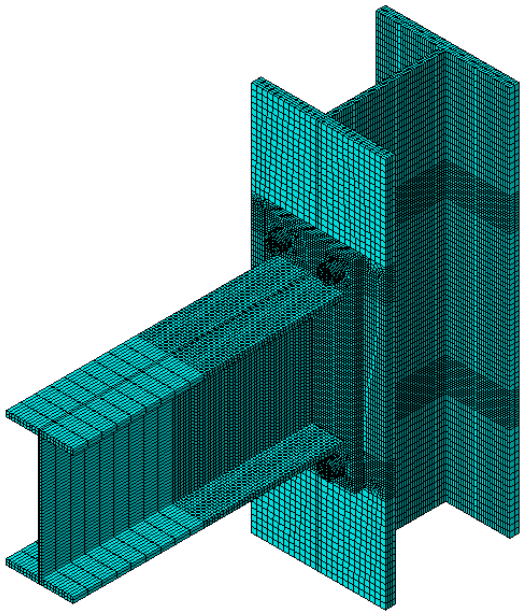

Figure 2.19: Mesh pattern of the finite element model

In the other hand, the steel material, type S355, for the components involved the creation of the gap: column-flange, end-plate and bolts, is considered as ductile and behave as elastic-perfectly plastic. Whilst, the other components have an elastic behavior.

In this analysis displacement control was applied, rotation, to a rigid surface at the end of the beam. The applied rotation was cyclic and controlled by amplitude function.

- **Results and discussions** The Moment-Rotation curve results from FE

model is compared to the mechanical model response developed in section 2.3 and implemented in MATLAB, the two responses are demonstrated in Fig. 2.20. It can be observed that the connection response from the developed mechanical model has a good agreement with that from 3D FE mainly in the initial stiffness and moment resistance. It is worth to mention that in this example there is no group effect because the two bolt-rows do not work together under bending moment.

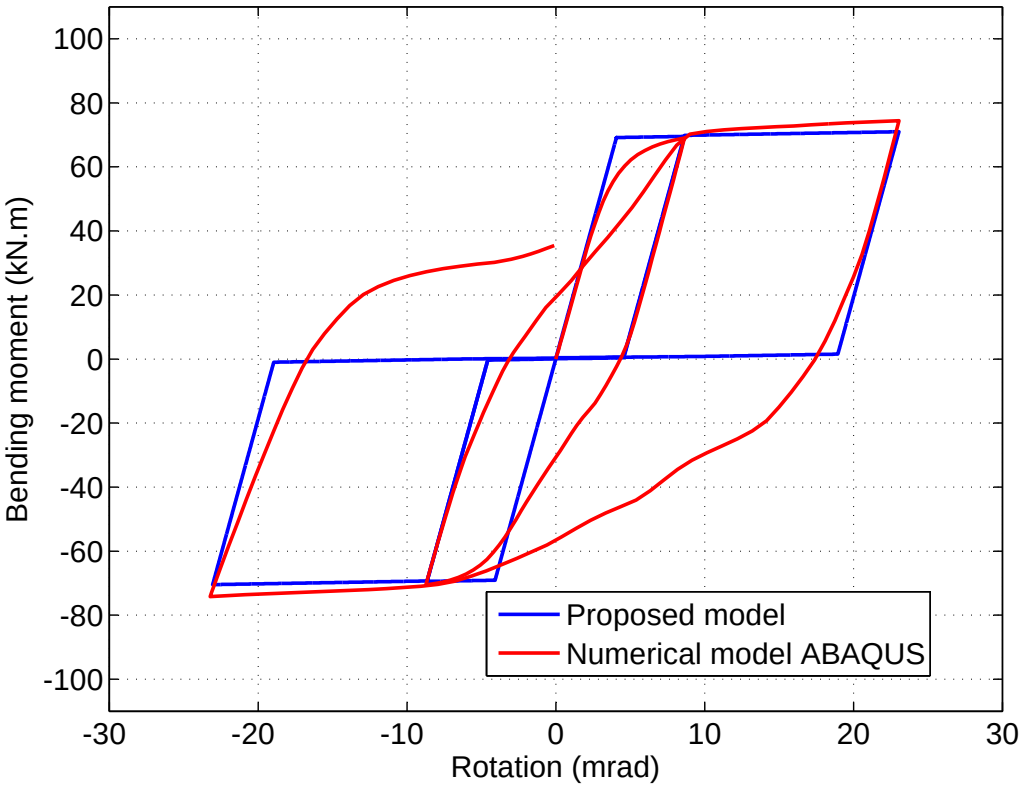

Figure 2.20: Moment vs. rotation curves

The creation of the gap is very clear in the 3D finite element simulation and this separation, as expected, comes from plastic deformation of the end-plate in bending (see Fig. 2.21).

The gap effect is demonstrated in the moment-rotation curve as the follow-

ing:

i In the proposed model a slipping phenomenon is adopted on the force-displacement curve of the equivalent spring therefore, the benching-effect is significant in the cyclic response.

ii For 3D FE model the benching –effect is not significant as in the response of the proposed model, in contrast a degradation of the stiffness is observed during closing the gap.

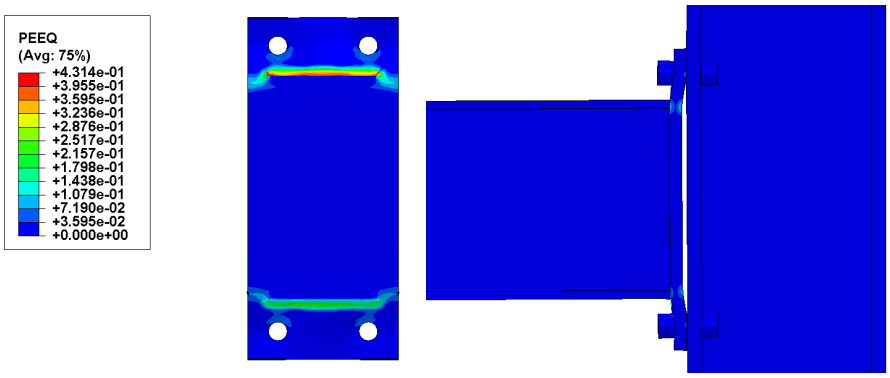

Figure 2.21: Plastic deformation in the connection at the end of the 3D FE simulation

2.7.2 Example for the group effect

The following application concerns an example of a semi-rigid connection that has been analyzed by Cerfontaine [13] (Fig. 2.22). This example consists of an IPE600 steel beam connected to a HEB400 steel column towards an end-plate with 5 bolt-rows denoted $T3_i$ $(i = 1, ..., 5)$. Table 2.3 summarizes the resistances and equivalent stiffnesses of each individual and group of bolt-rows. In addition, the same data are given for the Types $T2$ and $T4$ located at the top and the bottom beam flange levels, respectively. According to Eq. (2.54) (where $m = 5$)

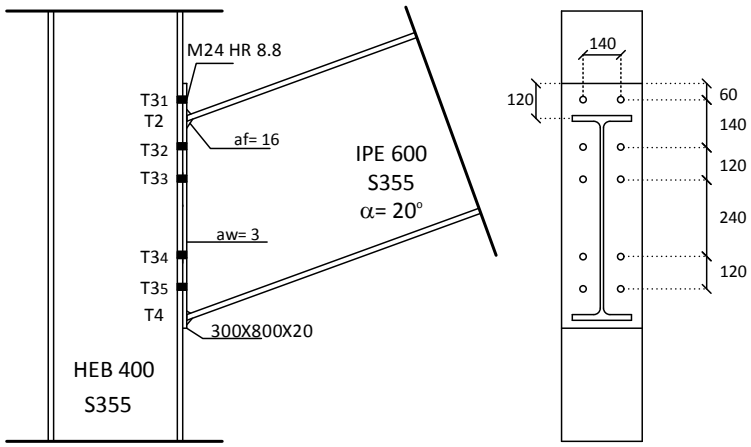

Figure 2.22: Bolted end-plate configuration

Table 2.3: Types and Groupes characterisation

□□d □□□d □□□□r□□s □□Types □□			
	Row (□□□□)	□ r□Rd(□□)	□ r□□(□□□□□□)
□o□ □r□ss□o□ □o□□	□o□ □□□□ □□□□□□(□□)	□□□□	□□□□
	□o□□o□ □□□□ □□□□□□(□□)	□□□□	□□□□
□□s□o□ □o□□	□□rs□ □o□□row (□□□)	□□□	□□□□□□
	□□□o□d □o□□row (□□□)	□□□	□□□□□□
	□□□rd □o□□row (□□□)	□□□	□□□□□□
	□o□r□□ □o□□row (□□□)	□□□	□□□□□□
	□□□□□□ □o□□row (□□□)	□□□	□□□□□□
□r□□p □□□□□□□□□□r□□s □			
□ro□□o□□ow □o□□rows		R□s□s□□□□□(□□)	
□□□□ □□□		□□□	
□□□□ □□□		□□□	
□□□□ □□□		□□□	
□□□□ □□□		□□□	
□ro□□o□□r□□ □o□□rows		R□s□s□□□□□(□□)	
□□□□ □□□□□□□		□□□□	
□□□□ □□□□□□□		□□□□	
□□□□ □□□□□□□		□□□□	
□ro□□o□□□ □o□□rows		R□s□s□□□□□(□□)	
□□□□ □□□□□□□□□□		□□□□	
□□□□ □□□□□□□□□□		□□□□	
□ro□□o□□□□□ □o□□rows		R□s□s□□□□□(□□)	
□□□□ □□□□□□□□□□□□□□		□□□□	

the yield surface criterion for different combination of group of bolt-rows are obtained and reported in Table 2.4. Two calculations have been performed:

- Calculation 1: the data given in Table 2.3 are the same as those of Cerfontaine [13]. In this conditions, it appears that no group effect is activated (Fig. 2.23).

- Calculation 2: in order to activate the group effects, it is proposed to increase (arbitrary) the resistance of Type $T4$ from 1011 kN to 1500 kN (Fig. 2.24).

Table 2.4: Yield surface criterion for this example(5 bolt-rows)

q	s	$F_{T3_q} + F_{T3_s} \leq$
2	3	$Min\left[F_{23,Rd}, (F_{13,Rd} - F_{T3_1})\right]$
3	4	$Min\left[F_{34,Rd}, (F_{14,Rd} - F_{T3_1} - F_{T3_2}), (F_{24,Rd} - F_{T3_2})\right]$
4	5	$Min\left[F_{45,Rd}, (F_{15,Rd} - F_{T3_1} - F_{T3_2} - F_{T3_3}), (F_{25,Rd} - F_{T3_2} - F_{T3_3}), (F_{35,Rd} - F_{T3_3})\right]$

Both figures represent the (Moment-Rotation) curve of the joint corresponding to each calculation. It is worth to mention that in order to reach a significant rotation of the joint, for both calculations an elastic- perfectly plastic behavior is adopted for all the components of the mechanical model. The algorithm is able to give the force at each bolt-row during the loading history. It can be easily observed that the equilibrium is always satisfied. These forces are highlighted at each point where the slop is changing.

For the first calculation (Fig. 2.23), it can observed that:

- At point "1" (Fig. 2.23) and at the point "A" (Fig.2.24), same distribution of forces is obtained. This step corresponds to the case where $T3_1$ reaches its individual resistance. All other bolt-rows are still in elastic range.

- From point "2" (Fig. 2.23), the force at the Type $T4$ reaches its individual resistance (1011 kN). Therefore, with respect to the equilibrium between

tension and compression zones, the tension force is too low to activate a group effect.

- Point "3" (Fig. 2.23) corresponds to the maximum of the bending moment in the connection ($M_{j,max} = 567.5\ kN.m$). This obtained value is in accordance with the maximum value of the bending moment ($M_{j,max} = 567\ kN.m$) that obtained by Cerfontaine [13]. At this point an unloading of the force at $T3_4$ to zero leads to a redistribution of this force to the upper bolt-rows which have not reaching their individual resistance yet ($T3_2$ and $T3_3$). It appears that with this redistribution, $T3_2$ reaches its individual resistance ($407\ kN$).

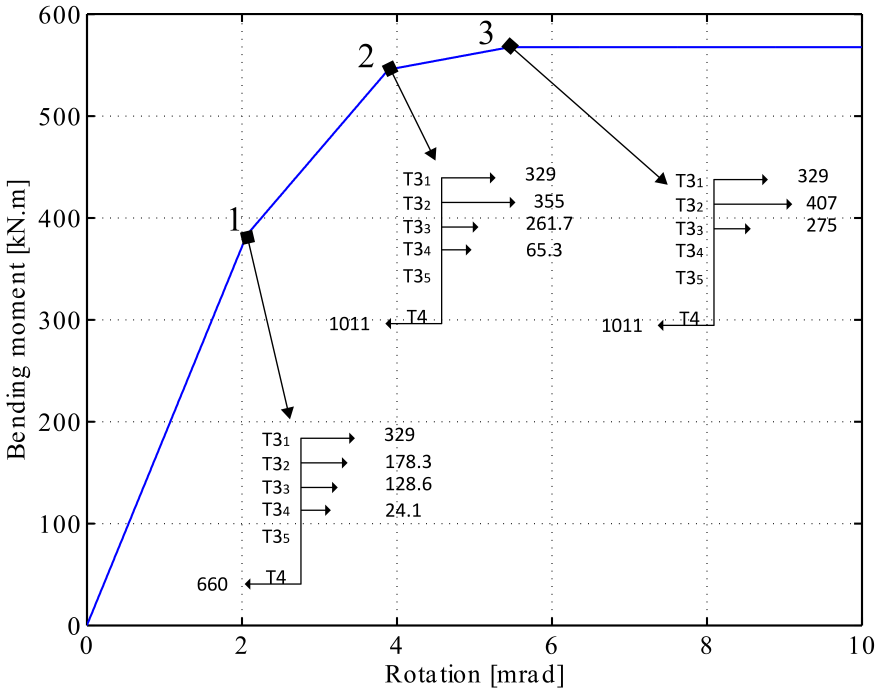

Figure 2.23: Moment vs. rotation curve

For the second calculation (Fig. 2.24), it can be observed that:

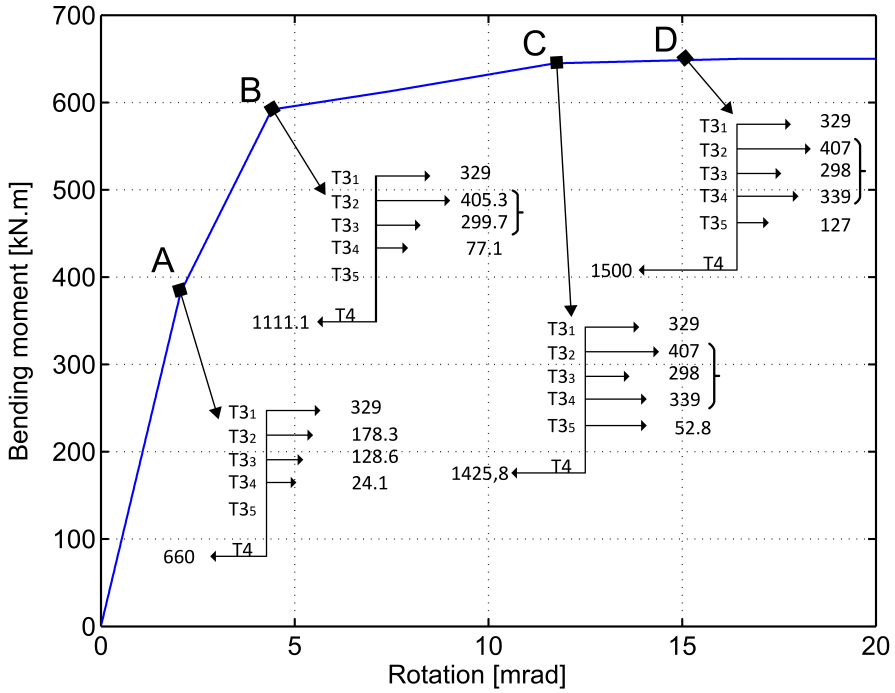

Figure 2.24: Moment vs. rotation curve

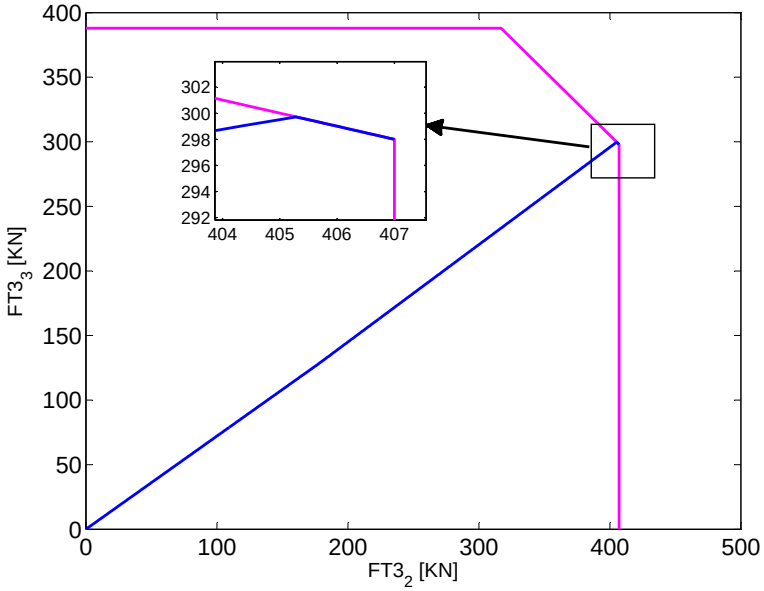

Figure 2.25: $(F_{T3_2} - F_{T3_3})$ interaction diagram

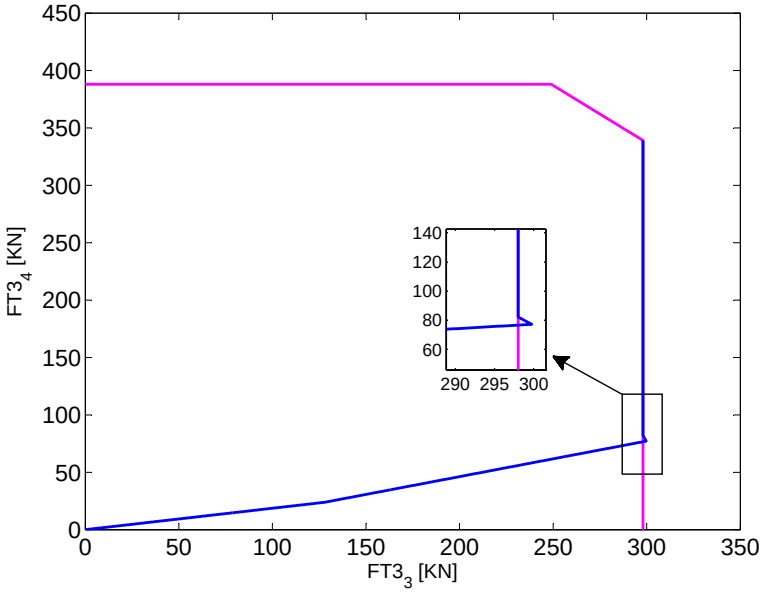

Figure 2.26: $(F_{T3_3} - F_{T3_4})$ interaction diagram

- At point B (Fig. 2.24), the force at Type $T4$ (1111,1 kN) is less than its resistance (1500 kN). However, a group resistance is activated by $T3_2$ and $T3_3$. In accordance with Table 2.4 where $q = 2$ and s = 3, it follows:

$$405,3 + 299,7 = 705\ kN \leq Min\,[705\ ,(1200 - 329 = 871\ kN)] = 705\ kN$$

- At point C (Fig. 2.24), the force at Type $T4$ (1425,8 kN) is also less than its resistance (1500 kN). On one hand, it can be observed that the activation of the previous group effect leads to a first influence on the redistribution force respecting the criterion of this group $(407 + 298 = 705\ kN)$ (see Fig. 2.25 and Fig. 2.26). On the second hand, the group of 3 bolt-rows is activated by $T3_2$, $T3_3$ and $T3_4$. In accordance with Table 2.4 where $q = 3$ and s = 4, it follows:

$$298 + 339 = 637\,kN \leq Min\begin{bmatrix} 728,(1627 - 329 - 407 = 891\ kN), \\ (1044 - 407 = 637\ kN) \end{bmatrix} = 637\ kN$$

It can be observed that the group of 3 bolt-rows is activated at this point.

- At point D (Fig. 2.24), the force at Type $T4$ reaches its resistance (1500 kN). The bolt-rows from 1 to 4 are in plastic range (individual or group limit resistance). The force at the last bolt-row $T3_5$ reaches the value (127 kN) that insures the equilibrium between compression and tension zones. On one hand, it can be observed that the activation of the previous group effects leads to a first influence on the redistribution force respecting following criteria (407 + 298 = 705 kN) and (407 + 298 + 339 = 1044 kN). On the second hand, there is no other group effect activated. In accordance with Table 2.4 where $q = 4$ and s = 5, it follows:

$$339 + 127 = 466\,kN \leq Min \left[\begin{array}{l} 706, (1772 - 329 - 407 - 298 = 738\,kN), \\ (1363 - 407 - 298 = 658\,kN), (1046 - 298 = 748\,kN \end{array} \right] = 658\,kN$$

2.7.3 Flush end-plate connection

This example concerns for a cantilever beam with semi-rigid connection under concentrated loads as depicted in Fig. 2.27 . The purpose of this example is to confirm the performance of the proposed finite joint element. It is worth to mention that an experimental test have been performed on this example and all the results are reported in [26]. Mechanical properties of the connection are as those shown in Table **??**. Components characteristic values, determined in accordance with Eurocode 3 [23] procedures, are taken from [26] and represented in Table 2.5. All the geometric properties are shown in Fig 2.27. The beam is discretized just by one element and it subjected to simultaneous vertical and horizontal forces. The horizontal load, H, is given several values as a percentage of the axial beam plastic resistance,N_{pl}. However, the vertical load, F, takes a constant value for all the specimens.

The moment-rotation curves for the tested specimens are provided by Fig. 2.28. It is observed that the influence of the presence of axial force is predicted by the proposed model. It is seen that the bending moment increases with increasing of the compressive axial force but this increasing is limited. The maximum

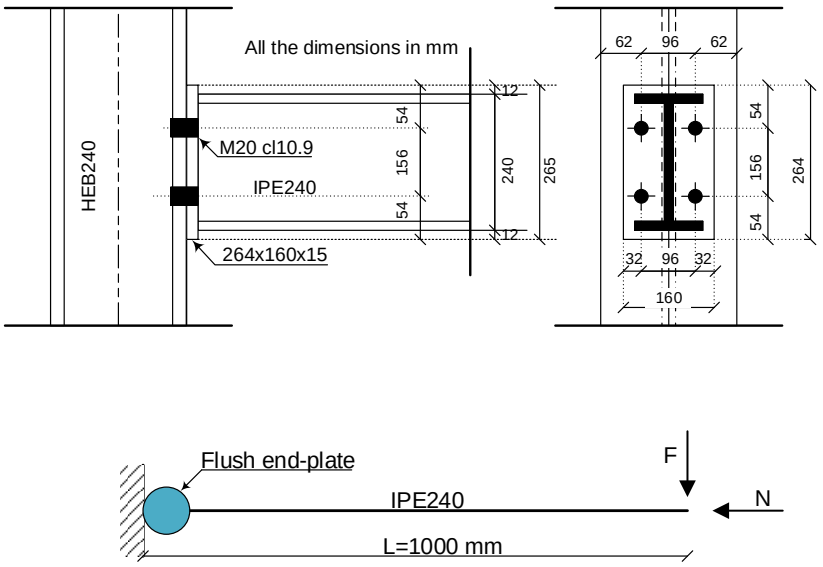

Figure 2.27: Cantilever beam and its semi-rigid configuration

Table 2.5: Components characterisation

Component	T3-1/T3-2		T2/T4	
	F_{Rd} (kN)	k/E(kN/mm)	F_{Rd} (kN)	k/E(kN/mm)
CWT	498.9	7.03	-	-
CFB	406.1	38.22	-	-
EPB	321.7	13.35	-	-
BWT	476.8	∞	-	-
BT	441	7.76	-	-
CWC	-	-	598.2	10.40
BFWC	-	-	529.8	∞

bending moment was observed for $H = 20\%\ N_{pl}$. In contrast, The tensile axial force reduce the connection bending moment capacity. It is worth to mention that these results are in accordance with those of the experimental tests, Fig. 2.29.

In the other hand, the interaction diagrams of bending moment-axial force for all the specimens are also captured and illustrated with the analytical one that drawn according to [13] and represented in Fig. 2.30. It is clearly that the interaction diagram for all the specimens remain inside and on the boundary of the analytical one. This result confirm the accuracy and efficiency of the proposed finite joint element.

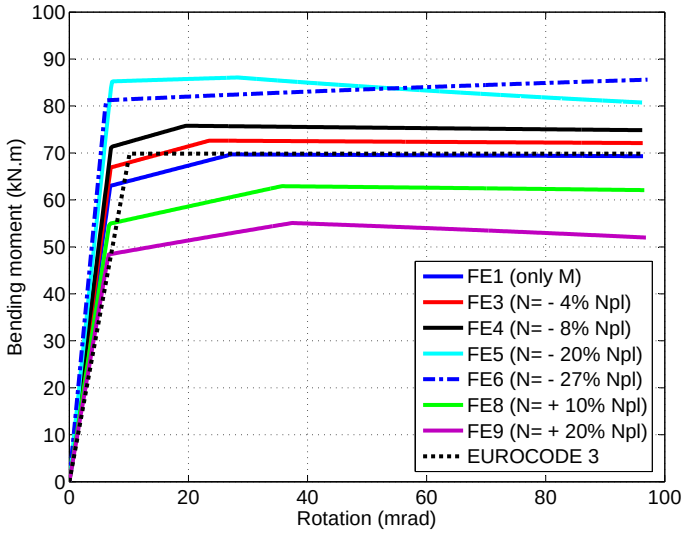

Figure 2.28: Moment-rotation curves of the specimens, proposed model

2.8 Conclusion

The performance of the beam-to-column joint model proposed in this chapter is due to its simplicity. It appears as an easy-to-compute tool that is very useful in practice to be implemented in structural analysis program, i.e. MATALB and

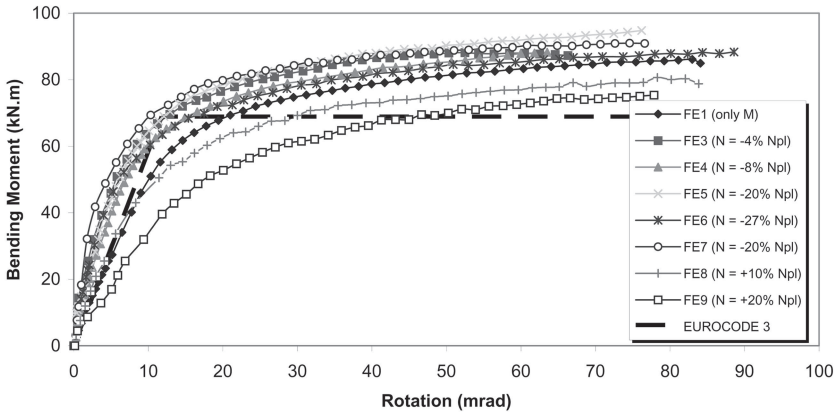

Figure 2.29: Moment-rotation curves of the specimens, experimental tests [26]

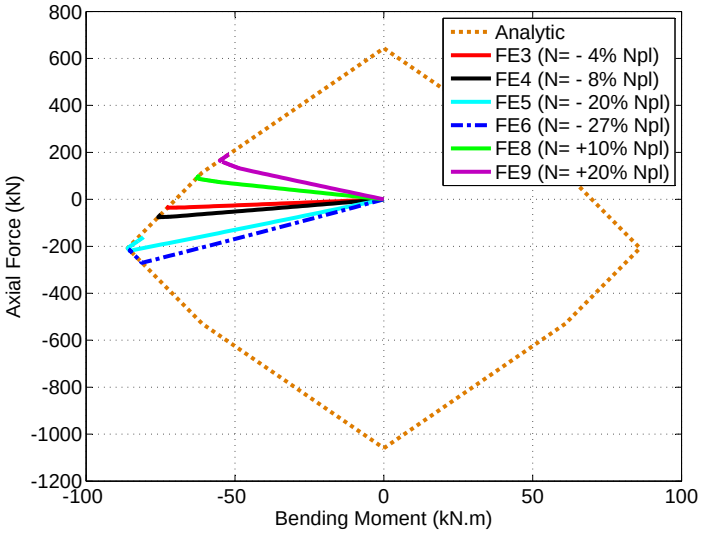

Figure 2.30: Bending moment-axial force interaction diagrams of the specimens

Fortran 90, to study frame behavior in dynamic for example. It is based on the component-based analysis that is nowadays well-known by the designers of the joints. It worth to remind that its performance has been extended to solve the problem of the gap that could appear between the column flange and the end-plate during the cyclic loading. This problem has never been considered before, especially when it is included as a part of the plasticity algorithm.

In addition, the group effect of two bolt-rows has been detailed to show how to implement this effect into the plasticity algorithm. This model has been generalized to take into account the group effect including more than two bolt-rows.

Both phenomena have been developed for simple cases of joints in order to simplify the validation of the proposed model. Nevertheless, both improvements proposed to the component based-model remain available for any bolted end-plate connection configuration.

i Concerning the gap effect, special care during computation is required for several tests that have to be computed for the gap to control the plasticity of each component within the joint. This care insures to approach the real behaviour of the joint including appropriate slipping to recover different gaps.

ii Concerning the solution proposed for the group effect, more the number of bolt-rows increases, more the number of criteria increases. The generalisation of the interaction formula has been easily verified for the case of a group of 3 bolt-rows and remains available for more.

Finally, The joint element with zero-length that derived from the component based model have been assembled with a beam element. The new joint finite element consists of a beam element with two joint elements connected at its ends. A numerical study was carried out on a steel beam-to-column flush end-plate connection subjected to axial force and bending moment. The results present the ability of this model to capture the joint response and the influence of the axial force on the moment-rotation curve.
For further developments:

i At first time, the example considered for the group of bolt-rows have to be treated under cyclic loading including the gap solution.

ii At second time, the model will be implemented in a structural analysis code to test frame behaviour under cyclic loading.

Bibliography

***

[1] R.M. Richard, P.E. Gillett, J.D. Kriegh, and B.A. Lewis (1980). The analysis and design of single plate framing connections. Engineering Journal, 1980, vol. 17, no 2.

[2] Moncarz, P.D., Gerstle, K.H. (1981). Steel frames with non-linear connections. Journal of the Structural Division, ASCE, 107, N° ST8, Proc. paper 16440, 1427-1441.

[3] POGGI, C. et ZANDONINI, R. (1985) Behaviour and strength of steel frames with semi-rigid connections. In : Connection Flexibility and Steel Frames. ASCE, 1985. p. 57-76.

[4] Nethercot, D. (1989). Methods of prediction of joint behaviour: beam-to-column connections. Elsevier Applied Science, Structural Connections. Stability and Strength,, 23-62.

[5] Patel, K. V., and Chen, W. F. (1985). Analysis of a fully bolted moment connection using NONSAP. Computers and structures, 1985, vol. 21, no 3, p. 505-511.

[6] Bursi, O. S., and Jaspart, J.P. (1997). Benchmarks for finite element modelling of bolted steel connections. Journal of Constructional Steel Research, 43(1), 17-42.

[7] Yang, J. G., Murray, T. M., and Plaut, R. H. (2000). Three-dimensional finite element analysis of double angle connections under tension and shear. Journal of Constructional Steel Research, 2000, vol. 54, no 2, p. 227-244.

[8] Maggi, Y.I., Goncalves, R.M. and Malite, M. (2002). Comparative analysis of bolted T-stub and corresponding extended endplate connections: a numerical approach European Conference on Steel Structure, Eurosteel 2002, Coimbra, 1199-1218.

[9] DÍAZ, Concepción, MARTÍ, Pascual, VICTORIA, Mariano, et al (2011). Review on the modelling of joint behaviour in steel frames. Journal of Constructional Steel Research, vol. 67, no 5, p. 741-758.

[10] YANG, Bo et TAN, Kang Hai. (2012). Component-based model of bolted-angle connections subjected to catenary action. In : Proc., 10th Int. Conf. on Advances in Steel Concrete Composite and Hybrid Structures.

[11] JASPART, J.P. (1996). Etude de la semi-rigidité des noeuds poutre-colonne et son influence sur la résistance et la stabilité des ossatures en acier (Doctoral dissertation). Université de liège, Belgique.

[12] JASPART, J.P., BRAHAM, M., et CERFONTAINE, F. (1999). Strength of joints subjected to combined action of bending moment and axial force. In : Proceedings of the Conference Eurosteel. 1999. p. 26-29.

[13] CERFONTAINE, F (2004). Étude de l'interaction entre moment de flexion et effort normal dans les assemblages boulonnés. Centre Technique Industriel de la Construction Métallique.

[14] DEL SAVIO A.A., NETHERCOT D.A., VELLASCO P.C.G.S., S.A.L. ANDRADA, L.F. MARTHA et al. (2009). Generalised component-based model for beam-to-column connections including axial versus moment interaction. Journal of Constructional Steel Research, 2009, vol. 65, no 8, p. 1876-1895.

[15] BAYO, E., CABRERO, J. M., et GIL, B. (2006). An effective component-based method to model semi-rigid connections for the global analysis of steel and composite structures. Engineering Structures,vol. 28, no 1, p. 97-108.

[16] LEMONIS, Minas E. et GANTES, Charis J. (2009). Mechanical modeling of the nonlinear response of beam-to-column joints. Journal of Constructional Steel Research, 65(4), 879-890.

[17] LIU, Chang, TAN, Kang Hai, et FUNG, Tat Ching. (2015). Component-based steel beam–column connections modelling for dynamic progressive collapse analysis. Journal of Constructional Steel Research, 107, 24-36.

[18] Mazzolani, F. M. (1988). Mathematical model for semi-rigid joints under cyclic loads. Connections in Steel Structurs: Behaviour, Strength and Design, Elsevier Applied Science Publishers, London, 112-120.

[19] Gang Shi, Yongjiu Shi, Yuanging Wang (2006). Behaviour of end-plate moment connections under earthquake loading. Engineering structures, 29(5), 703-716.

[20] YANG, Pu et EATHERTON, Matthew R. (2014). A phenomenological component-based model to simulate seismic behavior of bolted extended end-plate connections. Engineering Structures, 2014, vol. 75, p. 11-26.

[21] Da SILVA L.S., AHAHBAZIAN A., GENTILI F. and AUGUSTO H. (2016). Implementation of a component model for the cyclic behaviour of steel joints. Eighth International Workshop on Connections in Steel Structures, CONNECTIONS VIII, Boston, Massachusetts, USA

[22] DE LIMA, L. R. O., DA SILVA, L. Simoes, VELLASCO, PCG da S., et al. (2004). Experimental evaluation of extended endplate beam-to-column joints subjected to bending and axial force. Engineering Structures, 26(10), 1333-1347.

[23] Eurocode. 3 (2005). Design of steel structures, Part 1.8: Design of joints. Brussels: European Committee for Standardization.

[24] Krawinkler H. (1978). Shear design of steel frames joints AISC Engineering Journal, 15(3), 82-91.

[25] J.C. Simo, T.J.R. Hughes (1998). Computational Inelasticity. Springer

[26] DA SILVA, L. Simoes, DE LIMA, L. R. O., , VELLASCO, PCG da S., et al. (2004). Behaviour of flush end-plate beam-to-column joints under bending and axial force. Steel and Composite Structures, Vol. 4, N0. 2 , 77-94.

[27] BRODERICK, B. M. et THOMSON, A. W. (2002). The response of flush end-plate joints under earthquake loading. Journal of Constructional steel research, vol. 58, no 9, p. 1161-1175.

Chapter 3

Generalized plastic hinge

***

Co-rotational planar beam element with generalized elasto-plastic hinges.

Slender elements in framed structures may undergo large displacement and experience high nonlinear behavior. This section presents a flexible co-rotational two-noded beam with generalized elastic-plastic hinges at the beam ends. A Condensation procedure is used to remove the internal degrees of freedom so that the formulation is easily incorporated with the standard co-rotational approach. A family of asymmetric and convex yield surfaces of super-elliptic shape is considered for the plastic behaviour of the hinges. By varying the roundness factor, an infinite number of yield surface are obtained making it possible to select the yield function that best fit experimental data of any type of cross-section and material. The nonlinear response of bolted connections subjected to both bending and tension are conveniently modeled with such a yield surface. Discrete constitutive equations for the hinge plastic deformations are derived using the implicit scheme for both smooth and non-smooth cases. Numerical examples demonstrate the accuracy of the model in predicting the large displacement inelastic response of framed structures. Effect of the roundness factor on the ultimate load strongly depends on the structure typology. It was observed that cyclic loading produces pinching effect, cyclic softening and ductile behavior. Those effects are more

pronounced with anisotropic yield criteria.

3.1 Introduction

Serviceability conditions exposes the buildings to various kinds of loadings such as dead load, live load and wind/snow load. Added to those loads, extreme and accidental loadings in exceptional events such as seismic load, explosion and impact can cause framed structures to exhibit inelastically substantial strain. Slender elements in framed structures may undergo large displacement and experience high nonlinear behavior. The nonlinearity can be principally triggered by two sources: geometrical and material. Nonlinear behaviour is generally complex which requires nonlinear inelastic analysis methods. Most of the studies have agreed that a nonlinear inelastic analysis can be distinguishably placed into two branches: the distributed plasticity analysis and the concentrated plastic hinge method (lumped plasticity analysis) [4–15]. In distributed plasticity method, structural elements are meshed along the length into a set of finite elements and the cross-section is subdivided into several fiber where the spread of plasticity is considered. The Bernoulli-type beam elements in distributed plasticity method as found in [12, 16–21] take into account only uniaxial stress–strain relation of the cross-section. With this model gradual spread of yielding can be simulated although local buckling may not be accounted for. More recently, interaction between normal and shear stress has been implemented in Timoshenko planar beam element [22]. However, this method is still regarded as inappropriate for practical design use since it requires a numerical computation using a large number of stress - strain sampling points through the cross sections and along the member length to accurately consider the coupled effect between bending, normal and shear forces and the spread of yielding [23]. More than that, the formulation is rather complicated for a practical engineer to acquire.

On the contrary, the plastic hinge method allows the possibility to use fewer elements to model frame member and to skip the necessity to integrate over the discretized cross-sections for internal forces, which makes it more efficient in engi-

neering practices. With the advantages of its simplicity and its applicabilities, the plastic hinge concept has been applied in various settings by adopting different levels of enhancements. The elasto-plastic hinge method is the earliest formulation to be dated back among the others. In this analysis, the yielding effect of the member is concentrated at specific cross-sections located at member's ends whose inelastic behaviour is modelled by a means of dimensionless plastic hinge in the form of rotational springs. In addition, the constitutive relationship between bending moment and relative cross-section rotation is considered elastic perfectly plastic. In other words, the behaviour of the concentrated hinge is either elastic or perfectly plastic. As a consequence of the lumped plasticity, the element between the plastic hinges is assumed to remain elastic. Quite many research works have adopted this method to investigate the inelastic behaviour of the steel or concrete frame members [24–31]. Orbison et al in [24] developed a three-dimensional beam column finite element using a single equation stress-resultant yield surface to formulate the plastification of some steel cross-sections in the form of zero-length plastic hinge. Lui and Chen in [26] presented two types of elements to analyse the behaviour of semi-rigid plane steel frames namely beam-column element and connection element. The member inelastic behaviour was also modelled by concentrated plastic hinges. Chi, in [28], also used the plastic hinge approach to investigate the nonlinear behaviour of composite beams. In addition to that, Cuong et al in [29] presented a numerical procedure for nonlinear static analysis of space semi-rigid steel frame adopting the lumped inelastic concept using yield surface defined in the stress-resultants space. The second-order effects were considered by using the stability functions. However, Donald White concluded in [30] that the zero-length elastic-plastic hinge approaches are not adequate to be considered as advanced inelastic analysis methods because the members are modeled as fully elastic between the plastic hinge locations. Surovek in [23] added that the inelastic stiffness and the strength are normally overestimated in the zero-length elastic-plastic hinge method and that the interaction between stability and plasticity effect as well as the residual stress effects are not properly accounted. Seeing these inconsistencies in such conventional zero length

elastic plastic hinge methods, a number of enhancements of the elastic-plastic hinge method have been developed. For instance, Powell and Chan in [34] for the first time introduced the generalized plastic hinge approach in which the interaction between the axial, torsional and bi-axial bending effects is incorporated. Similarly, Liew et al in [35] proposed a refined plastic hinge formulation that utilizes a column tangent modulus concept to represent the effective stiffness of the element when loaded with large axial forces. This refined plastic hinge method has been adopted for steel concrete structures in [36]. This method accounts for degradation of the element stiffness in the process where the second order forces at critical locations in the element reach the cross-section plastic strength. Apart from that, a non-zero quasi-plastic hinge method was introduced by Attalla et al in [37]. Their method consists of an element formulation that is developed to account for gradual plastification through the cross-section under combined bending and axial force based on fitting the nonlinear equations to data obtained from inelastic and numerical integration of the cross section model along the member length. Ali et al in [38] adopted this quasi-plastic hinge method to develop a new force-based hinge element using large increment method. The proposed model is able to include inelastic behaviour close to structural hinges as well as strain hardening in the material. El-Tawil and Deierlein in [39] proposed a beam column element developed, using stress - resultant plasticity concepts to model inelastic cross section behaviour, incorporating cross-section model in a flexibility-based beam column element, and employing a function of dissipated hysteretic energy to model strength and stiffness degradation. Ziemian and McGuire [40], on the other hand, suggested a modified tangent modulus approach in as a contribution to plastic hinge analysis of the nonlinear inelastic behaviour of frame members. The approach used an empirical constant that has been calibrated to a set of moment curvature relationships to find a simple expression that degrades the elastic modulus of the individual elements based on the amount of axial force and minor-axis bending moment resisted. Cuong in [11] provided a fiber plastic hinge method to evaluate the nonlinear behaviour of space steel frame. Instead of using a specific yield surface, this fiber model partitioned the cross-section

into fibers and the plastification of the hinge is accounted by treating the stress - strain relationship of each fiber on the cross section. The stability functions are adopted to capture the second order effects. Hoang et al in [4] presented an overview of the plastic-hinge approach for 3-dimensional steel frame using both rigid-plastic and elastoplastic methods. The 3D plastic deformations of the hinges derive from the normality rule. However, these methodologies adopted require the use of optimization techniques to solve the equilibrium equations. Most of the above cited authors considered second order effects by enhancing the member stiffness equations with stability functions to include terms that depends on the axial forces which are constantly changing during the analysis.

In this chapter, a beam-column elements for nonlinear inelastic analysis of framed structure considering nonlinear geometry and nonlinear material behavior are presented. The model consists of an elastic flexible beam element whose ends are connected to generalized plastic hinges. In this model, the generalized plastic hinges which are modeled by combined axial and rotational springs are used to reproduce the plastification of the member including the full interaction between the axial force and the bending moment. As a consequence, the generalized plastic hinges have the ability to elongate/shorten along the beam axis and to rotate. Lateral-torsional buckling and local buckling are not considered because of the assumptions of adequate lateral bracing and compact cross-section. Besides, the material constitutive model is assumed to be elastic-perfectly plastic. Geometric nonlinearity for second order effect is included by the use of the co-rotational coordinate transformation techniques. A condensation procedure is performed to eliminate the internal degrees of freedom between the springs and the beam element ends so that the condensed stiffness matrix of the beam element with generalized plastic hinges has the usual dimension ready for assemblage. A family of asymmetric and convex yield surfaces of super-elliptic shape is considered for the plastic behaviour of the hinges. By varying the roundness factor, an infinite number of yield surface are obtained making it possible to select the yield function that best fit experimental data of any type of cross-section and material. The nonlinear response of bolted connections subjected to both

bending and tension can also be conveniently modeled with such a yield surface. The discrete constitutive equations for the hinge are derived based on both the rate form of the flow rule and the variational formulation. The expression of the consistent tangent operator is given with details and the solution algorithm which involve two stage (local and global equilibrium is described. Numerical examples demonstrate the accuracy of the model in predicting the large displacement inelastic response of framed structures. Effect of the roundness factor on the ultimate load strongly depends on the structure typology. It was observed that cyclic loading produces pinching effect, cyclic softening and ductile behavior. Those effects are more pronounced with anisotropic yield criteria.

3.2 Co-rotating beam element with generalized hinges

With regard to the co-rotational formulation for rods we employ here the one originally proposed by Rankin and Nour-Omid [47, 48], further developed by Battini and Pacoste [45, 46] and many other authors. The fundamental idea of a co-rotational formulation is to decompose the large motion of the element into rigid body and pure deformation parts through the use of a local system which continuously rotates and translates with the element. The deformation is captured at the level of the local reference frame, whereas the geometric non-linearity induced by the large rigid-body motion, is incorporated in the transformation matrices relating local and global displacements. The main interest is that the pure deformation part can be assumed as small and can be represented by a linear or a low order non-linear theory. Avoiding the nonlinear relationship between the strain tensor and the displacement gradient makes the co-rotational approach very attractive and efficient for nonlinear static analysis. The efficiency is even more substantial if the material behavior is inelastic as large strain time stepping algorithms are far more complex than the small strain ones. For a general account we refer also to [41] where the kinematics and the derivation of the tangent stiffness matrix of the standard co-rotating element are detailed.

3.2.1 Beam kinematics

The structural member consists of three subelements: a standard flexible beam element and two generalized elasto-plastic hinges that are modeled by a combination of axial and rotational springs, see Fig. 3.1. Elongation/shortening of the hinges occur along the beam axis. The generalized hinges can be seen as finite element with zero initial length. Assembling these hinges with the beam element gives a two-node superelement that maybe regarded as an individual element for computational purposes. Since plasticity is assumed to be concentrated at the hinges, the beam element is allowed to bend and to stretch in pure elastic range. The generalized plastic hinges, on the other hand, are able to rotate and to stretch according to the elasto-plastic constitutive relationships expressed in incremental form considering a yield criterion in the stress-resultants space and the normality rule. The latter governs the plastic flow, i.e. the plastic rotation and the plastic elongation/shortening.

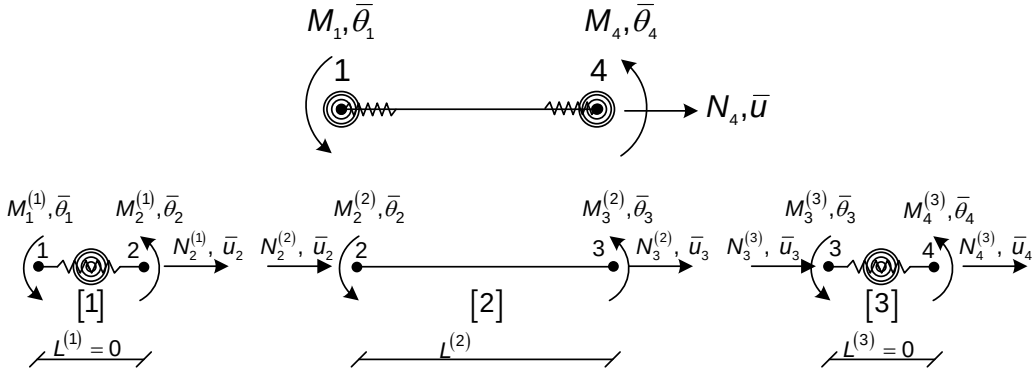

Figure 3.1: Local superelement

The co-rotational framework is applied to the structural member. The origin of the co-rotational frame is taken at node 1 located at the centroid of the cross-section. The x-axis of the local coordinate system is defined by the line connecting node 1 to node 4. The y-axis is orthogonal to the x-axis so that the result is right-

handedly orthogonal coordinate system. The motion of the element from the original undeformed to the actual deformed configuration can thus be separated into two parts. The first one, which corresponds to rigid motion of the local frame, is the translation of node 1 and the rotation α of the x-axis (see Fig. 3.2). The second one refers to the deformations in the co-rotating element frame.

The notations used in this section are defined in Figs. 3.1 and 3.2. The subscript and the superscript denote the node number and the subelement number, respectively. The coordinates of the nodes 1 and 4 in the global coordinate system (X, Y) are (X_1, Y_1) and (X_4, Y_4), respectively. In the deformed configuration (see Fig. 3.2), the global nodal rotations of the superelement nodes (node 1 and node 4) are θ_1 and θ_4 and the local ones are $\bar{\theta_1}$ and $\bar{\theta_4}$, respectively. In addition to this, the global rotations of the elastic beam element nodes (node 2 and 3) are described by θ_2 and θ_3 and the local ones by $\bar{\theta_2}$ and $\bar{\theta_3}$, respectively

$$\begin{aligned} \theta_2 &= \theta_1 - \hat{\theta}_1 \\ \theta_3 &= \theta_4 - \hat{\theta}_4 \end{aligned} \tag{3.1}$$

where $\hat{\theta}_1$ and $\hat{\theta}_4$ are the relative rotations between the local rotations of the superelement and the local rotations of the elastic flexible beam sub-element, respectively.

The total elongation, $\bar{u}$, is composed of the elongations of the first hinge $\bar{u}_{(12)}$, the elastic beam element $\bar{u}_{(23)}$ and the second hinge $\bar{u}_{(34)}$

$$\bar{u} = \bar{u}_{(12)} + \bar{u}_{(23)} + \bar{u}_{(34)} \tag{3.2}$$

with

$$\begin{aligned} \bar{u}_{(12)} &= \bar{u}_2 - \bar{u}_1 \\ \bar{u}_{(23)} &= \bar{u}_3 - \bar{u}_2 \\ \bar{u}_{(34)} &= \bar{u}_4 - \bar{u}_3 \end{aligned} \tag{3.3}$$

The vectors of global and local displacements are respectively defined by:

$$\boldsymbol{d}_g = \begin{bmatrix} u_1 & v_1 & \theta_1 & u_4 & v_4 & \theta_4 \end{bmatrix}^{\mathrm{T}} \tag{3.4}$$

$$\boldsymbol{d}_l = \begin{bmatrix} \bar{\mathrm{u}} & \bar{\theta_1} & \bar{\theta_4} \end{bmatrix}^{\mathrm{T}} \tag{3.5}$$

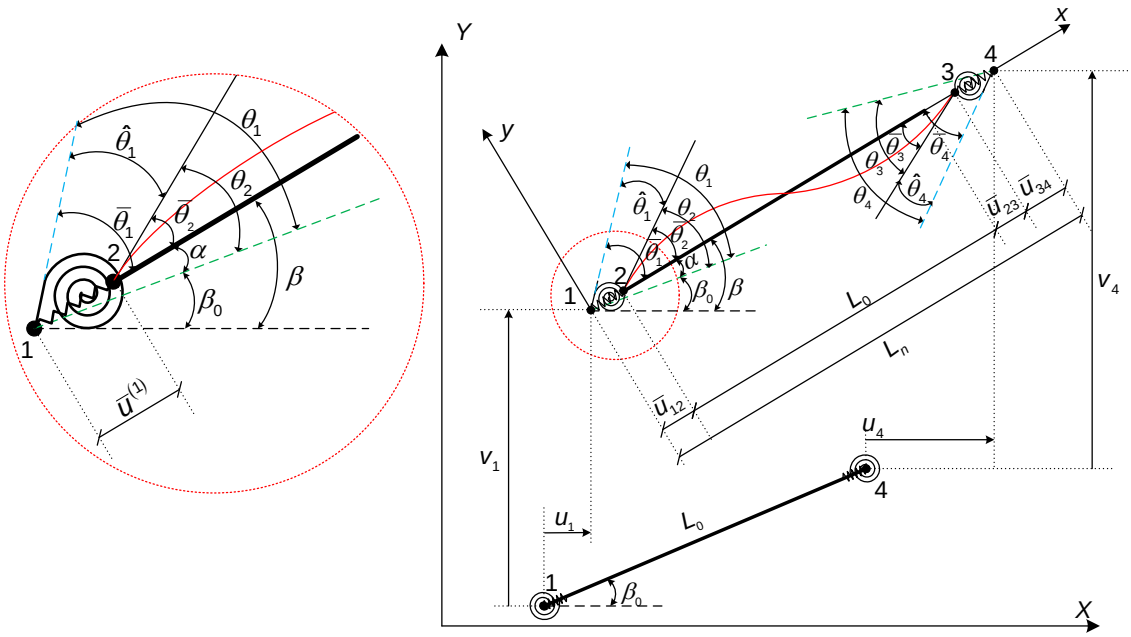

Figure 3.2: Initial and final configuration for the beam element

Referring to the definition of the co-rotating frame, the components of the local displacement vector $\mathbf{d}_l$ can be calculated as (see Fig. 3.2)

$$\bar{u} = L_n - L_0 \tag{3.6a}$$

$$\bar{\theta}_1 = \theta_1 - \alpha \tag{3.6b}$$

$$\bar{\theta}_4 = \theta_4 - \alpha \tag{3.6c}$$

where the initial and final length of the element defined as L_0 and L_n, respectively, are obtained by

$$L_0 = \sqrt{(X_4 - X_1)^2 + (Y_4 - Y_1)^2} \tag{3.7a}$$

$$L_n = \sqrt{(X_4 - X_1 + u_4 - u_1)^2 + (Y_4 - Y_1 + v_4 - v_1)^2} \tag{3.7b}$$

in which $(X_1 + u_1, Y_1 + v_1)$ and $(X_4 + u_4, Y_4 + v_4)$ are the global coordinates in the deformed configuration of node 1 and node 4, respectively. With the help of basic

geometric considerations, the rigid rotation of the x-axis α, that was mentioned in Eqs. (3.6b) and (3.6c), is computed as

$$\sin\alpha = c_0\, s - s_0\, c \tag{3.8a}$$

$$\cos\alpha = c_0\, c + s_0\, s \tag{3.8b}$$

with

$$c = \cos\beta = \frac{1}{L_n}(X_4 - X_1 + u_4 - u_1) \tag{3.9a}$$

$$c_0 = \cos\beta_0 = \frac{1}{L_0}(X_4 - X_1) \tag{3.9b}$$

$$s = \sin\beta = \frac{1}{L_n}(Y_4 - Y_1 + v_4 - v_1) \tag{3.9c}$$

$$s_0 = \sin\beta_0 = \frac{1}{L_0}(Y_4 - Y_1) \tag{3.9d}$$

The local - global displacement relationship can be derived through differentiation of Eqs. (3.6), therefore one can write:

$$\delta\bar{u} = \delta L_n \tag{3.10a}$$

$$\delta\bar{\theta_1} = \delta\theta_1 - \delta\alpha = \delta\theta_1 - \delta\beta \tag{3.10b}$$

$$\delta\bar{\theta_4} = \delta\theta_4 - \delta\alpha = \delta\theta_4 - \delta\beta \tag{3.10c}$$

By using (3.7b)and (3.9c), one obtains

$$\delta\bar{u} = c\,(\delta u_2 - \delta u_1) + s\,(\delta v_4 - \delta v_1) = \begin{bmatrix} -c & -s & 0 & c & s & 0 \end{bmatrix} \delta\boldsymbol{d}_g \tag{3.11}$$

$$\delta\beta = \frac{1}{cL_n}\begin{bmatrix} s & -c & 0 & -s & c & 0 \end{bmatrix} \delta\boldsymbol{d}_g \tag{3.12}$$

Finally, the global displacement vector is related to the local deformation vector by

$$\delta\boldsymbol{d}_l = \boldsymbol{B}\delta\boldsymbol{d}_g \tag{3.13}$$

where the transformation matrix, $\boldsymbol{B}$ is given by

$$\boldsymbol{B} = \begin{bmatrix} -c & -s & 0 & c & s & 0 \\ -\dfrac{s}{L_n} & \dfrac{c}{L_n} & 1 & \dfrac{s}{L_n} & -\dfrac{c}{L_n} & 0 \\ -\dfrac{s}{L_n} & \dfrac{c}{L_n} & 0 & \dfrac{s}{L_n} & -\dfrac{c}{L_n} & 1 \end{bmatrix} \tag{3.14}$$

3.2.2 Element formulation

The co-rotational method is convenient for establishing the relationship between the local and global variables. The relation between the global force vector $\boldsymbol{f}_g$ and the local one $\boldsymbol{f}_l$ is obtained by equating the virtual work in the local and global system as

$$\delta \boldsymbol{d}_g^{\mathrm{T}} \boldsymbol{f}_g = \delta \boldsymbol{d}_l^{\mathrm{T}} \boldsymbol{f}_l = \delta \boldsymbol{d}_g^{\mathrm{T}} \boldsymbol{B}^{\mathrm{T}} \boldsymbol{f}_l \tag{3.15}$$

Eq. (3.15) must apply for any arbitrary $\delta \boldsymbol{d}_g$. Hence, the global force vector $\boldsymbol{f}_g$ is given by

$$\boldsymbol{f}_g = \boldsymbol{B}^{\mathrm{T}} \boldsymbol{f}_l \tag{3.16}$$

By taking the differentiation of Eq. (3.16) with respect to global displacement vector, the global stiffness matrix is obtained as

$$\boldsymbol{k}_g = \boldsymbol{B}^{\mathrm{T}} \boldsymbol{k}_l \boldsymbol{B} + \frac{\boldsymbol{z}\boldsymbol{z}^{\mathrm{T}}}{L_n} N_4 + \frac{1}{L_n^2} \left(\boldsymbol{r}\boldsymbol{z}^{\mathrm{T}} + \boldsymbol{z}\boldsymbol{r}^{\mathrm{T}} \right) (M_1 + M_4) \tag{3.17}$$

where

$$\boldsymbol{r} = \begin{bmatrix} -c & -s & 0 & c & s & 0 \end{bmatrix}^{\mathrm{T}} \tag{3.18}$$

$$\boldsymbol{z} = \begin{bmatrix} s & -c & 0 & -s & c & 0 \end{bmatrix}^{\mathrm{T}} \tag{3.19}$$

3.3 Local element definition

This section will be devoted to the elaboration of the local tangent stiffness matrix of the superelement. Illustrated in Fig. 3.1, the superelement is composed of three sub-elements: an elastic beam element and two generalized elasto-plastic hinges. The introduction of the generalized hinges at the beam ends increases the number of degrees of freedom exceeding the original ones in the standard co-rotational formulation. The static condensation procedure is then used to eliminate the internal nodes (node 2 and node 3) and the corresponding degree of freedom. To establish the assembled tangent stiffness of the superelement consistent with the co-rotational format, the displacement of node 1 is restrained ($\bar{u}_1 = 0$). The

elongation/shortening or relative axial displacement jump of each subelement are denoted by $\bar{u}_{(ij)} = \bar{u}_j - \bar{u}_i$ (Eqs. 3.3). The subelement 1, i.e. an elasto-plastic hinge modeled by a combination of a rotational and an axial springs, has an axial elongation $\bar{u}_{(12)}$ and a relative rotation $\hat{\theta}_1 = \bar{\theta}_1 - \bar{\theta}_2$. The incremental relation between the stress-resultants and their conjugates can be formally written as

$$\left\{ \begin{array}{c} \Delta N_2^{(1)} \\ \Delta M_2^{(1)} \end{array} \right\} = \begin{bmatrix} C_{11}^{(1)} & C_{12}^{(1)} \\ C_{21}^{(1)} & C_{22}^{(1)} \end{bmatrix}_{n+1} \left\{ \begin{array}{c} \Delta \bar{u}_2 \\ \Delta \bar{\theta}_2 - \Delta \bar{\theta}_1 \end{array} \right\} \tag{3.20}$$

in which, n is the number of step. The tangent operator matrix $\mathbb{C}$ defined in Eq. (3.21) is obtained from the plastic constitutive law of the hinges that is given in Section 3.5.

$$\mathbb{C}_{n+1}^{(1)} = \begin{bmatrix} C_{11}^{(1)} & C_{12}^{(1)} \\ C_{21}^{(1)} & C_{22}^{(1)} \end{bmatrix}_{n+1} \tag{3.21}$$

The incremental equilibrium of the first element imposes that

$$\Delta M_1^{(1)} + \Delta M_2^{(1)} = 0 \tag{3.22}$$

Combining Eqs. (3.20) and (3.22) gives

$$\left\{ \begin{array}{c} \Delta M_1^{(1)} \\ \Delta N_2^{(1)} \\ \Delta M_2^{(1)} \end{array} \right\} = \begin{bmatrix} C_{22}^{(1)} & -C_{12}^{(1)} & -C_{22}^{(1)} \\ -C_{12}^{(1)} & C_{11}^{(1)} & C_{12}^{(1)} \\ -C_{22}^{(1)} & C_{12}^{(1)} & C_{22}^{(1)} \end{bmatrix}_{n+1} \left\{ \begin{array}{c} \Delta \bar{\theta}_1 \\ \Delta \bar{u}_2 \\ \Delta \bar{\theta}_2 \end{array} \right\} \tag{3.23}$$

Using the same procedure for the sub-element 3 we obtain the incremental equilibrium equations for this element:

$$\begin{aligned} \Delta M_3^{(3)} + \Delta M_4^{(3)} &= 0 \\ \Delta N_3^{(3)} + \Delta N_4^{(3)} &= 0 \end{aligned} \tag{3.24}$$

Hence,the relation between the stress-resultants and their conjugates in the second generalized elasto-plastic hinge is given as

$$\left\{ \begin{array}{c} \Delta N_3^{(3)} \\ \Delta M_3^{(3)} \\ \Delta N_4^{(3)} \\ \Delta M_4^{(3)} \end{array} \right\} = \begin{bmatrix} C_{11}^{(3)} & C_{12}^{(3)} & -C_{11}^{(3)} & -C_{12}^{(3)} \\ C_{12}^{(3)} & C_{22}^{(3)} & -C_{12}^{(3)} & -C_{22}^{(3)} \\ -C_{11}^{(3)} & -C_{12}^{(3)} & C_{11}^{(3)} & C_{12}^{(3)} \\ -C_{12}^{(3)} & -C_{22}^{(3)} & C_{12}^{(3)} & C_{22}^{(3)} \end{bmatrix}_{n+1} \left\{ \begin{array}{c} \Delta \bar{u}_3 \\ \Delta \bar{\theta}_3 \\ \Delta \bar{u}_4 \\ \Delta \bar{\theta}_4 \end{array} \right\} \tag{3.25}$$

On the other hand, the beam element (subelement 2) is assumed to deform elastically. Having an elastic elongation $\bar{u}_{(12)}$ and elastic rotations θ_2 and θ_3 on each side of its ends, the incremental stress-resultants are related to their conjugates, for this subelement, by

$$\begin{Bmatrix} \Delta N_2^{(2)} \\ \Delta M_2^{(2)} \\ \Delta N_3^{(2)} \\ \Delta M_3^{(2)} \end{Bmatrix} = \begin{bmatrix} k_{11}^{(2)} & 0 & -k_{11}^{(2)} & 0 \\ 0 & k_{22}^{(2)} & 0 & k_{24}^{(2)} \\ -k_{11}^{(2)} & 0 & k_{11}^{(2)} & 0 \\ 0 & k_{42}^{(2)} & 0 & k_{44}^{(2)} \end{bmatrix}_{n+1} \begin{Bmatrix} \Delta\bar{u}_2 \\ \Delta\bar{\theta}_2 \\ \Delta\bar{u}_3 \\ \Delta\bar{\theta}_3 \end{Bmatrix} \tag{3.26}$$

in which, $k_{11}^{(2)} = \dfrac{EA}{L}$, $k_{22}^{(2)} = k_{44}^{(2)} = \dfrac{4EI}{L}$ and $k_{24}^{(2)} = k_{42}^{(2)} = \dfrac{2EI}{L}$. E, I, A and L denote the Young modulus, the second moment of area, the cross-section area and the beam length, respectively. The tangent stiffness matrix for the superelement is assembled using the standard direct stiffness method based on nodal force equilibrium equations. The sum of internal forces exerted by all members that meet at a joint balances the external force applied to that joint. Further, as shown in Fig. 3.1, the flexural beam element has two ends: node 2 and 3. The nodal equilibrium equations for these nodes, used to eliminate the extra degrees of freedom, are given as follows

$$\begin{aligned} \Delta N_2^{(1)} + \Delta N_2^{(2)} &= 0 \\ \Delta M_2^{(1)} + \Delta M_2^{(2)} &= 0 \\ \Delta N_3^{(2)} + \Delta N_3^{(3)} &= 0 \\ \Delta M_3^{(2)} + \Delta M_3^{(2)} &= 0 \end{aligned} \tag{3.27}$$

The above equilibrium equations are supplemented with equilibrium equations pertaining to the end nodes (node 1 and node 4):

$$\begin{aligned} \Delta M_1 &= \Delta M_1^{(1)} \\ \Delta N_4 &= \Delta N_4^{(3)} \\ \Delta M_4 &= \Delta M_4^{(3)} \end{aligned} \tag{3.28}$$

Equilibrium equations Eq.3.27 and Eq.3.28 are combined together with the member stiffness equations Eq.3.23, Eq.3.25 and Eq.3.26 to give:

$$\Delta \boldsymbol{f} = [\boldsymbol{k}]_{n+1}\ \Delta \boldsymbol{d} \tag{3.29}$$

with

$$\boldsymbol{f}^{\mathrm{T}} = \begin{bmatrix} M_1 & 0 & 0 & 0 & 0 & N_4 & M_4 \end{bmatrix} \quad , \quad \boldsymbol{d}^{\mathrm{T}} = \begin{bmatrix} \bar{\theta}_1 & \bar{u}_2 & \bar{\theta}_2 & \bar{u}_3 & \bar{\theta}_3 & \bar{u}_4 & \bar{\theta}_4 \end{bmatrix} \tag{3.30}$$

and

$$[\boldsymbol{k}]_{n+1} = \begin{bmatrix} C_{22}^{(1)} & -C_{12}^{(1)} & -C_{22}^{(1)} & 0 & 0 & 0 & 0 \\ -C_{12}^{(1)} & C_{11}^{(1)} + k_{11}^{(2)} & C_{12}^{(1)} & -k_{11}^{(2)} & 0 & 0 & 0 \\ -C_{22}^{(1)} & C_{12}^{(1)} & C_{22}^{(1)} + k_{22}^{(2)} & 0 & k_{24}^{(2)} & 0 & 0 \\ 0 & -k_{11}^{(2)} & 0 & k_{11}^{(2)} + C_{11}^{(3)} & C_{12}^{(3)} & -C_{11}^{(3)} & -C_{12}^{(3)} \\ 0 & 0 & k_{42}^{(2)} & C_{21}^{(3)} & k_{44}^{(2)} + C_{22}^{(3)} & -C_{12}^{(3)} & -C_{22}^{(3)} \\ 0 & 0 & 0 & -C_{11}^{(3)} & -C_{12}^{(3)} & C_{11}^{(3)} & C_{12}^{(3)} \\ 0 & 0 & 0 & -C_{12}^{(3)} & -C_{22}^{(3)} & C_{12}^{(3)} & C_{22}^{(3)} \end{bmatrix} \tag{3.31}$$

To carry out the condensation process, the assembled stiffness equations of the superelement (Eq.3.29) are rearranged and partitioned as follows:

$$\begin{Bmatrix} \Delta \boldsymbol{f}_l \\ \boldsymbol{0} \end{Bmatrix} = \begin{bmatrix} [\boldsymbol{k}_{ll}]_{n+1} & [\boldsymbol{k}_{li}]_{n+1} \\ [\boldsymbol{k}_{il}]_{n+1} & [\boldsymbol{k}_{ii}]_{n+1} \end{bmatrix} \begin{Bmatrix} \Delta \boldsymbol{d}_l \\ \Delta \boldsymbol{d}_i \end{Bmatrix} \tag{3.32}$$

where the subvector $\Delta \boldsymbol{d}_i$ collects the interior degrees of freedom and the subvector $\Delta \boldsymbol{d}_l$ comprises the co-rotational kinematic variables pertaining to the superelement (elongation and local rotations at the end nodes):

$$\boldsymbol{d}_l = \begin{Bmatrix} \bar{u}_4 \\ \bar{\theta}_1 \\ \bar{\theta}_4 \end{Bmatrix} \quad , \quad \boldsymbol{d}_i = \begin{Bmatrix} \bar{u}_2 \\ \bar{\theta}_2 \\ \bar{u}_3 \\ \bar{\theta}_3 \end{Bmatrix} \tag{3.33}$$

In the above equation, the subvector $\boldsymbol{f}_l$ collect the independent stress-resultants pertaining to the superelement which corresponds to the so-called local force vector in the co-rotational formulation:

$$\boldsymbol{f}_l = \begin{Bmatrix} N_4 \\ M_1 \\ M_4 \end{Bmatrix} \tag{3.34}$$

The sub-matrices in Eq.(3.32) have the following expressions:

$$\boldsymbol{k}_{ll} = \begin{bmatrix} C_{11}^{(3)} & 0 & C_{12}^{(3)} \\ 0 & C_{22}^{(1)} & 0 \\ C_{12}^{(3)} & 0 & C_{22}^{(1)} \end{bmatrix}_{n+1} \tag{3.35}$$

$$\boldsymbol{k}_{li} = \begin{bmatrix} 0 & 0 & -C_{11}^{(3)} & -C_{12}^{(3)} \\ -C_{12}^{(1)} & -C_{22}^{(1)} & 0 & 0 \\ 0 & 0 & -C_{12}^{(3)} & -C_{22}^{(3)} \end{bmatrix}_{n+1} \tag{3.36}$$

$$\boldsymbol{k}_{il} = \begin{bmatrix} 0 & -C_{12}^{(1)} & 0 \\ 0 & -C_{22}^{(1)} & 0 \\ -C_{11}^{(3)} & 0 & -C_{12}^{(3)} \\ -C_{12}^{(3)} & 0 & -C_{22}^{(3)} \end{bmatrix}_{n+1} \tag{3.37}$$

$$\boldsymbol{k}_{ii} = \begin{bmatrix} C_{11}^{(1)} + k_{11}^{(2)} & C_{12}^{(1)} & -k_{11}^{(2)} & 0 \\ C_{12}^{(1)} & C_{22}^{(1)} + k_{22}^{(2)} & 0 & k_{24}^{(2)} \\ -k_{11}^{(2)} & 0 & k_{11}^{(2)} + C_{11}^{(3)} & C_{12}^{(3)} \\ 0 & k_{42}^{(3)} & C_{12}^{(3)} & C_{22}^{(3)} + k_{33}^{(3)} \end{bmatrix}_{n+1} \tag{3.38}$$

Solving for the interior degrees of freedom:

$$\Delta \boldsymbol{d}_i = -\left[\boldsymbol{k}_{ii}\right]_{n+1}^{-1} \left[\boldsymbol{k}_{il}\right]_{n+1} \Delta \boldsymbol{d}_l \tag{3.39}$$

and replacing the outcome into the first matrix equation yield the condensed stiffness equations

$$\Delta \boldsymbol{f}_l = \left[\boldsymbol{k}_l\right]_{n+1} \Delta \boldsymbol{d}_l \tag{3.40}$$

with

$$\left[\boldsymbol{k}_l\right]_{n+1} = \left[\boldsymbol{k}_{ll}\right]_{n+1} - \left[\boldsymbol{k}_{li}\right]_{n+1} \left[\boldsymbol{k}_{ii}\right]_{n+1}^{-1} \left[\boldsymbol{k}_{il}\right]_{n+1} \tag{3.41}$$

$\left[\boldsymbol{k}_l\right]_{n+1}$ is the local tangent stiffness matrix. To ease the computations, the above stiffness equations are slightly modified by replacing the axial displacements with

sub-element elongations using

$$\begin{aligned} \Delta\bar{u}_2 &= \Delta\bar{u}_{(12)} \\ \Delta\bar{u}_3 &= \Delta\bar{u}_{(12)} + \Delta\bar{u}_{(23)} \\ \Delta\bar{u}_4 &= \Delta\bar{u}_{(12)} + \Delta\bar{u}_{(23)} + \Delta\bar{u}_{(34)} = \Delta\bar{u} \end{aligned} \tag{3.42}$$

where $\Delta\bar{u}$ is the elongation of the superelement. Full expressions of the new assembled stiffness matrix along with the corresponding sub-matrices are given in the appendix.

3.4 Generalized plastic hinge model

We apply the general plasticity theory [42] to the generalized elasto-plastic hinges. The present model assumes that plasticity are lumped into axial and rotational springs located at the end of flexible beam element. The elastic behavior of the generalized hinge is uncoupled whereas axial-moment interaction is considered in the plastic range. We adopt the total generalized strain rate decomposition into elastic and plastic parts

$$\dot{\boldsymbol{\Xi}} = \dot{\boldsymbol{\Xi}}_e + \dot{\boldsymbol{\Xi}}_p \tag{3.43}$$

where $\dot{\boldsymbol{\Xi}} = \left[\, \dot{\theta} \;,\; \dot{\delta} \,\right]^{\mathrm{T}}$. For an associated flow rule, the direction of the generalized plastic strain rate vector is given by the gradient to the yield function, with its magnitude given by the plastic multiplier rate $\dot{\lambda}$:

$$\dot{\boldsymbol{\Xi}}_p = \dot{\lambda}\, \frac{\partial f}{\partial \boldsymbol{\Sigma}} \tag{3.44}$$

where $\boldsymbol{\Sigma} = [\, M, N \,]^{\mathrm{T}}$ is the generalized stress vector containing the bending and axial forces in the hinge. The plastic multiplier $\dot{\lambda}$ is determined by the classical complementary conditions:

$$\dot{\lambda} \geq 0, \qquad f(M,N) \leq 0, \qquad \dot{\lambda}\, f(M,N) = 0 \tag{3.45}$$

The set of allowable stress resultants K defined by

$$K = \left\{ \boldsymbol{\Sigma} \in \mathbb{R}^2 \middle|\, f(\boldsymbol{\Sigma}) \leq 0 \right\} \tag{3.46}$$

An alternative formulation of the rate form of the flow rule given in Eq(3.44) is the Hill variational inequality:

$$\boldsymbol{\Sigma} \in K, \qquad \dot{\boldsymbol{\Xi}}^p \cdot (\boldsymbol{\Sigma}^* - \boldsymbol{\Sigma}) \leq 0, \qquad \forall \boldsymbol{\Sigma}^* \in K \tag{3.47}$$

Both formulation will be used to derive the discrete counterpart of the constitutive equations. Assuming linear elastic behaviour, the generalized stresses are given as:

$$\boldsymbol{\Sigma} = \mathbb{C}_e \left(\boldsymbol{\Xi} - \boldsymbol{\Xi}^p \right) \tag{3.48}$$

in which the elastic stiffness matrix is given by:

$$\mathbb{C}_e = \begin{bmatrix} k_\theta & 0 \\ 0 & k_\delta \end{bmatrix}$$

In this model, the classical distributed plasticity model is replaced by transforming the stress-space yield surface of fiber model, denoted by $f(\sigma_x)$, to stress-resultant space yield surface, denoted by $f(M, N)$ due to the assumption that the plasticization of the cross section is controlled by a yield surface of the combined effects of axial and bending forces disregarding shear and torsional actions. In this chapter, we consider a family of asymmetric and convex yield surface of superelliptic shape:

$$f(M, N) = \|\boldsymbol{\Sigma}\|_q - 1 \tag{3.49}$$

where

$$\|\boldsymbol{\Sigma}\|_q = \left(\left| \frac{N + |N|}{2N_{p+}} + \frac{N - |N|}{2N_{p-}} \right|^q + \left| \frac{M + |M|}{2M_{p+}} + \frac{M - |M|}{2M_{p-}} \right|^q \right)^{\frac{1}{q}} \tag{3.50}$$

with $1 \leq q < \infty$. The curve intersects the x-axis at N_{p+} and N_{p-} and the y-axis at M_{p+} and M_{p-}. The coefficient q, called roundness factor, controls the shape of the (M-N) interaction criterion. This shape evolves from a parallelogram ($p = 1$) to a rectangle ($p \mapsto \infty$). Its shape is plot in Fig. (3.3) for $q = 1$, 2, 4 and 12. The super-elliptic yield surface is defined in Eq. (3.49), and its anisotropic super-elliptic norm can be reformulated as

$$\|\boldsymbol{\Sigma}\|_q = \left(|\varrho_N N|^q + |\varrho_M M|^q \right)^{\frac{1}{q}} \tag{3.51}$$

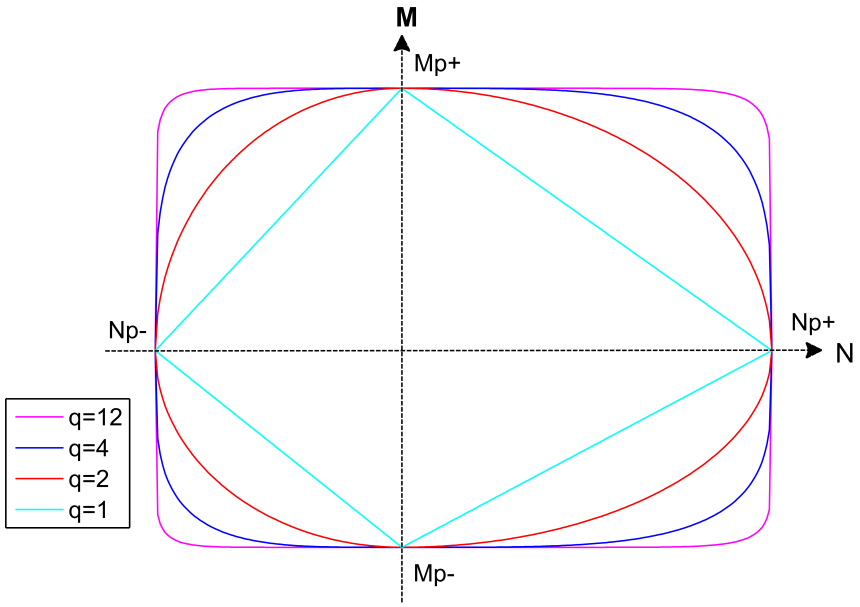

Figure 3.3: General case of anisotropic yield surface

where the sign dependent coefficients ϱ_M and ϱ_N are defined by

$$\varrho_M = a_M + b_M \operatorname{sgn}(M) \quad \text{and} \quad \varrho_N = a_N + b_N \operatorname{sgn}(N) \tag{3.52}$$

in which the constants $a_\bullet$ and $b_\bullet$ are defined by

$$a_\bullet = \left(\frac{1}{2\bullet_{p+}} + \frac{1}{2\bullet_{p-}} \right) \quad \text{and} \quad b_\bullet = \left(\frac{1}{2\bullet_{p+}} - \frac{1}{2\bullet_{p-}} \right) \tag{3.53}$$

and the *signum* function $\operatorname{sgn}(\bullet)$ is defined by

$$\operatorname{sgn}(x) = \begin{cases} 1 & \text{for } x > 0 \\ 0 & \text{for } x = 0 \\ -1 & \text{for } x < 0 \end{cases}$$

3.5 Discrete constitutive equations of the generalized plastic hinge

The plastic behavior is completely specified by the flow rule and the loading/unloading conditions. Its analytical transcription can take different but equivalent forms. Probably, the most familiar version of the flow rule is the rate equation (3.44) completed by the complementary conditions (3.57). An alternative formulation is provided by Hill's principle of maximum dissipation. This principle takes the form of a variational inequality (3.47). The discrete constitution are derived for the general case using the rate form of the flow rule. For the linear and quadratic yield criteria, we adopt the variational formulation. In order to enforce the flow rule at the end of each time step, we apply the Euler-backward type approximation scheme. We recall here that the time t is conceived as a monotonically increasing arbitrary parameter, which merely orders successive events since a time-independent behavior of the hinges is assumed. The current state of the stress-resultants given by Hook's law:

$$\boldsymbol{\Sigma}_{n+1} = \mathbb{C}_e \left(\boldsymbol{\Xi}_{n+1} - \boldsymbol{\Xi}^p_{n+1} \right) = \boldsymbol{\Sigma}_n + \mathbb{C}_e \left(\Delta\boldsymbol{\Xi} - \Delta\boldsymbol{\Xi}_p \right) \tag{3.54}$$

with

$$\boldsymbol{\Sigma}_{n+1} = \left\{ \begin{array}{c} M_{n+1} \\ N_{n+1} \end{array} \right\}, \qquad \Delta\boldsymbol{\Xi}_p = \left\{ \begin{array}{c} \Delta\theta_p \\ \Delta\delta_p \end{array} \right\} \tag{3.55}$$

The increment of plastic deformation vector is obtained by integrating Eq. (3.44) using the Euler-Backward scheme:

$$\Delta\boldsymbol{\Xi}_p = \Delta\lambda \left. \frac{\partial f}{\partial \boldsymbol{\Sigma}} \right|_{n+1} \tag{3.56}$$

The plastic multiplier $\Delta\lambda$ must be determined to satisfy the complementarity (loading/unloading) conditions:

$$\Delta\lambda \geq 0, \qquad f_{n+1} \leq 0, \qquad \Delta\lambda \, f_{n+1} = 0 \tag{3.57}$$

with f_{n+1} being the yield criterion at time instant t_{n+1}:

$$f_{n+1} = f(M_{n+1}, N_{n+1}) = \|\boldsymbol{\Sigma}_{n+1}\|_q - 1 \tag{3.58}$$

Introducing the trial state

$$\boldsymbol{\Sigma}_{n+1}^{trial} = \boldsymbol{\Sigma}_n + \mathbb{C}_e \Delta \boldsymbol{\Xi} \tag{3.59}$$

Eq. (3.54) becomes

$$\boldsymbol{\Sigma}_{n+1} = \boldsymbol{\Sigma}_{n+1}^{trial} - \mathbb{C}_e \Delta \boldsymbol{\Xi}_p \tag{3.60}$$

By combining Eq. (3.60) and (3.56), the stress resultant vector at time t_{n+1} becomes

$$\boldsymbol{\Sigma}_{n+1} = \boldsymbol{\Sigma}_{n+1}^{trial} - \mathbb{C}_e \Delta\lambda \left.\frac{\partial f}{\partial \boldsymbol{\Sigma}}\right|_{n+1} \tag{3.61}$$

the component form of Eq. (3.61) is

$$M_{n+1} = M_{n+1}^{trial} - k_\theta \Delta\lambda \left|\varrho_{M_{n+1}}\right|^q |M_{n+1}|^{q-1} \operatorname{sgn}(M_{n+1}) \left[\|\boldsymbol{\Sigma}_{n+1}\|_q\right]^{1-q} \tag{3.62}$$

$$N_{n+1} = N_{n+1}^{trial} - k_\delta \Delta\lambda \left|\varrho_{N_{n+1}}\right|^q |N_{n+1}|^{q-1} \operatorname{sgn}(N_{n+1}) \left[\|\boldsymbol{\Sigma}_{n+1}\|_q\right]^{1-q} \tag{3.63}$$

with

$$\left[\|\boldsymbol{\Sigma}_{n+1}\|_q\right]^{1-q} = \left(\left|\varrho_{N_{n+1}} N_{n+1}\right|^q + \left|\varrho_{M_{n+1}} M_{n+1}\right|^q\right)^{\frac{1-q}{q}} \tag{3.64}$$

In the next section, the applications of method are provided for the general super-elliptic criterion as well as the linear and quadratic-form yield surface. It will be shown that, for the case of linear surface, $q = 1$, the analytical solution to the optimization can be attained whereas it is not the case for the non-linear curve, $q > 1$, in which Newton Raphson iteration method is used. This technique is powerful for the reason that the formulation has the form of a minimization of a convex function on a convex set. This secures the existence of a unique solution. As the yield surface may have high curvature at corners, it is possible that one meets the convergence problems. But, the formulation of this technique gives a means of applying algorithms from mathematical programming theory which gives unique plastic strain increments when the trial stresses are found in the dual cone.

3.5.1 Smooth yielding criterion

The super-elliptic yield surface is illustrated in Fig. 3.3. The surface should have regular smooth curve at all points for $q > 1$. For $q = 1$, the curve will be linear

and have four singular point, whose integration is provided in the next section. Within the boundaries of the surface, the behaviour is regarded as elastic and the update of the stresses is not needed. If the trial stresses lie outside of the convex set of elastic domain K, only one constraint is active at a time. The yield criterion at time t_{n+1} becomes

$$f(M_{n+1}, N_{n+1}) = \|\boldsymbol{\Sigma}_{n+1}\|_q - 1 \tag{3.65}$$

where

$$\|\boldsymbol{\Sigma}_{n+1}\|_q = \left(\left|\varrho_{N_{n+1}} N_{n+1}\right|^q + \left|\varrho_{M_{n+1}} M_{n+1}\right|^q\right)^{\frac{1}{q}} \tag{3.66}$$

The plastic multiplier $\Delta\lambda$ in Eqs (3.62) and (3.63) is computed to satisfy the consistent condition (3.47), i.e. $f(M_{n+1}, N_{n+1}) = 0$. As the Eqs. (3.65), (3.62) and (3.63) are non-linear, Newton Raphson iteration is adopted to solve for M_{n+1}, N_{n+1}, and $\Delta\lambda$.

The tangent operator for the case of nonlinear yield surface requires the derivative of stress resultant vector $\boldsymbol{\Sigma}\left(\boldsymbol{\Xi}_{n+1}, \Delta\lambda\right)$ with respect to deformation vector $\boldsymbol{\Xi}_{n+1}$. Using Eq. (3.61), the derivative of the stress resultant $\boldsymbol{\Sigma}_{n+1}$ is

$$d\boldsymbol{\Sigma}_{n+1} = d\boldsymbol{\Sigma}_{n+1}^{trial} - \mathbb{C}_e \left[d\Delta\lambda \left.\frac{\partial f}{\partial \boldsymbol{\Sigma}}\right|_{n+1} + \Delta\lambda \left.\frac{\partial^2 f}{\partial \boldsymbol{\Sigma}^2}\right|_{n+1} d\boldsymbol{\Sigma}_{n+1} \right] \tag{3.67}$$

Rearranging Eq. (3.67) for $d\boldsymbol{\Sigma}_{n+1}$ gives

$$d\boldsymbol{\Sigma}_{n+1} = \boldsymbol{H}_{n+1}^{-1} \left(d\boldsymbol{\Sigma}_{n+1}^{trial} - \mathbb{C}_e \, \boldsymbol{A}_{n+1} \, d\Delta\lambda\right) \tag{3.68}$$

where

$$\boldsymbol{H}_{n+1} = \boldsymbol{I} - \Delta\lambda \left.\frac{\partial^2 f}{\partial \boldsymbol{\Sigma}^2}\right|_{n+1} \tag{3.69}$$

$$\boldsymbol{A}_{n+1} = \left.\frac{\partial f}{\partial \boldsymbol{\Sigma}}\right|_{n+1} \tag{3.70}$$

in which $\boldsymbol{I}$ is a 2×2 unit matrix. Making derivation of Eq. (3.65) results in

$$df\left(\boldsymbol{\Sigma}_{n+1}\right) = \left.\frac{\partial f}{\partial \boldsymbol{\Sigma}}\right|_{n+1}^{\mathrm{T}} d\boldsymbol{\Sigma}_{n+1} = 0 \tag{3.71}$$

Replacing $d\boldsymbol{\Sigma}_{n+1}$ (Eq. (3.68)) in Eq. (3.71) obtains

$$\boldsymbol{A}_{n+1}^{\mathrm{T}} \, \boldsymbol{H}_{n+1}^{-1} \left(d\boldsymbol{\Sigma}_{n+1}^{trial} - \mathbb{C}_e \, \boldsymbol{A}_{n+1} \, d\Delta\lambda\right) = 0 \tag{3.72}$$

Rearranging Eq. (3.72) gives the expression of $d\Delta\lambda$ as

$$d\Delta\lambda = \frac{\boldsymbol{A}_{n+1}^{\mathrm{T}}\,\boldsymbol{H}_{n+1}^{-1} d\boldsymbol{\Sigma}_{n+1}^{trial}}{\boldsymbol{A}_{n+1}^{\mathrm{T}}\,\boldsymbol{H}_{n+1}^{-1}\mathbb{C}_e\,\boldsymbol{A}_{n+1}} \tag{3.73}$$

Using Eq. (3.73), Eq. (3.68) becomes

$$d\boldsymbol{\Sigma}_{n+1} = \boldsymbol{H}_{n+1}^{-1}\left(d\boldsymbol{\Sigma}_{n+1}^{trial} - \mathbb{C}_e\,\boldsymbol{A}_{n+1}\,\frac{\boldsymbol{A}_{n+1}^{\mathrm{T}}\,\boldsymbol{H}_{n+1}^{-1} d\boldsymbol{\Sigma}_{n+1}^{trial}}{\boldsymbol{A}_{n+1}^{\mathrm{T}}\,\boldsymbol{H}_{n+1}^{-1}\mathbb{C}_e\,\boldsymbol{A}_{n+1}}\right) \tag{3.74}$$

Provided that

$$d\boldsymbol{\Sigma}_{n+1}^{trial} = \mathbb{C}_e\, d\boldsymbol{\Xi}_{n+1} \tag{3.75}$$

from Eq. (3.74), the tangent operator $\mathbb{C}$ has the following form

$$\mathbb{C} = \frac{d\boldsymbol{\Sigma}_{n+1}}{d\boldsymbol{\Xi}_{n+1}} = \boldsymbol{H}_{n+1}^{-1}\mathbb{C}^e\left[\boldsymbol{I} - \boldsymbol{A}_{n+1}\frac{\boldsymbol{A}_{n+1}^{\mathrm{T}}\boldsymbol{H}_{n+1}^{-1}\mathbb{C}^e}{\boldsymbol{A}_{n+1}^{\mathrm{T}}\boldsymbol{H}_{n+1}^{-1}\mathbb{C}^e\boldsymbol{A}_{n+1}}\right] \tag{3.76}$$

3.5.2 An anisotropic linear yield surface

This section addresses the particular case of anisotropic multi-linear yield surfaces. Equations derived in Section 3.5.1 cannot be used because the multi-linear yield surface possesses singular points. Applying the Euler-backward scheme to the variational inequality (3.47), one obtains the discrete flow rule

$$\boldsymbol{\Sigma}_{n+1} \in K, \qquad \Delta\boldsymbol{\Xi}^p \cdot (\boldsymbol{\Sigma}^* - \boldsymbol{\Sigma}_{n+1}) \leq 0, \qquad \forall \boldsymbol{\Sigma}^* \in K \tag{3.77}$$

By inserting Eqs. (3.60) into Eqs. (3.77), we obtain:

$$\boldsymbol{\Sigma}_{n+1} \in K, \qquad (\boldsymbol{\Sigma}^* - \boldsymbol{\Sigma}_{n+1}) \cdot \mathbb{C}_e^{-1}\left(\boldsymbol{\Sigma}_{n+1} - \boldsymbol{\Sigma}_{n+1}^{trial}\right) \geq 0, \qquad \forall \boldsymbol{\Sigma}^* \in K \tag{3.78}$$

The last inequality (3.78) means that $\boldsymbol{\Sigma}_{n+1}$ is the projection of $\boldsymbol{\Sigma}_{n+1}^{trial}$ onto the closed convex set K with respect to the norm $\| \bullet \|_{\mathbb{C}_e^{-1}}$.

$$\boldsymbol{\Sigma}_{n+1} = proj\left(\boldsymbol{\Sigma}_{n+1}^{trial}, K\right) \tag{3.79}$$

In other words, the generalized stress vector $\boldsymbol{\Sigma}_{n+1}$ is the solution of the following nonlinear optimization problem:

$$proj\left(\boldsymbol{\Sigma}_{n+1}^{trial}, K\right) = \inf_{\boldsymbol{\Sigma}\in K} \left\|\boldsymbol{\Sigma}_{n+1}^{trial} - \boldsymbol{\Sigma}_{n+1}\right\|_{\mathbb{C}_e^{-1}}^2 \tag{3.80}$$

Then, the expression in Eq. (3.80) can be solved as:

$$\min_{f(\boldsymbol{\Sigma})\leq 0}\left[\left(\boldsymbol{\Sigma}_{n+1}^{trial}-\boldsymbol{\Sigma}_{n+1}\right)\cdot\mathbb{C}_e^{-1}\left(\boldsymbol{\Sigma}_{n+1}^{trial}-\boldsymbol{\Sigma}_{n+1}\right)\right] \tag{3.81}$$

Next, Eq. (3.81) can be reformulated as a constrained minimisation problem by means of the Lagrange multiplier technique:

$$(\boldsymbol{\Sigma}_{n+1},\mu^{(i)})=\frac{1}{2}\left[\left(\boldsymbol{\Sigma}_{n+1}^{trial}-\boldsymbol{\Sigma}_{n+1}\right)\cdot\mathbb{C}_e^{-1}\left(\boldsymbol{\Sigma}_{n+1}^{trial}-\boldsymbol{\Sigma}_{n+1}\right)\right]+\mu^{(i)}f^{(i)}(\boldsymbol{\Sigma}_{n+1}) \tag{3.82}$$

The stationary conditions can then be expressed as:

$$\frac{\partial\left(\boldsymbol{\Sigma}_{n+1},\mu^{(i)}\right)}{\partial\boldsymbol{\Sigma}_{n+1}}=0,\qquad\frac{\partial\left(\boldsymbol{\Sigma}_{n+1},\mu^{(i)}\right)}{\partial\mu^{(i)}}=0 \tag{3.83}$$

By solving the system equations given by stationary conditions in Eq. (3.83), the expression of the generalized stresses at the end of the time step $\boldsymbol{\Sigma}_{n+1}$ is found. The tangent operator is obtained by taking the derivative of these stresses:

$$\mathbb{C}_{n+1}=\frac{\partial\boldsymbol{\Sigma}_{n+1}}{\partial\boldsymbol{\Xi}_{n+1}} \tag{3.84}$$

The linear yield surface is illustrated in Fig. 3.4. The surface has a parallelogram shape and consists of four constraints depending on the sign of the axial and bending forces. The intersections between each two constraints are singular points of the curve which create the dual cones. If the trial stresses are found in the dual cone, a special treatment must be done by considering the two associated constraints active. If the trial stresses lie outside of the convex set of elastic domain K and the dual cones, only one constraint is active at a time. The yield condition can be defined as:

$$N>0 \text{ and } M>0\ :\quad f^{(1)}=\frac{N}{N_{p_+}}+\frac{M}{M_{p_+}}-1 \tag{3.85}$$

$$N<0 \text{ and } M>0\ :\quad f^{(2)}=-\frac{N}{N_{p_-}}+\frac{M}{M_{p_+}}-1 \tag{3.86}$$

$$N<0 \text{ and } M<0\ :\quad f^{(3)}=-\frac{N}{N_{p_-}}-\frac{M}{M_{p_-}}-1 \tag{3.87}$$

$$N>0 \text{ and } M<0\ :\quad f^{(4)}=\frac{N}{N_{p_+}}-\frac{M}{M_{p_-}}-1 \tag{3.88}$$

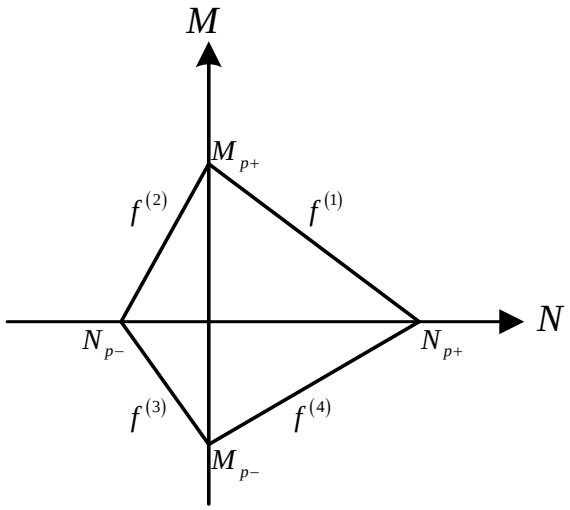

Figure 3.4: linear yield surface

3.5.2.1 One active constraint

If only $f^{(1)}$ is active, $\mu^{(1)} > 0$ and $\mu^{(2)} = \mu^{(3)} = \mu^{(4)} = 0$. The Lagrangian in Eq. (3.82) is given in this case as:

$$(\boldsymbol{\Sigma}_{n+1}, \mu^{(i)}) = \frac{1}{2}\left[(\boldsymbol{\Sigma}_{n+1}^{trial} - \boldsymbol{\Sigma}_{n+1}) \cdot \mathbb{C}_e^{-1}\left(\boldsymbol{\Sigma}_{n+1}^{trial} - \boldsymbol{\Sigma}_{n+1}\right)\right] + \mu^{(1)} f^{(1)} \tag{3.89}$$

The stationary conditions in Eqs. (3.83) are applied:

$$\begin{aligned}
\frac{\partial}{\partial M_{n+1}} &= -\frac{1}{k_\theta}\left(M_{n+1}^{trial} - M_{n+1}\right) + \frac{\mu^{(1)}}{M_{p_+}} &&= 0 \\
\frac{\partial}{\partial N_{n+1}} &= -\frac{1}{k_\delta}\left(N_{n+1}^{trial} - N_{n+1}\right) + \frac{\mu^{(1)}}{N_{p_+}} &&= 0 \\
\frac{\partial}{\partial \mu^{(1)}} &= \frac{M_{n+1}}{M_{p_+}} + \frac{N_{n+1}}{N_{p_+}} - 1 &&= 0
\end{aligned} \tag{3.90}$$

Solving Eqs. (3.90) for M_{n+1}, N_{n+1} and $\mu^{(1)}$ gives:

$$\begin{aligned} M_{n+1} &= M_{n+1}^{trial} - k_\theta \frac{\mu^{(1)}}{M_{p_+}} \\ N_{n+1} &= N_{n+1}^{trial} - k_\delta \frac{\mu^{(1)}}{N_{p_+}} \\ \mu^{(1)} &= \left(\frac{M_{n+1}^{trial}}{M_{p_+}} + \frac{N_{n+1}^{trial}}{N_{p_+}} - 1 \right) \left(\frac{k_\theta}{(M_{p+})^2} + \frac{k_\delta}{(N_{p_+})^2} \right)^{-1} \end{aligned} \tag{3.91}$$

The tangent operator for this case is derived as:

$$\begin{aligned} C_{11} &= \frac{\partial M_{n+1}}{\partial \theta_{n+1}} = k_\theta - \left(\frac{k_\theta}{M_{p+}} \right)^2 \left(\frac{k_\theta}{(M_{p_+})^2} + \frac{k_\delta}{(N_{p_+})^2} \right)^{-1} \\ C_{22} &= \frac{\partial N_{n+1}}{\partial \delta_{n+1}} = k_\delta - \left(\frac{k_\delta}{N_{p_+}} \right)^2 \left(\frac{k_\theta}{(M_{p_+})^2} + \frac{k_\delta}{(N_{p_+})^2} \right)^{-1} \\ C_{12} = C_{12} &= \frac{\partial N_{n+1}}{\partial \theta_{n+1}} = \frac{\partial M_{n+1}}{\partial \delta_{n+1}} = -\frac{k_\theta k_\delta}{M_{p_+} N_{p_+}} \left(\frac{k_\theta}{(M_{p_+})^2} + \frac{k_\delta}{(N_{p_+})^2} \right)^{-1} \end{aligned} \tag{3.92}$$

The same approach can be followed for the other cases of one activate constraint.

3.5.2.2 two active constraints

At each corner of the surface (see Fig. 3.4), two constraints at most are active. The case of top corner ($f^{(1)}$ and $f^{(2)}$ are active) is given as an example whereas the other three corners will follow the same procedure. The Lagrangian in Eq. (3.82) becomes:

$$(\boldsymbol{\Sigma}_{n+1}, \mu^{(i)}) = \frac{1}{2} \left[(\boldsymbol{\Sigma}_{n+1}^{trial} - \boldsymbol{\Sigma}_{n+1}) \cdot \mathbb{C}_e^{-1} \cdot (\boldsymbol{\Sigma}_{n+1}^{trial} - \boldsymbol{\Sigma}_{n+1}) \right] + \sum_{i=1}^{2} \mu^{(i)} f^{(i)} \tag{3.93}$$

The stationary conditions in Eq. (3.83) are then evaluated:

$$\begin{aligned} \frac{\partial}{\partial M_{n+1}} &= -\frac{1}{k_\theta} \left(M_{n+1}^{trial} - M_{n+1} \right) + \frac{\mu^{(1)}}{M_{p_+}} + \frac{\mu^{(2)}}{M_{p_+}} = 0 \\ \frac{\partial}{\partial N_{n+1}} &= -\frac{1}{k_\delta} \left(N_{n+1}^{trial} - N_{n+1} \right) + \frac{\mu^{(1)}}{N_{p_+}} - \frac{\mu^{(2)}}{N_{p_-}} = 0 \\ \frac{\partial}{\partial \mu^{(1)}} &= \frac{M_{n+1}}{M_{p_+}} + \frac{N_{n+1}}{N_{p_+}} - 1 = 0 \\ \frac{\partial}{\partial \mu^{(2)}} &= \frac{M_{n+1}}{M_{p_+}} - \frac{N_{n+1}}{N_{p_-}} - 1 = 0 \end{aligned} \tag{3.94}$$

Solving Eqs.(3.94) gives

$$\begin{aligned}
M_{n+1} &= M_{p_+} \\
N_{n+1} &= 0 \\
\mu^{(1)} &= \frac{N_{p+}\left(N_{n+1}^{trial} N_{p_-} k_\theta + M_{p_+} M_{n+1}^{trial} k_\delta - M_{p_+}^2 k_\delta\right)}{k_\delta k_\theta \left(N_{p_+} + N_{p_-}\right)} \\
\mu^{(2)} &= -\frac{N_{p_-}\left(N_{n+1}^{trial} N_{p_+} k_\theta - M_{p_+} M_{n+1}^{trial} k_\delta + M_{p+}^2 k_\delta\right)}{k_\delta k_\theta \left(N_{p_+} + N_{p_-}\right)}
\end{aligned} \tag{3.95}$$

The tangent operator for the cases of two active constraints are the following:

$$\boldsymbol{C}_{ij} = 0 \tag{3.96}$$

3.5.3 An anisotropic quadratic yield surface

The quadratic form of the yield surface, illustrated in Fig. 3.5, is a particular case of the nonlinear shape in Eq. (3.49), which is defined with $q = 2$ as

$$f(M, N) = \sqrt{\left(\varrho_N N_{n+1}\right)^2 + \left(\varrho_M M_{n+1}\right)^2} - 1 \tag{3.97}$$

The lagrangian in Eq. (3.82) is given in this case as

$$(\boldsymbol{\Sigma}_{n+1}, \mu) = \frac{1}{2}\left[\left(\boldsymbol{\Sigma}_{n+1}^{trial} - \boldsymbol{\Sigma}_{n+1}\right) \cdot \mathbb{C}_e^{-1}\left(\boldsymbol{\Sigma}_{n+1}^{trial} - \boldsymbol{\Sigma}_{n+1}\right)\right] + \mu f \tag{3.98}$$

where and the stationary conditions consist of:

$$\begin{aligned}
\frac{\partial(\boldsymbol{\Sigma}_{n+1}, \mu)}{\partial M_{n+1}} &= -\frac{1}{k_\theta}\left(M_{n+1}^{trial} - M_{n+1}\right) + \frac{\mu \varrho_M^2 M_{n+1}}{\sqrt{\left(\varrho_N N_{n+1}\right)^2 + \left(\varrho_M M_{n+1}\right)^2}} = 0 \\
\frac{\partial(\boldsymbol{\Sigma}_{n+1}, \mu)}{\partial N_{n+1}} &= -\frac{1}{k_\delta}\left(N_{n+1}^{trial} - N_{n+1}\right) + \frac{\mu \varrho_N^2 N_{n+1}}{\sqrt{\left(\varrho_N N_{n+1}\right)^2 + \left(\varrho_M M_{n+1}\right)^2}} = 0 \\
\frac{\partial(\boldsymbol{\Sigma}_{n+1}, \mu)}{\partial \mu} &= \sqrt{\left(\varrho_N N_{n+1}\right)^2 + \left(\varrho_M M_{n+1}\right)^2} - 1 = 0
\end{aligned} \tag{3.99}$$

According to Eq. (3.97), we can write

$$\sqrt{\left(\varrho_N N_{n+1}\right)^2 + \left(\varrho_M M_{n+1}\right)^2} = 1 \tag{3.100}$$

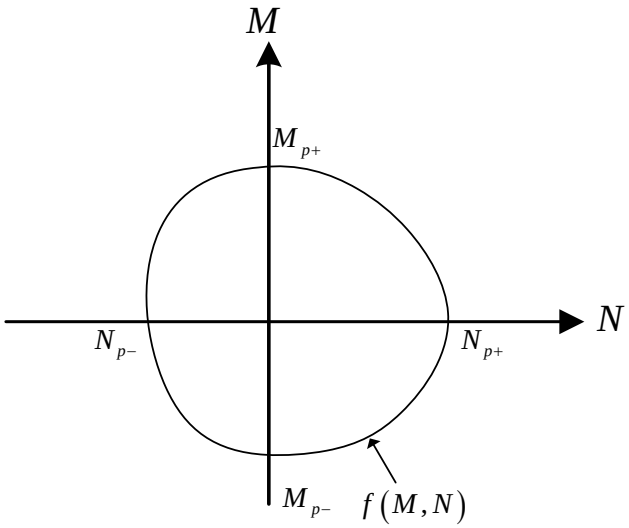

Figure 3.5: Anisotropic yield surface

Replace Eq. (3.100) into Eq. (3.99) gives

$$\begin{aligned} M_{n+1} &= \frac{M_{n+1}^{trial}}{1+\mu k_\theta \varrho_M^2} \\ N_{n+1} &= \frac{N_{n+1}^{trial}}{1+\mu\ k_\delta \varrho_N^2} \end{aligned} \tag{3.101}$$

By combined Eq. (3.101) and Eq. (3.100),the optimization problem is reduced to finding the positive zeros of the following quartic equation:

$$\frac{\left(\varrho_M M_{n+1}^{trial}\right)^2}{\left(1+\mu k_\theta \varrho_M^2\right)^2} + \frac{\left(\varrho_N N_{n+1}^{trial}\right)^2}{\left(1+\mu\ k_\delta \varrho_N^2\right)^2} = 1 \tag{3.102}$$

Further insight into Eq. (3.102) is gained by letting

$$\bar{M} = 1+\mu\ k_\theta \varrho_M^2 \tag{3.103}$$

$$\bar{N} = 1+\mu\ k_\delta \varrho_N^2 \tag{3.104}$$

so that Eq. (3.102) reduces to finding the intersection of a quadratic and a straight line

$$\frac{\left(\varrho_M M_{n+1}^{trial}\right)^2}{\left(\bar{M}\right)^2} + \frac{\left(\varrho_N N_{n+1}^{trial}\right)^2}{\left(\bar{N}\right)^2} = 1 \tag{3.105}$$

$$\bar{M} = \frac{k_\theta \varrho_M^2}{k_\delta \varrho_N^2}\bar{N} + \frac{k_\delta \varrho_N^2 - k_\theta \varrho_M^2}{k_\delta \varrho_N^2} \tag{3.106}$$

This is illustrated graphically in Fig. 3.6. Note that the first equation of the

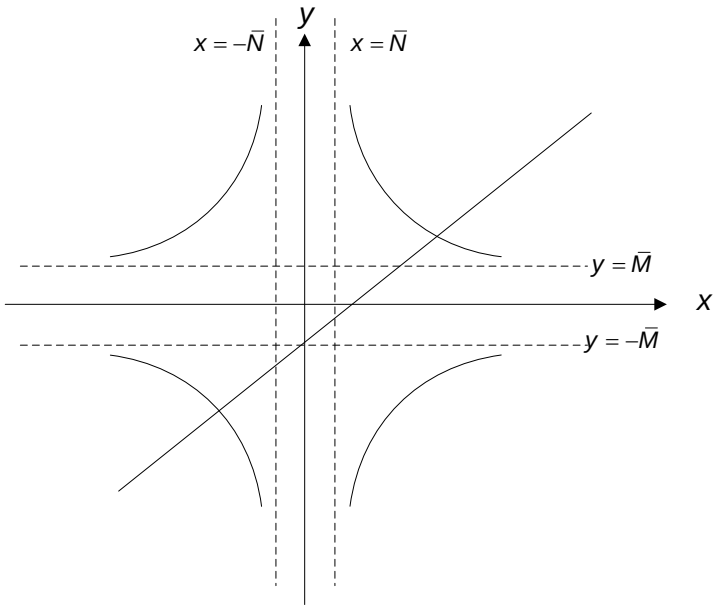

Figure 3.6: Geometric interpretation of the projection solution

system has orthogonal asymptotes $x = \pm\bar{N}$ and $y = \pm\bar{M}$. Since the straight line always has positive slope,direct inspection of Fig. 3.6 reveals that the system of equation has one negative root,one positive root and a pair of complex conjugate roots. According to Eqs. (3.99), the process is iterative and the Newton-Raphson method will be adopted to determine M_{n+1}, N_{n+1} and μ. The tangent operator for these cases of nonlinearity will be determined according to Eq. (3.76).

3.6 Elasto-plastic finite step procedure

In this section, we briefly describe the solution strategy employed to solve the nonlinear structural equilibrium equations. Assuming that the internal forces pertaining to the superelements balance the external loading at the time instant t_n, we seek to update all mechanical variables such that structural equilibrium is achieved at t_{n+1}

$$\boldsymbol{F}_{n+1}^{\text{int}} - \boldsymbol{F}_{n+1}^{\text{ext}} = \boldsymbol{0} \tag{3.107}$$

and the constitutive equations (Eq. 3.56 and Eq. 3.57) are fulfilled. The iterative procedure employed to solve this nonlinear problem involve several steps and proceeds as follows. Let $(\bullet)_{n+1}^{(k)}$ be the value of a variable $(\bullet)$ at the k^{th} iteration during the time increment $[t_n, t_{n+1}]$, we have:

$$\Delta \boldsymbol{U}_{n+1}^{(k+1)} = -\left[\boldsymbol{K}_{n+1}^{(k)}\right]^{-1}\left[\boldsymbol{F}_{n+1}^{\text{int}(k)} - \boldsymbol{F}_{n+1}^{\text{ext}}\right] \tag{3.108}$$

where $\boldsymbol{K}$ is the structural tangent stiffness matrix. The nodal displacement are updated according to:

$$\boldsymbol{U}_{n+1}^{(k+1)} = \boldsymbol{U}_n + \Delta \boldsymbol{U}_{n+1}^{(k+1)} \tag{3.109}$$

The above steps pertain to the global stage where the vector $\boldsymbol{U}$ collects the nodal displacement of the suprelements. The internal degrees of freedom are determined in a local stage. From $\boldsymbol{U}_{n+1}^{(k+1)}$, we immediately build the vector $\Delta \boldsymbol{d}_{g,n+1}^{(k+1)}$ for each superelement from which we compute $\Delta \boldsymbol{d}_{l,n+1}^{(k+1)}$ using Eq.3.6. Initialization of vector $\Delta \boldsymbol{d}_{i,n+1}^{(j=1)}$ is performed using Eq. 3.39:

$$\Delta \boldsymbol{d}_{i,n+1}^{(j=1)} = -\left([\boldsymbol{k}_{ii}]_{n+1}^{(k)}\right)^{-1}[\boldsymbol{k}_{il}]_{n+1}^{(k)}\,\Delta \boldsymbol{d}_{l,n+1}^{(k+1)} \tag{3.110}$$

Next, the "internal" forces are obtained iteratively by solving equilibrium equations Eq. 3.27:

$$\Delta \boldsymbol{R}_{i,n+1}^{(j)} + \frac{\partial \Delta \boldsymbol{R}_{i,n+1}^{(j)}}{\partial \Delta \boldsymbol{d}_{i,n+1}^{(j)}}\,\delta\left(\Delta \boldsymbol{d}_{i,n+1}^{(j+1)}\right) = \boldsymbol{0} \tag{3.111}$$

where $\boldsymbol{R}_i$ stands for the "internal" equilibrium residual of Eq. 3.27. Once the displacement vector $\Delta \boldsymbol{d}_{i,n+1}^{(j+1)}$ has been found, the internal force as well as the

stiffness matrices are updated and the out-of-balance force vector is evaluated. With this strategy equilibrium is enforced at both global and local levels for each load step.

3.7 Numerical examples

This section provides four numerical examples of standard framed structures with the purposes to show the features of the model which include both geometric and material non-linearities and to investigate the response of framed structures undergoing both large displacements and inelastic deformations. Computations were driven using an appropriate version of the arc-length method [43] in order to capture the whole force-displacement curve. The effects of the roundness factor q affecting the shape of the yield surface as well as the consequence of significant changes in structural geometry on the frame's response are studied within the examples.

3.7.1 Fixed-end beam with asymmetric concentrated load

This first example concerns with a clamped beam under an asymmetric point load. Firstly, in order to validate our proposed model, we compare its prediction against the co-rotational fiber beam model (see [**?**]). The adopted (M,N) interaction criterion is consistent with the beam cross section shape. Duan and Chen in [**?**] gave an approximated equation to the yield surface of the double symmetrical steel section subjected to bending moment and axial force:

$$\frac{M}{M^P} + \left(\frac{N}{N^P}\right)^{\beta} = 1 \tag{3.112}$$

Here M^P and N^P are plastic resistances for the bending moment and the axial force respectively. β is a section-dependent parameter.(β equal 2 for a solid rectangular; 2.1 for a solid circular section; 1.75 for a thin-walled circular section; 1.3 for a wide flange section under strong axis bending). Secondly, the effect of the roundness factor q on the response of the clamped beam under both monotonic

and cyclic loading is investigated. Isotropic as well as anisotropic yield criterion with varying values of q are considered. For the monotonic loading the following values of q are considered: $1, 1.5, 2, 4$ and 12 whereas $q = 2$ and 4 are taken for cyclic loading condition. While only isotropic yield criterion is considered in the case of monotonic loading. Yield surface anisotropy is considered for cyclic loading with the plastic limits $\left|M_{p_-}\right| = \frac{1}{2}M_{p_+}$ and $\left|N_{p_-}\right| = \frac{1}{2}N_{p_+}$. The isotropic and anisotropic yield criterion for q equal 2 anf 4 are plotted in Fig. 3.9 and constant amplitudes (see Fig. 3.11). The cyclic loading histories adopted involve both increasing and constant amplitudes (see Fig. 3.10). The point load is applied at one-third of the total length of the beam, as being depicted in Fig. 3.7. The beam has a cross-section of type HEB 220 S355, whose yield limit $f_y = 355\,MPa$ and Young modulus $E = 210\,GPa$.

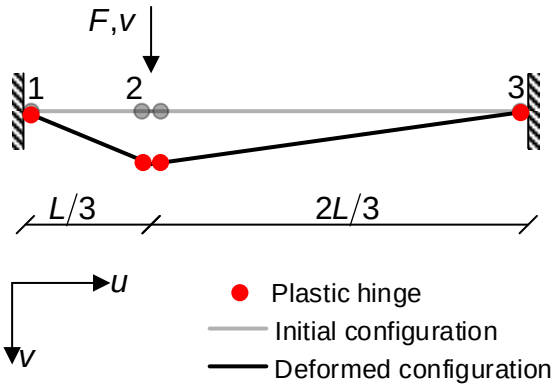

Figure 3.7: Two-dimensional fixed-end beam

The comparative study that shown in Fig.3.8 demonstrates a good agrement with the fiber model and presents the capability of the proposed model to capture the nonlinearity geometric and material in the studied structures.

In the other hand, Fig. 3.12 illustrates the force-displacement curve of the beam under monotonic loading. Up until the formation of the second hinge, the

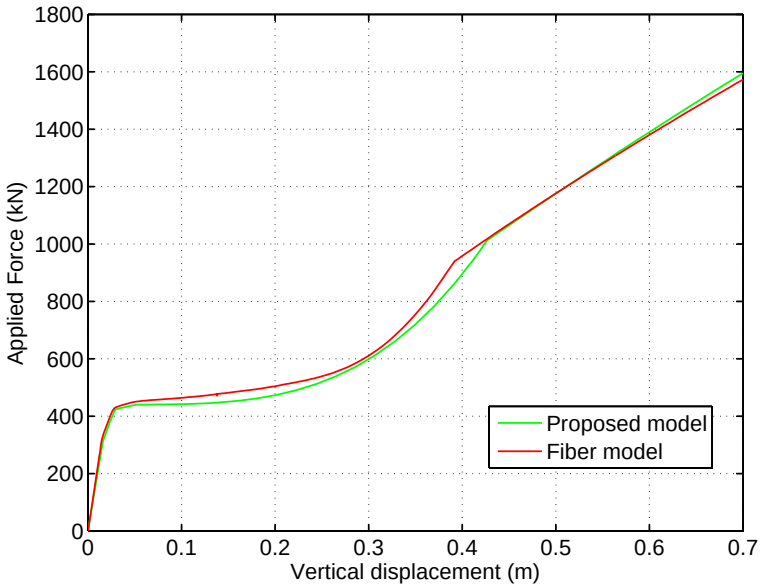

Figure 3.8: Load vs. deflection curve - comparative study

force-displacement curve almost does not vary with the value of q because the normal force developed in the beam is still small as a result of small displacements. Between the formation of the second and the third hinge, the beam displacements become moderate producing slight differences in the load-displacement curve showing a dependance of the latter on the value of the roundness factor of q. After the third plastic hinge has formed, second order effects modify the load carrying mechanism with increasing value of the normal force. Consequently the curve begins to change significantly with the value of q. For same level of large displacement, the beam is able to sustain larger load with increasing value of q. Indeed, the load carrying capacity can be doubled in the case of q = 12 with respect to q =1. The roundness of the yield curve strongly influence the load level at which plastification of a hinge occurs. Membrane effect in the beam are more significant for increasing value of q. It is worth mentioning also that the computation may experience difficulties in convergence if the value of q is too

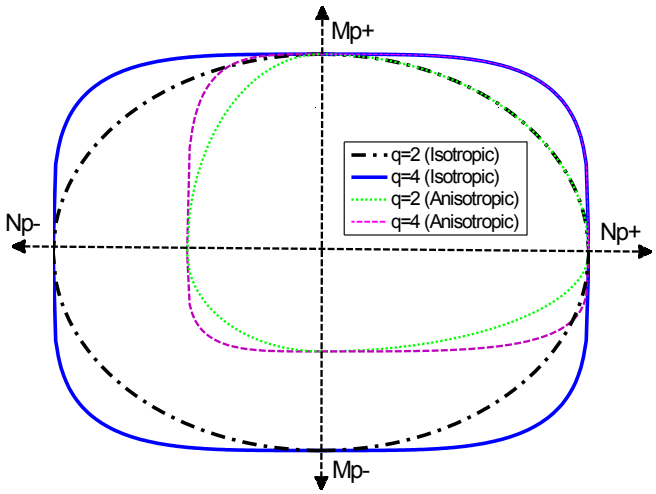

Figure 3.9: Yield surface criteria

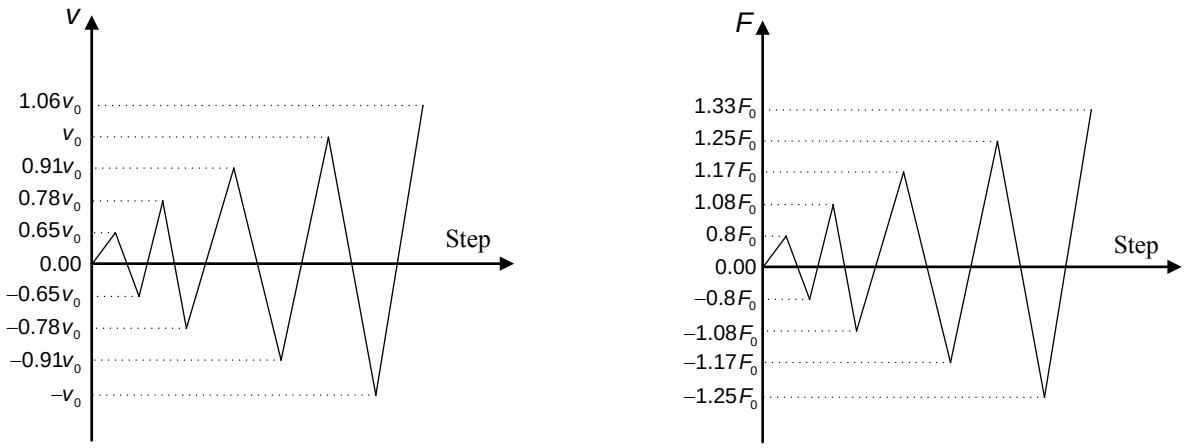

(a) Displacement imposed (b) Force imposed

Figure 3.10: Load history: reversed cyclic loading with increasing amplitudes

large (the shape becomes close to rectangle).

Figs. 3.13 present the response of the beam under reversed and force-controlled cyclic loading with increasing amplitude. The loading history is symmetric with, for each cycle, the same force magnitude in both directions (upward and downward). The amplitudes of the cyclic force are determined by a multiplying the force $F_0 = 500\,kN$ with an increasing factor. For the first cycle, the amplitude

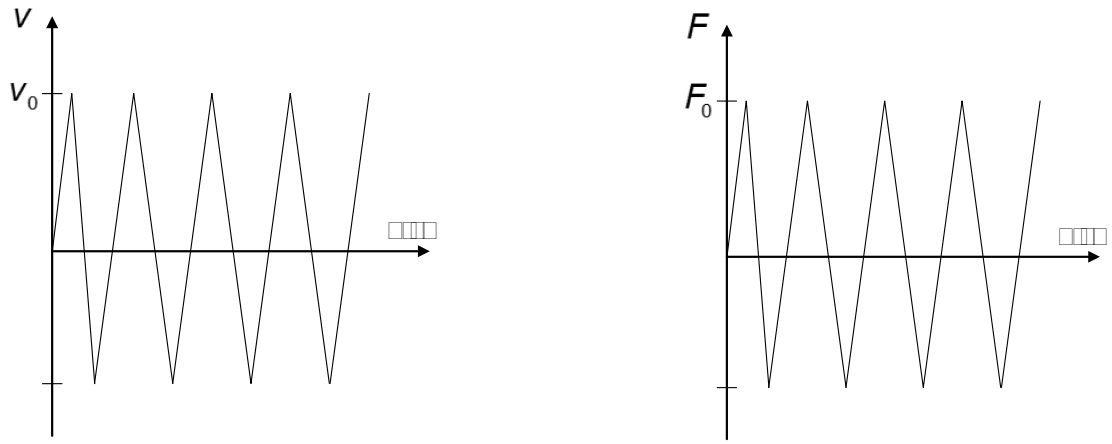

(a) Displacement imposed (b) Force imposed

Figure 3.11: Load history: reversed cyclic loading with constant amplitudes

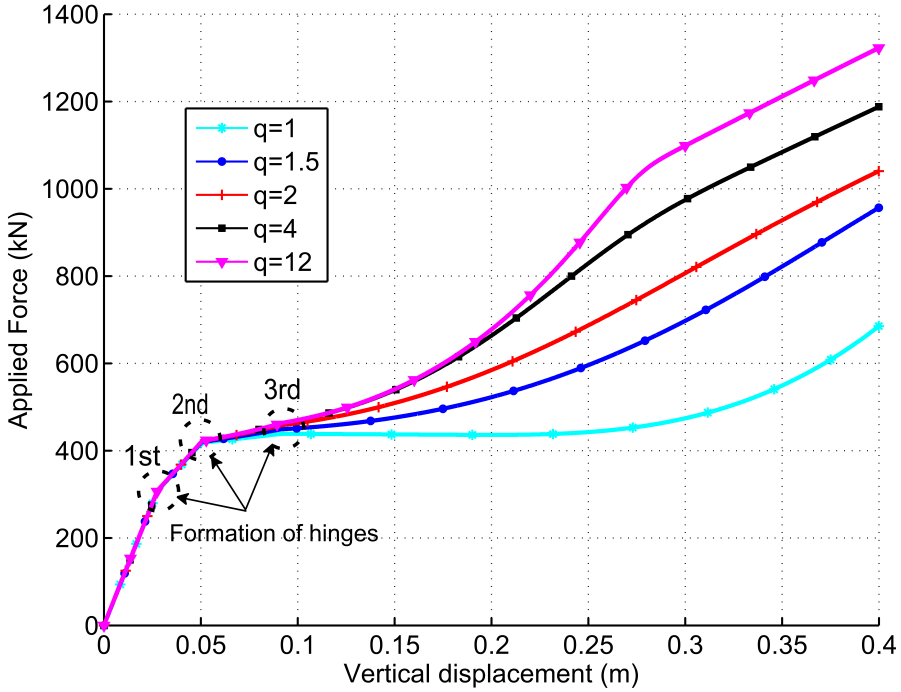

Figure 3.12: Beam load-deflection curve

of the force is $0.8\,F_0$. The amplitude is increased to $1.08\,F_0$ for the second cycle, $1.17\,F_0$ for the third cycle and $1.25\,F_0$ for the last cycle. After the last cycle, the

force continues to increase and stop at $1.33\,F_0$. As can be seen in Fig. 3.13(a) and 3.13(b), the beam response is symmetric for the isotropic case and slightly asymmetric for the anisotropic yield criterion, regardless of the value of the roundness factor. It can also be seen that the shape of the loop does not change during the loading history in both cases but the amplitude increases from cycle to cycle. An anisotropic yield surface seems to produce a more ductile behavior with large plateau and larger displacement amplitudes. Increasing values of the roundness factor q have the tendency to reduce the beam displacement amplitude. The anisotropic yield curve is the cause of a pronounced pinching effect indicating the ability of such model to reproduce well the behavior of bolted connection.

Figs. 3.14 present the response of the beam under reversed and displacement-controlled cyclic loading with increasing amplitude. In a similar manner as the force-controlled cyclic loading, the loading history is symmetric with, for each cycle, the same displacement magnitude in both the downward and the upward directions. The amplitudes of the cyclic displacement are determined by a multiplying the nominal displacement $v_0 = 200\,mm$ with an increasing factor. For the first cycle, the amplitude of the displacement is $0.65\,v_0$. The amplitude is increased to $0.78\,v_0$ for the second cycle, $0.91\,v_0$ for the third cycle and v_0 for the last cycle. After the last cycle, the displacement is applied up to $1.06\,v_0$ and the loading is stopped. Shown in Fig. 3.14(a) and 3.14(b), the beam response is symmetric for isotropic yield criterion but not for the case of anisotropic yield criterion, regardless of the value of the roundness factor. Like the reversed force-controlled case, increasing values of the roundness factor q have the tendency to increase the force amplitude.

Figs. 3.15 present the response of the beam under reversed and force-controlled cyclic loading with constant amplitude. The loading history is symmetric with, for all the cycles, the same force magnitude in both the downward and the upward directions. The amplitudes are constant at $F_0 = 665\,kN$ from one cycle to another. As shown in 3.15(a) and 3.15(b), the beam response is almost symmetric for both isotropic and anisotropic yield criterion regardless of the value of

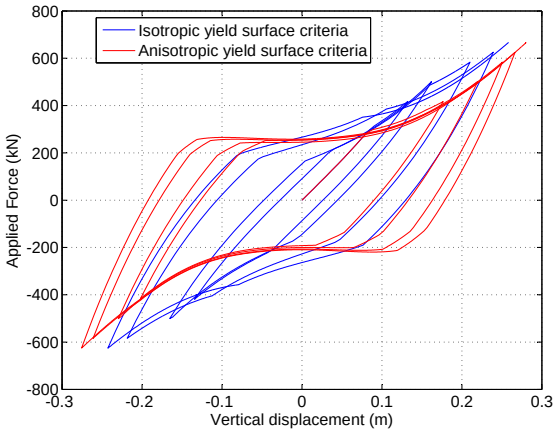

(a) q=2

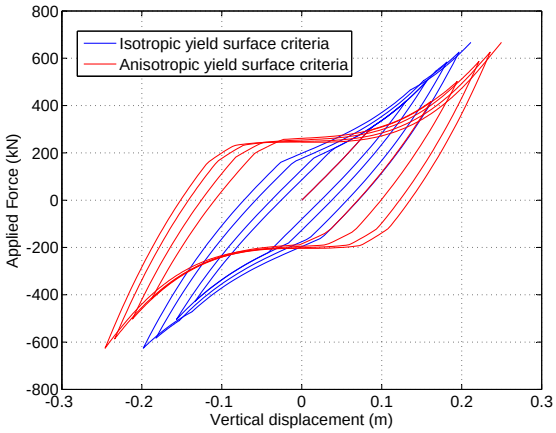

(b) q=4

Figure 3.13: Reversed force-controlled cyclic loading with increasing amplitude: Isotropic versus Anisotropic yield criteria

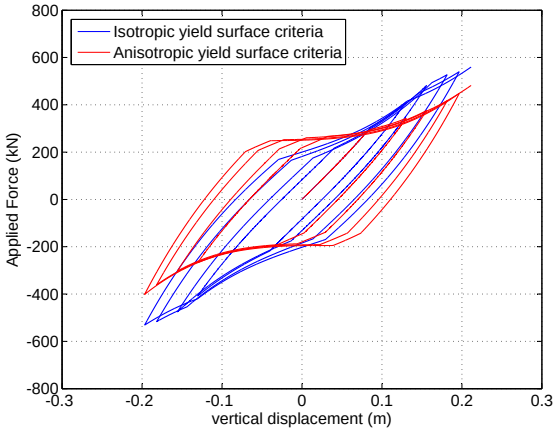

(a) q=2

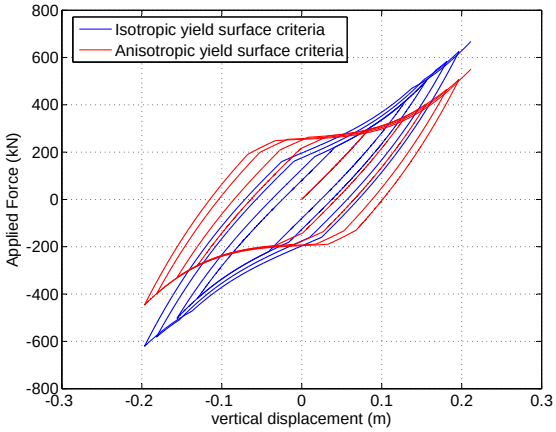

(b) q=4

Figure 3.14: Reversed displacement-controlled cyclic loading with increasing amplitude: Isotropic versus Anisotropic yield criteria

the roundness factor. Although the force is imposed with the same amplitude in all cycles, the amplitudes of the displacement become larger disregarding of the roundness factor as well as the yield criterion. This phenomenon is known as cyclic softening. Pinching effect is more pronounced with an anisotropic yield criteria.

A low value of the roundness factor q combined with an isotropic yield criteria produces a force-displacement curve with significant pinching effect. With the same amplitudes of imposed force, the displacement is larger with the anisotropic yield criteria and for both values of q. The largest displacement is obtained with $q = 2$.

Figs. 3.16 present the response of the beam under reversed and displacement-controlled cyclic loading with constant amplitude. The loading history is symmetric with, for all the cycles, the same displacement magnitude in both the downward and the upward directions. The amplitudes are constant at $v_0 = 212\,mm$ from one cycle to another. Although the displacement is imposed with the same amplitude in all cycles, the amplitudes of the force become smaller disregarding of the roundness factor as well as the yield criterion. As shown in 3.16(a) and 3.16(b), the beam response is almost symmetric for both isotropic and anisotropic yield criterion regardless of the value of the roundness factor. Again, cyclic softening which is characterized by a reduction of the force amplitude during successive cycles is observed. Similarly to the force-controlled case, an anisotropic yield criteria will induces more pinching effect in the force-displacement curve.With the same amplitudes of imposed displacement, the force is larger with the isotropic yield criteria and for both values of q. The largest force is obtained with $q = 4$.

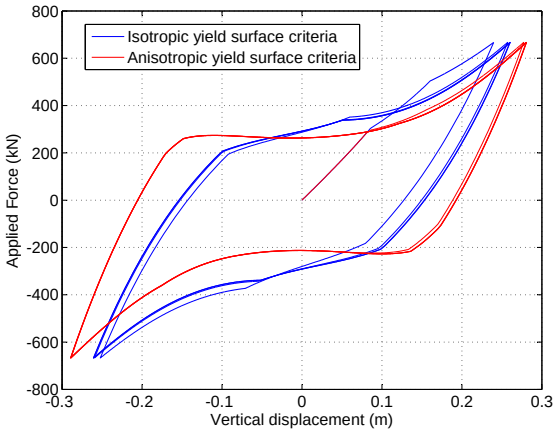

(a) q=2

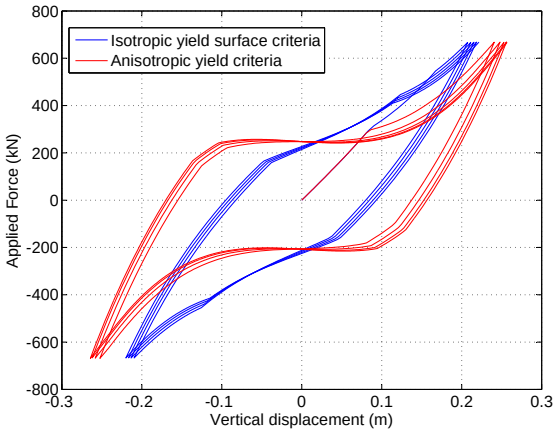

(b) q=4

Figure 3.15: Reversed force-controlled cyclic loading with constant amplitude: Isotropic versus Anisotropic yield criteria

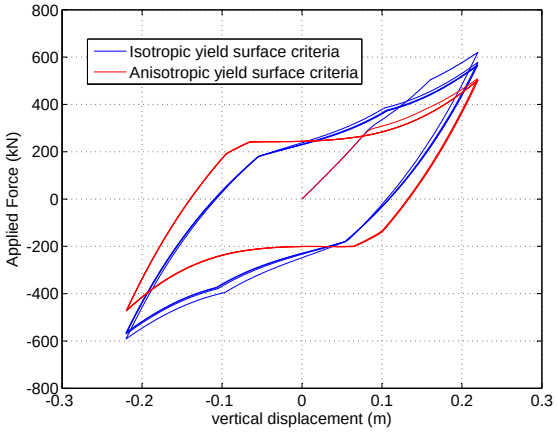

(a) q=2

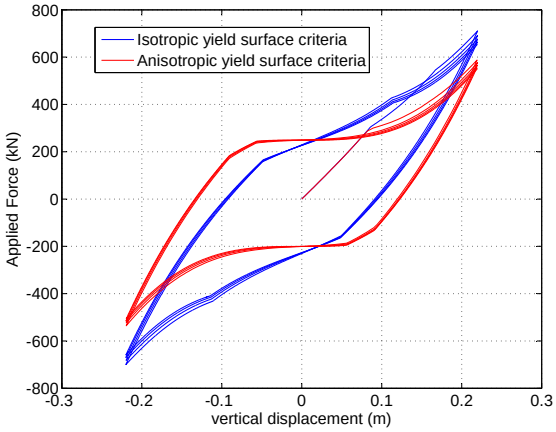

(b) q=4

Figure 3.16: Reversed displacement-controlled cyclic loading with constant amplitude: Isotropic versus Anisotropic yield criteria

3.7.2 Limit load of a two-bay frame with single storey

This section presents a response of a two-bay frame with single storey as illustrated in Fig. 3.17. Again, the effect of the roundness factor q on the value of the ultimate load factor λ for this kind of structure is explored by varying the value

of $q = 1$, 2 and 10. The isotropic yield criterion is employed in this example. The second order effect and the influence of interaction between axial and bending forces are also examined for the roundness factor of $q = 2$ by performing four different calculations: first order analysis without $M - N$ interaction (OM-1st order), first order analysis with $M - N$ interaction (IMN-1st order), second order analysis without $M - N$ interaction (OM-2nd order) and second order analysis with $M - N$ interaction (IMN-2nd order). The first order elasto-plastic analysis of this frame, without M-N interaction, has been performed using mathematical programming technique by Spiliopoulos et al. [44]. For first order analyses (OM-1st order and IMN-1st order), the transformation matrix $\boldsymbol{B}$ defined by Eq. (3.14) becomes $\boldsymbol{B}_0$ that is constant and independent of displacement by replacing L_n with L_0. Without considering nonlinear geometry, the tangent stiffness matrix in this case is given by

$$\boldsymbol{k}_g = \boldsymbol{B}_0^{\mathrm{T}} \boldsymbol{k}_l \boldsymbol{B}_0 \tag{3.113}$$

For the analyses without $M - N$ interaction (OM-1st order and OM-2nd order), the axial spring has been removed and only a elastic perfectly plastic rotational spring is considered. The cross-section properties for each element of the frame is described in table 3.1. The yield limit and the Young modulus are taken as $f_y = 220\,\mathrm{MPa}$ and $E = 210\,\mathrm{GPa}$, respectively. Fig. 3.18 gives a

Table 3.1: Mechanical properties

Member	$I\,(\times 10^{-5} m^4)$	$A\,(\times 10^{-3} m^2)$	$M_p\,(kNm)$	$N_p\,(kN)$
1	1	3	45	660
2	4	4	78	880
3	4	4	78	880
4	0.5	2	17.5	440
5	4	4	78	880
6	4	4	78	880
7	1	2	45	660

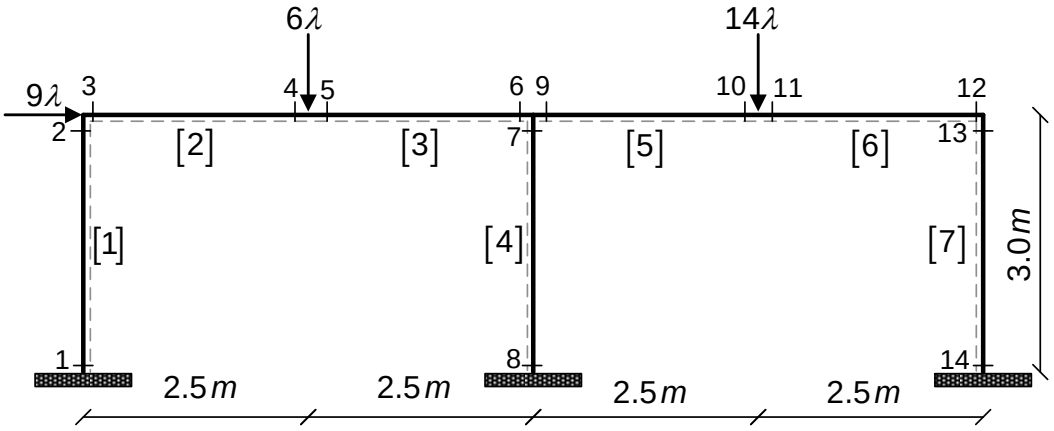

Figure 3.17: Two-bay frame with a single storey

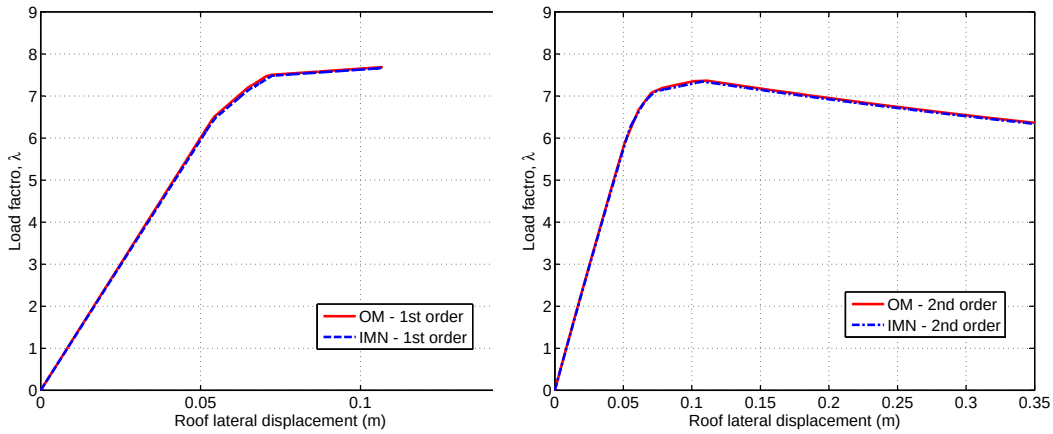

(a) First order analysis

(b) Second order analysis

Figure 3.18: Load factor λ versus roof lateral displacement with and without $M-N$ interaction / second order effects

comparison of force-displacement response of the frame between the each type of analysis: OM-1st order, IMN-1st order, OM-2nd order and IMN-2nd order. As expected, the load factor obtained with first order analysis (with or without $M-N$ interaction) is larger than the one computed with large displacement analysis considering or not $M-N$ interaction. The first order analysis without

interaction compare very well with the result obtained by Spiliopoulos et al. using mathematical programming[44]. It can be seen from Fig. 3.18 that second order effects manifest themselves soon after the first hinge has formed. For the same value of the displacement, the corresponding load is smaller with a second order analysis. The difference between the load multiplier obtained via first and second order analyses continue to grow with increasing value of the displacement. Once the maximum load has been reached, one can observe the typical descending branch associated with second order analysis of framed structures. For the problem under consideration, neglecting the $M - N$ interaction does not affect much the response of the structure. Only a very small difference is observed with a higher value of the load multiplier obtained from computations without $M - N$ interaction. This is due to the fact that the axial forces developed in the elements are ineffectively small making insignificant influence on the value of the plastic bending moments. Next, we investigate the effect of the roundness factor q on the frame response. The load factor is plotted against the lateral displacement in Fig. 3.19. The ultimate load factor obtained is $\lambda = 6.899$ for $q = 1$, $\lambda = 7.345$ for $q = 2$ and $\lambda = 7.387$ for $q = 10$. There is a significant difference between the ultimate load factor computed with $q = 1$ and $q = 2$. However, this difference is less important when comparing the load carrying capacity evaluated with $q = 2$ and $q = 10$.

3.7.3 One storey portal frame of Vogel

We investigate the response of the one-storey portal frame suggested by Vogel (see Fig. 3.20). The cross-section properties are given as following: the Young modulus $E = 205\,GPa$, yield stress 235 MPa and the columns of HEB 300 and the beam of HEA 340. As in example 3.7.2 we explore the effect of the roundness factor q on the value of the ultimate load factor λ by varying the value of $q = 1$, 2 and 10. The second order effect and the influence of interaction between axial and bending forces are also examined for the roundness factor of $q = 2$. The

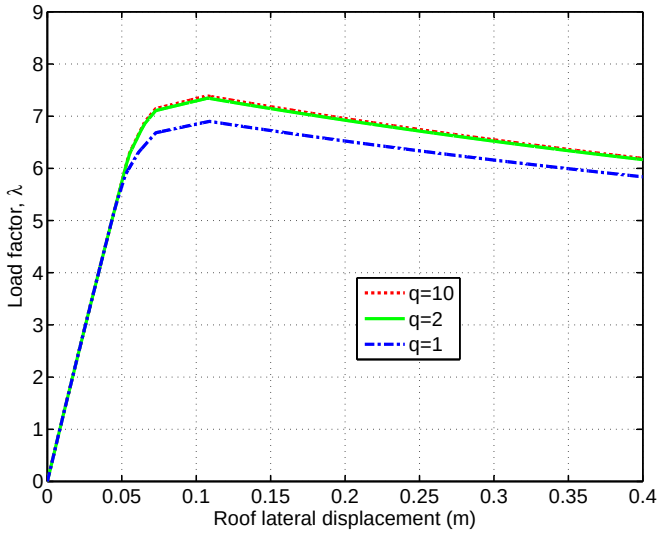

Figure 3.19: Influence of the roundness parameter q on the Load factor λ.

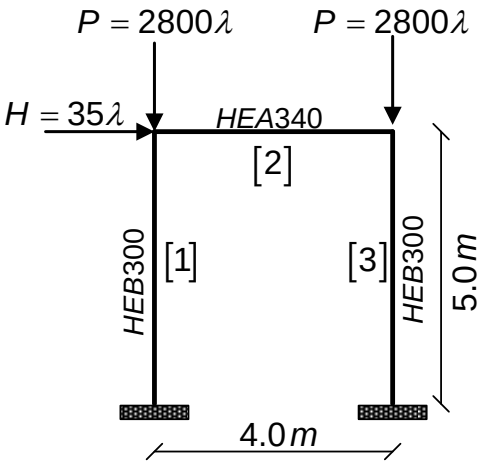

Figure 3.20: Configuration of Vogel's frame

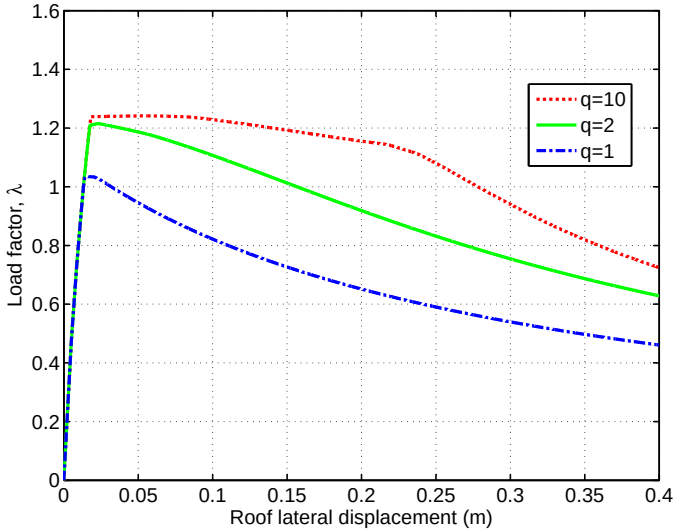

Figure 3.21: Influence of the roundness parameter q on the Load factor λ.

load factor versus lateral displacement is illustrated in Fig. 3.21. In this figure, the roundness effect is more significant than in the previous example. At the beginning of the descending branch, the difference between the ultimate load factors computed with $q = 2$ and $q = 10$ is quite small but progressively increases as the curve for $q = 2$ drops more dramatically than for $q = 10$. The load factor is much lower for the case of $q = 1$ compared to the other two. The axial forces in this example grow so largely that their influence on the bending moments are noticeable. This effect is confirmed in Fig. 3.22 where the curves relating the load factor to the lateral displacement obtained from different types of analyses are compared against each other. It is clearly evident that the load factor is much lower with second order analysis when $M - N$ interaction is not considered. This difference almost dissapear once $M - N$ interaction is taken nto account.

3.7.4 Two-storey frame

Two-storey frame shown in Fig. 3.23 is also analysed to determine the effect of roundness parameter q as well as to discuss the different behaviors of the structure according to the method of analysis and the plasticity model (with or without

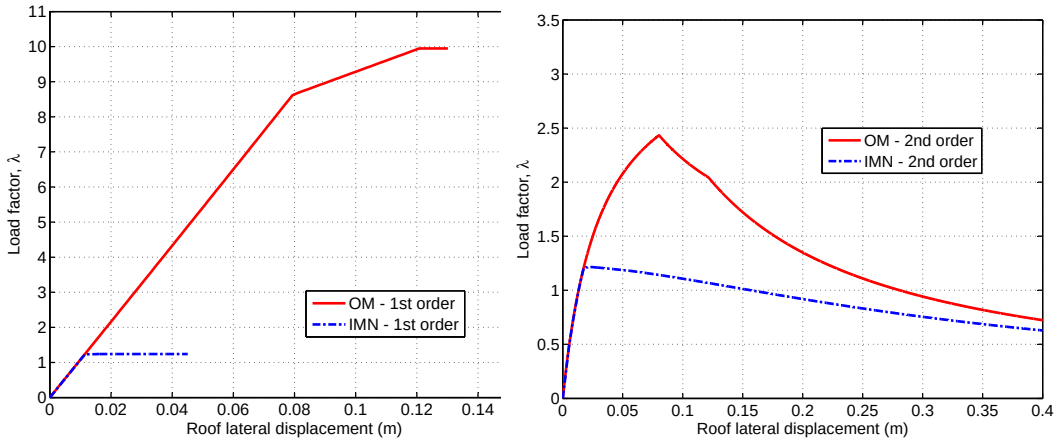

(a) First order analysis (b) Second order analysis

Figure 3.22: Load factor λ versus roof lateral displacement with and without $M-N$ interaction / second order effects

$M-N$ interaction). The cross-section properties are given as following: the Young modulus $E = 210\,GPa$, yield stress 220 MPa. The member properties are given in Table 3.2 .

Table 3.2: Mechanical properties of the members

Member	$I\,(\times 10^{-5} m^4)$	$A\,(\times 10^{-4} m^2)$	$M_p\,(kNm)$
I	2.77	43	162
II	1.51	21.5	81

Fig. 3.24 exhibits the relation between load factor and the lateral displacement of two-storey frame corresponding to different value of q. In this example, the roundness factor significantly affect the behavior of the two storey frame structure. Again, the largest carrying load is obtained with a first order analysis considering a pure bending plasticity model Fig. 3.25.

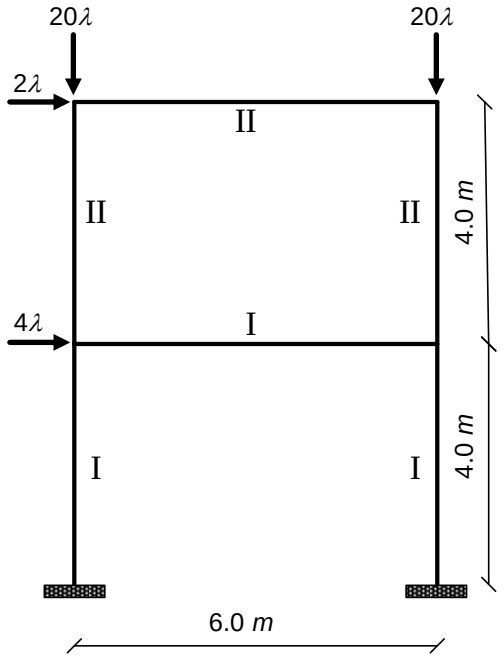

Figure 3.23: Configuration of the two-storey frame

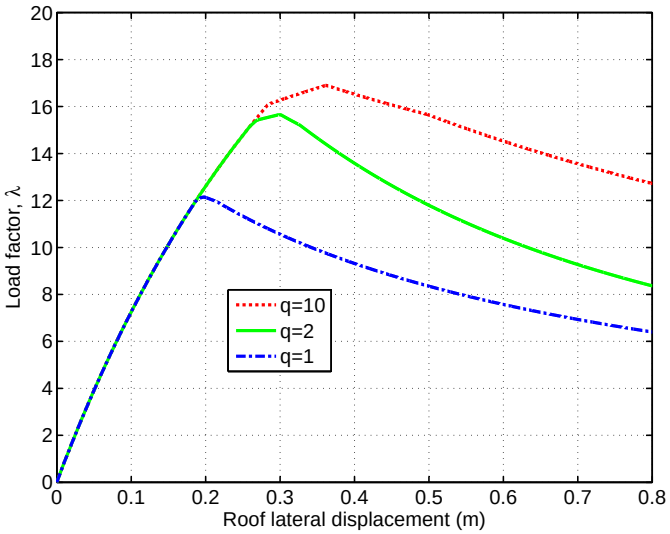

Figure 3.24: Influence of the roundness parameter q on the Load factor λ.

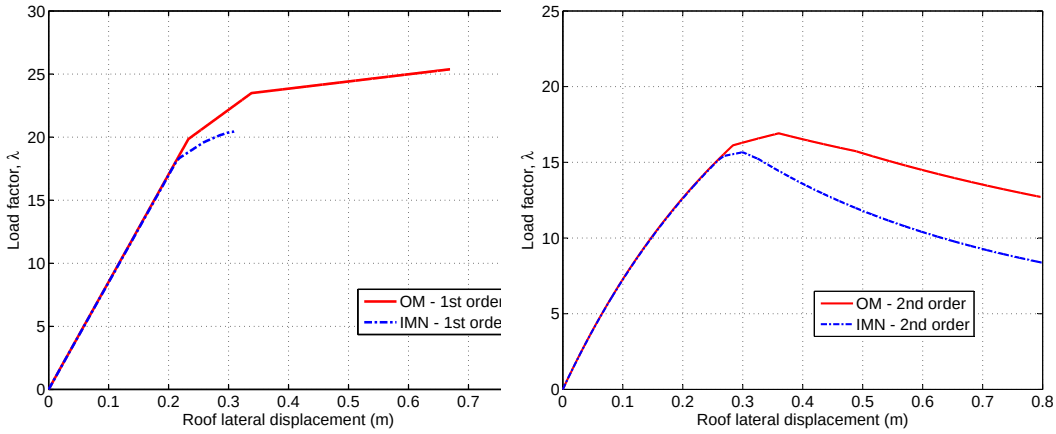

(a) First order analysis (b) Second order analysis

Figure 3.25: Load factor λ versus roof lateral displacement with and without $M - N$ interaction / second order effects.

3.8 Conclusion

This section presented a co-rotational beam elements for large-displacement inelastic analysis of planar framed structures. The local beam formulation consists of a flexible beam element whose ends are connected to generalized plastic hinges. In this model, the generalized plastic hinges which are modeled by combined axial and rotational springs are used to reproduce the plastification of the member. The plastic behavior of the hinges is described by an anisotropic super-elliptic yield surface and the normality rule. By varying the roundness factor, an infinite number of yield surface are obtained making it possible to select the yield function that best fit experimental data of any type of cross-section and material. In addition to that, an integration of the constitutive law using Euler backward scheme was provided for any typical value of roundness factor q. The integration was also provided for special cases such linear and quadratic yield surface. For the application to linear yield surface, close form solution to the optimization was obtained. A proof of unique root was also given for the case of the quadratic yield surface ($q = 2$) although close form expressions could not be found. Aside from that, the numerical examples were additionally provided to show the ability

of the model to capture the structural nonlinearities of the frame's response and to study the effect of the roundness factor q as well as the second order effects on the frame structure's response. The study on a clamped beam subjected to monotonic and cyclic loading showed that the increase of load carrying capacity of the beam with the increasing value of the roundness factor. The pinching effect and cyclic softening were also seen in the beam's response under cyclic loading. In addition, three portal frames were also investigated by varying the value of q and by performing different calculations (1st order/2nd order and with/without $M - N$ interaction). Small difference between the force-displacement curves obtained from calculations with and without $M - N$ interaction could be found for the two-bay frame with single storey due to the reason that the axial forces developed in the elements are small. As expected, the other two frames gave significant difference between the force-displacement curves obtained from calculations with and without $M - N$ interaction because the axial forces were large in these two examples.

Bibliography

***

[1] Teh, Lip, and Clarke, J. Murray (1998). Plastic-Zone Analysis of 3D Steel Frames Using Beam Elements. Journal of Structural Engineering, Vol. 125, No. 11, pp. 1328-1337.

[2] Ziemian, R.D., McGuire, W., and Deierlein, G.G. (1992). Inelastic Limit States Design: Part I –Planar Frame Studies. Journal of Structural Engineering, ASCE, Vol. 118, No.9, pp. 2532-2549.

[3] Bulent N. Alemdar, Donald W. White (2005). Displacement, Flexibility, and Mixed Beam–Column Finite Element Formulations for Distributed Plasticity Analysis. Journal of Structural Engineering, Vol. 131, No. 12, December 1, 2005.

[4] Van-Long Hoang, Hung Nguyen Dang, Jean-Pierre Jaspart, Jean-François Demonceau (2015). An Overview of the Plastic – Hinge Analysis of 3D Steel Frames. Asia Pac. J. Comput. Engin. Volume 2, page 1-34.

[5] Ahmed H. Zubydan (2010). A simplified model for inelastic second order analysis of planar frames. Engineering Structures, Volume 32, Issue 10, October 2010, Pages 3258-3268, ISSN 0141-0296, http://dx.doi.org/10.1016/j.engstruct.2010.06.015.

[6] Gong, Y. (2006). Adaptive gradual plastic hinge model for nonlinear analysis of steel frameworks. Canadian Journal of Civil Engineering 33(9): 1125–1139.

[7] Chiorean, C.G. (2013). A computer method for nonlinear inelastic analysis of 3D composite steel–concrete frame structures. Engineering Structures, Volume 57, December 2013, Pages 125-152, ISSN 0141-0296, http://dx.doi.org/10.1016/j.engstruct.2013.09.025.

[8] Philip Avery, Mahen Mahendran (2000). Distributed plasticity analysis of steel frame structures comprising non-compact sections. Engineering Structures, Volume 22, Issue 8, June 2000, Pages 901-919, ISSN 0141-0296, http://dx.doi.org/10.1016/S0141-0296(99)00038-3.

[9] Ahmed H. Zubydan (2013). Inelastic large deflection analysis of space steel frames including H-shaped cross sectional members. Engineering Structures, Volume 48, March 2013, Pages 155-165, ISSN 0141-0296, http://dx.doi.org/10.1016/j.engstruct.2012.09.024.

[10] Hoon Yoo, Dong-Ho Choi (2008). New method of inelastic buckling analysis for steel frames. Journal of Constructional Steel Research, Volume 64, Issue 10, October 2008, Pages 1152-1164, ISSN 0143-974X, http://dx.doi.org/10.1016/j.jcsr.2008.01.024.

[11] Cuong Ngo-Huu, Seung-Eock Kim, Jung-Ryul Oh (2007). Nonlinear analysis of space steel frames using fiber plastic hinge concept. Engineering Structures, Volume 29, Issue 4, April 2007, Pages 649-657, ISSN 0141-0296, http://dx.doi.org/10.1016/j.engstruct.2006.06.008.

[12] Huu-Tai Thai, Seung-Eock Kim (2011). Nonlinear inelastic analysis of space frames. Journal of Constructional Steel Research, Volume 67, Issue 4, April 2011, Pages 585-592, ISSN 0143-974X, http://dx.doi.org/10.1016/j.jcsr.2010.12.003.

[13] Phu-Cuong Nguyen, Ngoc Tinh Nghiem Doan, Cuong Ngo-Huu, Seung-Eock Kim (2014). Nonlinear inelastic response history analysis of steel frame structures using plastic-zone method. Thin-Walled Structures, Volume 85, December 2014, Pages 220-233, ISSN 0263-8231.

[14] Seung-Eock Kim, Dong-Ho Lee (2002). Second-order distributed plasticity analysis of space steel frames. Engineering Structures, Volume 24, Issue 6, June 2002, Pages 735-744, ISSN 0141-0296, http://dx.doi.org/10.1016/S0141-0296(01)00136-5.

[15] Huu-Tai Thai, Seung-Eock Kim (2011). Second-order inelastic dynamic analysis of steel frames using fiber hinge method. Journal of Constructional Steel Research, Volume 67, Issue 10, October 2011, Pages 1485-1494, ISSN 0143-974X, http://dx.doi.org/10.1016/j.jcsr.2011.03.022.

[16] Humberto Breves Coda, Rodrigo Ribeiro Paccola (2014). A total-Lagrangian position-based FEM applied to physical and geometrical nonlinear dynamics of plane frames including semi-rigid connections and progressive collapse. Finite Elements in Analysis and Design, Volume 91, 15 November 2014, Pages 1-15, ISSN 0168-874X.

[17] Clarke, M.J., Bridge, R.Q., Hancock, G.J., Trahair, N.S. (1992). Advanced analysis of steel building frames. Journal of Constructional Steel Research, Volume 23, Issues 1–3, 1992, Pages 1-29, ISSN 0143-974X.

[18] Phu-Cuong Nguyen, Seung-Eock Kim (2014). Distributed plasticity approach for time-history analysis of steel frames including nonlinear connections. Journal of Constructional Steel Research, Volume 100, September 2014, Pages 36-49, ISSN 0143-974X.

[19] Liew, J. R., Chen, H. (2004). Explosion and fire analysis of steel frames using fiber element approach. Journal of structural engineering, 130(7), 991-1000.

[20] Rui He, Hongzhi Zhong (2012). Large deflection elasto-plastic analysis of frames using the weak-form quadrature element method. Finite Elements in Analysis and Design, Volume 50, March 2012, Pages 125-133, ISSN 0168-874X.

[21] Teh, L. H., Clarke, M. J. (1999). Plastic-zone analysis of 3D steel frames using beam elements. Journal of structural engineering, 125(11), 1328-1337.

[22] Quang-Huy Nguyen, Mohammed Hjiaj, Van-Anh Lai (2014). Force-based FE for large displacement inelastic analysis of two-layer Timoshenko beams with interlayer slips. Finite Elements in Analysis and Design, Volume 85, August 2014, Pages 1-10, ISSN 0168-874X, http://dx.doi.org/10.1016/j.finel.2014.02.007.

[23] Surovek, A. (2012). Advanced Analysis in Steel Frame Design. American Society of Civil Engineers, 2012. http://ascelibrary.org/doi/book/10.1061/9780784411964

[24] Orbison, J.G., McGuire, W., Abel, J.F. (1982) Yield surface applications in nonlinear steel frame analysis. Computer Methods in Applied Mechanics and Engineering, 1982, volume 33, pages:557–73.

[25] Lui, E. M. (1985). Effect of Connection Flexibility and Panel Zone Deformation on the Behaviour of Plane Steel Frames. PhD. dissertation, School of Engineering, Purdue University, West Lafayette, IN.

[26] Lui, E.M., Chen, W-F. (1986). Analysis and behaviour of flexibly-jointed frames. Engineering Structures, Volume 8, Issue 2, April 1986, Pages 107-118, ISSN 0141-0296, http://dx.doi.org/10.1016/0141-0296(86)90026-X.

[27] J.Y.Richard Liew, H. Chen, N.E. Shanmugam, W.F. Chen (2000). Improved nonlinear plastic hinge analysis of space frame structures. Engineering Structures, Volume 22, Issue 10, October 2000, Pages 1324-1338, ISSN 0141-0296, http://dx.doi.org/10.1016/S0141-0296(99)00085-1.

[28] Chi Kin Iu (2008). Inelastic finite element analysis of composite beams on the basis of the plastic hinge approach. Engineering Structures, Volume 30, Issue 10, October 2008, Pages 2912-2922, ISSN 0141-0296, http://dx.doi.org/10.1016/j.engstruct.2008.04.005.

[29] Cuong Ngo-Huu, Phu-Cuong Nguyen, Seung-Eock Kim (2012). Second-order plastic-hinge analysis of space semi-rigid steel frames. Thin-Walled

Structures, Volume 60, November 2012, Pages 98-104, ISSN 0263-8231, http://dx.doi.org/10.1016/j.tws.2012.06.019.

[30] Donald W. White (1993). Plastic-Hinge Methods for Advanced Analysis of Steel Frames. J. Construct. Steel Research 24 (1993) 121-152.

[31] Alexandre Landesmann (2010). Plastic-hinge approach for inelastic analysis of steel–concrete framed structures. Journal of Constructional Steel Research, Volume 66, Issue 3, March 2010, Pages 323-334, ISSN 0143-974X, http://dx.doi.org/10.1016/j.jcsr.2009.10.014.

[32] Zhou, Z., Chan, S. (2004). Elasticplastic and large deflection analysis of steel frames by one element per member, I: One hinge along member. J. Struct. Eng. 130(4), 538-544.

[33] Liew, J.Y., White, D.W., Chen, W.F. (1993). Second-order refined plastic-hinge analysis for frame design: Part I. Journal of Structural Engineering, ASCE, 119(11), pp. 3196-3216

[34] Powell, G., Chen, P. (1986). 3D Beam-Column Element with Generalized Plastic Hinges. Journal of Engineering Mechanics 112, 627–641. doi:10.1061/(ASCE)0733-9399(1986)112:7(627).

[35] Liew, J., White, D., Chen, W. (1993). Second-Order Refined Plastic-Hinge Analysis for Frame Design. Part I. J. Struct. Eng., 10.1061/(ASCE)0733-9445(1993)119:11(3196), 3196-3216.

[36] Alexandre Landesmann (2012). Refined plastic-hinge model for analysis of steel-concrete structures exposed to fire. Journal of Constructional Steel Research, Volume 71, April 2012, Pages 202-209, ISSN 0143-974X, http://dx.doi.org/10.1016/j.jcsr.2011.09.009.

[37] Attalla, M., Deierlein, G., McGuire, W. (1994). Spread of Plasticity: Quasi-Plastic-Hinge Approach. Journal of Structural Engineering 120, no. 8 (August 1, 1994): 2451–73. doi:10.1061/(ASCE)0733-9445(1994)120:8(2451).

[38] Ali Biglari, Philip Harrison, Nenad Bicanic (2014). Quasi-hinge beam element implemented within the hybrid force-based method. Computers & Structures, Volume 137, June 2014, Pages 31-46, ISSN 0045-7949.

[39] El-Tawil, S. and Deierlein, G. (2001). Nonlinear Analysis of Mixed Steel-Concrete Frames. I: Element Formulation. J. Struct. Eng., 10.1061/(ASCE)0733-9445(2001)127:6(647), 647-655.

[40] Ziemian, R. and McGuire, W. (2002). Modified Tangent Modulus Approach, A Contribution to Plastic Hinge Analysis. J. Struct. Eng., 10.1061/(ASCE)0733-9445(2002)128:10(1301), 1301-1307.

[41] Cristfield, M. A. (1997). Non-linear finite element analysis of solids and structures. In: Essentials, vol 1. Wiley, Chischester, pp 201-233.

[42] Simo, J. C., Hughes, T. J. (2006). Computational inelasticity (Vol. 7). Springer Science & Business Media.

[43] Carrera, E. (1994). A study on arc-length-type methods and their operation failures illustrated by a simple model. Computers & structures, 50(2), 217-229.

[44] Spiliopoulos, K.V., Patsios, T.N. (2010). An efficient mathematical programming method for the elastoplastic analysis of frames. Engineering Structures, 32(5), 1199-1214.

[45] Battini, J.-M., Pacoste C. (2002). Co-rotational beam elements with warping effects in instability problems. Computer Methods in Applied Mechanics and Engineering 191 (2002) 1755-1789

[46] Battini, J.-M., Pacoste, C. (2002). Plastic instability of beam structures using co-rotational elements. Computer Methods in Applied Mechanics and Engineering 191 (2002) 5811–5831.

[47] Rankin, C.C., Nour-Omid, B. (1988). The use of projectors to improve finite element performance. Computers and Structures 30 (1988) 257–267.

[48] Nour-Omid, B., Rankin, C.C. (1988). Finite rotation analysis and consistent linearization using projectors. Computer Methods in Applied Mechanics and Engineering 93 (1991) 353–384.

3.9 Appendix

$$[\boldsymbol{k}]_{n+1} = \begin{bmatrix} C_{22}^{(1)} & C_{21}^{(1)} & -C_{22}^{(1)} & 0 & 0 & 0 & 0 \\ C_{21}^{(1)} & C_{11}^{(1)} & -C_{12}^{(1)} & -k_{11}^{(2)} & 0 & 0 & 0 \\ -C_{22}^{(1)} & -C_{21}^{(1)} & C_{22}^{(1)} + k_{22}^{(2)} & 0 & k_{23}^{(2)} & 0 & 0 \\ 0 & C_{11}^{(3)} & 0 & k_{11}^{(2)} + C_{11}^{(3)} & C_{12}^{(3)} & -C_{11}^{(3)} & -C_{12}^{(3)} \\ 0 & C_{21}^{(3)} & k_{32}^{(2)} & C_{21}^{(3)} & k_{33}^{(2)} + C_{22}^{(3)} & -C_{21}^{(3)} & -C_{22}^{(3)} \\ 0 & -C_{11}^{(3)} & 0 & -C_{11}^{(3)} & -C_{12}^{(3)} & C_{11}^{(3)} & C_{12}^{(3)} \\ 0 & -C_{21}^{(3)} & 0 & -C_{21}^{(3)} & -C_{22}^{(3)} & C_{21}^{(3)} & C_{22}^{(3)} \end{bmatrix}_{n+1}$$

$$\boldsymbol{k}_{ll} = \begin{bmatrix} C_{11}^{(3)} & 0 & C_{12}^{(3)} \\ 0 & C_{22}^{(1)} & 0 \\ C_{21}^{(3)} & 0 & C_{22}^{(1)} \end{bmatrix}_{n+1}$$

$$\boldsymbol{k}_{li} = \begin{bmatrix} -C_{11}^{(3)} & 0 & -C_{11}^{(3)} & -C_{12}^{(3)} \\ C_{21}^{(1)} & -C_{22}^{(1)} & 0 & 0 \\ -C_{21}^{(3)} & 0 & -C_{21}^{(3)} & -C_{22}^{(3)} \end{bmatrix}$$

$$\boldsymbol{k}_{il} = \begin{bmatrix} 0 & C_{12}^{(1)} & 0 \\ 0 & -C_{22}^{(1)} & 0 \\ -C_{11}^{(3)} & 0 & -C_{12}^{(3)} \\ -C_{12}^{(3)} & 0 & -C_{22}^{(3)} \end{bmatrix}_{n+1}$$

$$\boldsymbol{k}_{ii} = \begin{bmatrix} C_{11}^{(1)} & -C_{12}^{(1)} & -k_{11}^{(1)} & 0 \\ -C_{21}^{(1)} & C_{22}^{(1)} + k_{22}^{(1)} & 0 & k_{23}^{(1)} \\ C_{11}^{(3)} & 0 & k_{11}^{(2)} + C_{11}^{(3)} & C_{12}^{(3)} \\ C_{21}^{(3)} & k_{32}^{(3)} & C_{21}^{(3)} & C_{22}^{(3)} + k_{33}^{(3)} \end{bmatrix}_{n+1}$$

Chapter 4

Contact problem

***

A new concept for the contact at the interface of steel-concrete composite beams.

This chapter deals with the problem of contact at the interface of steel-concrete composite beams. The F.E. model "Pontmixte", able to study continuous composite beams at real scale, was based on a finite element of composite beam which considers only 4 degrees of freedom per node: both longitudinal displacements of the slab and the steel beam and common vertical displacement and rotation of the whole composite cross-section. This assumption did not allow any uplift at the interface between both materials. A "new" finite element is proposed in this work with 6 degrees of freedom per node in the aim to include a contact algorithm in the model. The originality of the method is to use the Augmented Lagrangian Method to solve the contact problem at the steel-concrete interface including a new concept so-called:"Flying Node Concept". This concept solves the problem of "continuous" contact at the interface that could sometimes occur along the beam especially in the case of distributed loads. The influence on the loading capacity of the beam and also the influence on some design variables are highlighted.

4.1 Introduction

In the past few years, several finite element models have been proposed for the analysis of composite steel-concrete beams; most of them are based on one-dimensional beam elements with embedded interlayer slip. "Pontmixte" [1] is one of the most innovative programs able to study composite continuous beams at real scale making two numerical integrations - the first on the height of the cross-section and the second along the longitudinal axis of the beam -. Nevertheless, the first version of this model assumed that there is no uplift between the concrete slab and the steel beam. The whole composite cross-section had same vertical displacement and same rotation. This assumption prevents the prediction of possible uplift which could occur in particular loading cases for continuous beams and especially on both sides of the intermediate supports.

Huang et al.[2], [3], proposed a non-linear layered finite element procedure for predicting the structural response of reinforced concrete slabs subjected to fire. The proposed procedure based on Mindlin/Reissner (thick plate) theory includes both geometric and material non-linearities. In this study a total Lagrangian approach was adopted in which displacements are referred to the original configuration and small strains were assumed. In the case of beams subjected to fire, contact problem needs a special attention.

Amilton et al. [4], presented a family of zero-thickness interface elements developed for the simulation of composite beams with horizontal deformable connection, or interlayer slip. The proposed elements include formulations to be employed with Euler-Bernoulli as well as with Timoshenko beam theories, combined to displacement-based beam elements sharing the same degrees of freedom. The elements that can be employed for the simulation of steel-concrete composite beams, was computed more recently by Batista et al. [5] combining with the plate formulation of Huang. The proposed model used to analyse composite floor that includes interface elements appeared able to give the relative longitudinal and transversal displacements between the slab and the steel beam as-well-as the relative vertical displacements in the transverse plane. Recently, Qureshi et al.

[6], studied the effect of shear connector spacing and layout on the shear connector capacity in composite beams. A proposed 3D model (Plan dimensions: 1500 mm × 1500 mm), is loaded as a horizontal push test. This model developed with ABAQUS, includes profiled sheeting and the interfaces concerned by the contact algorithm are: (top profile sheeting – bottom of the concrete slab) and (shaft of the headed studs – surrounding concrete). Running time and convergence difficulty lead to consider 3D models inappropriate to study a continuous bridge beam at real scale. Due to the non-linear nature of contact mechanics, such problems in the past were often approximated by special assumptions within the design process. Due to the rapid improvement of modern computer technology, one can today apply the tools of computational mechanics to simulate applications which include contact mechanisms numerically [7].

The model proposed herein takes into account the slip and lengthening-shortening nonlinear behaviours of the connection. Whatever the zone where the contact occurs after uplift, the relative vertical displacements along the longitudinal axis of the beam is obtained without interpenetration between materials.

Different methods exist to solve the contact problem [8]. For example, in penalty method, increasing the penalty factor to infinity would lead to the exact solution, but in computational application it is not possible to use very high penalty factors because of ill-conditioning of the system. The Lagrange multiplier method fulfill the contact constraints exactly by introducing additional variables; for this reason the Lagrange multiplier generate an increment in the system-matrix size. A combination of the penalty method and the Lagrangian multiplier method leads to the so-called Augmented Lagrangian Method (ALM). With this method, the penalty factor does not need to reach a high value to get the convergence of the iterative process. This method will be used in the proposed model to solve the contact problem at the interface between the concrete slab and the steel beam subjected to the inequality constraint corresponding to the non-penetrability between both materials.

For special loading cases, it could happen that the contact at the interface is not only “node-to node” and concerns a part of the finite element length. The

"Flying Node Concept (FNC)" is a new method proposed in this work to make the appropriate adjustments to the final solution of the problem.

Practically, the connection design leads to a number of studs which are distributed uniformly along the continuous beam or by portions of it (Eurocode recommendations for studs' design). This uniform distribution is generally validated by models that use a node-based connection. In order to take into account the actual continuous contact by using a node-based connection, the FNC algorithm is proposed. The main objective is to propose a longitudinal stud distribution that could be as realistic as possible by taking into account the continuous contact. The first mesh of the beam (same as studs' location) begins uniform and at the end of calculation, a new stud location is proposed. If the studs' distribution does not change significantly from the beginning until the end of calculation; this means that the FNC algorithm was not activated significantly and so, no continuous contact zones have been occurred.

4.2 The "node-to-node" contact

4.2.1 Uplift tests

Before solving the contact problem at some composite cross-sections along the beam during the loading history, other cross-sections where the uplift could occur or the contact without penetration between both materials is satisfied should be located.

With the index *(s)* for the slab and (g) for the steel beam, the following notation is used:

$d^{(s)}$: distance between the interface and the centroid of the slab cross-section,

$d^{(g)}$: distance between the interface and the centroid of the steel beam cross-section,

γ_j: stud slip at the node j,

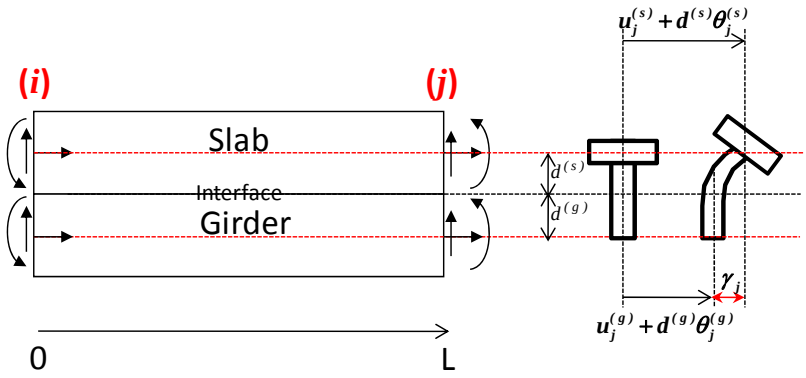

Figure 4.1: Contact at the node j – Slip only.

$\begin{pmatrix} u_j^{(s)} & v_j^{(s)} & \theta_j^{(s)} \end{pmatrix}$: horizontal displacement, vertical displacement and rotation of the slab cross-section at the node j, and

$\begin{pmatrix} u_j^{(g)} & v_j^{(g)} & \theta_j^{(g)} \end{pmatrix}$: horizontal displacement, vertical displacement and rotation of the steel beam cross-section at the node j, and

The following tests must be activated depending on the sign of the variable $\alpha_j = v_j^{(s)} - v_j^{(g)}$:

- Case 1: the contact without penetration is satisfied at the node $j \rightarrow$ the stud is only subjected to a slip (Fig. 4.1).

- Case 2: the uplift of the concrete slab with the bending of the steel beam $\rightarrow$ the contact does not exist at the node j and the bolt is subjected to both slip and lengthening (Fig. 4.2).

- Case 3: the uplift of the concrete slab greater (in absolute value) then the uplift of the steel beam $\rightarrow$ the contact does not exist at the node j and the stud is subjected to both slip and lengthening (Fig. 4.3).

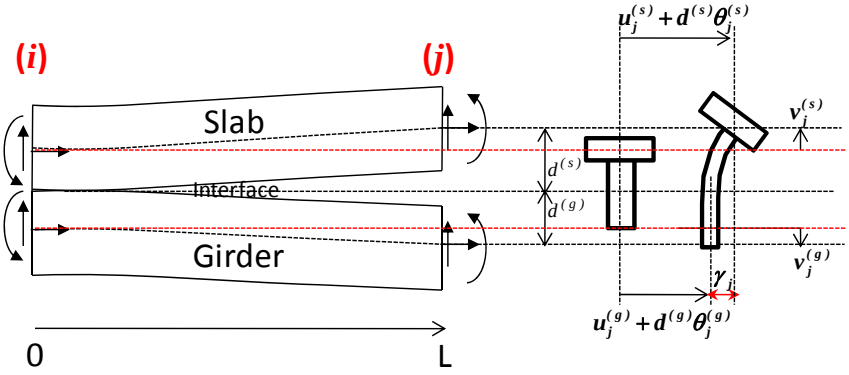

Figure 4.2: Contact at the node j – Slip and slab uplift + steel beam lowering.

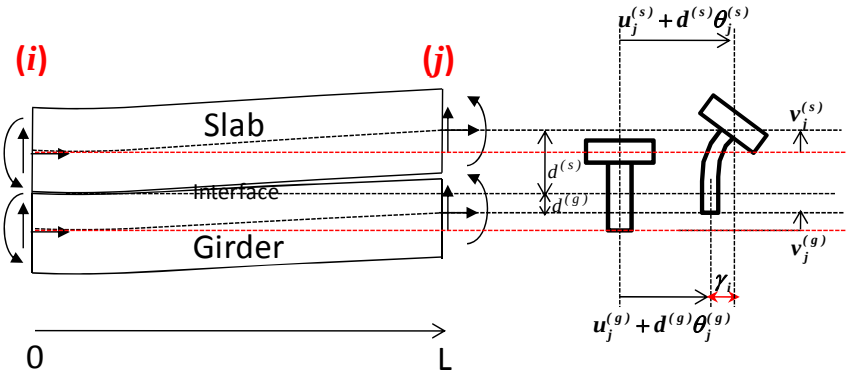

Figure 4.3: Contact at the node j – Slip and slab uplift + steel beam uplift.

4.2.2 "Node-to-node" contact solution

4.2.2.1 Equilibrium equations

The Augmented Lagrangian Method is used to solve the "node-to-node" contact problem. For elastic deformation in solid mechanics, the kinematically admitted displacements that satisfy a stable equilibrium state are those whom minimize the total potential energy – this is the kinematic approach. In our problem, the total potential energy is:

$$V = \frac{1}{2}\boldsymbol{\Delta}^t \boldsymbol{K} \boldsymbol{\Delta} - \boldsymbol{\Delta}^t \boldsymbol{F} \tag{4.1}$$

with: $\boldsymbol{\Delta} = \sum \boldsymbol{d_e}$, $\boldsymbol{K} = \sum \boldsymbol{K_e}$ ***and*** $\boldsymbol{F} = \sum \boldsymbol{f_e}$ where: $\boldsymbol{d_e}$ is the finite element displacement vector, $\boldsymbol{K_e}$ is its stiffness matrix and $\boldsymbol{F_e}$ is its load vector. The minimization of Eq. (4.1) corresponds to:

$$\boldsymbol{K\Delta - F} = 0 \tag{4.2}$$

The problem of partial derivative equations is replaced by a linear system of equations and the minimal value of V in classical finite element approach of unconstrained problem is:

$$Min\ V = -\frac{1}{2}\boldsymbol{\Delta^t F} \tag{4.3}$$

4.2.2.2 Application of ALM to total potential energy

The constrained problem to solve at each connected node can be written as follows:

$$\begin{cases} \text{Min } V \\ \text{subjected } to\ \alpha \geq 0 \end{cases} \tag{4.4}$$

The problem can be solved as a series of unconstrained minimization problems. It is pointed out that the contact depends on the behaviour of the connectors. Even if the shear failure of a connector (for example) corresponds to 6 mm slip, all along the beam its maximum slip remains around 2 mm (always in elastic range) in serviceability limit state. Similar remark could be done for the tension of a

connector. The use of Minimum Potential Energy in this case is then justified. The penalty method approach gives:

$$\begin{cases} \Pi = V + \frac{p}{2}\sum {\alpha_j}^2 \\ \text{After each iteration:updating } \ p \end{cases} \tag{4.5}$$

At iteration (I), penalty method solves this problem, then at iteration $(I+1)$ it re-solves the problem using a largest value of the penalty factor p using the old solution as the initial guess.

The ALM combines the penalty method with the Lagrangian multipliers method. The ALM uses the following constrained objective:

$$\begin{cases} \Pi = V + \frac{p}{2}\sum {\alpha_j}^2 - \sum \lambda_j \alpha_j \\ \text{After each iteration: updating } \ p \text{ and replacing } \lambda_j \text{ by } \lambda_j - p\alpha_j \end{cases} \tag{4.6}$$

The advantage of the ALM is that unlike the penalty method, it is not necessary that p have a very large value in order to solve the original constrained problem. Instead, because of the presence of the Lagrangian multiplier λ_j, p can stay much smaller.

According to Eq. (4.6), the modifications that have to be done to the assembled stiffness matrix and to the corresponding loading vector, at each connected node j, are: It is easy to verify that the equilibrium is satisfied in Fig. (4.4). The stiffness matrix remains symmetric and there is one line and one column added for each node being in contact. In practice, it is easier to add the supplementary equations corresponding to the nodes being in contact, at the end of the initial system as shown in Fig. (4.5). The system of equations to be solved has finally a variable dimension between $(n \times n)$ and $(2n \times 2n)$ maximum depending on the number of nodes being in contact $(q_1, q_2, q_3, ...)$. In Fig. (4.5), each value of the Lagrangian multiplier λ_{qi} corresponds to a node q_i being in contact. A penalty factor p_{qi} will be adjusted for each node q_i; its initial value is equal to 1 and it increases during iterations (multiplying by 10 at each iteration). During the material nonlinear iterative process, the number of nodes being in contact could change.

$u_j^{(s)}$	$v_j^{(s)}$	$\theta_j^{(s)}$	$u_j^{(g)}$	$v_j^{(g)}$	$\theta_j^{(g)}$	λ_j		
							$u_j^{(s)}$	$N_j^{(s)}$
	$* + p_j$			$* - p_j$		-1	$v_j^{(s)}$	$T_j^{(s)} + p_j\alpha_j$
							$\theta_j^{(s)}$	$M_j^{(s)}$
							$u_j^{(g)}$	$N_j^{(g)}$
	$* - p_j$			$* + p_j$		$+1$	$v_j^{(g)}$	$T_j^{(g)} - p_j\alpha_j$
							$\theta_j^{(g)}$	$M_j^{(g)}$
	-1			$+1$		$-\frac{1}{p_j}$	λ_j	$-\alpha_j$

Figure 4.4: ALM is activated at node j.

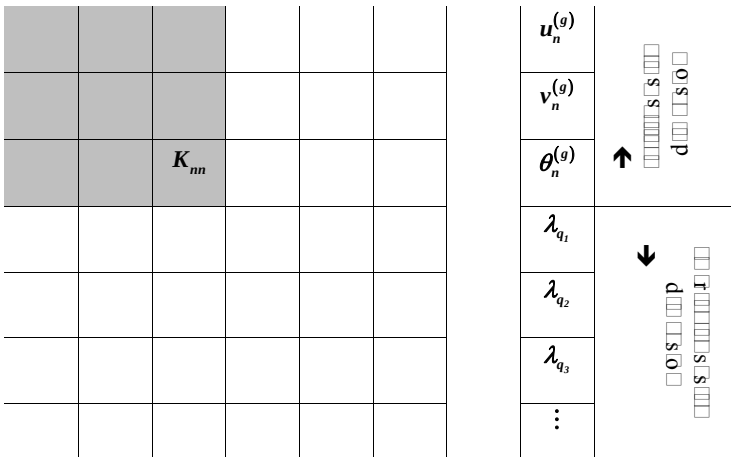

Figure 4.5: ALM is activated at q nodes .

4.2.3 "Continuous" contact solution

During the loading history, it is possible to have some zones subjected to a contact that concerns a part of the element-length and not only its nodes. This could occur in case of distributed load more than in case of concentrated loads. In order to take into account this actual phenomenon, one proposes an approach so called "Flying Node Concept (*FNC*)". This method should be included in the iterative process that solves the contact problem at the interface previously described.

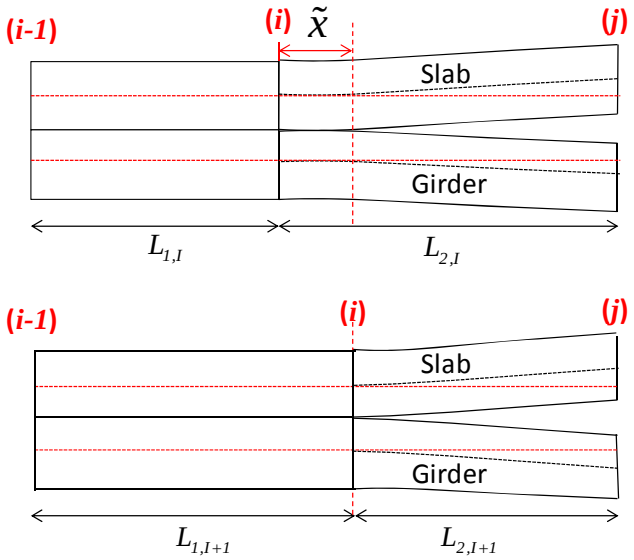

Figure 4.6: Adaptive mesh - *FNC*

The *FNC* adapts the longitudinal mesh of the beam during the iterative process in order to take into account the "*continuous*" contact to a "*node-to-node*" connection. If the initial mesh of the beam appears unchanged at the end-loading history, it means that all the contacts have been "*node-to-node*"; otherwise, the final mesh will inform about the zones that have been subjected to a "*continuous*" contact. It is worth to mention out that these zones could sometimes appear and sometime disappear depending on the loading history of the beam. The final solution corresponding to the end-loading and to the real final mesh depends on

all intermediate calculation steps. If the *FNC* leads to major changes to the mesh and thus to the connection in certain zones of the continuous beam, the connection should be correctly distributed in these zones during the steel beam conception.

One considers two consecutive finite elements $[(i-1)\breve{}i]$ and $[i\breve{}j]$ with respective element lengths $L_{1,I}$ and $L_{2,I}$ at iteration I (Fig. 4.6.a). One suppose that the test concerns the node i of the finite element $[i-j]$ and using appropriate shape functions $N_{i=1,...4}$ one calculates the vertical displacements of both the slab and the steel beam as follows:

$$\begin{cases} v^{(s)}(x) = N_1(x)\, v_i^{(s)} + N_2(x)\, \theta_i^{(s)} + N_3(x)\, v_j^{(s)} + N_4(x)\, \theta_j^{(s)} \\ v^{(s)}(x) = N_1(x)\, v_i^{(g)} + N_2(x)\, \theta_i^{(g)} + N_3(x)\, v_j^{(g)} + N_4(x)\, \theta_j^{(g)} \end{cases} \tag{4.7}$$

The difference between both vertical displacements of the concrete slab and the steel beam, previously called α, is easily obtained with following equation:

$$\alpha_i(x) = N_1(x)\left[v_i^{(s)} - v_i^{(g)}\right] + N_2(x)\left[\theta_i^{(s)} - \theta_i^{(g)}\right] + N_3(x)\left[v_j^{(s)} - v_j^{(g)}\right] + N_4(x)\left[\theta_j^{(s)} - \theta_j^{(g)}\right]$$

or:

$$\alpha_i(x) = N_1(x)\,\Delta v_i + N_2(x)\,\Delta\theta_i + N_3(x)\,\Delta v_j + N_4(x)\,\Delta\theta_j \tag{4.8}$$

This function depends only on the longitudinal x position of the node i. the objective now is to calculate, if it exists, the distance $\bar{x}$ given by $\alpha_i(\tilde{x}) = 0$.

With:

$$N_1(x) = \left(1 - 3\frac{x^2}{L_{2,I}^2} + 2\frac{x^3}{L_{2,I}^3}\right),\ N_2(x) = \left(x - 2\frac{x^2}{L_{2,I}} + \frac{x^3}{L_{2,I}^2}\right)$$
$$N_3(x) = \left(3\frac{x^2}{L_{2,I}^2} - 2\frac{x^3}{L_{2,I}^3}\right) \text{ and } N_4(x) = \left(-\frac{x^2}{L_{2,I}} + \frac{x^3}{L_{2,I}^2}\right)$$

Eq. (4.8) leads to following equation:

$$\alpha_i(x) = 2x^3\left[\frac{\left(\Delta v_k^i - \Delta v_k^j\right)}{L_{2,I}^3} + \frac{\left(\Delta\theta_k^i + \Delta\theta_k^j\right)}{2L_{2,I}^2}\right] - 3x^2\left[\frac{\left(\Delta v_k^i - \Delta v_k^j\right)}{L_{2,I}^2} + \frac{\left(2\Delta\theta_k^i + \Delta\theta_k^j\right)}{3L_{2,I}}\right] + x\Delta\theta_k^i + \Delta v_k^i \tag{4.9}$$

Finally, the equation $\alpha_i(\tilde{x}) = 0$ can be easily solved using trigonometric method for example. Only real solutions are considered and if there is more than one

solution, the maximum one is restrained while it remains less than actual finite element length. The beam mesh changes at considered node for next iteration $I + 1$ as follows:

$$L_{1,I+1} = L_{1,I} + \tilde{x} \quad \text{and} \quad L_{2,I+1} = L_{2,I} - \tilde{x} \tag{4.10}$$

Only shape function on the right side of the node i are employed because the *FNC* tests all the nodes from the left side to the right side of the beam (x axis sense); the first node being the first support which never moves like the other nodes located at each support of the continuous beam. If the test beings from the second element at the node i, appropriate length changes will concern both elements $[(i-1)-i]$ and $[i-j]$ and so on...

Fig. 4.6 shows how the *FNC* runs as an adaptive mesh depending on the value

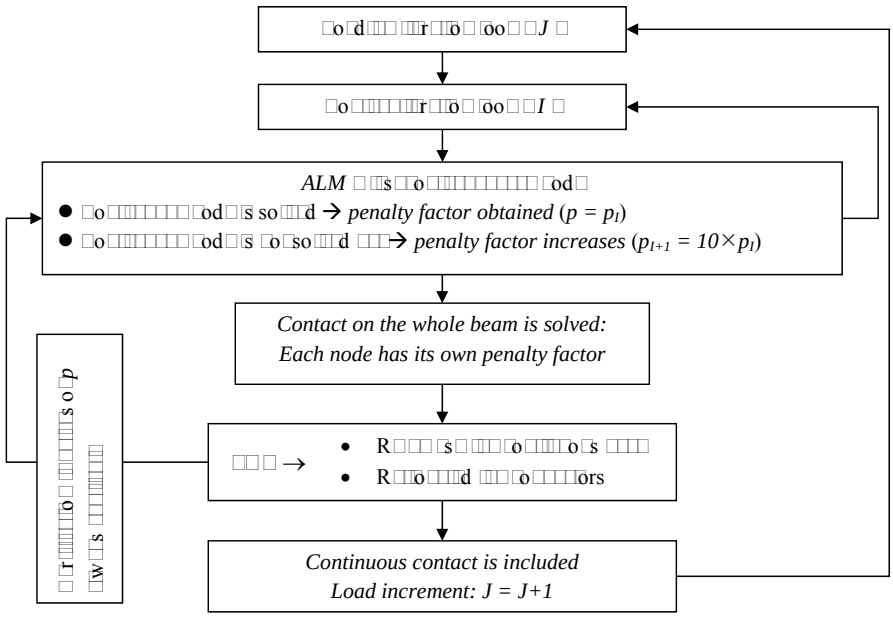

Figure 4.7: Contact algorithm (*ALM + FNC*)

of the distance $\tilde{x}$ obtained from Eq. (4.9). In the case where $\tilde{x}$ is too close to the finite element length, one observes from Eq. (4.10) that $L_{2,I+1}$ could be very low

and then the convergence of the iterative process could be affected. Two methods could be adopted:

- Method 1: Limiting $\tilde{x}$ to an arbitrary value (less than half of the finite element length for example). This method insures to keep constant the number of finite element, it remains easy to compute and it gives enough accurate results.

- Method 2: If $L_{2,I+1}$ is too low, actual finite element disappears and the number of finite elements changes. In (Fig. 4.6.b), both finite elements $[(i-1),(i)]$ and $[(i),(j)]$ merge and become only one finite element $[(i-1),(j)]$. This method is more difficult to compute because it needs a renumbering of the mesh during the iterative process. In addition, the solution could be affected by the final mesh density that is not suitable.

In Fig. 4.7, the *FNC* algorithm is shown with its links to the *ALM* in order to solve the contact problem. It is worth to mention out that the set of values obtained for the penalty factor p is verified by reconnecting *FNC* to *ALM* (at same contact iteration). Generally, these values are still available and the verification is directly satisfied; this is due probably to: $\alpha_i(\tilde{x}) = 0$ (Eq. 4.8).

4.3 THE COMPOSITE BEAM F.E.

4.3.1 Nodal variables

The user-friendly software "Pontmixte" has been upgraded to a "new" version based on a new finite element formulation for the composite beam element. Six degrees of freedom are necessary (instead of four in the preceding version), to take into account the contact/uplift at the interface. The concrete slab as well as the steel beam has 3 degrees of freedom at each node (i) and (j) Fig. 4.8. Nodal displacements vector of the composite finite element is:

$$\{d_e\} = \left\{ \begin{array}{cccccccccccc} u_i^{(s)} & v_i^{(s)} & \theta_i^{(s)} & u_i^{(g)} & v_i^{(g)} & \theta_i^{(g)} & u_j^{(s)} & v_j^{(s)} & \theta_j^{(s)} & u_j^{(g)} & v_j^{(g)} & \theta_j^{(g)} \end{array} \right\}^t \tag{4.11}$$

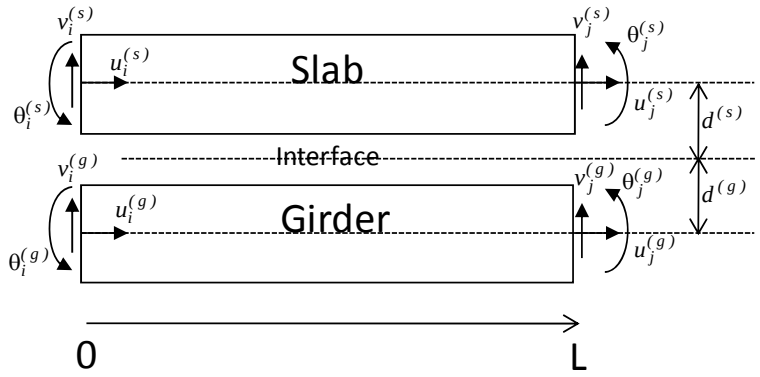

Figure 4.8: Definition of the nodal variables

Using corresponding classical shape function $\boldsymbol{N}$, the displacement at each fibre of the composite cross-section is then

$$\{d\,(x,y)\} = [N\,(x,y)]\,\{d_e\} \tag{4.12}$$

Where

$$[N\,(x,y)] = \begin{bmatrix} \mathbf{N}_i^{(s)} & 0 & \mathbf{N}_i^{(g)} & 0 \\ 0 & \mathbf{N}_j^{(s)} & 0 & \mathbf{N}_j^{(g\,)} \end{bmatrix} \tag{4.13}$$

In Eq. 4.13, $\boldsymbol{N}$ includes (3×3) matrices. The stud slip and lengthening of (shortening) are calculated considering the translation and the rotation of each material. Concerning the lengthening, the stud will be supposed fixes to the concrete:

$$\text{Stud-slip: } \gamma_j = \left[u_j^{(s)} + d^{(s)}\theta_j^{(s)}\right] - \left[u_j^{(g)} + d^{(g)}\theta_j^{(g)}\right] \tag{4.14}$$

$$\text{Stud-slip: } \alpha_j = v_j^{(s)} - v_j^{(g)} \tag{4.15}$$

4.3.2 Kinematic relationships

The kinematic variables are respectively the longitudinal strain and the curvature of each material cross-section:

$$\begin{cases} \varepsilon_x^{(s)} = \frac{\partial u^{(s)}}{\partial x} \quad and \quad \varepsilon_x^{(g)} = \frac{\partial u^{(g)}}{\partial x} \\ \kappa_x^{(s)} = \frac{\partial^2 v^{(s)}}{\partial x^2} \quad and \quad \kappa_x^{(g)} = \frac{\partial^2 v^{(g)}}{\partial x^2} \end{cases} \tag{4.16}$$

Kinematic relationship and corresponding strain vector are

$$\{\varepsilon\} = [B]\{d_e\} \quad with \quad \{\varepsilon\}^t = \left\langle \begin{array}{cccc} \varepsilon_x^{(s)} & \kappa_x^{(s)} & \varepsilon_x^{(g)} & \kappa_x^{(g)} \end{array} \right\rangle \tag{4.17}$$

The kinematic matrix can be written explicitly as follows:

$$[B] = \left[\begin{array}{cccccccccccc} -B_1 & B_2 y & B_3 y & 0 & 0 & 0 & B_1 & -B_2 y & \left(B_3 - \frac{2}{L}\right) y & 0 & 0 & 0 \\ 0 & -B_2 & -B_3 & 0 & 0 & 0 & 0 & B_2 & -\left(B_3 - \frac{2}{L}\right) & 0 & 0 & 0 \\ 0 & 0 & 0 & -B_1 & B_2 y & B_3 y & 0 & 0 & 0 & B_1 & -B_2 y & \left(B_3 - \frac{2}{L}\right) y \\ 0 & 0 & 0 & 0 & -B_2 & -B_3 & 0 & 0 & 0 & 0 & B_2 & -\left(B_3 - \frac{2}{L}\right) \end{array} \right] \tag{4.18}$$

with: $B_1 = 1/L$, $B_2 = 6/L^2 - 12\,(x/L^3)$, and $B_3 = 4/L - 6\,(x/L^2)$

4.3.3 Stiffness matrix of the composite finite element

Paying attention to the kinematic matrix, one observes that it depends on the axial x position of the concerned cross-section and on the depth position$y$ of each material-fiber at the same cross-section. The composite beam cross-section is then divided into a number of horizontal fibers (m for each steel beam flange, n fibers for the steel beam web and p fibers for the slab). The algorithm takes firstly a Gauss-Legendre numerical integration towards the element-depth with 2 gauss-points for each fiber (1st integration along y axis- Fig. 4.9). By summing different stiffnesses along y axis, the result (that correspond to the stiffness of the composite cross-section) is affected to one of the Gauss points in order to understand the 2nd integration along x axis (Fig. 4.9) that uses also 2 Gauss points.

In order to simplify the presentation, the first numerical integration will not appear explicitly. One begins by the element stiffness matrix of the unconnected $[(i)\,,\ (j)]$ composite beam that can be easily obtained by:

$$\left[\tilde{K}_e\right] = \int_0^L [B]^t\,[D]\,[B] \tag{4.19}$$

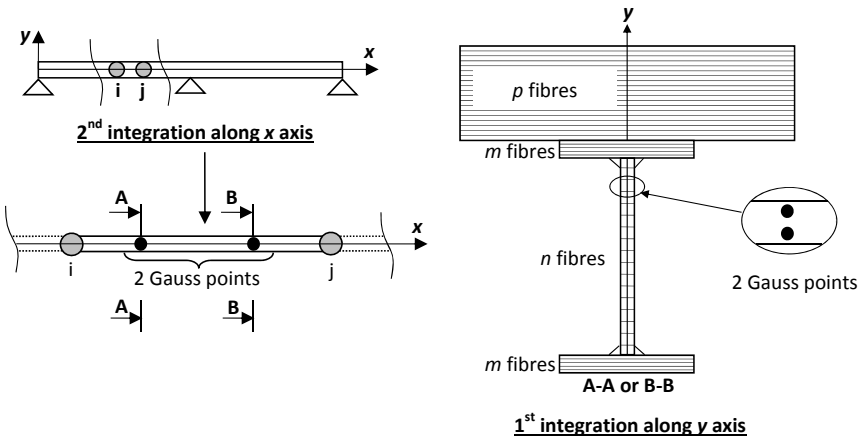

Figure 4.9: Two numerical integrations (one along each axes y and x)

with the behaviour matrix $[D]$ in accordance with Eq. 4.16:

$$[D] = \begin{bmatrix} (EA)^{(s)} & 0 & 0 & 0 \\ 0 & (EI)^{(s)} & 0 & 0 \\ 0 & 0 & (EA)^{(g)} & 0 \\ 0 & 0 & 0 & (EI)^{(g)} \end{bmatrix} \tag{4.20}$$

E: Secant Young's modulus, A: cross section area and I: quadratic inertia of the cross-section.

A secant algorithm is used to solve nonlinear equations due to nonlinear behaviour of materials.
In order to include a connector at the node (j) of the finite element $[(i)\,,\ (j)]$ for example, the principe of virtual work is applied to set the global relationship of the stud behaviour under shear loading as-well-as under a tension.

- The internal work of an infinitesimal slip of the stud at the node (j) and corresponding nodal variable are

$$\delta W_{\text{int}}^{ss} = Q_j \gamma_j = Q_j \left\langle \begin{array}{cccc} 1 & d^{(s)} & -1 & -d^{(g)} \end{array} \right\rangle \left\{ \delta d_j^{ss} \right\} \tag{4.21}$$

$$\left\{ \delta d_j^{ss} \right\}^t = \left\langle \begin{array}{cccc} \delta u_j^{(s)} & \delta\theta_j^{(s)} & \delta u_j^{(g)} & \delta\theta_j^{(g)} \end{array} \right\rangle \tag{4.22}$$

Q_j is the stud shear force and $d^{(s)}$ and $d^{(g)}$ are defined in Fig. 4.8.
Corresponding nodal forces are

$$\left\{F_j^{ss}\right\}^t = \left\langle \begin{array}{cccc} N_j^{(s)} & M_j^{(s)} & N_j^{(g)} & M_j^{(g)} \end{array} \right\rangle \tag{4.23}$$

- The internal work of an infinitesimal lengthening of the stud at the node (j) and corresponding nodal variables are

$$\delta W_{\text{int}}^{st} = P_j \delta\alpha_j = P_j \left\langle \begin{array}{cc} 1 & -1 \end{array} \right\rangle \left\{\delta d_j^{st}\right\} \tag{4.24}$$

$$\left\{\delta d_j^{st}\right\}^t = \left\langle \begin{array}{cc} \delta v_j^{(s)} & \delta v_j^{(g)} \end{array} \right\rangle \tag{4.25}$$

Corresponding nodal forces are

$$\left\{F_j^{st}\right\}^t = \left\langle \begin{array}{cc} T_j^{(s)} & T_j^{(g)} \end{array} \right\rangle \tag{4.26}$$

- External works related to the nodal forces given in Eqs. (4.23) and (4.26)are:

$$\delta W_{ext}^{ss} = \left\{\delta d_j^{ss}\right\}^t \left\{F_j^{ss}\right\} \tag{4.27}$$

$$\delta W_{ext}^{st} = \left\{\delta d_j^{st}\right\}^t \left\{F_j^{st}\right\} \tag{4.28}$$

- The principle of the virtual works leads to

$$\delta W_{\text{int}}^{ss} = \delta W_{ext}^{ss} \tag{4.29}$$

$$\delta W_{\text{int}}^{st} = \delta W_{ext}^{st} \tag{4.30}$$

The stud slip behaviour is defined as the relationship between the force at the stud head and the slip calculated between its base and the force point application. This stud slip has been defined previously in Eq. (4.14) and R^{ss} is the stub slip-resistance

$$Q_j^{ss} = R^{ss}\gamma_j \tag{4.31}$$

From Eq. (4.29), the stud stiffness matrix $[K^{ss}]$ related to its slip-resistance can be easily obtained

$$\left\{ \begin{array}{l} \delta W_{\text{int}}^{ss} = Q_j\gamma_j = R^{ss}\left\{\delta d_j^{ss}\right\}^t \left\langle \begin{array}{cccc} 1 & d^{(s)} & -1 & -d^{(g)} \end{array} \right\rangle^t \left\langle \begin{array}{cccc} 1 & d^{(s)} & -1 & -d^{(g)} \end{array} \right\rangle \left\{d_j^{ss}\right\} \\ \delta W_{ext}^{ss} = \left\{\delta d_j^{ss}\right\}^t \left\{F_j^{ss}\right\} \end{array} \right. \tag{4.32}$$

$$\left\{F_j^{ss}\right\} = R^{ss}\left\langle \begin{array}{cccc} 1 & d^{(s)} & -1 & -d^{(g)} \end{array}\right\rangle^t \left\langle \begin{array}{cccc} 1 & d^{(s)} & -1 & -d^{(g)} \end{array}\right\rangle \left\{d_j^{ss}\right\} \tag{4.33}$$

The stud stiffness matrix related to its slip-resistance is finally

$$[K^{ss}] = \begin{bmatrix} 1 & d^{(s)} & -1 & -d^{(g)} \\ d^{(s)} & \left(d^{(s)}\right)^2 & -d^{(s)} & -d^{(s)}d^{(g)} \\ -1 & -d^{(s)} & 1 & d^{(g)} \\ -d^{(g)} & -d^{(s)}d^{(g)} & d^{(g\,)} & \left(d^{(g)}\right)^2 \end{bmatrix} \tag{4.34}$$

Concerning the stud lengthening behaviour, same procedure then the one developed for the stud slip-resistance is carried out. The stud tension resistance is called R^{st} and the stud lengthen has been previously defined in Eq. (4.15).

$$P_j^{st} = R^{st}\alpha_j \tag{4.35}$$

$$\begin{cases} \delta W_{\text{int}}^{st} = P_j\delta\alpha_j = R^{st}\left\{\delta d_j^{st}\right\}^t \left\langle \begin{array}{cc} 1 & -1 \end{array}\right\rangle^t \left\langle \begin{array}{cc} 1 & -1 \end{array}\right\rangle \left\{d_j^{st}\right\} \\ \delta W_{ext}^{st} = \left\{\delta d_j^{st}\right\}\left\{F_j^{st}\right\} \end{cases} \tag{4.36}$$

$$\left\{F_j^{st}\right\} = R^{st}\left\langle \begin{array}{cc} 1 & -1 \end{array}\right\rangle^t \left\langle \begin{array}{cc} 1 & -1 \end{array}\right\rangle \left\{d_j^{st}\right\} \tag{4.37}$$

The stud stiffness matrix related to its lengthening-resistance is finally

$$\left[K^{st}\right] = R^{st}\begin{bmatrix} 1 & -1 \\ -1 & 1 \end{bmatrix} \tag{4.38}$$

After replacing by the symbol $(*)$the terms of the stiffness matrix related to an unconnected composite beam element given in Eq. (4.19) concerning an unconnected composite beam, the stiffness matrix of the finite element $[(i)\,,\ (j)]$ representing a connected campsite beam is

$$[K_e] = \left[\tilde{K}_e\right] + [K^{ss}] + \left[K^{st}\right] \tag{4.39}$$

Respecting the nodal variables organization given in Eq. (4.11), this matrix can be written explicitly as follows:

$$[K_e] = \begin{bmatrix} * & * & * & 0 & 0 & 0 & * & * & * & 0 & 0 & 0 \\ & * & * & 0 & 0 & 0 & * & * & * & 0 & 0 & 0 \\ & & * & 0 & 0 & 0 & * & * & * & 0 & 0 & 0 \\ & & & * & * & * & 0 & 0 & 0 & * & * & * \\ & & & & * & * & 0 & 0 & 0 & * & * & * \\ & & & & & * & 0 & 0 & 0 & * & * & * \\ & & & & & & *+R^{ss} & * & *+d^{(s)}R^{ss} & -R^{ss} & 0 & -d^{(g)}R^{ss} \\ & & & & & & & *+R^{st} & * & 0 & -R^{st} & 0 \\ & & & & & & & & *+\left(d^{(s)}\right)^2 R^{ss} & -d^{(s)}R^{ss} & 0 & -d^{(s)}d^{(g)}R^{ss} \\ & & \text{Symmetry} & & & & & & & *+R^{ss} & * & *+d^{(g)}R^{ss} \\ & & & & & & & & & & *+R^{st} & * \\ & & & & & & & & & & & *+\left(d^{(g)}\right)^2 R^{ss} \end{bmatrix} \tag{4.40}$$

4.4 Numerical simulation

In order to proof that the use of contact algorithm is relevant to obtain accurate results, first numerical investigation concerns the comparison between experimental test results and the ones obtained by the "old" model with 4 degrees of freedom per node on one hand and the "new" model with 6 degrees of freedom per node on second hand.
Second numerical simulation will concerns an application for the *FNC* considering the same twin-beam subjected to a distributed load.

4.4.1 Comparison with an experimental test

The steel-concrete composite twin-beam considered (Fig. 4.10.a) has been subjected to an experimental test at Structural Laboratory of INSA-Rennes. The beam is loaded in accordance with the following stages:

- Stage 1: The self-weight is taken into account (4.17 kN/m for sagging zones and 4.26 kN/m for hogging ones).

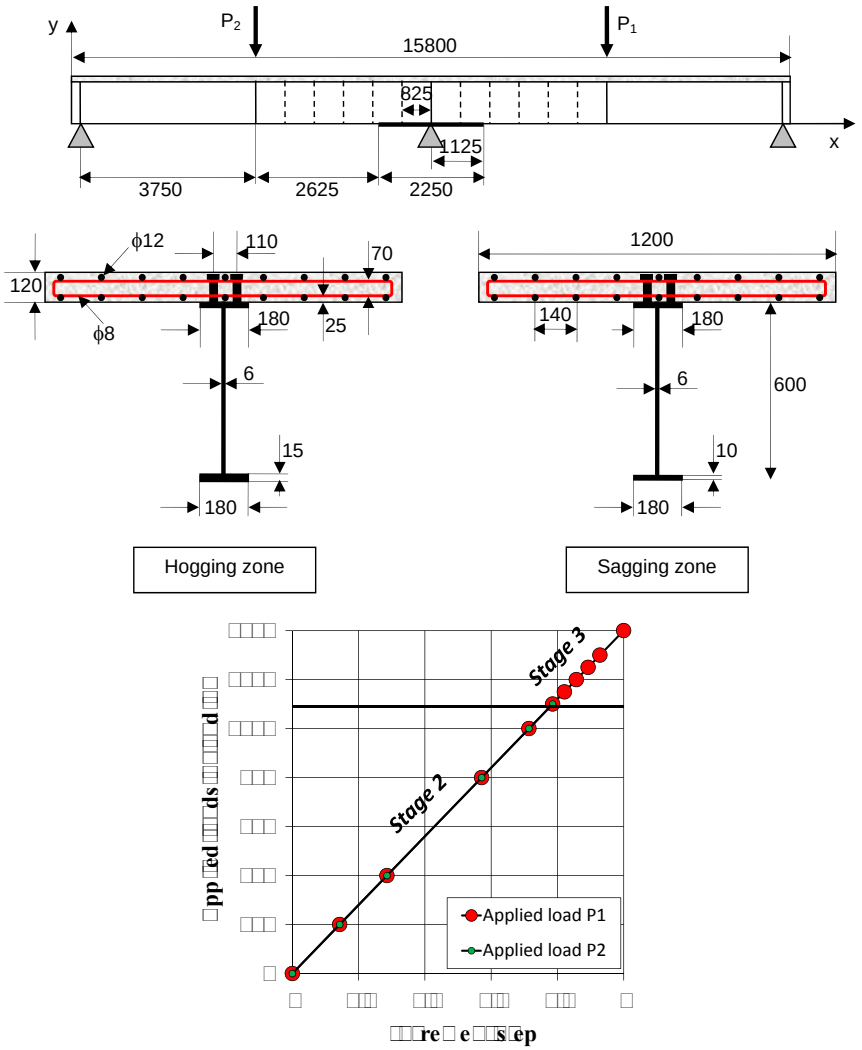

Figure 4.10: (a) Geometrical characteristics of the twin-beam. (b) Loading stage 2 and 3

- Stage 2: Concentrated loads “P1” and “P2” are applied at the mid-spans of the beam until the magnitude of 550 kN for each.

- The load “P2” remains constant and the load “P1” continue to increase from 550 kN to 850 kN.

In Fig. 4.10.b is plotted the loading history corresponding to the stages 2 and 3. The stage 1 is not represented because it represents a distributed load and it is

Table 4.1: Numerical values of mechanical characteristics

Material	Parameters
Concrete	$E_{cm} = 36,000\ MPa,\ f_{ck} = 40\ MPa,\ f_{ctm} = 2\ MPa,\ \varepsilon_m = 0.0022,\ \varepsilon_r = 0.004$
Steel profile	$E^{(a)} = 190,000\ MPa,\ f_y^{(a)} = 475\ MPa,\ f_u^{(a)} = 620\ MPa,\ \mu_1^{(a)} = 10,\ \mu_2^{(a)} = 28$
Rebar	$E^{(s)} = 200,000\ MPa,\ f_y^{(s)} = 443\ MPa,\ f_u^{(s)} = 565\ MPa,\ \mu_1^{(s)} = 1,\ \mu_2^{(s)} = 32$
Stud	$Q_u = 80,000\ MPa,\ C_1 = 0.7,\ C_2 = 0.8,\ \gamma_{max} = 6\ mm$

different on hogging and sagging zones of the continuous beam.
It is assumed that the hogging zone concerns 15% of the span length on each side of the intermediate support. For this zone, the thickness of the bottom flange is equal to 15 mm and for other cross-sections (in sagging zones) only 10 mm is required. The top flange thickness is equal to the bottom one. Related to mechanical behaviour of each material (Fig. 4.11), the mechanical properties are summarized in Table 4.1.

$$\text{Concrete: } \frac{\sigma^{(c)}}{f_{cm}} = \frac{k\eta - \eta^2}{1 + (k-2)\,\eta} \quad \text{with: } \eta = \frac{\varepsilon^{(c)}}{\varepsilon_m} > 0 \quad \text{and } k = 1.1 E_{cm} \frac{\varepsilon_m}{f_{cm}} \tag{4.41}$$

$$\text{Stud: } Q = Q_u \left(1 - e^{-c_1 |\gamma|}\right)^{c_2} \tag{4.42}$$

As mentioned previously, with the assumption of 4 degrees of freedom per node, the contact at the interface could not be taken into account as-well-as possible uplifts along the beam. With this assumption, the comparison between numerical and experimental results could not be totally satisfactory. In Fig. 4.12 obtained from [16], the comparison of the beam deflexion between numerical and experimental results with the previous "old" model "Pontmixte" shows a significant difference especially over the elastic range. This result was predictable because the penetration as-well-as the uplift at the material interface begin to be significant when the load increases. In this figure, one observes that the deflexion under "P1" has been underestimated with this numerical model since "P1" continues to increase over 550 kN. Unfortunately the measurements under the load "P2" have not been done, but the conclusion should be similar to "P1".

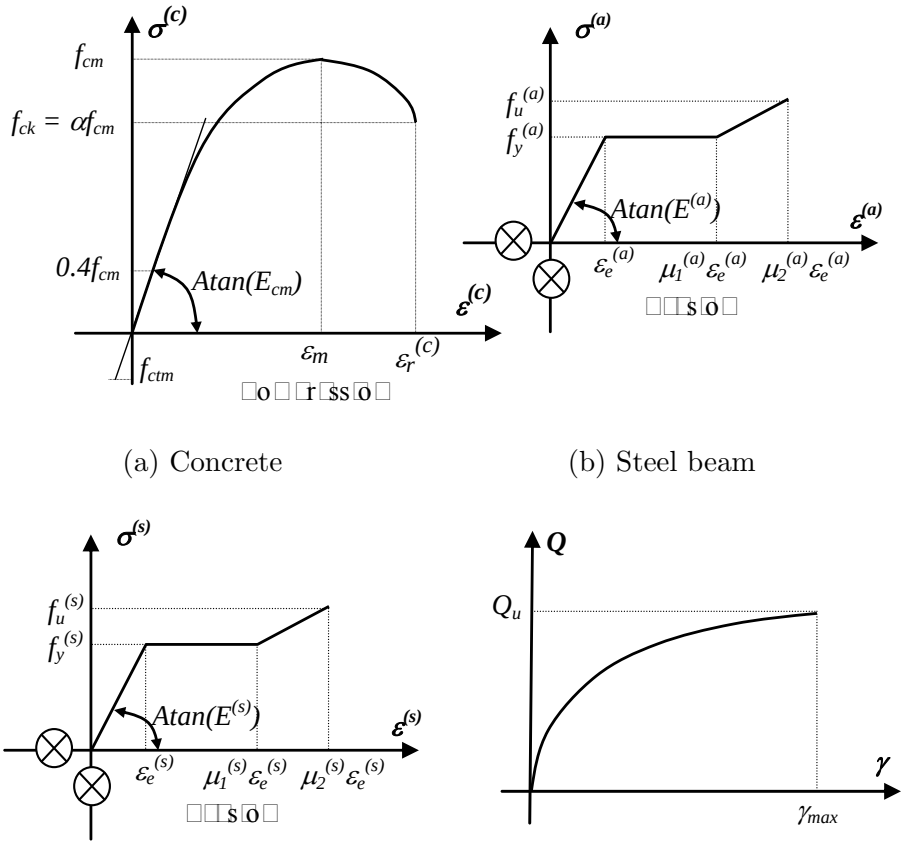

(a) Concrete (b) Steel beam

(c) Rebar (d) Stud

Figure 4.11: Material mechanical behaviour

It is clear that the effect of the interface "behaviour" becomes significant for high load level and especially under concentrated loads or at intermediate supports. For this reason, following numerical simulations, using the proposed "new" model (6 degrees of freedom per node), should help to understand how the contact algorithm could give more accurate results.

For the same twin-beam, are compared in Figs. 4.13 some design variables

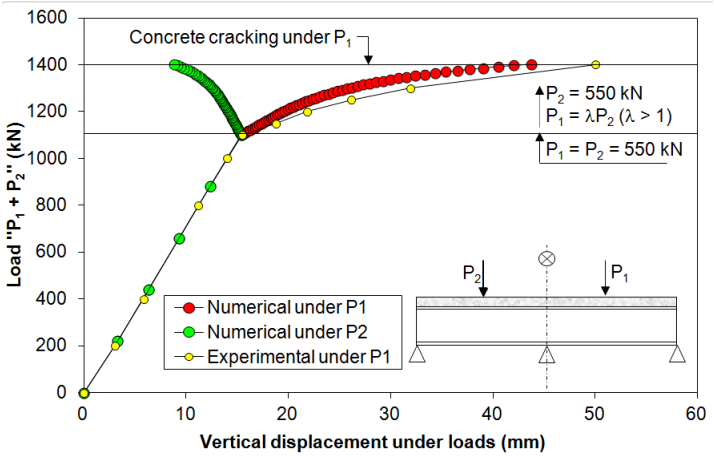

Figure 4.12: Comparison of deflexions – "old" model [16]

obtained with the "new" finite element model. The left curves correspond to the model without activating the *ALM* algorithm and the right ones with activating the *ALM* algorithm. The left curves are plotted in the aim to identify the critical cross-sections along the beam where the *ALM* algorithm should be activated. In Figs. 4.13.(a,b) and Figs. 4.13.(c,d) are plotted respectively the comparison of vertical displacements between the slab and the steel beam and the comparison of the rotations for the last-step loading. As it was predicted, the left curves related to the cross-sections located under the concentrated loads show a penetration of the concrete slab in the steel beam. This penetration is theoretical and not realistic and it will be corrected by activating the ALM algorithm (right curves). It is pointed out that the minimum gap at the interface is fixed to 10^3 mm for these numerical simulations. This value leads to reasonable time computation for convergence of the contact iterative process. In Figs. 4.13.(e,f), are plotted the stud slip curves and the lengthening-shortening ones. The penetration and the uplift observed in the left curves disappear in the right curves; maximum uplift is observed at each side of the intermediate support. The slip curves become more smoothed with the ALM algorithm especially under the concentrated loads.
One observes that the use of the *ALM* algorithm makes changes in the magnitude of the design variables and therefore should have a special attention.

In Fig. 4.14 are plotted similar curves as in Fig. 4.12 but for the "new' finite element model activating the *ALM* algorithm. One observes the incidence on the beam deflexion under the concentrated load "P1"; the correlation between numerical and experimental results is more satisfactory in the post-elastic range.

4.4.2 influence of the *FNC*

In order to show how "Pontmixte" solves the problem of the "continuous" contact, precedent twin-beam is now subjected to a distributed load p. The calculation is carried out until reaching elastic hogging bending at intermediate support. Initial mesh of the twin-beam contains 10 finite elements per beam; this mesh is called Mesh-0. The results of two calculations are compared:

- *Calculation1*: Contact solved with *ALM*

- *Calculation2*: Contact solved with *ALM + FNC*

In the aim to avoid additional differences between the results due to different numbers of finite elements, Method1 presented in section 4.2.3 will be used in this example. Initial mesh will change several times during the loading history of the beam (Fig. 4.15). Only the final mesh so called Mesh-n will be highlighted because it corresponds to the last step loading. Mesh-0 and Mesh-n are presented in Fig. 4.16. One observes that the difference between the finite element lengths mostly concerns both sides of the intermediate support and also the zones close to the end-supports. These zones correspond to the ones that are subjected to a "continuous" contact and solved by the *FNC*. It is pointed out that the symmetry of the problem is retained until convergence. For Calculation1 and Calculation2 same stopping criterion is used: reaching elastic hogging bending at intermediate support. Elastic hogging bending is reached for p = 280 kN/m and p = 264 kN/m respectively for *Calculation1* and for *Calculation2*. For both loading levels, the stresses in the composite cross-sections at mid-span and at intermediate support

are given in Fig. 4.17.a and b.

The hogging bending is obtained when the top beam-flange reaches its yield stress $\left(f_y^{(a)} = 475\ MPa\right)$. The stress difference observed on hogging bending between both calculations is due only to the precision and it appears neglectable and same corresponding hogging bending is $M_s^- = M_{el}^- = -871\ kN/m$. Nevertheless, in sagging zone, the stress difference is greater than the one on hogging and should not be neglected. In Calculation2, the sagging bending is greater than in Calculation1; this explains why the elastic hogging bending is reached faster (Table 4.2).

One compares now the stress distribution of both calculations for same load level

Table 4.2: Comparison of bending moments.

Calculation	Sagging bending	Hogging bending
Calculation 1 (ALM)		
P=280 kN/m	$M_s^+ = 570\ kN/m$	$M_s^- = M_{el}^- = 871\ kN/m$
Calculation 2 (ALM + FNC)		
P=264 kN/m	$M_s^+ = 548\ kN/m$	$M_s^- = M_{el}^- = 871\ kN/m$
Calculation 1 (ALM)		
P=264 kN/m	$M_s^+ = 534\ kN/m$	$\lvert M_s^- \rvert = 871\ kN/m\ < \left\lvert M_{el}^- \right\rvert$

(p = 264 kN/m). Fig. 4.17.b and Fig. 4.18 show that in Calculation1 the stresses are underestimated and the moments (Table 4.2) are around 3% less in sagging zone and 6% less on hogging zone. This difference is mostly due to the "continuous" contact that increases the stud slip in *Calculation 2* and not in *Calculation 1*.In Fig. 4.19 are plotted the stud-slip curves for both calculations, maximum differences are observed in the zones that are mostly subjected to a "continuous" contact (at each side of intermediate support and near the end-supports – see Fig. 4.16).

4.5 Conclusion

The finite element model (with 6 degrees of freedom per node) for steel-concrete composite beams presented in this research has been developed in order to solve the problem of contact at the steel-concrete interface using the Augmented Lagrangian Method. The first numerical example is provided to assess the accuracy and robustness of the proposed formulation by comparison to experimental test results to confirm the reliability of the model. A new concept (FNC) has been proposed to take into account the continuous contact that sometimes occurs for special loading cases. The proposed method is easy to compute and to include in the algorithm of the Augmented Lagrangian Method. The second numerical simulation is proposed to show the influence of the FNC on some design variables. Main conclusions for the present work could be summarized as follows:

- The numerical simulation shows that the "*old*" model of the program "*Pont-mixte*" (with 4 degrees of freedom per node) could not take into account the real behaviour at the steel-concrete interface. Consequently, the comparison with experimental results was not satisfactory especially for high load level and under concentrated loads as-well-as at intermediate support. The separation between the slab and the steel beam degrees of freedom appears necessary, the "*new*" model with 6 degrees of freedom per node is then proposed.

- Contact algorithm based on ALM is well-adapted for composite structures and appears easy to compute and the convergence is relatively fast. The practical organization of the system given in Fig. (4.5) permits to avoid the node-renumbering of the system. The comparison between "without" or "with" ALM algorithm highlights the "critical" zones in the continuous beam where the unrealistic penetration of the concrete slab in the steel beam occurs and then is corrected by the use of ALM algorithm. It is pointed out that the uplift obtained when the calculation does not take into account the ALM algorithm is also unrealistic and is corrected by the use of ALM algorithm.

- The proposed model solves the node-to-node contact that is enough accurate in case of concentrated loads. Nevertheless, for distributed loads, the contact becomes more continuous and then the model should include the *FNC*. The example presented in this work shows that the loading capacity of the beam could be lower than the one predicted by a calculation without *FNC* (about 6% in this example). This percentage even if it remains relatively low, should be taken into account during the design of the beam because it could be not neglectable for other loading cases (for example asymmetrical distributed load on the beam). Nevertheless, more numerical simulations and experimental tests should be carried out to conclude on practical purposes.

- Solving contact problem at the steel-concrete interface has an influence on the design variables especially on the stud slip. It could be interesting to study its influence on the degree of connection in order to optimize the connection design.

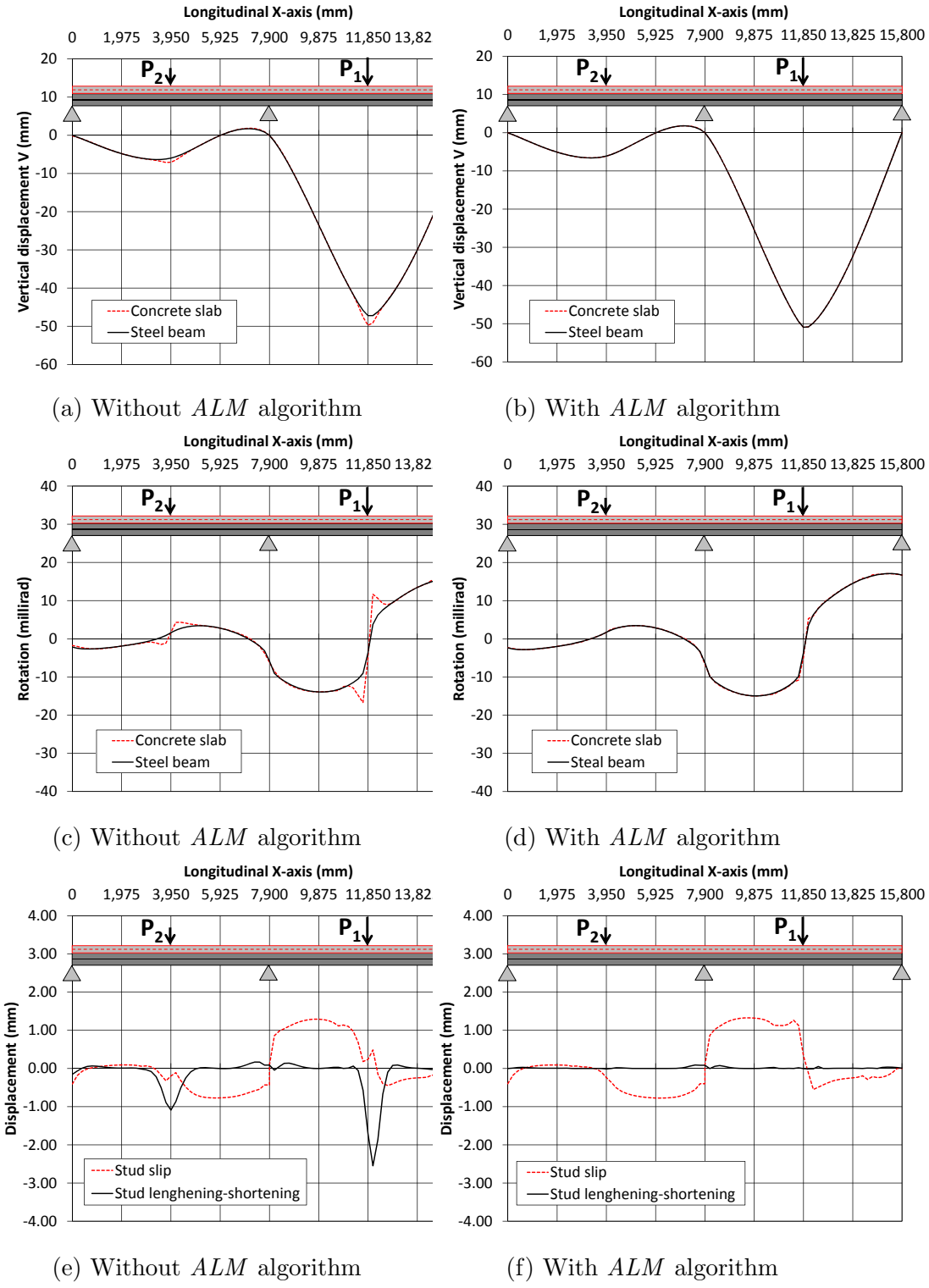

(a) Without *ALM* algorithm

(b) With *ALM* algorithm

(c) Without *ALM* algorithm

(d) With *ALM* algorithm

(e) Without *ALM* algorithm

(f) With *ALM* algorithm

Figure 4.13: (a,b) Comparison of the vertical displacement. (c,d) Comparison of the cross-section rotation. (d,e) Comparison of the stud slip and the stud lengthening-shortening.

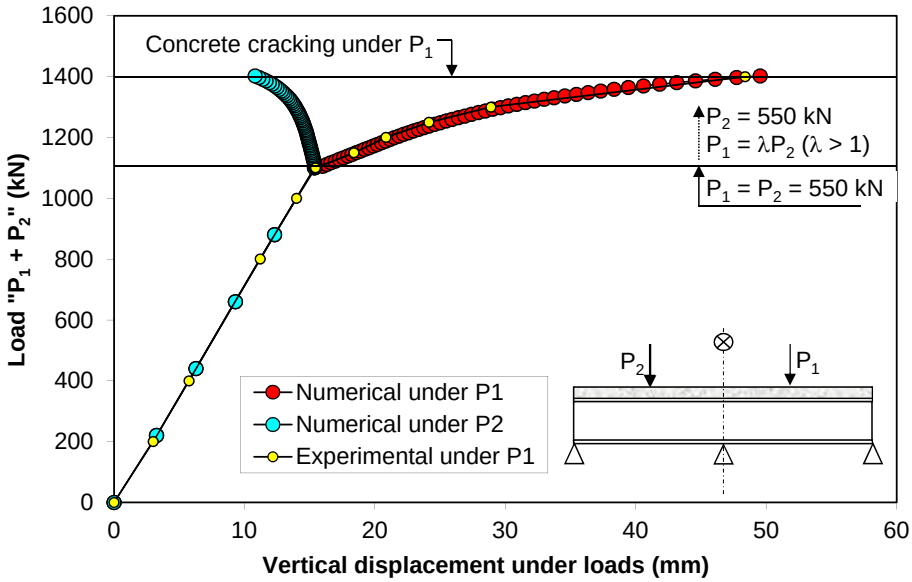

Figure 4.14: Comparison of deflexions – with *ALM* algorithm

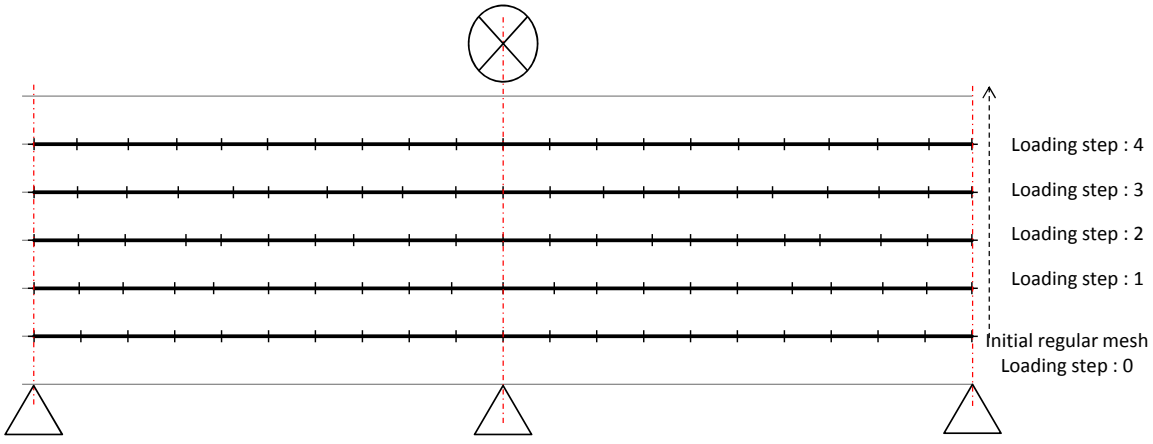

Figure 4.15: Successive beam meshes.

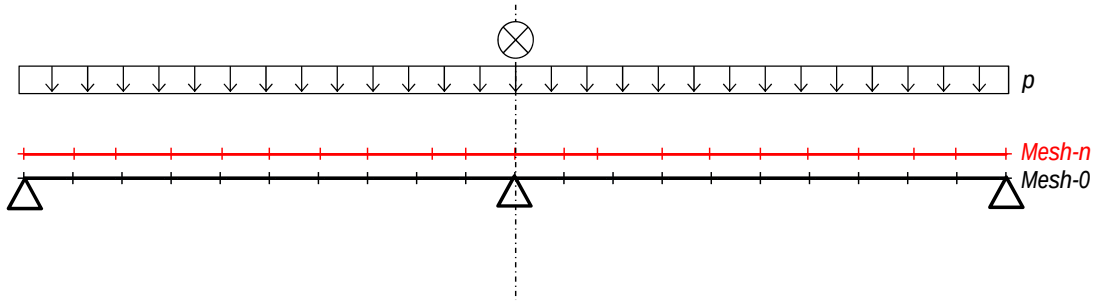

Figure 4.16: Comparison between initial and final mesh.

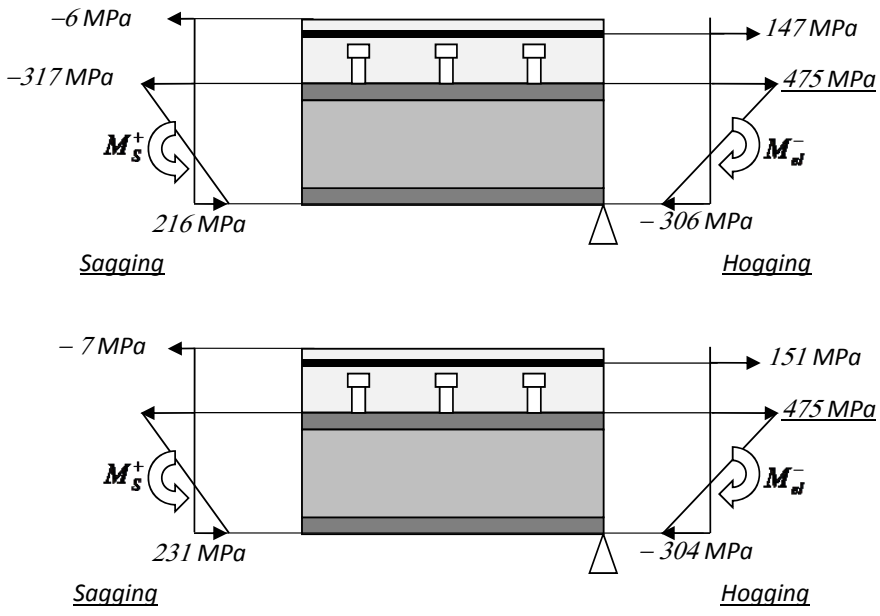

Figure 4.17: (a) Stress distribution in sagging and hogging cross-sections *Calculation1* (*ALM*)– $\mathbf{p = 280\ kN/m}$. (b)Stress distribution in sagging and hogging cross-sections *Calculation2* (*ALM + FNC*) – $\mathbf{p = 264\ kN/m}$.

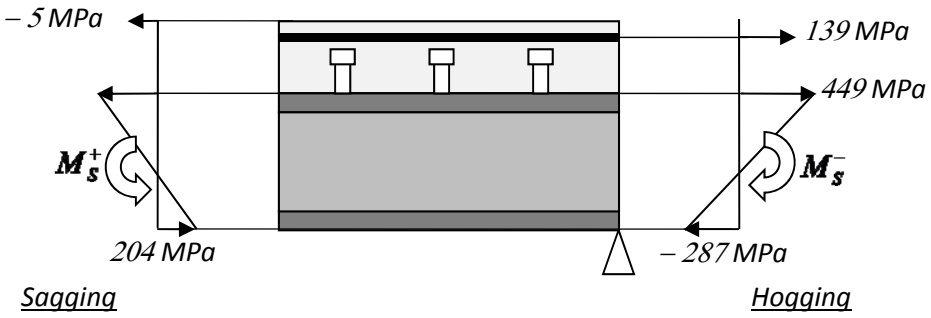

Figure 4.18: Stress distribution in sagging and hogging cross-sections *Calculation1 (ALM)* – $\mathbf{p = 264\ kN/m}$.

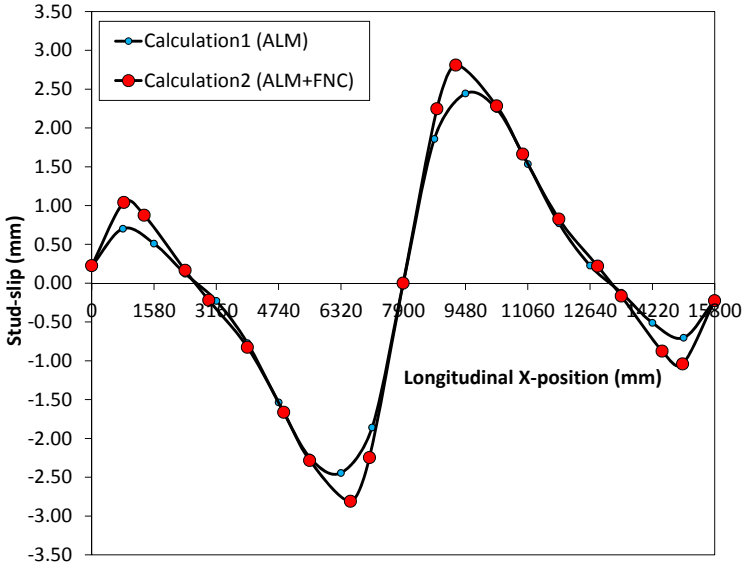

Figure 4.19: – Influence of the *FNC* on the stud-slip – $\mathbf{p = 264\ kN/m}$.

Bibliography

***

[1] Guezouli S. and Yabuki T. "Pontmixte" a User Friendly Program for Continuous Beams of Composite Bridges. International Colloquium on Stability and Ductility of Steel Structures (SDSS'06), Lisbon, September 6-8 2006.

[2] Huang Z., Burgess I.W. and Plank R.J. Nonlinear Analysis of Reinforced Concrete Slabs Subjected to Fire. Structural Journal, Vol. 96, Issue 1, January 1999.

[3] Huang Z., Burgess I.W. and Plank R.J. Modeling Membrane Action of Concrete Slabs in Composite Buildings in Fire. Journal of Structural Engineering, Vol. 129, Issue 8, August 2003.

[4] Amilton R. da Silva and João Batista M. de Sousa Jr. A family of interface elements for the analysis of composite beams with interlayer slip. Journal of Finite Elements in Analysis and Design, Vol. 45, Issue 5, April, 2009.

[5] João Batista M. de Sousa Jr. and Amilton R. da Silva Analytical and numerical analysis of multilayered beams with interlayer slip Journal of Engineering Structures, Vol. 32, $n°6$, 2010, pp. 1671-1680.

[6] Qureshi J., Lam D. and Ye J, Effect of shear connector spacing and layout on the shear connector capacity in composite beams. Journal of Constructional Steel Research, 67 (2011) 706-719.

[7] Kloosterman G. Contact methods in finite element Simulations. Proefschrift Enschede – Met lit. opg. – Met samenvatting in het Nederlands. ISBN 90-77172-04-1.

[8] Cavalieri F.J., Cardona A., Fachinotti V.D. and Risso J., A finite element formulation for nonlinear 3D contact problems. Mecanica Computacional, Vol. XXVI, pp. 1357-1372.

[9] Gara F., Ranzi G. and Leoni G. Displacement - based formulation for composite beams with longitudinal slip and vertical uplift. International Journal for Numerical Methods in Engineering 2006, 65(8) 1197-1220.

[10] Wriggers P. Computational Contact mechanics, Second edition. Springer-Verlag Berlin Neidelberg 2006, Printed in the Netherlands.

[11] Krofli A., Planinc I., Saje M., Turk G. and Cas B. Non-linear analysis of two layer timber beams considering interlayer slip and uplift. Journal of Engineering Structures, 2010.02.009.

[12] Krofli A., Saje M. and Planinc I. Non-linear analysis of two layer timber beams with interlayer slip and uplift. Journal of Computational Structures 2011.06.007.

[13] Robinson H. and Naraine K.S. Slip and uplift effects in composite beams, Proceedings of the Engineering Foundation Conference on Composite Construction (ASCE), 1988, pp. 487-497.

[14] Weyler R., Oliver J., Sain T. and Cante J.C. On the contact domain method: A comparison of penalty and Lagrange multiplier implementations. Computer Methods in Applied Mechanics and Engineering 205-208 (2012) 68-82.

[15] Oliver J., Hartmann S., Cante J.C., Weyler R. and Hernàndez J.A. A contact domain method for large deformation frictional contact. Problems, Part 1: Theoretical basis. Computer Methods in Applied Mechanics and Engineering 198 (2009) 2591-2606.

[16] Guezouli S., Hjiaj M. and Nguyen Q.H. Local buckling influence on the moment redistribution coefficient for composite continuous beams of bridges. The Baltic Journal of Road and Bridge Engineering (BJRBE), 2010, Vol.5, $n^{\circ}4$, pp. 207-217.

Chapter 5

Summary and Conclusion

***

We have developed in this thesis some computational tools for steel and steel-concrete composite structures of buildings and bridges.

The bibliographic study allowed us to review the state of the art concerning the component-based method and its performance in order to estimate the behavior of a bolted end-plate connection. This method is easy to compute and it has been the subject of various research during the last decade for finally been adopted in the design standard (Eurocode). It appears that different variants of the model have been developed this last decade for such type of connection. Under monotonic loading, these purposes allow to predict efficiently the Moment-Rotation curve of an isolated joint. However, the response of the connection under cyclic loading remains in progress. This field interests the research because of the performance of this semi-rigid connection, especially in seismic zones.

Therefore, in this work, we focus our attention on the cyclic response of the bolted end-plate connection by improving existing component-based model on one hand and deepen the well-known method of plastic hinges, on the other hand. Firstly, we concentrated our attention on the improvements that we considered necessary to take into account in the component-based model. Beginning by "purely steel" connection subjected to a cyclic rotation, we took into account the separation between the end-plate and the column flange by making appropriate changes in the behavior of each component within the joint. After that, for the most frequent case of two bolt-rows, if the group resistance could arise (in addition

to the individual resistances of each bolt-row), an elastoplastic formulation of the model proposed by Cerfontaine has been developed. It is highlighted that the group effect has a significant influence on the post-elastic behavior of the connection.

The proposed component-based model leaded to a finite element of joint with zero-length and appropriate degrees of freedom in order to be finally assembled with a beam finite element. The new macro-finite element consists of a beam finite element with one finite element of joint connected at each end. A numerical study has been carried out on a steel beam-to-column flush end-plate connection subjected to axial force and bending moment. The results present the ability of this model to capture the joint response and the influence of the axial force on the moment-rotation curve.

In the second stage, we followed the study by assuming plastic hinges at each end of the steel beam. This method is well-known and has its limits. Our objective was to make some numerical simulations in order to highlight the influence of the form of the yield surface on the bearing capacity of a framed structure. The yield surface defined in the plane (M-N) with M as the bending moment and N the axial force in the considered cross-section, can take different forms depending on the value given to a factor q so-called "roundness factor". It has been shown that the influence of the rolled factor has a significant influence on the membrane effect in large displacements as well as on the bearing capacity. Moreover, in cyclic behavior of an isostatic beam, the effect of this factor has been also observed on the pinching effect and also on the softening of the cyclic curve. Finally, the model tested with or without (M-N) interaction on framed structures shown that the bearing capacity depends on the number of frames in the structure.

In the third stage of this work, it has been proposed to connect a steel-concrete composite beam to the proposed model of connection developed in the first stage. This work requiring validations at different levels of the modeling, it was agreed to start by proposing an efficient model of composite beam (with 6 dof per node) in small displacements taking into account the material nonlinearity of the beam as well as the contact between the steel and the concrete. The approach using the

augmented Lagrangian method has been chosen for its rapidity with respect to the penalty method. The improvements made in this study mainly concerned the improvements made to include a continuous contact within the composite finite element by means of an adaptive mesh. This approach so-called "Flying Node Concept" gave more realistic results than those obtained with a unilateral contact approach.

In parallel, a simplified composite beam model (4 ddl per node) which does not take into account the contact between materials but only the slip at their interface, has been developed to test the assembly with the proposed joint model developed in the first section. This development includes only 2 non-linearities (material and geometrical) leaving out the third non-linearity that the contact could produce. This assumption, allows to make calculations in large displacements insuring a relative good convergence of the iterative process. This model has been presented in the Appendix of this thesis and is currently the subject of some numerical simulations for validation.

It will be appropriate in the immediate perspective to finalize a relatively "complete" model of steel-concrete composite beam in large displacements taking into account the contact and ready to be assembled to the proposed component-based model. The obtained macro-element will be easily used to carry out any structural analysis in large displacements. This model will be easy to compute and will give more accurate results than those obtained at this day.

In a more distant perspective, numerical simulations have to be envisaged on different framed structures with dissipative bolted connections in large displacements in order to achieve the validation of the proposed model. Experimental (small scale) experiments have to be planned at this stage.

Appendices

Appendix A

Composite joint

***

The composite joint is a result of the combination between steel connection and reinforcement slab. The analytical behavior of a beam-to-column composite joint (moment –rotation curve) can be evaluated depending on the component method that adopted by EC3 and EC4. Actually, the same procedure that used in the steel joint will be used for the composite joint. We can consider the steel joint as a particular case of the composite joint. Therefore, the same mechanical model, as in steel connection, with additional rows, for reinforcement slab component, will be used to derive the relationship between local forces and its corresponded deformations for an isolated composite connection.(See Fig A.1)

As depicted in Fig A.1 a component based model for an isolated composite joint, each components of the joint are simulated by a nonlinear springs. The two parts of the composite joint are not connected.

The slab part composite of reinforcement steel bar and concrete, herein each steel bar is represented by a nonlinear spring that will be activated in tension and compression. In the other hand, the concrete part is divided in several fibers and they work just in compression.

The second part represents the steel joint which have been study obviously. It consists of bot-rows and beam flange rows.

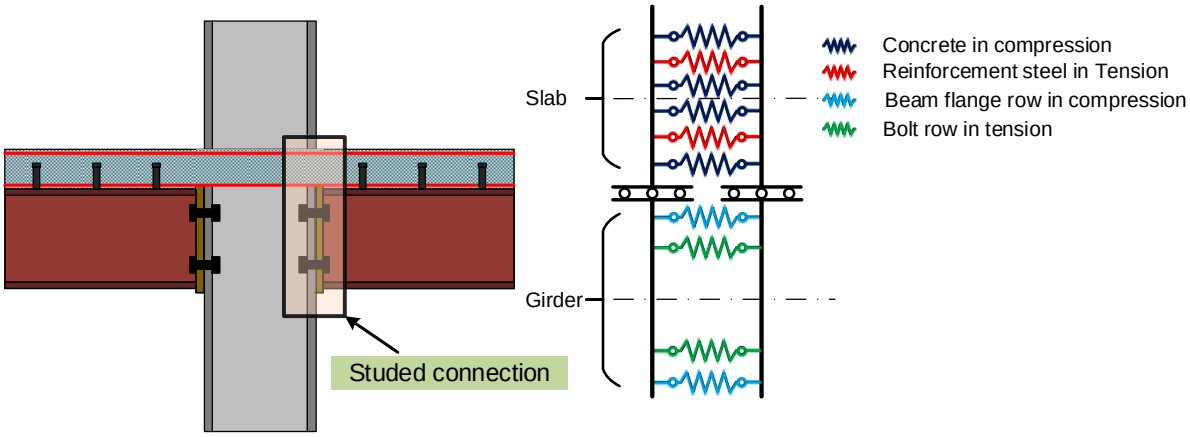

(a) Double sided composite joint configuration (b) Mechanical model – Initial configuration

Figure A.1: Composite joint and its corresponding mechanical model

A.1 Composite joint element formulation

The composite joint element is a zero-length element, it consists of rigid bars and extensional springs (Fig. A.2). the local displacement of this element can be written as:

$$\boldsymbol{U}_l = \begin{bmatrix} \bar{u}_{g1} & \bar{u}_{s1} & \bar{\theta}_1 & \bar{u}_{g2} & \bar{u}_{s2} & \bar{\theta}_2 \end{bmatrix}^T \tag{A.1}$$

The local force vector is given as

$$\boldsymbol{f}_l = \begin{bmatrix} \bar{N}_{g1} & \bar{N}_{s1} & \bar{M}_1 & \bar{N}_{g2} & \bar{N}_{s2} & \bar{M}_2 \end{bmatrix}^T \tag{A.2}$$

The deformation of each component of the reinforcement steel is defined by

$$\boldsymbol{\delta_{rs}} = \bar{u}_{s2} - y_{rs}\bar{\theta}_2 - \bar{u}_{s1} + y_{rs}\bar{\theta}_1 = \begin{bmatrix} 0 & -1 & y_{rs} & 0 & 1 & y_{rs} \end{bmatrix} \boldsymbol{U}_l \tag{A.3}$$

In which y_{rs} is the distance between the reinforcement steel component and $\Delta^{(s)}$.

Following the same procedure for determining the concrete slab component deformation, we can write

$$\boldsymbol{\delta_c} = \bar{u}_{s2} - y_c\bar{\theta}_2 - \bar{u}_{s1} + y_c\bar{\theta}_1 = \begin{bmatrix} 0 & -1 & y_c & 0 & 1 & y_c \end{bmatrix} \boldsymbol{U}_l \tag{A.4}$$

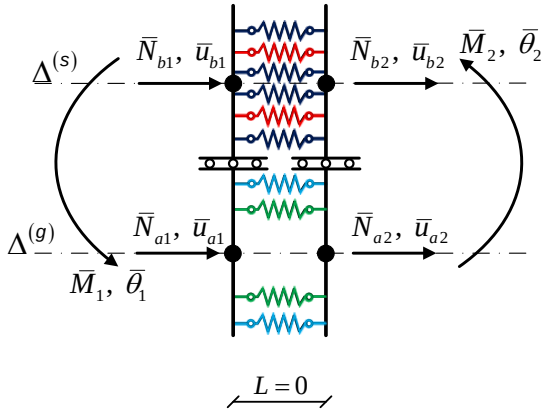

Figure A.2: Non connected mechanical model of composite joint

Where y_c is the distance between the concrete slab component and $\Delta^{(s)}$.

For the steel part component, the deformation is given respectively for bolt-rows and bottom/top beam flange as

$$\bar{\boldsymbol{u}}_{T3} = \bar{u}_{g2} - y_{T3}\,\bar{\theta}_2 - \bar{u}_{g1} + y_{T3}\,\bar{\theta}_1 = \begin{bmatrix} -1 & 0 & y_{T3} & 1 & 0 & -y_{T3} \end{bmatrix} \boldsymbol{U}_l \tag{A.5}$$

Where y_{T3} is the distance between the bolt-rows component and $\Delta^{(g)}$.

$$\bar{\boldsymbol{u}}_{T2/T4} = \bar{u}_{g2} - y_{T2/4}\,\bar{\theta}_2 - \bar{u}_{g1} + y_{T2/4}\,\bar{\theta}_1 = \begin{bmatrix} -1 & 0 & y_{T2/4} & 1 & 0 & -y_{T2/4} \end{bmatrix} \boldsymbol{U}_l \tag{A.6}$$

Where $y_{T2/4}$ is the distance between the top/bottom beam flange component and $\Delta^{(g)}$.

Depending on the virtual work theorem, the local stiffness matrix for composite joint element is given as follows

$$\boldsymbol{K}_l = \begin{bmatrix} k_{11} & 0 & -k_{13} & -k_{11} & 0 & k_{13} \\ 0 & k_{22} & -k_{23} & 0 & -k_{22} & k_{23} \\ -k_{13} & -k_{23} & k_{33} & k_{13} & k_{23} & -k_{33} \\ -k_{11} & 0 & k_{13} & k_{11} & 0 & -k13 \\ 0 & -k_{22} & k_{23} & 0 & k22 & -k23 \\ k_{13} & k_{23} & -k_{33} & -k13 & -k23 & k33 \end{bmatrix} \tag{A.7}$$

In which

$$
\begin{aligned}
k_{11} &= \sum k_{T3} + \sum k_{T2/4} \\
k_{13} &= \sum y_{T3}\ k_{T3} + \sum y_{T2/4}\ k_{T2/4} \\
k_{22} &= \sum k_{rs} + \sum k_c \\
k_{23} &= \sum y_{rs}\ k_{rs} + \sum y_c\ k_c \\
k_{33} &= \sum y_{T3}^2\ k_{T3} + \sum y_{T2/4}^2\ k_{T2/4} + \sum y_{rs}^2\ k_{rs} + \sum y_c\ k_c^2
\end{aligned}
$$

where k_{T3} and $k_{T2/4}$ are equivalent stiffnesses of the bolt-row and the top/bottom beam flange respectively. k_{rs} and k_c are the stiffnesses of the concrete and the reinforcement steel component successively .

In order to study an isolated composite joint we have to added, as in the composite concrete structure, connectors at the nodes. The connectors tied the two parts of the composite joint and make them work together. As known, the connector resists the shear forces at the interface therefore its stiffness is related to the slipping magnitude that can be written as follows:

$$R^{ss} = k^{ss}\ d^{ss} \tag{A.8}$$

where k^{ss} represents discrete connection stiffness. and d^{ss} is the slip at the interface steel-concrete.

As the two parts of the joint element have the same rotations, the produced slip between them at the node 1 is given as

$$d^{ss} = \bar{u}_{g1} - \bar{u}_{s1} - d\ \bar{\theta}_1 = \begin{bmatrix} 1 & -1 & d \end{bmatrix} \begin{bmatrix} \bar{u}_{g1} \\ \bar{u}_{s1} \\ \bar{\theta}_1 \end{bmatrix} \tag{A.9}$$

In which d is the distances between $\Delta^{(s)}$ and $\Delta^{(g)}$.

A.1.1 Stiffness matrix of the connector element

The connection between the two parts of an isolated joint will be simulated by a specific element with zero-length but it has a significant stiffness.

Substitute Eq. (A.9) into Eq. (A.8) gives

$$R^{ss} = k^{ss} \begin{bmatrix} 1 & -1 & d \end{bmatrix} \begin{bmatrix} \bar{u}_{g1} \\ \bar{u}_{s1} \\ \bar{\theta}_1 \end{bmatrix} \tag{A.10}$$

In the other side the vector force corresponding the node 1 is defined by.

$$\boldsymbol{f}_1^{ss} = \begin{bmatrix} \bar{N}_{g1} & \bar{N}_{s1} & \bar{M}_1 \end{bmatrix}^T \tag{A.11}$$

Using the virtual work theorem gives the connector stiffness matrix related to node 1

$$\boldsymbol{K}_1^{ss} = k^{ss} \begin{bmatrix} 1 & -1 & d \\ -1 & 1 & -d \\ d & -d & d^2 \end{bmatrix} \tag{A.12}$$

Following the same procedures for the connector stiffness at node 2 produces

$$\boldsymbol{K}_2^{ss} = k^{ss} \begin{bmatrix} 1 & -1 & d \\ -1 & 1 & -d \\ d & -d & d^2 \end{bmatrix} \tag{A.13}$$

Combined Eqs. (A.7),(A.12) and (A.13) gives the local stiffness for connected composite joint element

$$\boldsymbol{K}_j = \boldsymbol{K}_l + \boldsymbol{K}_1^{ss} + \boldsymbol{K}_2^{ss} \tag{A.14}$$

It is worth to indicate that assembling this composite joint element with a composite beam element do not need to add the connectors stiffness at the composite joint element because they have already considered in the composite beam element. (See Fig. A.3)

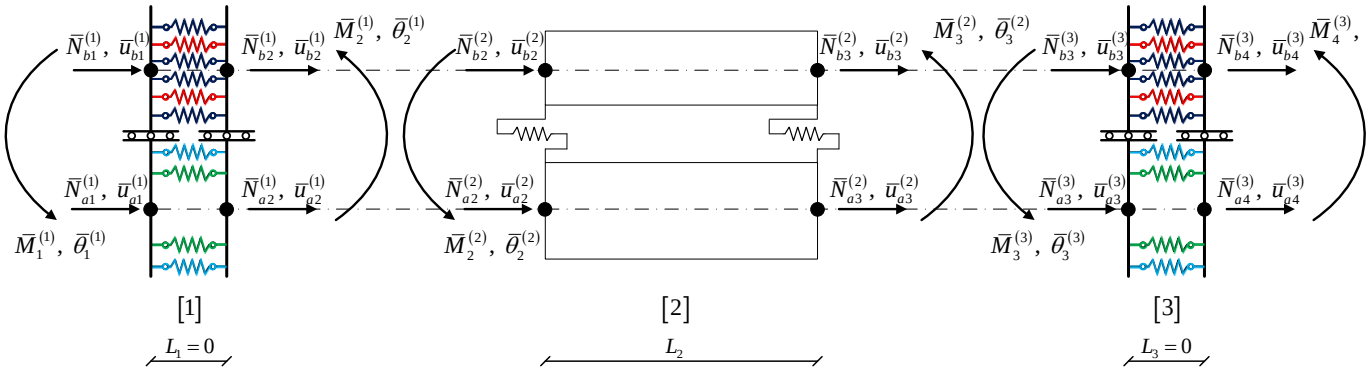

Figure A.3: Composite joint beam element

Chapter 6

Résumé en français

***

L'analyse de la réponse globale du comportement des structures métalliques et mixtes (acier-béton) en régime élastique a vu ces dernières années un développement très significatif autant sur le plan expérimental que sur le plan de la modélisation numérique. Ces structures destinées aux bâtiments ou aux ouvrages d'art (ponts) se doivent d'assurer deux propriétés fondamentales : résistance et ductilité. Beaucoup d'aspects restent néanmoins encore mal compris et risquent d'affecter la pérennité de l'ouvrage d'une part et le coût de sa construction, d'autre part.

Dans le cadre de ce travail de recherche, nous proposons d'apporter des solutions par le biais de modèles simples à certains de ces phénomènes qui ont été réellement observés aussi bien lors d'essais expérimentaux que lors des simulations numériques tridimensionnelles avancées. Une bonne modélisation se doit de reproduire le plus fidèlement possible le comportement de ces structures et de leurs assemblages afin d'assurer un acheminement correct des efforts autant sous chargement monotone que sous chargement cyclique.

Le travail de thèse comprend 3 parties qui correspondent chacune a un article scientifique.

6.1 Première partie de la thèse

On s'intéresse tout d'abord aux assemblages métalliques poteau-poutre de bâtiment de type boulonné avec platine d'extrémité. La performance de ce type d'assemblage a déjà été prouvée par différentes recherches et confirmée par une multitude d'essais expérimentaux. Cet assemblage assure une connexion semi-rigide très appréciée dans le cas d'un chargement cyclique grâce à son caractère dissipatif, son aspect économique et enfin, la simplicité de son exécution (Fig. 6.1). L'avantage d'adopter des assemblages semi-rigides au lieu d'assemblages articulés permet de modifier non seulement les sollicitations introduites dans la structure en acier mais aussi les déplacements. Cette étude est menée dans le

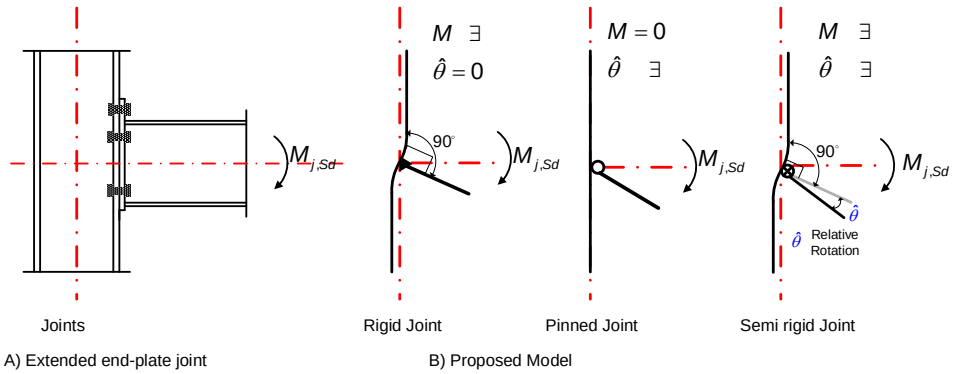

Figure 6.1: Des modèles adoptés pour l'assemblage.

cadre d'un projet de recherche européen intitulé ROBUSIMPACT mettant en collaboration: Universität Stuttgart, Université de Liège, Università degli Studi di Trento, Rheinisch Westfälische Technische Hochschule Aachen, ArcelorMittal Belval & Differdange S.A, MS3 Materials & Systems for Safety & Security and Institut National des Sciences Appliquées Rennes. Ce projet Européen s'étendait sur une durée de 36 mois à partir du 01/07/2012. L'objectif était de réaliser des essais expérimentaux d'une part et de proposer des modèles numériques d'autre part pour étudier des structures en portiques ayant perdu un poteau intérieur ou de périphérie suite à un impact. La robustesse de la structure est le mot clé de

l'étude. Notre équipe de Recherche avait la responsabilité sur 2 thèmes du projet :

- WP5 : Residual strength of impacted vertical members -numerical and analytical investigations.

- WP8: Development of a new joint element.

La première partie de la thèse concerne les développements proposés dans le cadre du WP8.

Afin d'aborder au mieux ce thème de recherche, nous avons tout d'abord consulté la bibliographie pour comprendre la première approche qui consiste à développer des modèles analytiques et mathématiques qui lissent au mieux les courbes (Moment-Rotation) obtenues expérimentalement. Cette première approche dépendra toujours de la configuration de l'assemblage étudié. Il faudra toujours calibrer les paramètres dont dépendent les modèles. Par la suite, bien que trop fastidieux, le développement de modèles numériques 3D ou parfois 3D simplifiés, s'est avéré comme une étape incontournable pour identifier des aspects locaux du comportement au sein de l'assemblage. Ces aspects aussi confirmés par des essais expérimentaux devraient être pris en compte lors du dimensionnement de ce type d'assemblage. Cette seconde approche est donc utile pour identifier les phénomènes particuliers du comportement mais ne peut être appropriée pour un calcul de structure à l'échelle réelle en raison du temps de calcul important qui en découle. Enfin, dans le but de proposer un modèle d'assemblage qui soit facilement programmable à des fins de calcul de structures à échelle réelle, nous profitons des informations recueillies des deux précédentes approches pour nous axer sur l'approche par un modèle mécanique. L'objectif est donc de proposer un modèle mécanique basé sur la méthode des composantes bien connue aujourd'hui car adoptée par les Eurocodes (EC3 et EC4). Le modèle mécanique à développer doit être adapté à une formulation par éléments finis (E.F.) afin que l'assemblage proposé puisse être facilement "connecté" aux éléments de poutres et poteaux de la structure (E.F. de type poutre). Cette troisième approche est donc un bon compromis qui peut allier "simplicité" et performance sous réserve que les aspects

identifiés lors des essais expérimentaux et dans les modèles 3D soient correctement pris en compte.

En effet, les aspects auxquels nous nous intéressons sont :

- La séparation entre la platine d'extrémité et la semelle du poteau (nommé "gap"). Ce phénomène est bien identifié lors d'un comportement cyclique de l'assemblage mais n'a jamais été pris en compte.

- Le comportement de groupe (de deux ou plusieurs rangées de boulons) qui vient se greffer au comportement individuel de chaque rangée. Cet aspect est aussi à inclure dans le comportement global de l'assemblage autant sous chargement monotone que cyclique.

Le travail proposé dans le cadre de ce thème est le développement d'un modèle mécanique qui combine la méthode des composantes et la formulation par éléments finis. Ce modèle s'inspire de la diversité des modèles mécaniques à composantes déjà proposés par différents chercheurs dans la littérature. Il inclue en plus la prise en compte du gap ainsi que de l'effet de groupe. L'objectif est d'obtenir un nouvel élément fini d'assemblage semi-rigide aussi bien facile à programmer que performant. Cette étude est réalisée pour des assemblages métalliques et est étendue aux assemblages mixtes (poutre mixte et poteau métallique).

6.1.1 Description du modèle mécanique

Le modèle mécanique à composantes considéré (Fig. 6.2) reprend l'effet de chaque composante individuelle (Tabel 6.1) dans le comportement global de l'assemblage. Certaines de ces composantes résistent à la traction et sont regroupées en composante-Type équivalente (Type 3) alors que d'autres composantes résistent à la compression et sont regroupées aussi en composante-Type équivalente (Type 2 ou Type 4). Les composantes-Types 3 sont localisées au niveau de chaque rangée de boulons, la composante-Type 2, est localisée au niveau de la semelle supérieure de la poutre connectée et la composante-Type 4 est localisée au niveau de la semelle inférieure de la poutre connectée. Lorsque l'assemblage est soumis à un moment positif, la

composante-Type 2 est active ainsi que toutes les composantes-Type 3 qui subissent une traction. Sous moment négatif, le processus s'inverse, la composante-Type 4 est active avec toutes les composantes-Type 3 qui subissent une traction. Dans le cas particulier d'une traction simple, toutes les composantes-Type 3 sont actives et dans le cas d'une compression simple, seules les composantes-Type 2 et Type 4 sont alors actives.

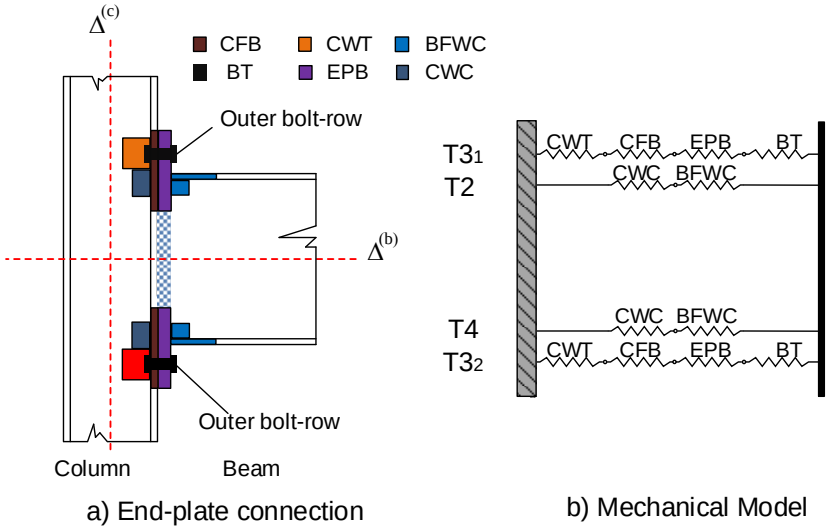

Figure 6.2: Modèle mécanique

6.1.2 Comportement cyclique de l'assemblage boulonné à platine d'extrémité

Avant d'aborder le phénomène de séparation entre la platine d'about et la semelle de poteau "gap", il convient de localiser cette séparation et de l'identifier par le bais de la notion de "T-stub". En réalité, la traction est transmise à l'assemblage par le biais de la partie tendue de la poutre à travers la platine d'about. L'effort de traction va solliciter certaines rangées de boulons en fonction de leurs positions par rapport au centre de rotation de l'assemblage.

Table 6.1: Liste et effet des différentes composantes

Symbols	**Components**
CWT	Beam Web in Tension
CFB	Column Flange in Bending
EPB	End-Plate in Bending
BWT	Beam Web in Tension
BT	Bolt in Tension
CWC	Column Web in transverse Compression
BFWC	Beam or column Flange and Web in Compression

Tant que tous les éléments sollicités en traction restent dans leurs domaines élastiques, toute séparation (négligeable ou quasi-nulle) entre la platine d'about et la semelle du poteau est aussitôt résorbée. Par contre, lorsqu'au moins un élément ,parmi les éléments suivants: semelle de poteau, platine d'extrémité et le boulon, migre vers le domaine plastique, les déformations plastiques engendrées provoquent l'apparition de "gap" permanents. Ce phénomène s'accentue et se cumule lorsque l'assemblage est soumis à un chargement cyclique aussi bien en partie haute qu'en partie basse de celui-ci. Il convient néanmoins de préciser que bien que ce gap soit localisé au niveau de la semelle tendue, il sera pris en considération dans le modèle au niveau des rangées de boulons qui sont susceptibles de résister à la traction (Fig. 6.3).

Afin de prendre en compte ce phénomène, nous avons opté de l'inclure dans le

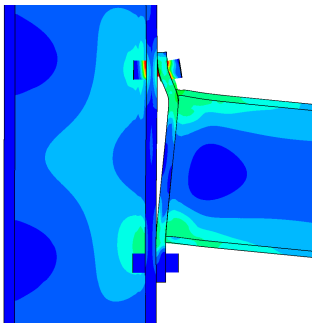

Figure 6.3: Modèle élément fini 3D - Apparition du Gap

modèle de comportement relatif à la composante équivalente Type 3 concernée. Le principe est de prévoir un glissement sur l'axe des déplacements du modèle de comportement permettant de refermer le "gap" après une décharge dans un sens avant d'activer une recharge de l'assemblage dans le sens inverse. Pour un assemblage symétrique soumis à un chargement cyclique symétrique, le "gap" en partie haute et basse seront identiques ce qui n'est pas le cas pour un assemblage asymétrique. L'hypothèse d'un glissement signifie que l'on néglige la résistance de la platine d'about déformée lors de la fermeture du "gap". Cette hypothèse est retenue tant que l'on ne peut pas quantifier cette raideur (faible mais en réalité non nulle).

6.1.2.1 Application numérique sur l'effet de gap

Afin de valider cette approche, le modèle a été appliqué à un exemple simple (Fig. 6.4) pour 2 cycles de chargement consécutifs ($\theta_{max} = \pm 8.65\ mrad$) puis ($\theta_{max} = \pm 23.05\ mrad$). Tous les aciers sont de nuance $S355$ et les boulons sont des M20. La première étape consiste à calculer les rigidités initiales ainsi que les efforts résistants pour chaque élément de l'assemblage conformément aux prescriptions de l'EC3. On rappelle que la résistance retenue pour l'assemblage est la plus faible de tous les éléments en traction et il en est de même pour la compression.

La seconde étape engage un processus itératif dont le résultat est présenté dans la Figure 6.5 qui représente la réponse de l'assemblage sous forme de courbe

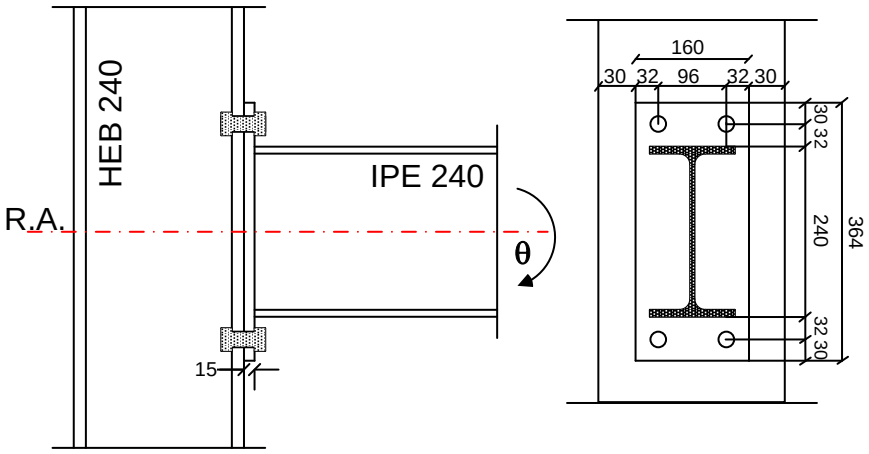

Figure 6.4: Configuration de l'assemblage traité

(Moment-Rotation) avec le traitement du "gap". On constate comme cela était prévisible, que la symétrie du comportement est retrouvée en raison de la symétrie de l'exemple traité (Fig. 6.5).

6.1.3 L'effet de groupe

Lorsqu'un assemblage boulonné comprend plusieurs rangées de boulons, le comportement de chaque élément-Type équivalent "i" présente son propre critère limite de résistance $F_{T3_i,Rd}$.

- Tant que le niveau de sollicitation de l'assemblage reste modéré (toutes les rangées se trouvent encore dans le domaine élastique), l'assemblage est alors gouverné par des critères de limites élastiques individuels et de groupe.

- Lorsque le chargement augmente (toujours dans le même sens), cette rangée de boulons peut à son tour atteindre sa limite de résistance individuelle ou de groupe.

La sollicitation de l'assemblage peut s'arrêter :

- soit par atteinte d'un chargement précis imposé

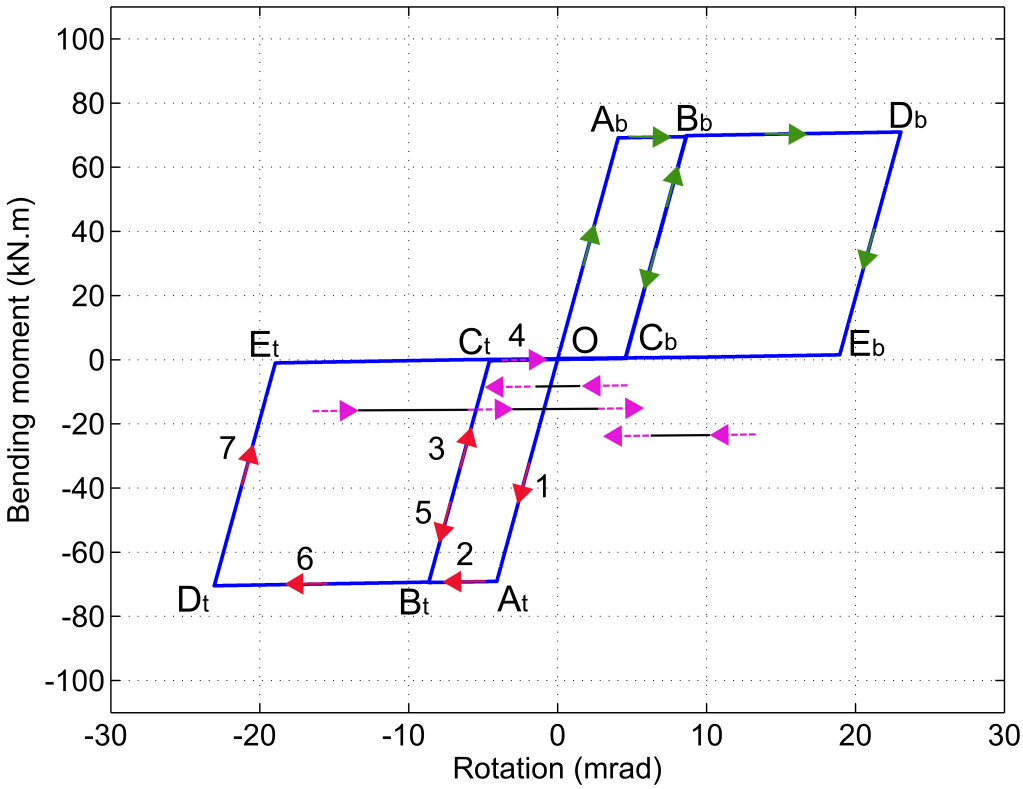

Figure 6.5: La courbe momoent - rotation

- soit par atteinte de l'un des critères de ruine imposé.

Il est claire qu'il existe des configurations d'assemblage qui peuvent activer un critère de résistance de groupe avant d'atteindre toute limite de résistance individuelle.
Prendre en compte ce critère de résistance de groupe, outre les critères de résistance individuelle, nous devons définir une surface de charge plus complexe. Cette surface de charge est d'autant plus complexe que le nombre de rangées de boulons susceptibles de générer un effet de groupe est élevé.
Dans le cadre de ce travail, nous avons adopté le modèle proposé par Cerfontaine pour prendre en compte l'effet de groupe engendré par 2 rangées de boulons. Ce cas sera étendu à plus que deux rangées de boulons. Il permet de travailler sur une surface de charge plane ce qui simplifie d'une façon significative la formulation élasto-plastique du problème.
Le principe est de projeter tout effort inadmissible sur la surface de charge après avoir localisé la zone concernée parmi celles définies sur la Fig. 6.6.

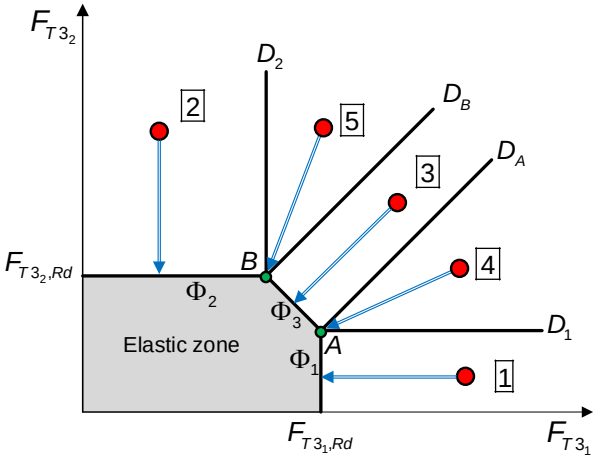

Figure 6.6: Interaction entre deux rangées de boulons

- Les zones 1 et 2 limitées par les droites D_1 et D_2 respectivement, activent l'un ou l'autre des critères individuels. La projection est normale à la partie de

la surface de charge concernée. La formulation élasto-plastique classique (algorithme tangent) engendre le calcul de l'incrément du multiplicateur de charge adéquat (λ_1 ou λ_2).

- La zone 3 délimitée par les droites D_A et D_B active le critère de groupe. La projection est normale à la partie de la surface de charge concernée. La formulation élasto-plastique classique engendre le calcul de l'incrément du multiplicateur de charge adéquat (λ_3).

- Les zones 4 et 5 délimitées par les droites (D_1 et D_A) et (D_2 et D_B) respectivement activent le critère de continuité entre un critère individuel et un critère de groupe (les points A et B respectivement). La formulation élasto-plastique classique engendre le calcul de l'incrément du multiplicateur de charge adéquat (λ_1 ou λ_2) puis le calcul de (λ_3).

6.1.3.1 Application numérique sur l'effet de groupe

Afin d'illustrer la prise en compte de l'effet de groupe, l'exemple présenté par la Fig. 6.7 est soumis à une simulation numérique. Les 2 rangées de boulons situées de part et d'autre de la semelle supérieure de la poutre connectée sont susceptibles de développer une résistance de groupe.

Comme pour tout assemblage, l'effort de résistance ainsi que la raideur initiale

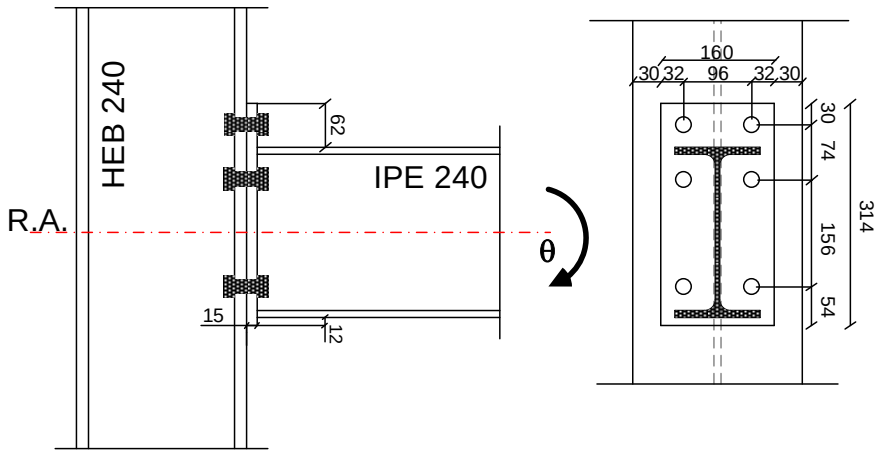

Figure 6.7: Assemblage boulonnées poutre-poteau

de chaque élément-Type équivalent sont calculés préalablement (toujours en considérant la plus faible résistance des éléments de base constituant l'élément-Type équivalent).

On observe tout d'abord sur la Fig. 6.8, qui représente la réponse de l'assemblage illustrée par la courbe (Moment-Rotation), que la prise en compte de l'effet de groupe diminue la valeur du moment résistant de l'assemblage de l'ordre de $4,8\%$ pour cet exemple. Il est clair que cette influence dépend étroitement de la configuration de l'assemblage vis-à-vis de la position et du nombre de rangées de boulons existants. D'autre part, la Fig. 6.9 montre la chronologie de l'atteinte de la surface de charge limite en fonction de l'augmentation du chargement. On observe que la plus haute rangée de boulon atteint sa limite individuelle en premier ; le critère de groupe est ensuite atteint à son tour alors que la seconde rangée de boulons et encore loin d'atteindre sa limite individuelle. On rappelle que le comportement individuel de chaque élément-Type équivalent est élasto-plastique parfait (pas d'écrouissage).

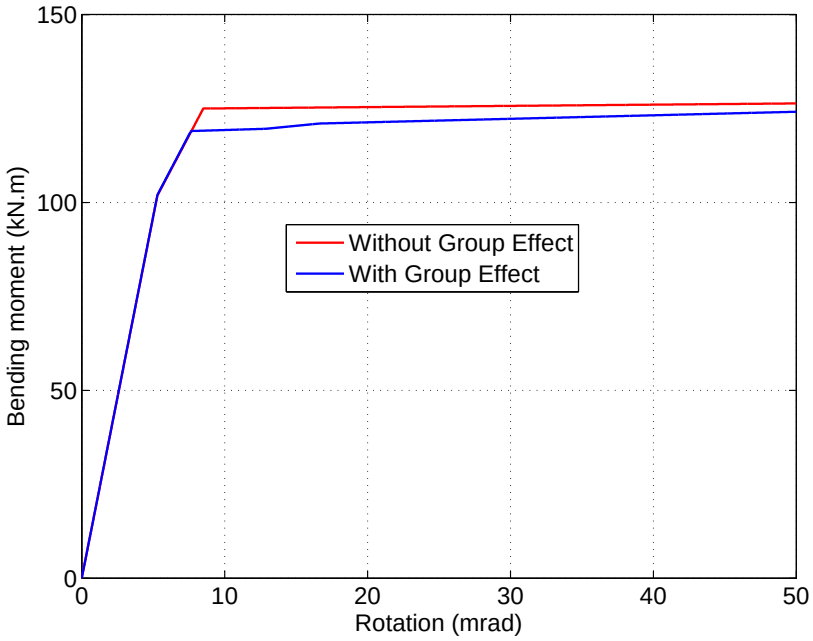

Figure 6.8: La courbe moment - rotation

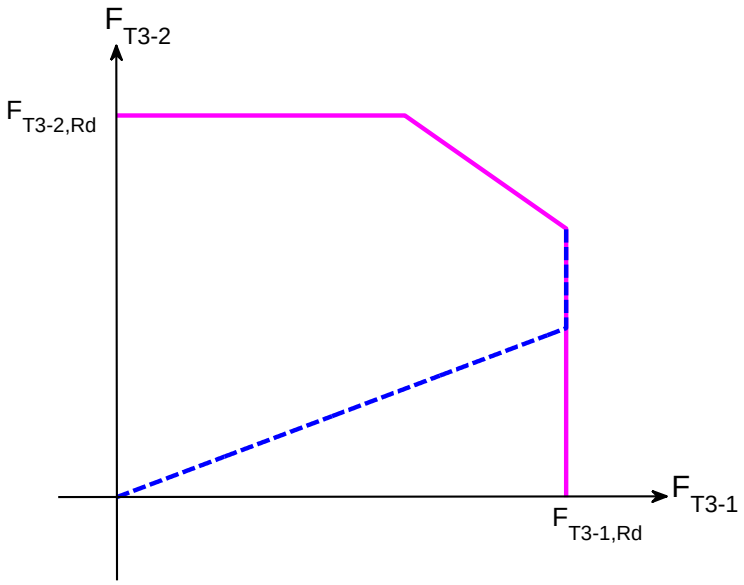

Figure 6.9: Interaction diagramme entre $(F_{T3_1} - F_{T3_2})$

6.1.4 Application numérique sur l'interaction M-N dans l'assemblage

En second exemple, on propose d'étudier le comportement de l'assemblage lié à un élément de structure : ici une poutre-console (Fig. 6.10). Cette poutre est soumise à son extrémité libre à un effort transversal F et à un effort axial N. L'assemblage ne présente que 2 rangées de boulons intérieures.

A partir de la Fig. 6.11, qui représente les courbes (Moment-rotation) de

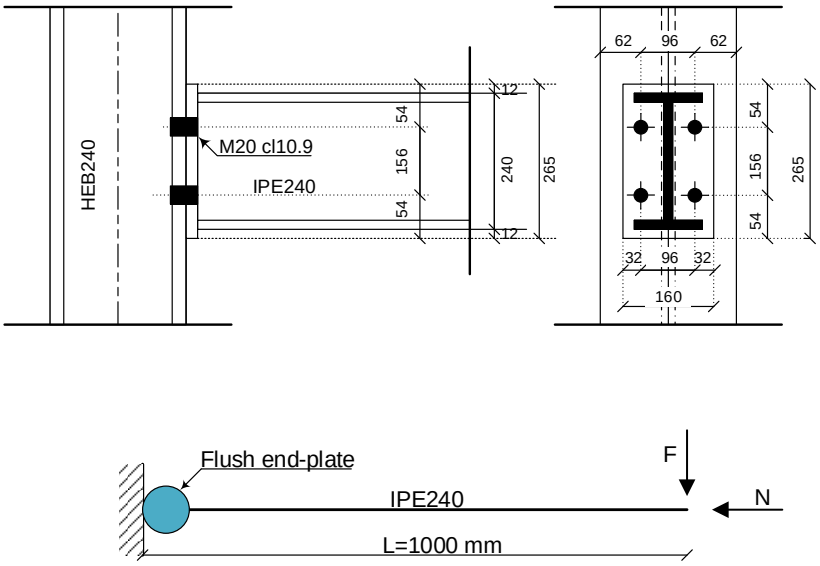

Figure 6.10: Poutre-console, assemblage avec platine non débordante

l'assemblage pour différents niveaux de compression axiale, on peut faire les observations suivantes :

i. Lorsque l'effort N est un effort de compression, le moment de flexion est supérieur au moment résistant calculé selon l'EC3. Il augmente avec l'augmentation de N mais il ne dépasse pas une limite maximale.

ii. Lorsque l'effort N est un effort de traction, le moment de flexion est inférieur ou proche du moment résistant calculé selon l'EC3.

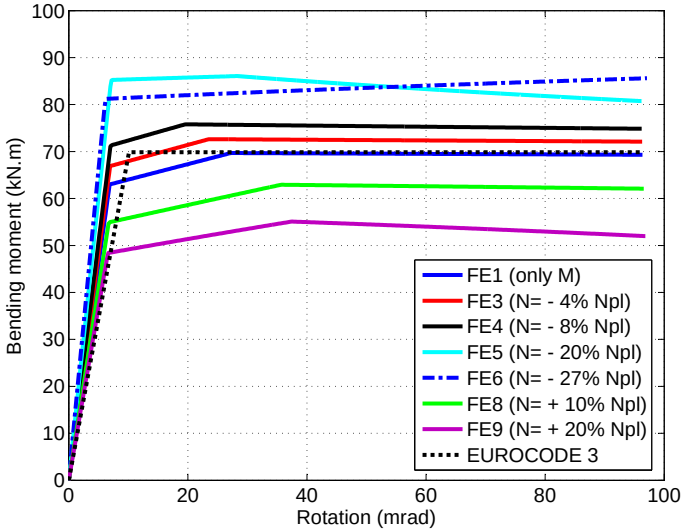

Figure 6.11: Moment-rotation

iii. Pour une flexion pure (N = 0), le moment résistant prédit par le modèle est égal au moment résistant calculé par l'EC3.

D'un autre côté, la Fig. 6.12, place tous les résultats de simulations numériques précédentes dans une représentation de diagramme d'interaction (M-N). Ce diagramme, déterminé analytiquement, représente le critère de limite de résistance de l'assemblage. On observe bien, que tous les cas calculés respectent bien ce critère limite, ce qui témoigne de l'efficacité et la performance du modèle proposé.

6.2 Seconde partie de la thèse

Elle consiste à développer un modèle de poutre avec rotules généralisées en formulation corotationnelle pour l'analyse non-linéaire (matérielle et géométrique) des structures à éléments élancés.

L'utilisation d'une procédure de condensation des *d.d.l.* internes facilite l'incorporation de cette formulation dans une approche corotationnelle classique. Le comportement plastique des rotules est contrôlé par une surface de charge qui peut prendre différentes formes selon la valeur donnée à un facteur q dit "facteur de forme".

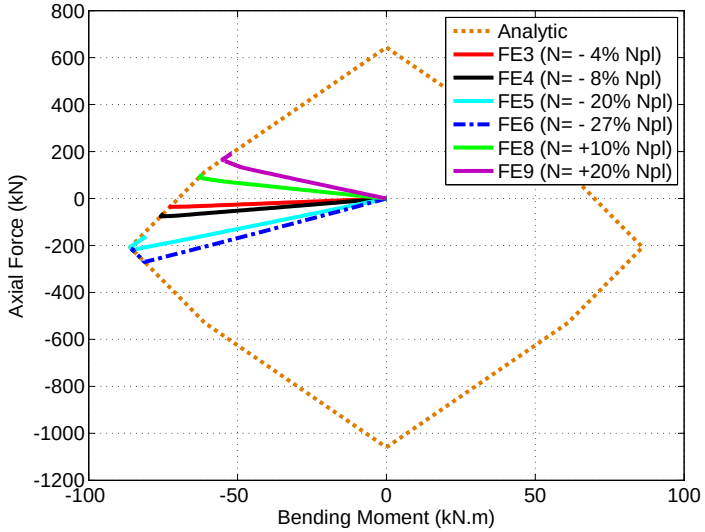

Figure 6.12: Diagramme d'interaction

La surface de charge retenue est bien sûr celle qui donne des résultats proches des valeurs expérimentales. Le modèle proposé inclue un élément de type poutre connecté à une rotule plastique à chacune de ses extrémités (Fig. 6.13). Chacune de ces rotules plastiques est dite rotule plastique généralisée car elle consiste en un ressort longitudinal pour le comportement axial qui reprend l'effort normal N, associé à un ressort spiral pour le comportement en flexion qui reprend le moment fléchissant M. L'interaction (M-N) entre ces deux efforts définit la surface de charge. Un comportement élastique-parfaitement plastic est adopté pour ces rotules généralisées tandis-que la poutre reste en comportement élastique. La prise en compte de la non-linéarité géométrique (effets du second ordre) est obtenue grâce à une formulation corotationnelle du problème. Le facteur q octroi différentes formes à la surface de charge autant dans le cas isotrope que dans le cas anisotrope. Le comportement élasto-plastique est traité par un schéma du type Backward-Euler.

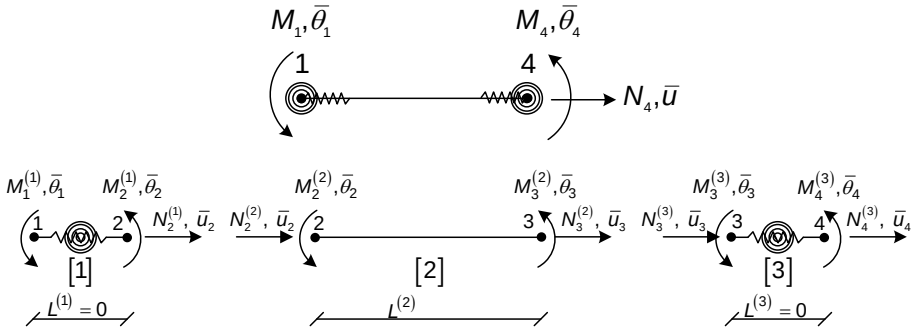

Figure 6.13: Présentation du modèle

6.2.1 Exemples numériques

Plusieurs simulations numériques ont été entreprises dans le cadre de cette étude pour assoir les performances du modèle proposé.

6.2.1.1 Poutre bi-encastrée sous une charge ponctuelle

La première simulation numérique (Fig. 6.14) représente une poutre bi-encastrée développant des rotules plastiques en ses extrémités et sous le point d'application de la charge. Etant donné que le modèle proposé consiste en une poutre avec ses deux rotules, il apparait de part et d'autre du point d'application de la charge une rotule plastique. Différentes surfaces de charge (isotropes et anisotropes) sont testées dont celles présentées sur la Fig. 6.15.

La poutre est testée tout d'abord sous un chargement monotone. La courbe (Force-Déplacement, Fig. 6.16) met en évidence l'apparition des rotules plastiques. On conclut de cette simulation que le comportement fait apparaitre trois étapes : une première étape où les effets du 2^{nd} ordre sont négligeables (avant apparition de la seconde rotule plastique), une seconde étape (avant l'apparition de la 3^{eme} rotule plastique) où les effets du second ordre deviennent modérés (début de la dépendance au facteur q) et une troisième étape où l'effet du 2^{nd} ordre devient significatif et la dépendance au facteur q aussi. L'effet membrane

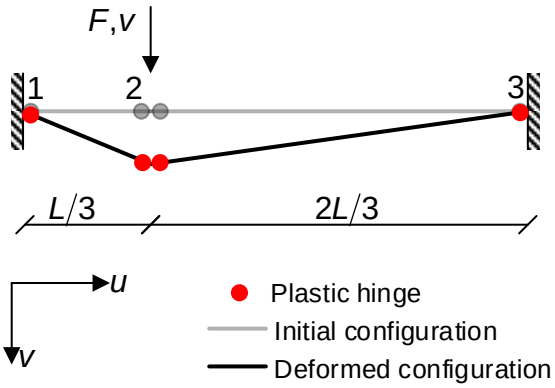

Figure 6.14: Première simulation numérique

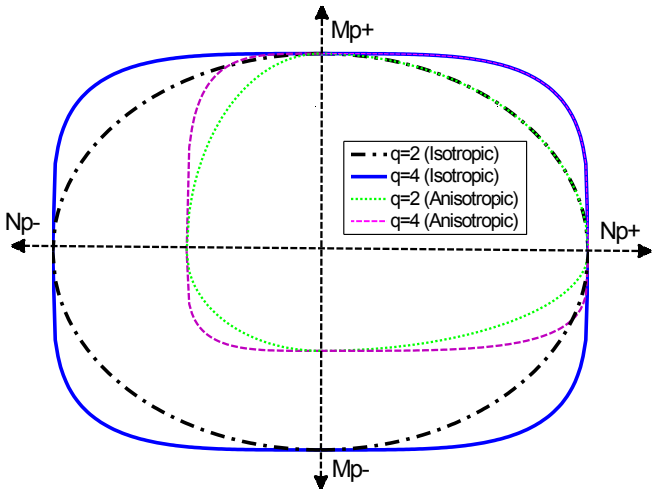

Figure 6.15: Quelques formes de surfaces de charge

devient de plus en plus important au fur et à mesure que le facteur q augmente.

La poutre est soumise ensuite à un chargement cyclique à amplitude croissante (Fig. 6.17) autant en déplacement imposé qu'en force imposée. La réponse de la poutre est symétrique dans le cas d'une surface de charge isotrope et légèrement asymétrique dans le cas anisotrope indépendamment du facteur q (Fig. 6.18). L'accroissement du facteur q a tendance à accroitre l'amplitude de la force.

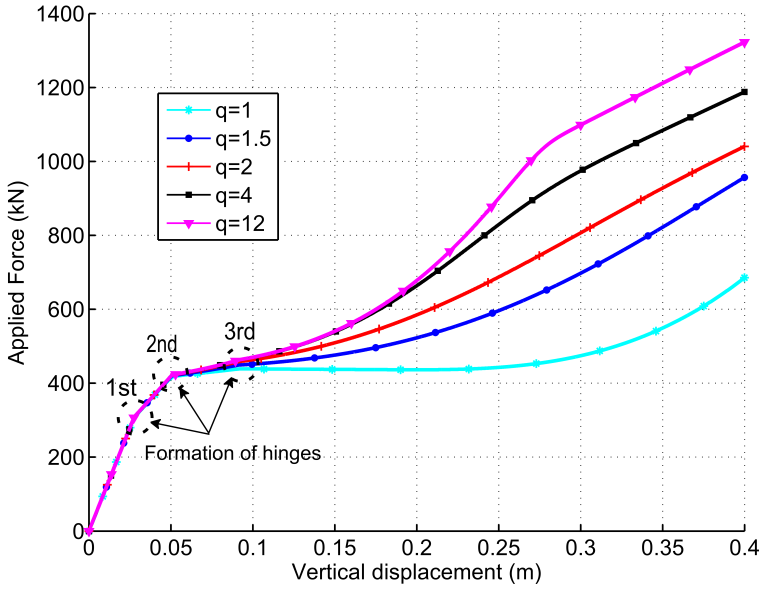

Figure 6.16: Réponse de la poutre sous chargement monotone

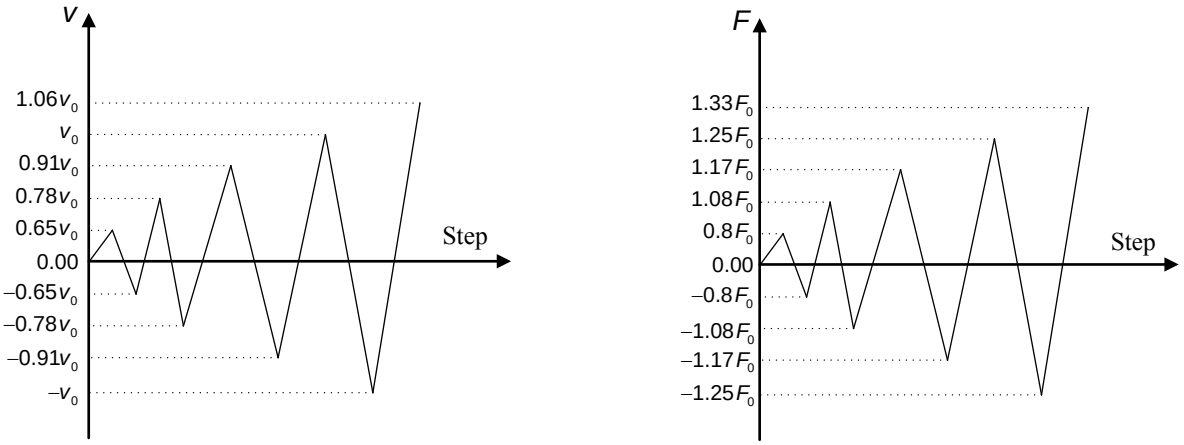

(a) Déplacements imposés (b) Forces imposées

Figure 6.17: Histoire du chargement à amplitude variable

La même poutre est enfin soumise à un chargement cyclique à amplitude constante (F0 = 665 kN). La réponse de la poutre est symétrique autant dans le

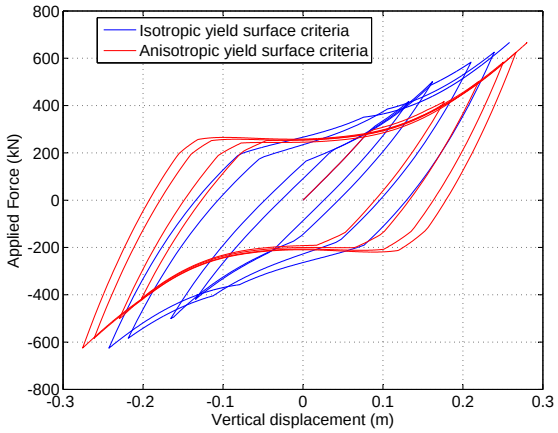

(a) q=2 - Forces imposées

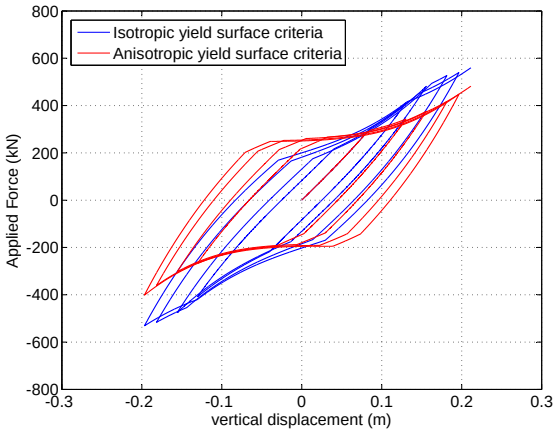

(b) q=2 - Déplacements imposés

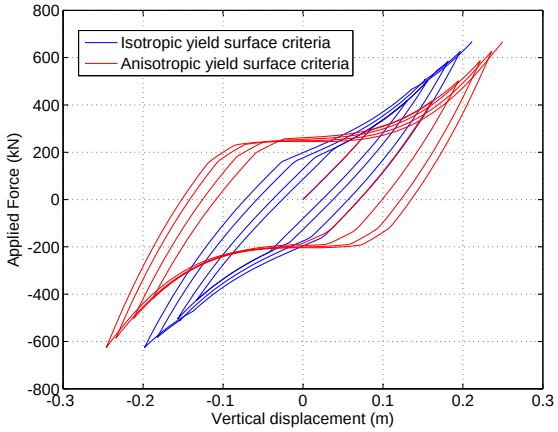

(c) q=4 - Forces imposées

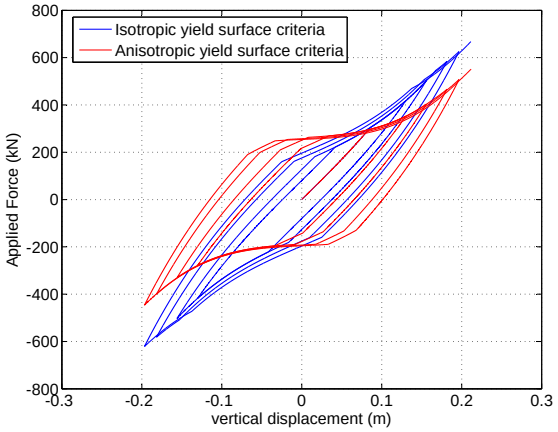

(d) q=4 - Déplacements imposés

Figure 6.18: Chargement cyclique à amplitude croissante

cas d'une surface de charge isotrope que dans le cas anisotrope indépendamment du facteur q (Fig. 6.19).

6.2.1.2 Portique à deux travées

La seconde simulation numérique (Fig. 6.20) traite d'un portique à 2 travées encastré parfaitement à la base de ses 3 poteaux. Les positions des rotules plastiques sont numérotées de 1 à 14. Les éléments finis du modèle proposé sont numérotés de [1] à [7].

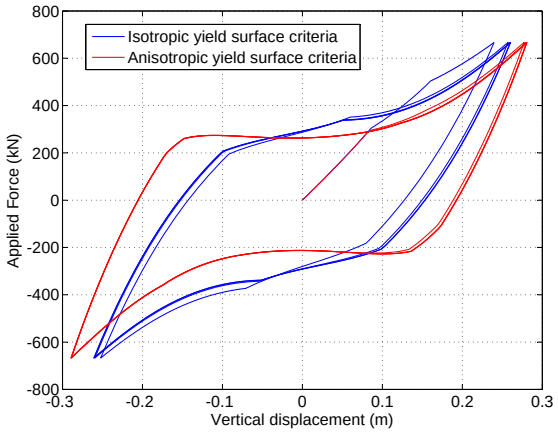

(a) q=2 - Forces imposées

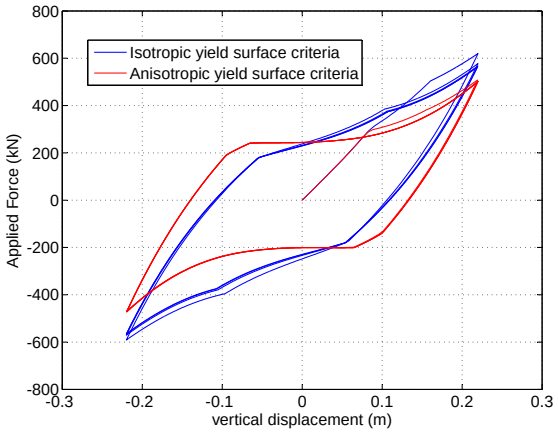

(b) q=2 - Déplacements imposés

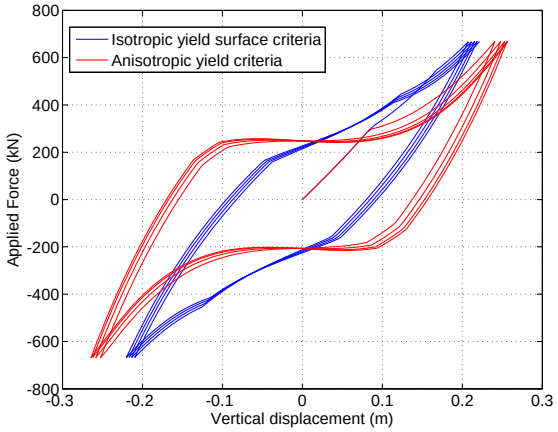

(c) q=4 - Forces imposées

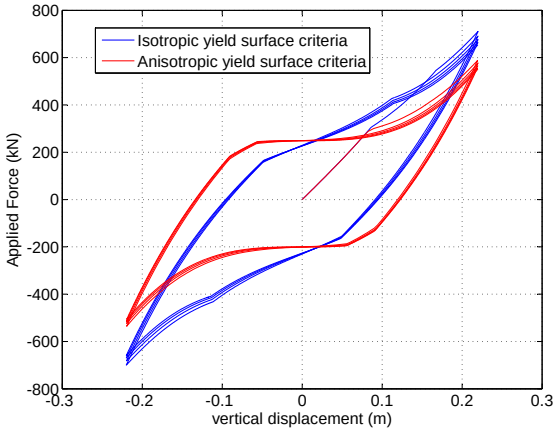

(d) q=4 - Déplacements imposés

Figure 6.19: Chargement cyclique à amplitude constante

L'objectif visé dans cet exemple est de comparer la prise en compte ou pas de l'interaction (M-N) et son effet sur le déplacement latéral de cette structure. Cette comparaison est menée au premier ainsi qu'au second ordre pour un même facteur de rondeur $q = 2$.

- OM-first order : Pas d'interaction (M-N) – 1^{er} ordre.
- OM-second order : Pas d'interaction (M-N) – 2^{nd} ordre.
- IMN-first order : Avec interaction (M-N) – 1^{er} ordre.

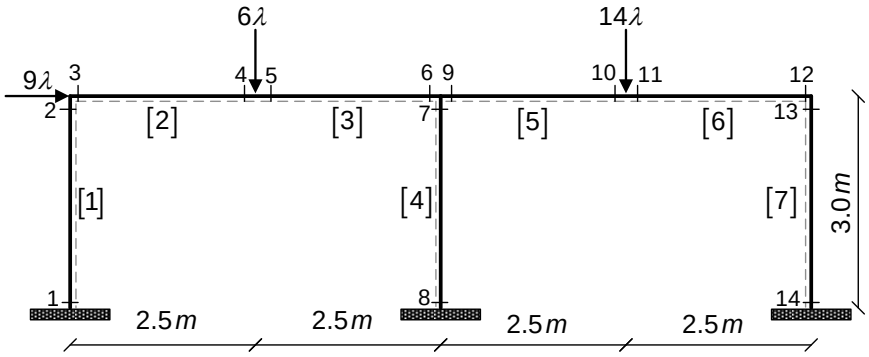

Figure 6.20: Portique à 2 travées

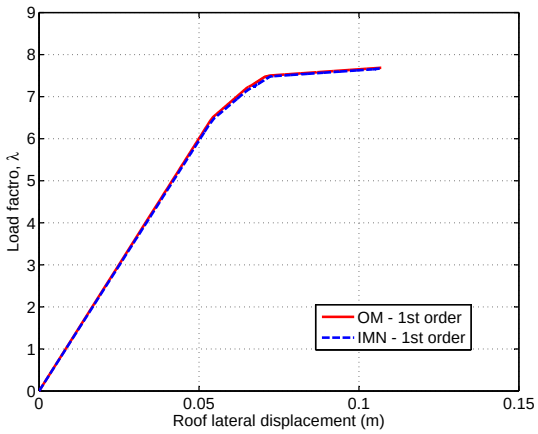

(a) 1^{er} ordre.

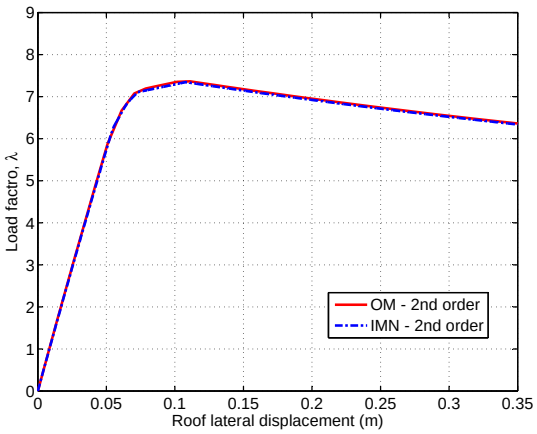

(b) 2^{nd} ordre.

Figure 6.21: Facteur de force λ - déplacement latéral

- IMN-second order : Avec interaction (M-N) – 2^{nd} ordre.

Sur les figures 6.21(a) et 6.21(b), la prise en compte ou pas de l'interaction (M-N) n'a pas une grande influence sur le déplacement latéral de la structure. L'effet du second ordre débute aussitôt que la première rotule plastique apparait (environ à 0,1 m de déplacement latéral). La branche descendante au-delà de cette valeur traduit bien le comportement au second ordre de structures en portiques.

On considère ensuite la configuration (IMN-second order) pour étudier le niveau

maximum de chargement atteint en fonction du facteur de forme q (qui aura pour valeurs : 1, 2 et 10). Le tableau 6.2, résume les résultats obtenus.

On remarque (Fig. 6.22) qu'au-delà de q = 2, l'augmentation de la valeur de

Table 6.2: Influence du facteur q sur le niveau maximum de chargement atteint

q	1	2	10
λ	6.899	7.345	7.387

ce facteur n'a quasiment pas d'influence sur le niveau maximum de chargement atteint. Par contre, entre q = 1 et q = 2 on observe une augmentation d'environ 7% du niveau maximum de chargement atteint.

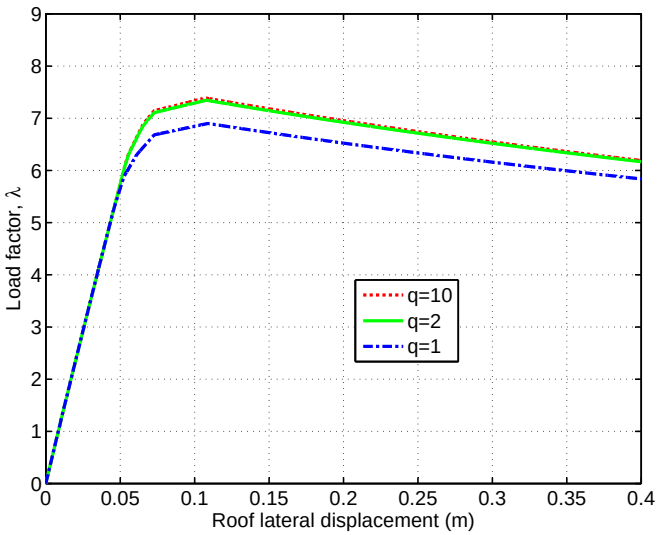

Figure 6.22: Influence du facteur q sur le niveau maximum de chargement atteint λ.

6.2.1.3 Portique simple à une travée

La troisième simulation numérique concerne un portique simple (1 travée) connu sous le nom de portique de Vogel (Fig. 6.23). Contrairement à la précédente

application, l'interaction (M-N) pour q = 2, a une influence significative sur la courbe (Charge-Déplacement latéral). Pour un calcul au 1er ordre, le facteur de charge maximum se trouve multiplié par environ 10 alors que pour un calcul au second ordre, celui-ci se trouve multiplié par environ 2. D'autre part, sur la Fig. 6.24 , on observe encore une fois qu'au-delà de q = 2, l'augmentation de ce facteur n'a quasiment pas d'influence sur le niveau maximum de chargement atteint. De même, entre q = 1 et q = 2 on observe une augmentation d'environ 7% du niveau maximum de chargement atteint.

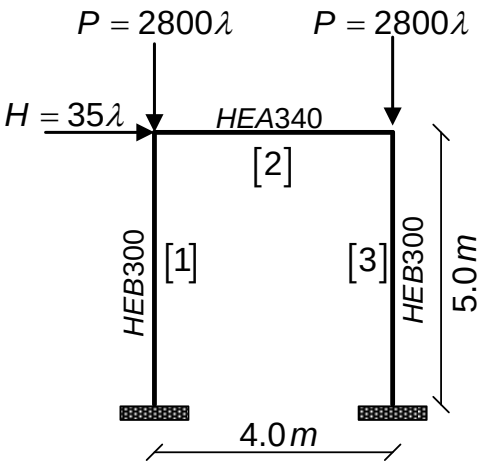

Figure 6.23: Configuration de portique de Vogel

6.2.1.4 Portique à une travée et deux niveaux

La quatrième simulation numérique concerne un portique à une travée et 2 niveaux (Fig. 6.25). l'interaction (M-N) pour q = 2, a une influence significative sur la courbe (Charge-Déplacement latéral). Pour un calcul au 1er ordre, le facteur de charge maximum se trouve augmenté d'environ 25% alors que pour un calcul au second ordre, celui-ci se trouve augmenté d'environ 9%. D'autre part, sur la Fig. 6.26, on observe cette fois-ci que l'augmentation de la valeur du fac-

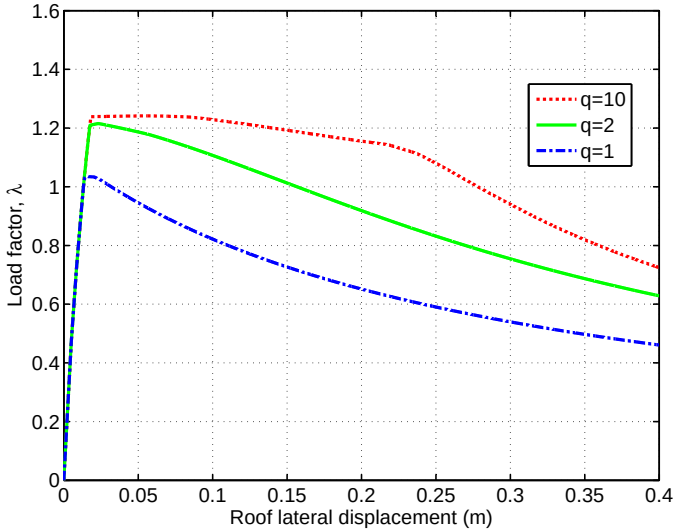

Figure 6.24: Influence du facteur q sur le niveau maximum de chargement atteint λ.

teur q au-delà de 2 augmente encore le niveau maximum de chargement atteint d'environ 10%. De même, entre q = 1 et q = 2 on observe une augmentation d'environ 29% du niveau maximum de chargement atteint. Ces variations sont plus significatives que celles des 2 cas précédents.

6.3 Troisième partie de la thèse

Le transfert des efforts à travers l'interface acier-béton conditionne les performances mécaniques du matériau composite. Outre la prise en compte du glissement de la connexion à l'interface (ce qui est déjà bien assimilé de nos jours), il convient d'inclure aussi le comportement de la connexion vis-à-vis de la traction-compression et de ce fait, le traitement du problème de contact s'impose. On propose dans cette troisième partie un nouveau modèle de contact à l'interface acier-béton des poutres mixtes qui permettra d'étudier son influence sur le glissement (variable de dimensionnement retenue pour la connexion) ainsi que sur la

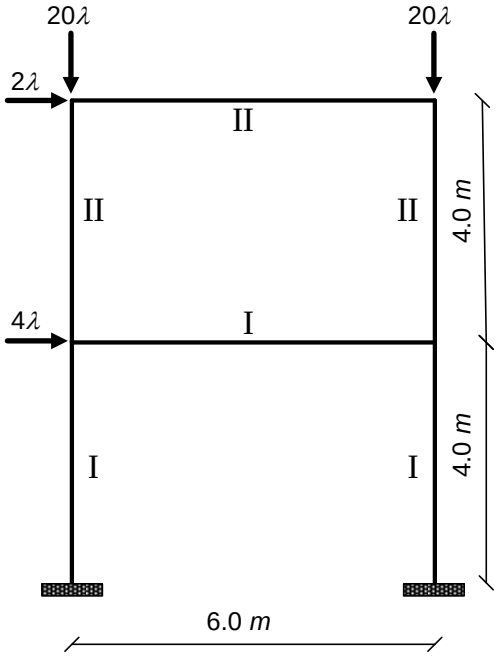

Figure 6.25: Configuration de portique

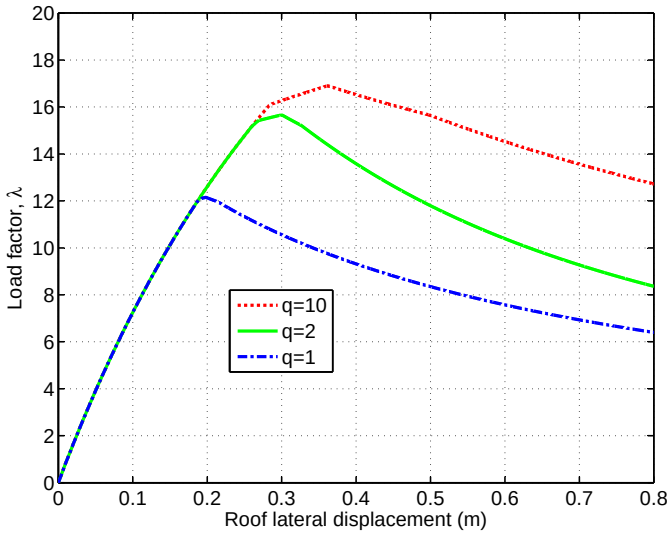

Figure 6.26: Influence du facteur q sur le niveau maximum de chargement atteint λ.

flèche de la poutre. Le problème est traité en petits déplacements, l'hypothèse de non-pénétrabilité entre les deux couches est retenue et la Méthode du Lagrangien augmenté (ALM) est utilisée pour corriger l'interpénétration des matériaux. Pour étendre le traitement du contact « nœud à nœud » à un nouveau contact continu, un concept dénommé «Flying Node Concept » (FNC), est proposé. Il est basé sur le principe d'un maillage adaptatif actualisé au cours du processus itératif.

Plusieurs approches ont été proposée dans la littérature pour traiter le problème de contact nœud-à-nœud notamment : la méthode du multiplicateur de Lagrange, la méthode de pénalité, la méthode d'élimination directe de Nitsche et la méthode du Lagrangien augmenté. Bien que la plupart des codes de calcul utilisent la méthode de pénalité, on préfèrera la méthode du Lagrangien augmenté car elle ne nécessite pas d'incrémenter le facteur de pénalité à des valeurs très élevées pour atteindre la convergence ; le temps de calcul se trouve par ce fait, très réduit.
Lorsque le problème de contact est traité en compression avec l'hypothèse de non pénétration, il va de soi que le soulèvement doit aussi être repéré sur la structure. Ce soulèvement (séparation entre les deux matériaux) peut se produire selon 3 configurations (Fig. 6.27). Dans ces zones, l'algorithme de contact reste inactif. Il convient de préciser que ces zones peuvent varier au cours de l'histoire du chargement.

Dans les zones où il y a contact, le problème consiste à minimiser le potentiel énergétique tout en respectant la condition de non pénétration. Numériquement, ceci consiste à rajouter une équation au système à résoudre pour tout nœud concerné du maillage. Cette équation inclut le multiplicateur de Lagrange, le facteur de pénalité ainsi que la pénétration actuelle. Lorsque le facteur de pénalité augmente, le multiplicateur de Lagrange qui correspond à la réaction induite par un ressort fictif placé en ce nœud augmente et de ce fait, la pénétration entre les deux matériaux est réduite. Lorsque cette pénétration est jugée admissible, le contact est considéré comme corrigé en ce nœud. Il est clair, qu'à chaque nœud correspond un facteur de pénalité adéquat obtenu automatiquement.

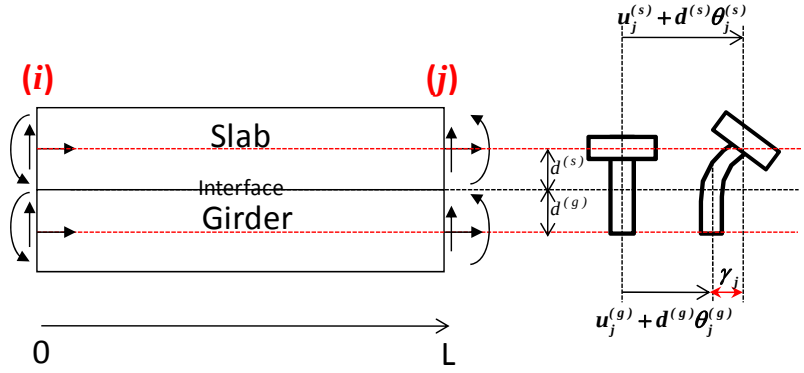

(a) Contact au nœud (i) et (j).

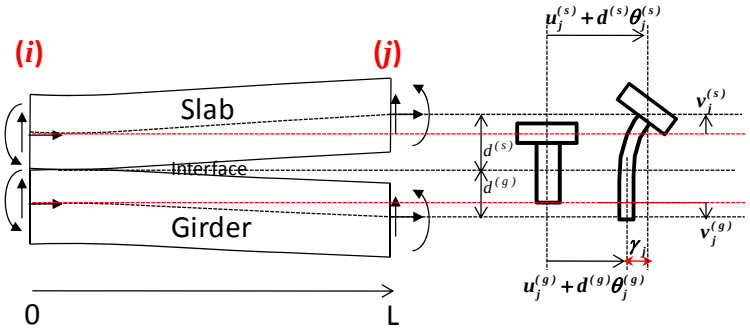

(b) Pas de contact au nœud (j).

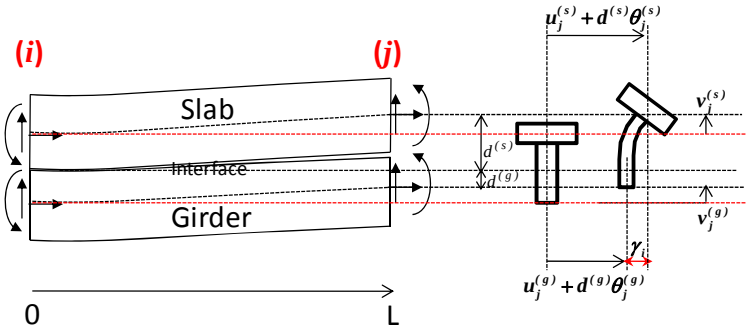

(c) soulèvement au nœud (j).

Figure 6.27: Configuration de soulèvement au poutre mixte

Comme pour le soulèvement, la pénétration peut concerner un nombre de nœuds variable au cours du chargement. Si la dimension réelle du système à résoudre est N et si le nombre de nœuds dont le contact doit être traité à une étape donné du chargement est Nc, le système à résoudre devient alors de dimension $(N + Nc)$. La première nouveauté de l'algorithme proposé est de placer systématiquement toutes les équations supplémentaires Nc à la suite de celles relatives au problème réel (correspondant à N) et non à la position des nœuds concernés dans le système à résoudre (Fig. 6.28). Cet aménagement, facilite la programmation en évitant une réorganisation complexe du système à dimension variable. Lorsque, pour un niveau de charge donné, Nc devient égal à zéro, le système retrouve sa dimension réelle et le chargement peut alors s'incrémenter.

La 2^{eme} nouveauté de l'algorithme proposé concerne le traitement du contact

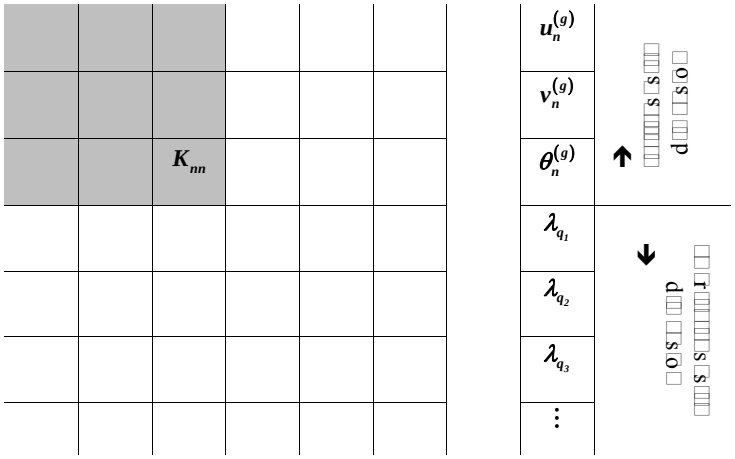

Figure 6.28: Contact est détecté au les nœuds q_i - MLA est activé .

continu au cours des itérations. En effet, au cours de l'histoire de chargement, il peut se produire, sous certaines configurations géométriques et de chargement de la structure étudiée, que le contact soit sur toute une longueur notée de l'élément fini testé en cours (Fig. 6.29).

On montre que cette longueur peut être déterminée en utilisant les fonctions d'interpolation de l'élément fini de poutre mixte. Si la longueur calculée du

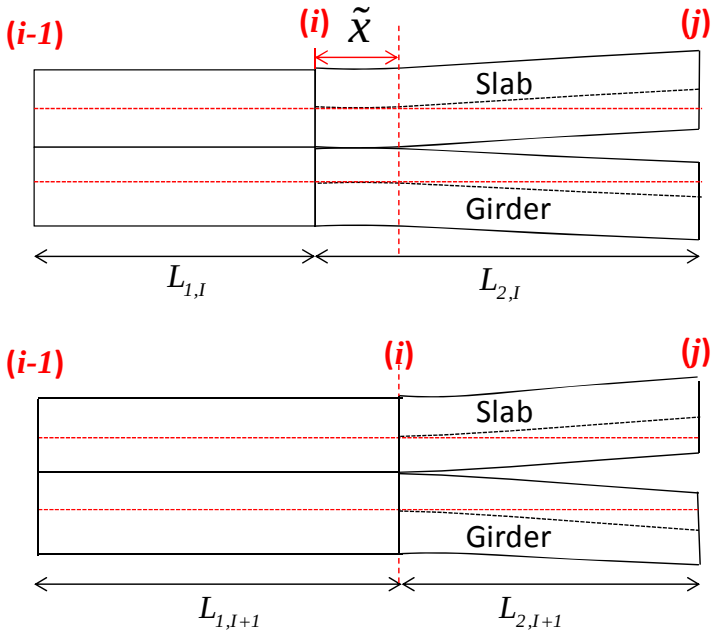

Figure 6.29: maillage adaptatif - *FNC*

contact continu s'avère non nulle, la longueur de l'élément fini est alors corrigée et par conséquent la position du connecteur qui reste lié au maillage aussi.
Dans cette considération (version actuelle du programme), si tous les contacts continus sont corrigés, le maillage modifié avec la répartition de la connexion qui lui correspond est alors traité par un algorithme « nœud-à-nœud » et le chargement se poursuit.
Ce maillage adaptatif, réajuste la répartition finale de la connexion et assure que le contact peut se poursuivre qu'aux nœuds du maillage et être traité par l'algorithme « nœud-à-nœud ». Une seconde option peut aussi être envisagée : ajouter des nœuds non connectés au maillage de la structure. Dans ce cas, même ces nœuds devront subir l'algorithme complet du contact (Fig.6.30).

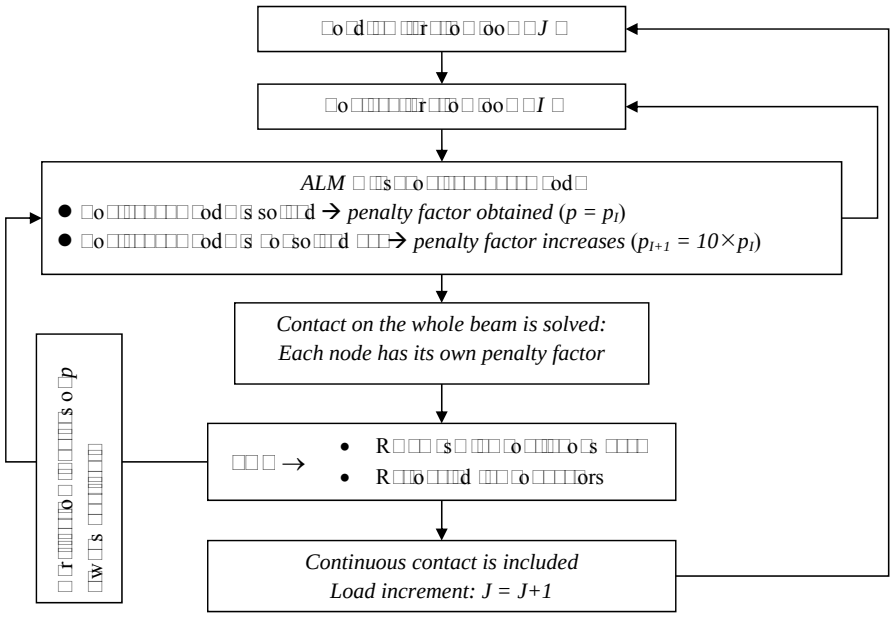

Figure 6.30: Algorithme de contact(ALM + FNC)

6.3.1 Applications numériques

Afin d'illustrer l'efficacité de l'algorithme deux applications sont présentées. Une poutre de pont mixte soumise d'une part, à deux charges concentrées et d'autre part, à une charge repartie et ce, afin d'illustrer l'influence du FNC sur le glissement à l'interface acier-béton.

6.3.1.1 Poutre de pont mixte sous deux chargements ponctuels

Une poutre de pont mixte continue à 2 travées (échelle réduite) a été testée expérimentalement (Fig. 6.31). Les travées sont identiques et de longueur $7900mm$. Deux charges ponctuelles sont appliquées simultanément jusqu'à $550kN$ puis la première charge est maintenue constante alors que la seconde continue d'augmenter jusqu'à $850kN$.

Après avoir mis en évidence l'erreur engendrée entre un calcul qui ne prend pas en compte le traitement du contact et le résultat de mesures expérimentales

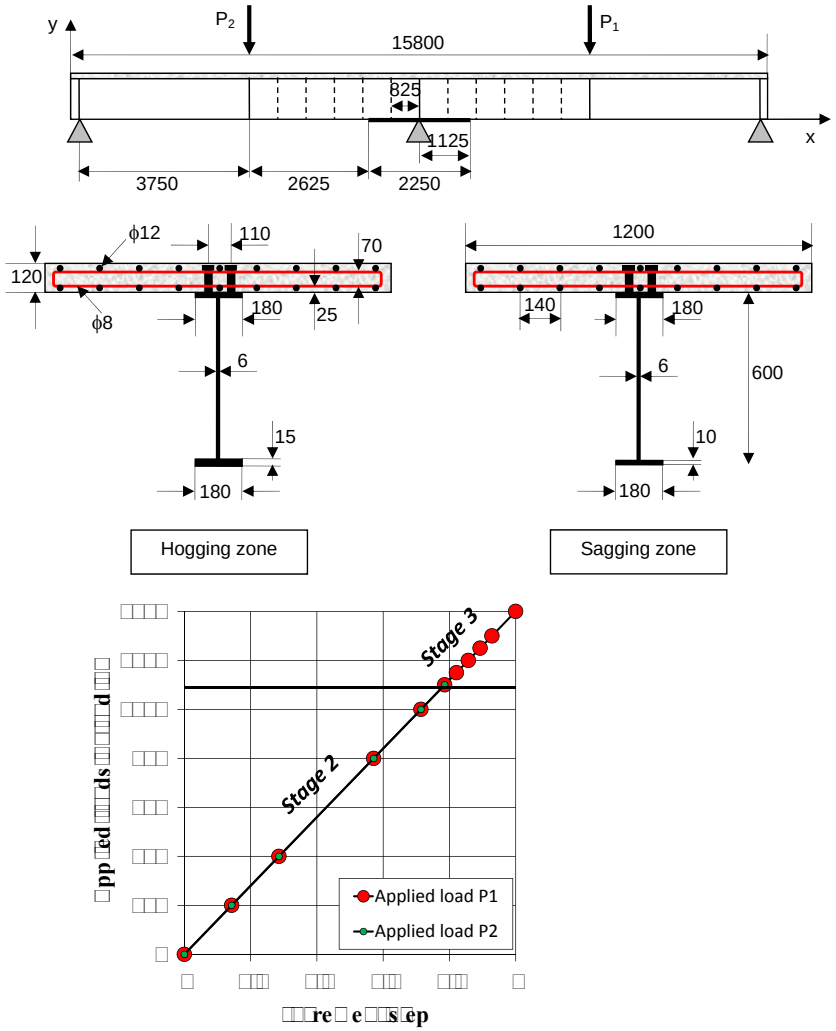

Figure 6.31: (a) Description de la poutre mixte. (b) Les étapes 2 et 3 de chargement

(par le biais d'une courbe charge cumulée-déplacement sous chaque charge), on montre sur un profile longitudinal que :

- Les zones traitées sont celles situées sous les charges concentrées.
- La pénétration du béton dans l'acier a été corrigée.
- Les zones de soulèvement ont été repérées (léger soulèvement proche de l'appui intermédiaire).

- Les rotations des sections sous charges ont aussi été par conséquent, corrigées.

- Le glissement des connecteurs sont aussi affectés lors du traitement du contact.

Le soulèvement pourrait être relativement plus important dans le cas de chargement fortement dissymétrique de part et d'autre de l'appui intermédiaire. Le glissement étant la variable de dimensionnement de la connexion, il convient donc de tenir compte de l'effet que peut engendrer le traitement du contact sur cette variable.
Bien que l'option FNC soit aussi activée, aucune zone de contact continu n'a été détectée.

6.3.1.2 Poutre de pont mixte sous un chargement réparti

Afin de mettre en évidence l'option FNC. La poutre continue de pont mixte de l'application précédente est soumise cette fois-ci à un chargement uniformément réparti p. En effet, sous un tel chargement, il y a plus de chance que le contact continu soit détecté. La simulation numérique montre comment le maillage s'adapte au contact continu détecté au cours de l'histoire du chargement (Fig. 6.32). Néanmoins, il semble plus important de regarder les changements engen-

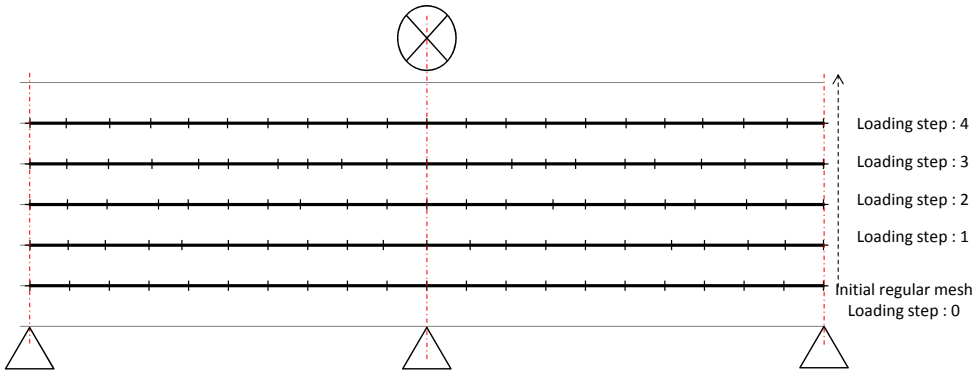

Figure 6.32: Le maillage au cours de chargement.

drés au niveau local. Les deux sections transversales les plus critiques (une en travée et l'autre sur appui intermédiaire). La charge est croissante jusqu'à atteinte

du moment élastique résistant sur appui intermédiaire. Le calcul des contraintes en sections permet d'obtenir les résultats illustrés en termes de moments sollicitant. On montre que le moment élastique résistant $\left(M^{-}_{el,Rd} = -871\ kNm\right)$ est atteint :

- pour $p = 280\ kN$ avec (ALM seul), et en travée le moment atteint est :$(M^{+}_{s} = 570\ kNm)$
- pour $p = 264\ kN$ avec (ALM+FNC), et en travée le moment atteint est :$(M^{+}_{s} = 548\ kNm)$

Pour des codes de calculs qui ne traitent que le contact ponctuel (ALM seul), une charge $p = 264\ kN$ donnerait les moments sollicitant suivants $(M^{+}_{s} = 534\ kNm)$ en travée et $(M^{-}_{s} = -821\ kNm)$ sur appui.
Pour cet exemple, le moment en travée est sous-estimé d'environ 3% et sur appui intermédiaire d'environ 6%.

INSA de RENNES
Service des Formations

AVIS DU JURY SUR LA REPRODUCTION DE LA THESE SOUTENUE

Titre de la thèse:
Computational tools for nonlinear analysis of steel and composite steel-concrete structures considering connection behaviour : Application to buildings and bridges

Nom Prénom de l'auteur : ALHASAWI ANAS

Membres du jury :
- Monsieur HJIAJ Mohammed
- Monsieur COUCHAUX Maël
- Monsieur GUEZOULI Samy
- Monsieur LIMAM Ali
- Monsieur JASPART Jean-Pierre
- Monsieur BOUCHAIR Hamid
- Monsieur FENG Zhi-Qiang

Président du jury : Zhi-Qiang FENG

Date de la soutenance : 17 Janvier 2017

Reproduction de la these soutenue

Thèse pouvant être reproduite en l'état
~~Thèse pouvant être reproduite après corrections suggérées~~

Fait à Rennes, le 17 Janvier 2017

Signature du président de jury

Le Directeur,

M'hamed DRISSI

17 JAN. 2017

INSTITUT NATIONAL des SCIENCES APPLIQUÉES · RENNES ·

Résumé

Cette thèse a pour objectifs de développer une modélisation aussi fine que possible des structures aciers et mixtes acier-béton sous sollicitations cycliques avec prise en compte d'une part du comportement des assemblages et d'autre part des non-linéarités géométriques et du contact à l'interface acier-béton. Notre attention porte en particulier sur l'assemblage de type poutre acier/mixte sur poteau métallique par platine d'extrémité boulonnée. L'objectif étant de proposer un modèle « élément fini » d'assemblage qui reproduit aussi fidèlement que possible le comportement cyclique de ce dernier pour ensuite l'assembler à un élément fini de poutre non-linéaire acier ou mixte avec prise en compte, pour ce dernier, du soulèvement à l'interface. Le travail se compose de 3 parties distinctes.

Un premier modèle qui se base sur la méthode des composantes a été développé ayant pour objectif de suivre la déformation de chaque composante au cours des cycles et de prendre en compte les non-linéarités induites par la séparation entre la platine d'extrémité et la semelle du poteau auquel elle est boulonnée. Ce modèle type composantes, a été développé pour une rangée de boulons. Dans le cas le plus fréquent, de deux rangées de boulons, une résistance de groupe (en plus des résistances individuelles de chacune des rangées) est susceptible de se développer. Pour rendre compte de ce phénomène, nous avons implanté le modèle proposé par Cerfontaine qui repose sur la définition d'une surface de charge et une règle d'écoulement associée pour déterminer les allongements des ressorts équivalents. Seul le cas de plasticité parfaite est considéré. Il est mis en évidence que l'influence de l'effet de groupe s'avère non négligeable sur le comportement post-élastique de l'assemblage et donc de la structure.

Dans une seconde phase, nous proposons un modèle de poutre métallique classique en grands déplacements (approche co-rotationnelle) avec rotules généralisées aux extrémités. Nous faisons l'hypothèse que les déformations plastiques sont concentrées aux rotules dont le comportement plastique est contrôlé par une surface de charge asymétrique (anisotrope) qui peut prendre différentes formes selon la valeur donnée à un facteur q dit « facteur de forme ». Chacune de ces rotules plastiques comprend un ressort longitudinal pour l'effort normal N et un ressort spiral pour le moment fléchissant M. L'interaction (M-N) entre ces deux efforts dans le domaine plastique est régie par le critère de plasticité. Le modèle de rotule plastique généralisé proposé permet de rendre compte de l'adoucissement cyclique, de la ductilité et du « pinching effect ». Nous montrons aux travers de plusieurs exemples la pertinence mais également les limites d'une telle approche.

Dans une troisième partie, nous proposons un nouvel élément fini de poutre mixte (à 6 ddl par nœud) en petits déplacements avec prise en compte de la non-linéarité matérielle de la poutre ainsi que du contact entre l'acier et le béton. Une stratégie efficace de type nœud mobile (Flying Node) est proposée pour déterminer l'étendue de la surface de contact au sein d'un élément fini et d'adapter le maillage de l'élément poutre/poteau. Pour la résolution du problème de contact, la technique du Lagrangien Augmenté a été retenue. On montre que dans certaines situations, le soulèvement modifie la redistribution des efforts.

Abstract

The goal of this thesis is to develop computational tools for the nonlinear analysis of steel and composite steel-concrete structures under cyclic loading taking into account the actual behaviour of joint, material and geometry non-linearities and contact conditions at the steel-to-concrete interface. In particular, our efforts focuses on typical bolted end-plate connection between steel or composite beam and steel column. The objective is to develop a new «joint finite element" able to reproduce accurately the cyclic behavior of the beam-to-column connection. Next this model is combined with a non-linear steel/composite beam element considering slip and possible uplift at the interface. The thesis consists of three major parts.

The first part deals with the behavior of a steel beam-to-column bolted end-plate connection under arbitrarily cyclic loading. The proposed model is based on an improved component method that closely follows the deformation of each component taking into account non-linearities induced by possible gap between the column flange and the end-plate. This model has been developed for a single row connection. In the case of multiple row bolted connection group effects may develop. Possible group effect between two bolt-rows has been implemented considering the model proposed by Cerfontaine based on the definition of the multi-surface yield criterion and the associated flow rule that govern deformation of equivalent springs. Only the case of perfect plasticity is considered. It is shown that the influence of the group effect is not negligible on the nonlinear response of the joint.

In the second part, we have developed a flexible co-rotational two-noded beam with generalized elasto-plastic hinges at the beam ends. It is assumed that plastic deformations concentrate at these hinges. These hinges have the ability to elongate/shorten along the beam axis and to rotate. A family of asymmetric and convex yield surfaces of super-elliptic shape is considered for the plastic behavior of the hinges. By varying the roundness factor, an infinite number of yield surface are obtained. It is shown that the nonlinear response of bolted connections subjected to both bending and tension are conveniently modeled with such a yield surface. It was observed that cyclic loading produces pinching effect, cyclic softening and ductile behavior. Advantages and limitations of the approach are discussed.

Finally, the third part is dedicated to the problem of contact at the interface of steel-concrete composite beams. A “new” finite element for composite steel-concrete beam is proposed. The beam element has 6 degrees of freedom per node. The concrete beam is allowed to separate from the steel beam. An efficient contact algorithm is proposed. The Flying node concept is introduced and used to determine the extent of the contact area within a single element and modify the mesh of the beam structure. The contact problem is solve using the Augmented Lagrangian Method. The influence of contact on the loading capacity of the beam and also its influence on some design variables are highlighted.

INSA RENNES

N° d'ordre : 17ISAR 01 / D17 - 01

Institut National des Sciences Appliquées de Rennes
20, Avenue des Buttes de Coësmes - CS 14315 - F-35043 Rennes Cedex
Tél : 02 23 23 82 00 – Fax : 02 23 23 83 96